Interaction laser-plasma ultra-intense à densité proche-critique pour l'accélération d'ions.

Florian Mollica

▶ To cite this version:

Florian Mollica. Interaction laser-plasma ultra-intense à densité proche-critique pour l'accélération d'ions.. Physique [physics]. Université Paris Saclay (COmUE), 2016. Français. NNT : 2016SACLX058 . tel-01690793

HAL Id: tel-01690793
https://pastel.hal.science/tel-01690793

Submitted on 23 Jan 2018

NNT : 2016SACLX058

Thèse de doctorat
de
L'Université Paris-Saclay
préparée à
L'École Polytechnique

École doctorale n° 572 : Ondes et Matières

Spécialité doctorale "Physique des plasmas"

par

Florian Mollica

Ultra-intense laser-plasma interaction at near-critical density for ion acceleration

Thèse présenté et soutenue à l'ENSTA le 19 Décembre 2016

Composition du Jury

Pr. P. McKenna,	University of Strathclyde	Rapporteur
Pr. E. D'Humières,	Université de Bordeaux	Rapporteur
Pr. J. Santos,	Université de Bordeaux	Président du Jury
Pr. Malka,	CNRS	Directeur de thèse
Dr. Flacco,	ENSTA	Co-encadrant de thèse

Pour Marie,

Résumé

L'interaction d'un laser ultra-intense et ultra-court avec la matière donne naissance à une grande variété de processus issus du couplage des champs électromagnétiques avec le plasma. Ce couplage hautement non-linéaire excite des phénomènes plasmas collectifs capables de soutenir des champs intenses pouvant dépasser le $\mathrm{TV} \cdot \mathrm{m}^{-1}$. Ces champs ouvrent la possibilité de réaliser des accélérateurs de particules compacts, aussi bien d'électrons que d'ions. Des sources laser-plasma d'ions de plusieurs dizaines de MeV ont été démontré au début des années 2000, et depuis, de nombreuses applications ont été proposées : création d'isotope d'intérêt médicaux, réaction de spallation, étude de la matière dense, chauffage de combustible de fusion nucléaire, radiobiologie à haut débit de dose. De nombreux mécanismes ont été suggérés afin d'améliorer les propriétés d'énergie, de collimation et de mono-chromaticité du faisceau d'ions. Historiquement, les sources d'ions par laser ont été obtenues sur des cibles solides, dîtes sur-dense, mieux adaptées à l'absorption du laser. L'innovation sur les cibles a été un moteur majeur de l'amélioration de ces sources. Dans la continuité de cette dynamique, l'utilisation de cibles gazeuses, auto-réparatrices par nature, a été proposé afin d'alléger les contraintes de contraste laser et de taux de répétitions. De récentes démonstrations expérimentales sont venus renforcer l'intérêt pour ces cibles, dîtes sous-denses ou proche-critiques, de par leur densité intermédiaire. Cette densité est propice à la propagation, à l'absorption du laser et à la création des structures accélératrices que sont les chocs plasmas, et les vortex magnétiques. Les travaux présentés dans cette thèse constituent une exploration expérimentale des paramètres plasmas nécessaires à l'accélération d'ion dans des cibles de jet de gaz de densité proche-critique. Pour la première fois ces régimes sont explorés avec un laser ultra-intense femtoseconde de 150 TW. Une partie des travaux est consacrée à la réalisation d'une cible innovante, adaptée aux contraintes de densité et de gradients plasma requises par ces régimes. Ensuite les travaux expérimentaux décrivent la propagation du laser et l'accélération d'électrons dans des cibles proche-critiques. Enfin une dernière partie décrit la production d'un faisceau d'atome issue d'une source d'ions laser.

Le premier chapitre introduit les notions de base de l'interaction laser-plasma, particulièrement aux densités proche-critiques. Sont présentés les grandeurs caractéristiques des mouvements collectifs plasmas. Les plasmas étudiés ici sont cinétiques et non-collisionnels. L'interaction avec le laser est dite relativiste, car les éléctrons soumis au champ laser atteignent des vitesses proches de c. Le laser subit des effets relativistes d'auto-focalisation, d'apparition d'un choc optique et de dérive de fréquence. Le plasma peut sous certaines conditions développer des chocs acoustiques ou des gradients raides : la séparation thermique de charge résultant de ces phénomènes peut créer un champ accélérateur pour des ions. Deux régimes sont décrits : le Collisionless Shock Acceleration (CSA) et Magnetic Vortex Acceleration (MVA). Le CSA requiert une densité électronique n_e de 10 à $20n_c$ et des longueurs de gradients de l'ordre de λ, tandis que le MVA requiert $n_e = 0.1$-$5n_c$ et des longueurs de gradients $\approx 20\lambda$.

Le second chapitre étudie la propagation d'un laser ultra-court et ultra intense dans un plasma proche-critique avec des gradients et des densités accessibles expérimentalement. Les caractéristiques de l'interaction sont telles que $a_0 = 4$, $P >> P_{cr}$, $w_0 > w_m$, $n_e = 0.15 n_c$ et la longueur de gradient est de 50λ. Dans une première phase le laser excite une onde de sillage non-linéaire dans le plasma, puis subis une auto-focalisation selon les lois d'échelle de Sprangle, jusqu'à un diamètre d'équilibre w_m. L'auto-compression démarre ensuite selon les lois de Vieira et al.. Ces deux phénomènes accroissent a_0 jusqu'à atteindre un régime instable dit de "blow-out" où une cavité vide d'élétrons se forme derrière le laser. L'injection et l'accélération d'électrons dans cette cavité se produit quand le diamètre d'équilibre du laser est atteint. Les électrons rattrapent le laser et l'énergie laser est transférée au plasma et au faisceau d'électrons. Le faisceau atteint des énergies $> 100\,\mathrm{MeV}$. Les ions légers du plasma (les protons) réagissent à l'onde de sillage électronique, qui leur donne un moment transverse. Les ions plus lourds (Argon, hélium) forment une onde de choc transverse. Dans ces conditions, aucune accélération d'ions vers l'avant, ni de choc longitudinal n'est observé. Les modulations du laser conduisent à sa filamentation et empêche sa propagation à travers une cible pourtant non-opaque ($n_e = 0.15 n_c$). Des gradients plus raides, et une énergie laser plus intense, sont nécessaires pour déclencher les mécanismes d'accélérations du CSA et du MVA. Le chapitre suivant décrit un nouveau type de cible proche-critique qui permet de raidir les gradients de densité et de se rapprocher des conditions voulues.

La découverte de nouveaux mécanismes d'interaction laser-plasma a souvent été portée par les innovations sur les cibles. Les limitations du TNSA sur cible solide par exemple, ont donné naissance aux cibles structurés, aux cible-réseaux, aux cible-gouttelettes, aux nanofilaments. Ces cibles permettent de mieux absorber et mieux confiner l'énergie laser. Devant le défi soulevé par la hausse du taux de répétition sur cibles solides, les cibles gazeuses (auto-réparatrices par nature) ont reçu un regain d'intérêt. Cependant elles avaient jusqu'à présent de faibles densités et des gradients peu raides. Nous démontrons dans le troisième chapitre la possibilité de surmonter ces défauts en façonnant un profil de jet de gaz par la superposition de ligne de chocs hydrodynamiques, avec une buse compacte. La position des lignes de choc peut être prédit avec précision. Notre buse crée une densité d'hélium gazeux de $3.5 \times 10^{20}\,\mathrm{cm}^{-3}$ ($n_e = 0.4 n_c$) avec une largeur à mi-hauteur de $120\,\mu\mathrm{m}$ à une distance de sécurité de $600\,\mu\mathrm{m}$ de la buse. La longueur de gradient de $\approx 50\lambda$ est meilleur que celles explorées dans le reste de la littérature sur jet de gaz. Les moyens d'améliorer ces valeurs sont évoqués.

Le chapitre 4 présente les expériences réalisées dans la plateforme expérimentale SAPHIR au LOA ($a_0 =$ 4-7, $E = 3\,\mathrm{J}$, $w_0 = 5\,\mu\mathrm{m}$, $\tau = 25\,\mathrm{fs}$) avec des cibles de complexité croissante. L'objectif de ces expériences est d'observer la zone de déplétion du laser, sa perte de symétrie, les propriétés du faisceau d'électrons accéléré, ainsi que la présence d'ions accélérés vers l'avant. Nous observons que dans le gradient doux d'une cible sonique d'hélium à $0.1 n_c$, il est possible de guider le laser vers la face arrière de la cible. Le laser ne peut pas traverser une cible de densité équivalente aux gradients raidis par des chocs hydro. On observe l'expansion d'une onde de choc ionique transverse, ainsi qu'un faisceau d'électron jusqu'à $(100 \pm 25)\,\mathrm{MeV}$ modulé spatialement. Nous avons observé des protons accéléré vers l'avant ($> 1\,\mathrm{MeV}$) sur cible sonique, sans parvenir à identifier les paramètres nécessaires à la reproduction du résultat. Les améliorations des diagnostiques de mesure sont discutés.

Le cinquième chapitre explore une autre utilisation des jets de gaz : la neutralisation d'un faisceau d'ion accéléré par laser : Nous démontrons la création d'un jet d'hydrogène atomique par recombinaison collisionelle d'un faisceau de proton accéléré par TNSA. Le taux de conversion atteint $\approx$100 % pour des protons incidents de 80 keV. Une valeur bien au-dessus des prédictions de transfert de charge simples, mais en accord qualitatif avec d'autres observations récentes. Les rayons X mous et les électrons co-propageant peuvent altérer le jet de gaz neutralisant, ainsi que la présence de clusters. L'exploration de ces mécanismes est importante pour comprendre le transport et les altérations des faisceaux d'ions créés par laser.

La dernière section propose une perspective sur le futur développement des expériences sur cibles proches critiques. L'accent est porté sur 1) l'importance du développement des cibles raides grâce aux chocs hydro et d'une caractérisation in-situ des profils de gaz 2) La nécessité d'améliorer les diagnostiques plasmas et laser dans ces régimes de densité proche de l'opacité. 3) Le développement de diagnostiques de détection d'ion fiables et sans ambiguïtés, aussi bien spatial que spectral. A la lumière des premiers résultats présentés dans cette thèse, nous avons tracé une limite dans l'espace des paramètres adéquats pour l'accélération d'ions par laser et nous avons évalués les conditions que doivent remplir les diagnostiques. J'espère que cela ouvrira de nouveaux développement dans ce domaine fascinant.

Abstract

Interaction of ultra-intense, ultra-short laser with matter gives rise to a wealth of phenomena, due to the coupling between the electromagnetic fields and the plasma. The non-linear coupling excites collective plasma processes able to sustain intense electric fields, up to $1\,\mathrm{TV}\cdot\mathrm{m}^{-1}$. This property spurred early interest in laser accelerator as compact, next-generation source of accelerated electrons and ions. Laser-driven ion source of several MeV had been demonstrated in early 2000. In the wake of this result, numerous applications had been proposed: isotope production of medical interest, spallation reaction, isochoric heating for Warm-Dense-Matter or nuclear fusion, radiobiology at high dose rate, protontherapy. Various mechanisms had been suggested to improve the mains properties of the beam (chromaticity, maximum energy, collimation). These first ion sources have been obtained on solid targets, called "overdense", and better suited for laser absorption. Target innovation has driven the improvement of these sources. In the continuity of this dynamic, new gaseous targets had been proposed in order to relax the constraints that solid targets impose on laser contrast and repetition rate. Recent experimental demonstrations of monoenergetic ion acceleration in gas renew the interest in such targets, called under-dense or near-critical because of their intermediate density. At near-critical density the laser can propagate, but undergoes significant absorption, giving rise to the accelerating structures of plasma shock and magnetic vortex. The work presented in this thesis is an experimental exploration of the plasma conditions required to drive ion acceleration in gaseous near-critical target. For the first time, these regimes are explored with an ultra-intense, femtosecond laser of 150 TW. A part of this work has been dedicated to the design and construction of an innovative gas target, in order to achieve plasma density and gradients appropriate for these new acceleration regimes. Then the experimental works describe laser propagation and electron acceleration in near-critical targets. Finally the last part reports the efficient production of an atomic beam neutralized from a laser-driven ion source.

Contents

Introduction and state-of the art

Lasers have a special place in the history of science. They existed in the collective psyche before being discovered in laboratory. From the "burning lenses" of Archimede of Syracusa, to the premonitory "Heat Ray" of H.G. Wells in his "War of the Worlds", the idea of a directed beam of energy was a long time dream. After the first LASER was finally build in May 1960 [Maiman, 1960], applications and innovations exploded, often with less destructive outcomes than in Well's vision. The first laser eye-surgery was performed as early as December 1961. In 1962 Q-switching proved the possibility to emit bright pulses of laser light. Soon, the laser became an uniquely potent tool for communication, spectroscopy, imaging and surgery. In 1985, the breakthrough of the CPA technology (*Chirped Pulse Amplification*) [Strickland and Mourou, 1985] allowed to decrease dramatically laser pulse duration, and to pave the way for decades of innovation in the development of ultra-intense, ultra-short laser science. The interaction of intense laser pulses with matter gave rise to a number of new phenomena with a wealth of nonlinear physic processes. It opened numerous research fields, such as laser-particle acceleration, bright X-Ray sources, high harmonic generation, attosecond physics and XUV lasers.

The high intensities produced by laser beam today allow the rapid ionization of the irradiated target, The matter becomes a plasma, *i.e.* a gas of electrons and positive ions whose collective behaviour is coupled with electric and magnetic fields. Due to the coulombian interaction, plasmas are self-organized, and develop non-linear waves, instabilities, turbulences, and out-of-thermal-equilibrium dynamics. A laser pulse can excite and control these collective behaviors. Above $\approx 1 \times 10^{18}\,\mathrm{W \cdot cm^{-2}}$, an optical field is said *relativistic*: it is strong enough to drive electrons close to the speed of light. The resulting non-linearities in the laser propagation lead to intricate interactions between the plasma and the laser, yielding rich phenomenas. In addition, plasmas have the unique ability to sustain high electric fields up to $1\,\mathrm{TV \cdot m^{-1}}$ [Malka et al., 2002], six orders of magnitude above the fields of RF cavities from conventional accelerator. This property spurred early interest in laser accelerator as compact, next-generation source of accelerated electrons [Tajima and Dawson, 1979] and ions [Veksler, 1957]. Nowadays, several large-scale facilities demonstrated PetaWatt peak power [Danson et al., 2015], typical ultrashort PetaWatt laser systems deliver 30 J within 20 fs, resulting in a peak intensity of $\approx 1 \times 10^{21}\,\mathrm{W \cdot cm^{-2}}$. Intensities above $1 \times 10^{22}\,\mathrm{W \cdot cm^{-2}}$ will be soon available with new 10 PW projects, extending further this exciting field of research.

The work presented in this thesis is a part of the SAPHIR project, hosted in the Laboratory of Applied Optics, in Palaiseau (LOA). The SAPHIR project is a joint venture between several academic and industrial stakeholders, and is co-funded by OSEO-BPI. It includes the LOA, the Commissariat à l'Énergie Atomique (CEA) Lydil teams, The Gustave Roussy Institute, The Curie Institute, Amplitude Tech., Dosisoft and Imaging optics. The project's goals are split along two axes. First, the SAPHIR facility is exploring the possibility to use laser-accelerated ions for medical applications. Half of the experimental time is devoted to the study of radiobiology with extreme and unexplored dose rate ($> 1 \times 10^9\,\mathrm{Gy \cdot s^{-1}}$). The second axis, and the subject of this thesis work, is the experimental exploration of innovative ion acceleration scheme and targets.

This introduction presents the state of the art in laser ion acceleration, and replaces the objectives and conclusion of this work into their scientific context. A detailed outline is found at the end of this introduction.

Ion Acceleration Mechanisms

Target Normal Sheath Acceleration

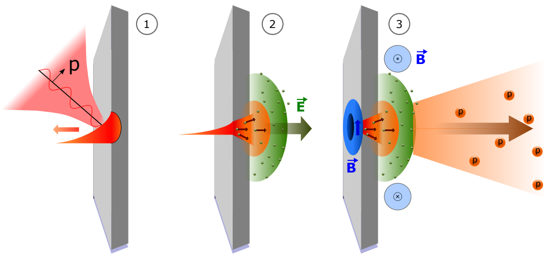

Figure 1 – Scheme of TNSA (1) The laser irradiates the front surface of a thin foil (µm thick). The laser field ionizes and heats electrons at the front surface. Hot relativistic electrons cross and scatter through the target and ionize the rear side. (2) A hot electron cloud co-exist with a sharp gradient of cold ions. The resulting charge separation induces a field normal to the rear surface. Mega Gauss magnetic fields at the front and rear surface collimate the hot electrons and sustain the E-field. (3) The rear plasma experiences a self similar and quasi neutral expansion into vacuum. Particle adsorbed at the surface are accelerated by this field inside a cone.

Early demonstrations of laser-accelerated ions were achieved in gas jet [Krushelnick et al., 1999], clusters [Ditmire et al., 1997] and thick solid targets [Fews et al., 1994]. These teams observed ions in the MeV range with an emission rather isotropic and thus, not suitable for most applications. In 2000, three independent teams demonstrated directional ion acceleration by intense irradiation of micrometer thick foils [Clark et al., 2000; Maksimchuk et al., 2000; Snavely et al., 2000]. Irradiation with intensity of $3 \times 10^{20}\,\mathrm{W \cdot cm^{-2}}$ yields up to $\approx 2 \times 10^{13}$ protons, with an energy cut-off of 58 MeV ([Snavely et al., 2000] see Fig. 2). The origin of the accelerated ions was the subject of active debates, but following works [Wilks et al., 2001; Hegelich et al., 2002] finally brought experimental evidences that the most energetic ions come from impurities adsorbed on the back side of the target. They introduce a new mechanism named *Target Normal Sheath Acceleration* (TNSA). In TNSA the laser field ionizes and heats electrons at the front surface. These hot relativistic electrons cross and scatter through the target and ionize the rear side, forming an hot electron cloud. The resulting charge separation between the hot electron cloud and the cold ions induces an intense field normal to the rear surface, reaching $1 \times 10^{12}\,\mathrm{V \cdot m^{-1}}$. It launches the similar self expansion of the plasma [Mora, 2003]. Particle adsorbed at the surface (typically H_2O or carbonate chains) are accelerated by this field inside a cone of several dozens of degree [Lindau et al., 2005], and exhibit a thermal spectrum, with an energy cut-off given by the hot electron temperature and density. The TNSA mechanism is illustrated Fig.1. The electric field and the sheath expand during picoseconds, as observed by [Romagnani et al., 2005] Fig. 3.

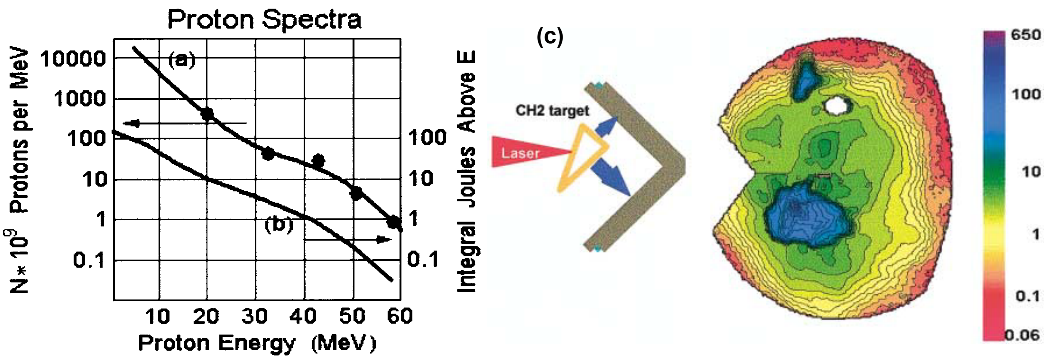

Figure 2 – (a) Proton spectrum obtained by [Snavely et al., 2000] on RCF. The 423 J, 500 fs laser pulse is shot at normal incidence on a 100 µm thick CH foil. (c) Irradiation of a 30 deg wedge target accelerates two proton beams, demonstrating that the protons are coming from rear surfaces and not from the target front. Colors show the dose in krd(10 Gy) as a function of angle recorded on a RC film through 300 µm Ta (proton $E > 18$ MeV).

TNSA's beam properties of brightness, high current and laminarity stimulated the proposal of various applications : proton probing [Borghesi et al., 2002; Mackinnon et al., 2004], isotope production [Fritzler et al., 2003; McKenna et al., 2004], study of Warm-Dense-Matter by isochoric heating [Patel et al., 2003; Koenig et al., 2005], ignitor beam in inertial confinement fusion [Roth et al., 2001], spallation and nuclear reactions [Ledingham et al., 2003; McKenna et al., 2005], and protontherapy [Malka et al., 2004; Bulanov et al., 2002]. Most applications make use of the peaked energy deposition of ion beams into matter: most of the ion kinetic energy is released at the end of the ion path, at the so-called *Bragg peak* [Knoll, 2010]. It is then possible to irradiate a specific area inside a volume. For instance, such proton beams can break DNA's of tumorous cells [Yogo et al., 2009], without damaging the surrounding healthy cells. Protontherapy (and more generally hadrontherapy) from ions accelerated in cyclotron is already an established oncology treatment and laser-driven accelerator brings the hope to reduced the scale of such facilities.

Despite these promising properties, TNSA beams present shortcomings preventing industrial applications. First, the beam is essentially the result of a thermal charge separation in space, and thus, exhibits a broad maxwellian spectrum, not suitable for most applications. No experiments demonstrated yet proton energy above $100\,\mathrm{MeV}\cdot\mathrm{u}^{-1}$, when optimal protontherapy energy is ≈ 230 MeV. Reviews of TNSA experiments performed in 2006 and 2007 [Fuchs et al., 2006; Robson et al., 2007] found a $(I\lambda^2)^{1/2}$ scaling of the maximum proton energy, where I is the laser intensity and λ the laser wavelength. A more recent review from [Zeil et al., 2014] is shown Fig.4 and exhibits the $(I\lambda^2)^{1/2}$ scaling for long pulses, and a $I\lambda^2$ scaling for short (femtosecond) pulses. TNSA efficiency rises for thinner targets [Neely et al., 2006; Ceccotti et al., 2007], but the process is also highly dependent from the laser contrast, as Amplified Spontaneous Emission (ASE) may degrade the rear-side ion gradient prior to the main pulse

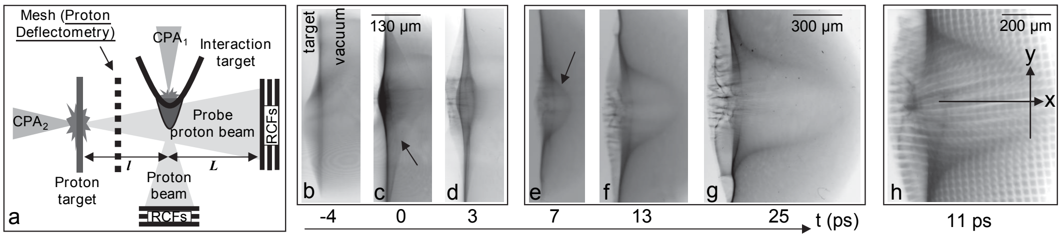

Figure 3 – Field expansion at the rear side of a TNSA target, imaged by proton probing (b-g) and deflectometry (h) measured by [Romagnani et al., 2005]. The interaction target is a 40 µm thick Al foil irradiated by 1.5 ps laser at $3.5 \times 10^{18}\,\mathrm{W \cdot cm^{-2}}$. A second laser accelerates a TNSA proton beam used as a probe. The probe source is laminar and features a virtual source size of few microns, making it suitable for the probing of intense fields.

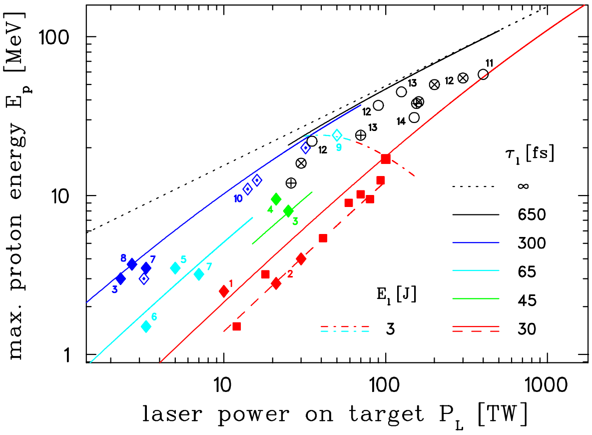

Figure 4 – Scaling of the maximum proton energy with laser power on solid target ([Zeil et al., 2010]). Red squares represent experimental results obtained with the Draco laser (30 fs, $1 \times 10^{21}\,\mathrm{W \cdot cm^{-2}}$, energy between 0.3 and 3 J). Open circles (11,12,13,14) stand for single shot experiments at glass laser facilities. References in [Zeil et al., 2010]. For laser of high energy and long pulse, the cut-off ion energy scale with $I^{1/2}$ while [Zeil et al., 2010] exhibits a I scaling for ultrashort pulses of moderate energy with tight focusing.

interaction [Kaluza et al., 2004]. These constraints impose the use of contrast cleaning technologies (XPW [Jullien et al., 2005] or plasma mirror [Doumy et al., 2004]), decreasing the laser transmission and finally the energy on target. Numerous work focused on the increase of laser absorption by using innovative targets, like foam targets [Passoni et al., 2014], nanowire and microstructured targets [Schwoerer et al., 2006; Zigler et al., 2011; Floquet et al., 2013]. Grating targets [Ceccotti et al., 2013] demonstrates as well enhanced ion acceleration through the coupling of the laser with surface plasmon waves. These enhanced-TNSA unveiled exciting new physics, without changing dramatically the maximum ions energy. Other technical difficulties arise from the use of solid target: debris management, and difficulty to work at high repetition rate.

Alternative schemes on solid target

These difficulties foster researchs on a variety of new mechanisms introduced thereafter. The reader would find a more complete description in the review articles from [Macchi et al., 2013] and [Daido et al., 2012]. Decreasing further the target thickness, down to few dozens nanometers, uncovers a mechanisms where the ions interact directly with the laser field. In Radiation Pressure Acceleration (RPA), the laser ponderomotive force push electrons of a solid target inwards, while ions are still immobile. The coulomb force resulting from the charge separation equates the laser radiation pressure and eventually accelerates inwards the ions. Different regimes arise depending on the target thickness [d'Humieres et al., 2005]: for a "thick" target (i.e. thicker than the plasma skin depth), RPA leads to Hole-Boring [Palmer et al., 2011; Schlegel et al., 2009; Robinson et al., 2009], while RPA on "thin" target leads to Light Sail Acceleration [Esirkepov et al., 2004; Macchi et al., 2010; Kim et al., 2016]. RPA in non-absorptive condition, as derived in 1D model by [Macchi et al., 2010, 2013], yields a I^2 scaling of the ion energy at low fluence ($< 1 \times 10^8\,\mathrm{J \cdot cm^{-2}}$), and a linear one at high fluence. It has been exhibited experimentally by Kim et al. [Kim et al., 2013, 2016] through several evidences shown Fig.5: the energy scaling changes from $I^{1/2}$(TNSA) to I(RPA high fluence) as the laser intensity increases, while the I^2 scaling (RPA low fluence) is visible with circular polarization, as less laser light is absorbed, bringing the condition closer to the 1D non-absorptive RPA. Transverse target deformations [Macchi et al., 2010] as well as Rayleigh-Taylor instabilities [Pegoraro and Bulanov, 2007] and relativistic transparency of thin targets [Dollar et al., 2012] limit the efficiency and stability of the Light Sail regime. Nonetheless in transparency conditions, effective acceleration of C^{6+} ions [Henig et al., 2009], with up to 10 % efficiency, was observed. Extra electron heating was reported in 3D PIC simulations [Yin et al., 2007, 2011] that enhances ions acceleration. This regime is named "Break-out Afterburner" and its description involves complex successive stages. Emission of ions with a narrower spectrum have now been reported in this regime and linked to relativistice transparency [Palaniyappan et al., 2015, 2012].

If the plasma temperature and density enable the propagation of a collisionless electrostatic shock waves (as described in [Tidman and Krall, 1971]), light ions are reflected by the shock field and gain twice its velocity. This mechanism, called Collisionless Shock Acceleration (CSA), has been proposed by [Silva et al., 2004] and observed experimentally early on in transverse acceleration [Wei et al., 2004]. More

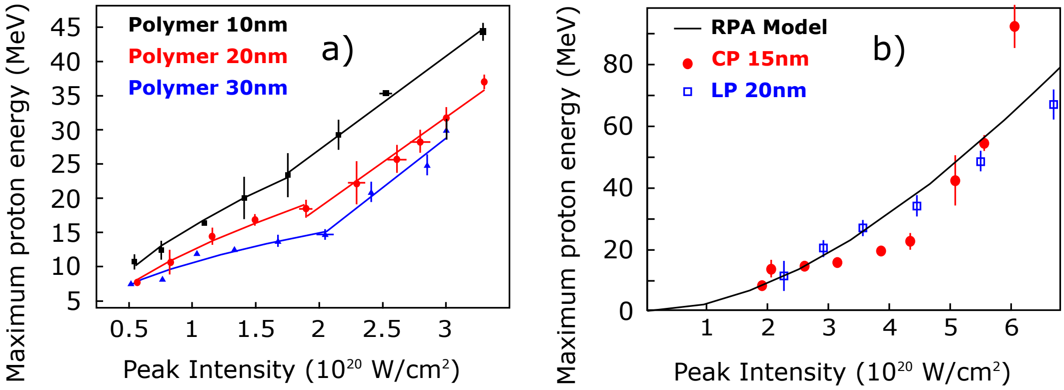

Figure 5 – Maximum proton energy versus the laser intensity from (a) [Kim et al., 2013] with linearly polarized 30 fs, 8.3 J laser on CH nm targets, and (b) [Kim et al., 2016] with both linearly polarized laser and circularly polarized laser (same system as [Kim et al., 2013] with better focalisation). Both experiments use double plasma mirrors to achieve a 6 ps contrast of 3×10^{-11}. (a) The energy scaling changes from $I^{1/2}$ to I as the laser intensity increases, at a threshold depending on the target thickness. (b) The energy scaling for circularly polarized pulse gets closer to the 1D reflective RPA (scaling of I^2)

recently forward acceleration of monoenergetic protons up to 22 MeV with CO_2 laser, and C^{6+} peaked at 7.5 MeV with Ti:Sa laser was attributed to CSA [Haberberger et al., 2012; Zhang et al., 2015]. Hole boring and CSA are sometimes mixed in the literature [Daido et al., 2012] because they feature similar structures, and Hole-boring may launch a Collisionless Shock (CS) [Tresca et al., 2015]. Nonetheless Hole Boring is driven by the laser radiation pressure, while a CS may rise from a hot and perturbed plasma without laser fields [Sorasio et al., 2006].

Acceleration regimes in gas target

Numerous works investigate the opportunity of gas targets for ion acceleration. Beyond relieving the constraints on laser contrast, repetition rate, and debris management, gas jets offer as well the possibility to be optically probed. With the complete picture given by the electronic density and the magnetic fields [Flacco et al., 2015], in-depth mechanism description is made possible. Gas targets have specific drawbacks: smooth gradients that decrease charge separation fields, and limited density. High density is determinant for the laser absorption. A laser of wavelength λ cannot propagate in plasma whose electronic density is higher than the so-called *critical density* $n_c = m_e \epsilon_0 c^2/(e^2\lambda^2)$ where c is the speed of light in vacuum, n_e is the electronic density, m_e,e the electron mass and charge, and ϵ_0 the vacuum permititivity. Near the critical density, the laser undergoes numerous absorption processes, favorable to electron heating, and eventually to thermal charge separation. In gas jet plasma, the electronic density is limited to ≈ 1 at $\lambda = 800\,\text{nm}$, to compare with $n_e \approx 200 n_c$ in solid. Early on, transverse, non-collimated acceleration in gas was attributed to coulomb explosion [Krushelnick et al., 1999] and CSA [Wei et al., 2004] with multi-joule picosecond lasers. Such lasers drill a plasma channel depleted of electrons into the underdense plasma, and the resulting transverse wakefield drives the ion acceleration. Recently, transverse coulomb

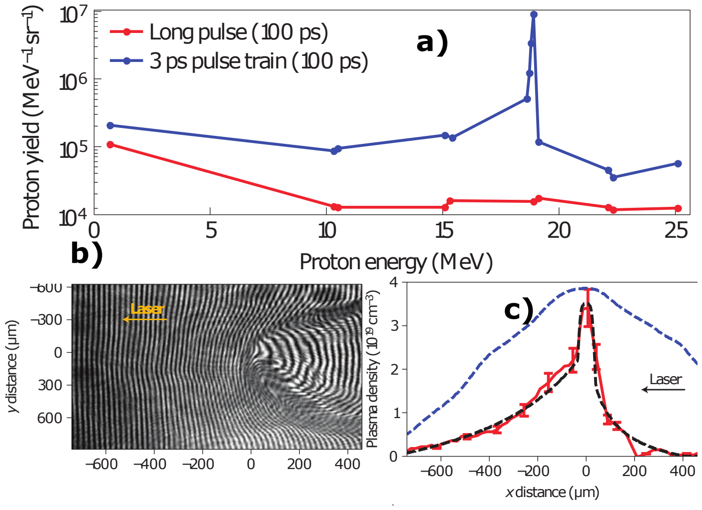

Figure 6 – (a) Proton spectra obtained by [Haberberger et al., 2012] on CR39 detector, with a 100 ps long CO_2 laser pulse (red) and a 100 ps macropulse consisting of a number of 3 ps micropulses (blue) both containing 60 J, with $a_0 = 2$. The laser irradiates a gas target whose profile is shown in (b), before interaction (dashed blue line) and when the main pulse of the pulse train hits the gas (red line), extracted from the interferogram in (c). It is compared with a simulated plasma density in black dashed line.

acceleration was observed with ultra-short, femtosecond lasers as well. [Lifschitz et al., 2014; Kahaly et al., 2016]

Large wavelength of CO_2 lasers ($\lambda = 10.3\,\mu\mathrm{m}$) brings closer the critical regime, by lowering the critical density ($n_c = 1.1 \times 10^{21}\,\mathrm{cm}^{-3}/(\lambda/\mu\mathrm{m})^2$), and reduces the normalized gradient length $L = n_e(\partial(n_e)/\partial x)^{-1}\lambda^{-1}$. Long (picosecond) CO_2 laser pulses demonstrated hole-boring in overdense target of $10n_c$ with gradient $L = 40$ [Palmer et al., 2011]. Several teams [Haberberger et al., 2012; Tresca et al., 2015] demonstrate how the front gradient is critical to launch CSA. They used the inherent properties of CO_2 lasers to generate trains of pulses, the first ones tailoring the plasma before the main pulse. [Haberberger et al., 2012] irradiate a gas jet of few n_c by trains of CO_2 pulses, it launches shock blast-waves achieving monoenergetic proton beam at 22 MeV. The blast-wave velocity was found to be higher than the Hole-boring velocity, and therefore the authors interpret the forward ions production with a peaked spectrum as CSA. Proton spectrum obtained from RCF stacks and plasma profile before the central pulse are shown Fig. 6. 2D PIC simulations shown that CSA could be efficient as well with underdense realistic targets between 4 and $0.4n_c$ [d'Humières et al., 2013b] irradiated by femtosecond lasers. Investigations of this regimes was performed in exploded solid targets [Antici et al., 2009; d'Humières et al., 2013a]. This experiment shows that targets of $\sim n_c$ with front gradient of length 30 μm could yields proton with significant energy (8 MeV) with a medium energy laser pulses (5 J).

In 2006 [Willingale et al., 2006] demonstrates the acceleration of alpha particules from an underdense helium gas target up to 40 MeV. This results was somewhat surprising, because the large rear-side gradient of their target is unfavorable to efficient charge separation and "TNSA-like" self-similar expansion. Following discussions revealed that

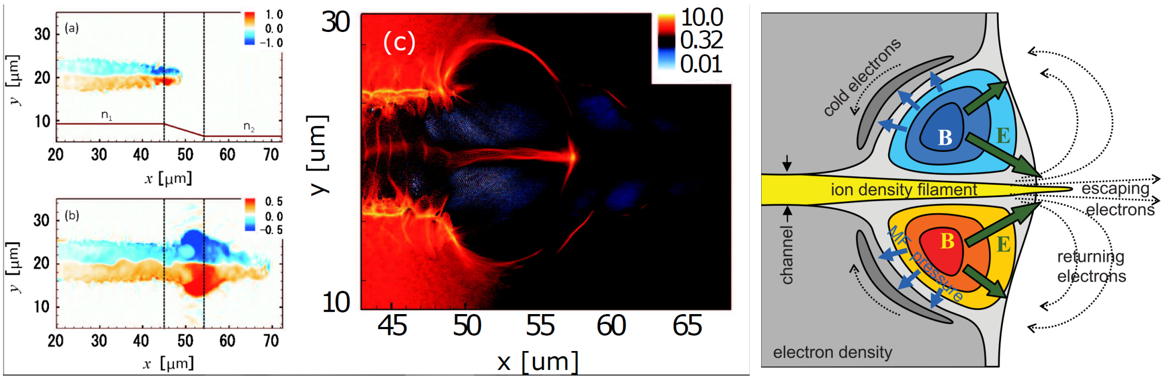

Figure 7 – (a-b) Image from [Nakamura et al., 2010]. A laser of pulse duration 30 fs and $a_0 = 19$ propagates through a relativistic underdense target at $2n_c$ over 25 µm. At the target rear side, the density goes from $2n_c$ to $0.25n_c$ in 10 µm. The distributions of magnetic field Bz in gigagauss from 2D PIC simulation at (a) $t = 220$ fs and (b) $t = 300$ fs. A magnetic dipole vortex is formed at the end of the high density region, and it expands as it moves in the density decreasing region. The solid red line in (a) shows a density distribution of initial plasma. (c) Ion density at $t = 320$ fs normalized by n_c (d) Scheme from [Bulanov and Esirkepov, 2007] of the magnetic vortex sustaining an electrostatic field pinching and accelerating the ion filament at the rear side of an underdense target. The magnetic field prevents the cold electrons to neutralize the charge separation.

charge separation at the rear side is sustained by a quasi-static magnetic field indirectly observed experimentally [Willingale et al., 2007; Yogo et al., 2008; Fukuda et al., 2009] and in simulations [Bulanov and Esirkepov, 2007; Nakamura et al., 2010; Matsukado et al., 2003; Bulanov et al., 2010]. This regime, called Magnetic Vortex Acceleration (MVA), occurs in near-critical or underdense targets, at the difference of RPA or CSA, and thus is especially suitable for gas targets. The laser propagates into the underdense plasma, driving a wakefield and accelerating a high current electron beam. This "hot" current together with cold return current forms a toroidal Megagauss magnetic field. The B-Field pinches and accelerates the ion filament created by the wakefield during the ion response time, typically picoseconds. [Nakamura et al., 2010] shows in simulation that this regime is accessible for femtosecond lasers of moderate energy, but it requires a gradient as sharp as 10 µm. Fig. 7 shows the magnetic vortex expansion into the rear gradient of the target in simulations, with the pinched ion filament. Right scheme illustrates the position of the magnetic fields and the electron recirculating flux. The permanence and stability of magnetic field vortex inside an underdense target was recently observed with ultrashort laser [Flacco et al., 2015].

Summary of experimental and numerical parameters explored in the literature for ion acceleration in gas jet is summarized table 1 and 2. The field amplitude is given with the normalized potential vector $a_0 = Ee/\omega m_e c$ where E is the E-field amplitude, and ω the laser pulsation. High energy picosecond lasers ([Palmer et al., 2011; Willingale et al., 2006]), or CO_2 lasers ([Haberberger et al., 2012; Tresca et al., 2015]) operate in large facilities and feature slow repetition rate, with several shots per hours or even per days. In comparison, multi-joule femtosecond lasers repetition rate is typically 10 Hz, and therefore more suitable for applications. Up to now, no experimental demonstrations of forward CSA, Hole-boring or magnetic vortex were achieved into gas

Authors	**Mechanism**	**Wavelength** [µm]	**Laser**	[a_0]	**Density** [n_c]	**Gradient** [λ]	**Shock speed**	**Energy max** [$\mathrm{MeV} \cdot \mathrm{u}^{-1}$]
[Krushelnick et al., 1999]	CE-T	1	0.9 ps, 50 J	6.5	0.05			0.9
[Wei et al., 2004]	CSA-T	1	0.7 ps, 180 J	15	0.14		$0.06c$	3.3
[Willingale et al., 2006]	MV	1	1 ps, 340 J	21	0.12	25		10
[Antici et al., 2009]	TNSA	1	320 fs, 4 J	2.7	1	20		8
[Palmer et al., 2011]	HB	10.3	8 ps, 7 J	0.5	6	80	$0.03c$	5
[Haberberger et al., 2012]	CSA	10.3	5×3 ps, 60 J	2	6	20	$0.02c$	22
	CSA	20 fs	10	0.4	250		22	
[Zhang et al., 2015](*)	CSA	0.8	65 fs, 8.4 J	4	3	4	$0.02c$	5
[Tresca et al., 2015]	HB-CSA	10.3	5 ps, 11 J	1.4	6	4	$0.02c$	1.5
[Kahaly et al., 2016]	CE-T	0.8	35 fs, 0.8 J	2.4	0.035			0.05

Table 1 – Lasers and targets parameters, shock front velocity (if relevant) and ion kinetic energy for chosen experimental results in gas targets. CSA, HB, CE, MV stand for Collisionless Shock Acceleration, Hole-Boring, Coulomb Explosion and Magnetic Vortex. (*) [Zhang et al., 2015; Antici et al., 2009] made use of exploded foils: the target data corresponds to the plasma parameters at the arrival of the main pulse.

targets with a femtosecond laser. Hole boring is more efficient with circularly polarized pulses [Macchi et al., 2005] and has been only demonstrated with long and energetic pulses [Palmer et al., 2011]. The SAPHIR laser provided by Amplitude Tech. produces a linearly polarized pulse of 25 fs, 3 J on target and $a_0 = 4$-7.

We present also a gas target reaching $0.4n_c$ in helium, $4n_c$ in argon, with a gradient of characteristic length 50 µm, and which is preceeded by a long "low" density background ($n_e < 0.005n_c$). Under these conditions, simulations exhibits the possibility to trigger either magnetic vortex acceleration [Nakamura et al., 2010; Matsukado et al., 2003] or CSA [Silva et al., 2004], and to achieve moderate ion acceleration of few MeV. This work investigated experimentally the opportunity to trigger these mechanisms with femtosecond laser in gas target.

A first question arises from the propagation of the laser through the background density preceding the spike, or up to the rear down gradient. In this region the laser

Author	**Mechanism**	**Laser**	$[a_0]$	**Density** $[n_c]$	**Gradient** $[\lambda]$	**Shock speed**	**Energy max** $[\mathrm{MeV}\cdot\mathrm{u}^{-1}]$
[Matsukado et al., 2003]	MV	50 fs, 3.2 J	4	0.5	12		8
	MV	50 fs, 3.2 J	4	0.1	20		4
[Silva et al., 2004]	CSA	100 fs	16	10	30	$0.15c$ M=2	80
	CSA	100 fs	4	10	30		4
[Macchi et al., 2005]	HB	35 fs	2	5	2	$0.03c$	0.5
[Nakamura et al., 2010]	MV	30 fs, 3 J	20	0.7-5	12	$0.28c^*$	150
[Willingale et al., 2009]	TNSA	560 fs, 270 J	36	0.9	250		35
[Palmer et al., 2011]	HB	8 ps, 7 J	0.6	7.5	10	$0.03c$	1
[Fiuza et al., 2012]	CSA	7 ps	2.5	10	20	M=1.7	28
[Macchi et al., 2012]	AW	10 fs	16	20	10	$0.05c$	5
[d'Humières et al., 2013b]	CSA	20 fs	10	0.4	25		77
	CSA	20 fs	10	0.4	250		22
[d'Humières et al., 2013a]	CSA	700 fs, 180 J	7	1	25		300
[Haberberger et al., 2012]	CSA	2×3 ps, 60 J	2.5	6	10	$0.05c$	20
[Tresca et al., 2015]	HB-CSA	5 ps, 11 J	1.4	6	4	$0.05c$	3.5

Table 2 – Lasers and targets parameters, velocity of the shock front (if relevant) and ion kinetic energy for PIC simulations results. CSA, AW, HB, MV stand for Collisionless Shock Acceleration, Acoustic Wave, Hole-Boring, and Magnetic vortex. For some references, the shock Mach number M is given. (*) The speed in [Nakamura et al., 2010] denotes the expansion velocity of the magnetic structure and correspond to the Alfven velocity.

power is well above the relativistic limit of self-focusing and self-steepening, and the laser envelope encounters dramatic change and instabilities. The resulting wakefield accelerates electrons, and the measure of the electron beam properties is a first step towards the description of the magnetic vortex. Multi-parametric PIC simulations by [Matsukado et al., 2003] suggest that the laser energy and target density in LOA are suitable for MVA, but the effect of the smooth gas gradient is an open question. The electrons heating and the suitability of our gradients to launch CS is investigated as well.

Outline

The first chapter explains the basics of plasma physics and intense laser-matter interaction physics relevant for the discussion, and describes CSA and MVA: the most promising acceleration mechanisms suitable for the SAPHIR facility. The second chapter presents PIC simulation unraveling the laser propagation into the target. We discovered, in 1D and 2D, an heating mechanism susceptible to heat the plasma above the ponderomotive scaling and to trigger CSA. The third chapter presents the development and properties of the supersonic shock nozzle, achieving unmatched density maximum and gradients, without prepulse tailoring. We present how a simple compressible flow model can predict main properties of this target, and how Computational Fluid Dynamic describes accurately the flow properties. The fourth chapter presents the experiments. We tested successive targets with increasing complexity, either in the tailoring of the flow or in the use of new gas mixtures. The results present the laser propagation and its limits. We observed relativistic electron beams whose properties suggest a different acceleration regime than the bubble regime, with several evidences of Direct Laser Acceleration. In the fifth chapter we explored another use of a gas target in laser-driven acceleration: the efficient neutralization of a TNSA ion beam through a gas target, and the subsequent neutral beam production.

Chapter 1

Basics of ion acceleration by laser-plasma interaction at near-critical density

This chapter introduces the basics of the physical phenomena at work in intense laser-plasma interaction, and especially at near-critical density. It starts with the essential notions of plasma physics and the relevant characteristic lengths and times of the collective plasma behaviour. A second section describes the propagation of an ultra-short laser in an underdense plasma, with an emphasis on the relativistic effects affecting the laser pulse. Finally the last section describes the regimes of ion acceleration in near-critical target we explored experimentally: the Collisionless Shock Acceleration and the Magnetic Vortex Acceleration. We derive the experimental parameter range required to trigger these regimes.

Contents

1.1 Collective phenomena in plasma

A plasma is a gas of electrons and positive ions whose collective behaviour is coupled with electric and magnetic fields. The variety of phenomena found in plasmas arise from the inherent non-linearity and self-consistency of the coupling between particles and fields. The fields **E** and **B** act on the charges through the Lorentz force:

$$\mathbf{F} = q(\mathbf{E} + \frac{\mathbf{p}}{\gamma m} \times \mathbf{B}) \tag{1.1}$$

where q is the charge, p the relativistic momentum, m the particle mass at rest, and $\gamma = \sqrt{1 + p^2/(mc)^2}$ the relativistic Lorentz factor. We write here directly the relativistic form. Charges are set in motion and the resulting current **J** and density ρ act back on the fields through the Maxwell equations:

$$\nabla \cdot \mathbf{E} = \frac{\rho}{\epsilon_0} \tag{1.2}$$

$$\nabla \cdot \mathbf{B} = 0 \tag{1.3}$$

$$\nabla \times \mathbf{E} = -\frac{\partial \mathbf{B}}{\partial t} \tag{1.4}$$

$$\nabla \times \mathbf{B} = \mu_0(\mathbf{J} + \epsilon_0 \frac{\partial \mathbf{E}}{\partial t}) \tag{1.5}$$

where bold letters denote vectors, $\epsilon_0 = 8.85\,\mathrm{pF} \cdot \mathrm{m}^{-1}$ the vacuum permittivity and $\mu_o = 1.26\,\mathrm{\mu H} \cdot \mathrm{m}^{-1}$ the vacuum magnetic permeability are linked to the speed of light into vacuum by $c = 1/\sqrt{\epsilon_0 \mu_0}$. In most industrial plasmas, the kinetic energy of the particles dominates the coulomb potential, the coupling parameter $\mathit{\Gamma}$ is expressed as the ratio of the Coulomb energy over the kinetic energy :

$$\mathit{\Gamma} = \frac{|\langle E_p \rangle|}{\langle E_c \rangle} \approx 10^{-5} \left[\frac{n_e}{10^{12}\,\mathrm{cm}^{-3}}\right]^{1/3} \left[\frac{T}{10^6\,\mathrm{K}}\right]^{-1} \tag{1.6}$$

.

where n_e is the electronic density. For $\mathit{\Gamma} << 1$ the plasma is said *kinetic*, and if $\mathit{\Gamma} >> 1$ it is said *strongly coupled.* Despite the thermal agitation, the coulomb potential develops collective behaviour, instabilities, and out-of-equilibrium kinetics not present in coupled plasma, which behaves much more like a fluid.

1.1.1 Debye Length

Lets consider a positive ion added to a uniform and neutral plasma. The ion attracts electrons around him and its potential is eventually screened. The characteristic length above which the potential is screened is named the *Debye length* λ_D. The Debye length is the result of the competition between the thermal electron agitation and the plasma coulomb potential. It is given (assuming immobile ions) by:

$$\lambda_D[\mathrm{cm}] = \sqrt{\frac{\epsilon_0 k_B T_e}{n_e e^2}} \approx 743 \left[\frac{T_e}{[\mathrm{eV}]}\right]^{1/2} \left[\frac{n_e}{[\mathrm{cm}^{-3}]}\right]^{-1/2} \tag{1.7}$$

where T_e is the electronic temperature and k_B the Boltzmann constant. For a typical electron temperature of 1 MeV and density of $1 \times 10^{20}\,\mathrm{cm}^{-3}$ $\lambda_D = 0.7\,\mu\mathrm{m}$. The Debye length is also the characteristic length of the electron sheath at the interface between plasma and vacuum. The electrons are expelled from the plasma by the electronic thermal agitation, before being pulled back by the coulomb force. The thickness of this electron sheath is typically λ_D. More generally the plasma fields can be separated in two components, with distinct scale lengths. The first one represents the rapid fluctuations due to particles interaction and collisions. The second represents the averaged field over a distance greater than the screening length. This last field is generated by the deviation from the local neutrality, and it is the one giving birth to the collective motion of charge.

1.1.2 Electron-ion collision in plasma

The collision cross section of particle is therefore limited by the Debye length, as no potential extends beyond the Debye sphere surrounding each charge. The collision frequency of one electron on cold ions is given by:

$$\nu_{ei}(v) = \frac{n_i Z^2 e^2 \Lambda}{4\pi\epsilon_0^2 m_i m_e v^3} \tag{1.8}$$

Where λ_C is the minimal impact parameter given by quantum mechanic, $\Lambda = \ln \lambda_D/\lambda_C \approx 15$, Z is the ion atomic number and v the electron velocity. The electron-on-ion collision frequency is given for a Maxwellian velocity distribution by:

$$\langle \nu_{ei} \rangle_v [\mathrm{Hz}] \approx 5 \times 10^{-6} \Lambda \left[\frac{T_e}{[\mathrm{eV}]}\right]^{-3/2} \left[\frac{n_e}{[\mathrm{cm}^{-3}]}\right] \tag{1.9}$$

and the ion-ion collision frequency:

$$\langle \nu_{ii} \rangle_v [\mathrm{Hz}] \approx 5 \times 10^{-8} Z^4 \left(\frac{m_i}{m_p}\right)^{-1/2} \Lambda \left[\frac{T_i}{[\mathrm{eV}]}\right]^{-3/2} \left[\frac{n_i}{[\mathrm{cm}^{-3}]}\right] \tag{1.10}$$

$$\tag{1.11}$$

For a typical electron temperature of 1 MeV and density of $1 \times 10^{20}\,\mathrm{cm}^{-3}$ from a hydrogen plasma $Z = 1$, $\nu_{ei} = 8 \times 10^6$ Hz and $\nu_{ii} = 3 \times 10^9$ Hz for $T_i = 1$ keV. These collision rates are related to the mean free path λ_{mfp} and the cross section σ by:

$$\nu(v) = \sigma v n \qquad\qquad \lambda_{mfp} = v/\nu(v) \tag{1.12}$$

To evaluate the importance of collision, these time scales must be compared with the typical response time of the electron motion in the plasma.

1.1.3 Plasma frequency

After perturbation of its neutrality, the plasma reorganises itself at a frequency ω_p named *plasma frequency*, or *Langmuir frequency*. This frequency characterises the coulomb collective phenomena, and has a critical importance in the dynamics of the plasmas. Field perturbations would result in the oscillation of the electron cloud around the ions, at a frequency ω_p. Over a time $1/\omega_p$ ions barely move due to their inertia. The plasma frequency is :

$$\omega_p = \sqrt{\frac{n_e e^2}{\epsilon_0 m_e}} \qquad \nu_p = \frac{\omega_p[\mathrm{Hz}]}{2\pi} = 8981\sqrt{n_e[\mathrm{cm}^{-3}]} \tag{1.13}$$

Similar frequency can be given for ions:

$$\omega_i = \sqrt{\frac{n_i e^2}{\epsilon_0 m_i}} \qquad \nu_i = \frac{\omega_i[\mathrm{Hz}]}{2\pi} = 200\sqrt{n_i[\mathrm{cm}^{-3}]} \tag{1.14}$$

For a plasma at $n_e = n_i = 1 \times 10^{20}\,\mathrm{cm}^{-3}$, it gives $\nu_p = 9 \times 10^{13}\,\mathrm{Hz}$ and $\nu_i = 2 \times 10^{12}\,\mathrm{Hz}$, or a characteristic time $(1/\nu)$ respectively of $\approx 10\,\mathrm{fs}$ and $500\,\mathrm{fs}$. Finally this dynamic is orders of magnitude faster than electron-ion and ion-ion collision. In the following we will study the plasma dynamic at the plasma frequency scale, up to the ion-plasma frequency, and therefore we will neglect the collision effects. The plasmas in our experiments are *collisionless*, and thus the velocity distribution of electrons and ions cannot relax towards a maxwellian distribution after a perturbation, and the velocity distribution may be anisotropic. For the same reason, *a priori*, ion and electron populations have different temperatures.

1.1.4 Kinetic equations

The most complete description of a collisionless plasma is, for each particle species the knowledge of the distribution function $f_a = f_a(\mathbf{r}, \mathbf{p}, t)$. f_a give the density of particle at the point $(\mathbf{r}, \mathbf{p})$ in the six-dimension phase space, at time t. This formulation will give us the tools required for the study of shock in plasma. Later in this chapter a more comprehensive description of collisionless plasma shock will be given. For a collisionless plasma with constant number of particle, f_a verifies the continuity equation in phase space for the species a:

$$\partial_t f_a + \nabla_r \cdot (\dot{\mathbf{r}}_a f_a) + \nabla_p \cdot (\dot{\mathbf{p}}_a f_a) = 0 \tag{1.15}$$

where $\dot{\mathbf{r}}_a = \mathbf{v} = \mathbf{p}/(m_a\gamma_a) = \mathbf{p}c/(m_a^2c^2 + \mathbf{p}^2)^{1/2}$, $\dot{\mathbf{p}}_a = \mathbf{F}_a$ with $\mathbf{F}_a = \mathbf{F}_a(\mathbf{r}, \mathbf{p}, t)$ the sum of forces on the particles. The local density $n_a(\mathbf{r}, t)$, the average velocity $\mathbf{u}_a(\mathbf{r}, t)$, and the pressure $\mathbf{P}_a$ are given by:

$$n_a = \int f_a d^3p \qquad \mathbf{u}_a = n_a^{-1}\int \mathbf{v} f_a d^3p \tag{1.16}$$

$$\mathbf{P}_a = \int (\mathbf{v} - \mathbf{u}_a) \cdot (\mathbf{v} - \mathbf{u}_a) f_a d^3p \tag{1.17}$$

The Vlasov-Maxwell equation is obtained by assuming that $\mathbf{F}_a$ is the Lorentz force $F_L = q_a(\mathbf{E} + \frac{\mathbf{p}}{\gamma_a m} \times \mathbf{B})$ and that the fields $\mathbf{E}$ and $\mathbf{B}$ are obtained through the charge

$\rho(n_a)$ and current density $\mathbf{J}(n_a, \mathbf{u}_a)$ and the Maxwell equations. The standard Vlasov-Maxwell equation is given by:

$$\partial_t f_a + \mathbf{v} \cdot \nabla_r f_a + q_a(\mathbf{E} + \frac{\mathbf{p}}{\gamma_a m} \times \mathbf{B}) \cdot \nabla_p f_a = C \tag{1.18}$$

In presence of collisions, C is not zero, and the continuity equation for f_a is not verified any more, due to dissipation effects. We have seen in the previous section that our plasma is *collisionless*, thus $C = 0$. Nonetheless in plasma shock models, turbulence may have a similar effect. It is convenient to separate the average behaviour of the plasma from the turbulence. Averaging over time :

$$f = \langle f \rangle + \delta f \qquad \mathbf{E} = \langle \mathbf{E} \rangle + \delta \mathbf{E} \qquad \mathbf{B} = \langle \mathbf{B} \rangle + \delta \mathbf{B} \tag{1.19}$$

and the collisionless Vlasov-Maxwell equation 1.18 gives:

$$\partial_t \langle f_a \rangle + \mathbf{v} \cdot \nabla_r \langle f_a \rangle + q_a(\langle \mathbf{E} \rangle + \frac{\mathbf{p}}{\gamma_a m} \times \langle \mathbf{B} \rangle) \cdot \nabla_p \langle f_a \rangle = C_{turb} \tag{1.20}$$

where:

$$C_{turb} = q_a \langle (\delta \mathbf{E} + \frac{\mathbf{p}}{\gamma_a m} \times \delta \mathbf{B}) \cdot \nabla_p \delta f_a \rangle \tag{1.21}$$

The quantity C_{turb} is related to the correlation function $\langle \delta f \delta f \rangle$, it plays the role of collision by changing the averaged distribution by the interaction between the turbulent fields and the turbulent distribution. If $C_{turb} = 0$, no shock solutions can be found [Tidman and Krall, 1971], as demonstrated later on. Stationary solutions exist nonetheless and are named *solitons*. They propagate in the plasma and leave it unchanged. The collisionless shocks studied later on in this chapter are said laminar. It means C_{turb} is small before the other term of the equation 1.20, but the system is nonetheless subject to a small dissipation. In the following derivations, the quantities are implicitly the averaged ones.

1.1.5 Fluid equations

It is now possible to derive a set of equations for the averaged quantities n_a and $\mathbf{u}_a$. We will limit ourself to the non-relativistic case $\gamma_a \approx 1$. By integrating Eq. 1.18 over momentum leads to the continuity equation:

$$\partial_t n_a + \nabla \cdot (n_a \mathbf{u}_a) = 0 \tag{1.22}$$

By multiplication of Eq. 1.18 by v and integration over momentum one obtains the second moment of the Vlasov equation. We will assume also that the Pressure tensor is isotropic $\mathbf{P}_{a,i,j} = P_a \delta_{i,j}$:

$$m_a n_a (\partial_t \mathbf{u}_a + \mathbf{u}_a \cdot \nabla \mathbf{u}_a) = q_a n_a (\mathbf{E} + \mathbf{u}_a \times \mathbf{B}) - \nabla P_a \tag{1.23}$$

In order to close the equation system, it is necessary to relate the pressure to the density and temperature in an *equation of state* (EoS) using other arguments. Let's assume that the phenomena of interest has a frequency ω and wave number k. (1) If $\omega/k << u_{T_a}$ (where $u_{T_a} = \sqrt{3k_B T_a/\gamma m_a}$ is the quadratic mean thermal velocity), the heat flow is fast compared to the phenomena.The EoS is said isothermal : $P = nT$ with the temperature T constant. If we assume that electrons reached an equilibrium $\mathbf{u}_e = 0$ in an electrostatic field $\mathbf{E} = -\nabla\mathit{\Phi}$. Eq. 1.23 is reduced to $en_e\nabla\mathit{\Phi} - \nabla P_e = 0$. Using the isothermal EoS (with constant temperature) yields the classical Boltzmann equilibrium condition :

$$n_e = n_0 \exp(e\mathit{\Phi}/T_e) \tag{1.24}$$

(2) If $\omega/k >> u_T$, the heat flow is negligible and the adiabatic EoS is valid:

$$P/n^{\kappa} = \mathtt{cst} \tag{1.25}$$

where $\kappa = d + 2/d$ is the adiabatic coefficient in dimension d. If the plasma has a thermal velocity negligible with respect to the average, coherent fluid speed $|\mathbf{u}_a|$, then $P_a = 0$. It leads to the *cold* fluid equations, which is relevant when the electron population motion for instance is dominated by the oscillation imposed by an intense laser field. The EoS completes the two-fluid plasma model, where electrons and ions act each one as a fluid, coupled by the Poisson equation :

$$-\nabla^2\mathit{\Phi} = e(n_e - Zn_i)/\epsilon_0 \tag{1.26}$$

Where Z is the ion atomic number.

1.1.6 Non-magnetic waves in plasma

Without magnetic fields, the two-fluid plasma model can propagate only two kinds of waves. One at high frequency named *electron plasma wave*, and one at lower frequency named *ion acoustic wave.* These modes results respectively from the coupling of the E-field with the electron motion and from a coupling between ion motion, electron motion, and E-field. For high frequencies we will assumme the ion immobile, and we will use the adiabatic EoS for the electron fluid. The fluid equations 1.22 and 1.23, together with the EoS give in 1D the system:

$$\partial_t n_e + \partial_x(n_e u_e) = 0 \tag{1.27}$$

$$n_e me(\partial_t(u_e) + u_e\partial_x(u_e) = -n_e e\mathbf{E} - \partial_x P_e \tag{1.28}$$

$$\frac{P_e}{n_e^3} = cst \tag{1.29}$$

with the Poisson's equation to relate the electric field to density:

$$\partial_x\mathbf{E} = e(n_e - Zn_{0i})/\epsilon_0 \tag{1.30}$$

Assuming small perturbations $n_e = n_0 + \tilde{n}$, $u_e = \tilde{u}$, $P_e = n_0 T_e + \tilde{p}$ and $\mathbf{E} = \tilde{\mathbf{E}}$, and a wave-like solution $\tilde{n} \sim e^{ikx - i\omega t}$ we find the dispersion relation for electron plasma oscillation :

$$\omega^2 = \omega_{pe}^2 + 3k^2 u_{Te}^2 \tag{1.31}$$

where $|u_{Te}|^2 = 3k_BT_e/m_e$ is the average quadratic thermal velocity and $\omega_{pe} = \sqrt{e^2n_0/m_e\epsilon_0}$ the plasma frequency we have seen beforehand. Essentially, the electronic density oscillates at the plasma frequency, with a small thermal correction.

To derive the low frequency plasma wave, we will assume that electrons are massless, meaning that the time scale of interest is large with respect to $1/\omega_{pe}$, and that electrons adapt instantly to the coulomb potential. In this case $u_{Ti} << w/k << u_{Te}$, and we apply the isothermal EoS to the electrons and the adiabatic EoS to the ions. Finally the dispersion relation is :

$$\omega = \pm kc_s \tag{1.32}$$

where $c_s = \sqrt{(ZT_e + 3T_i)/m_i}$ is the ion sound velocity. Ion density oscillates due to the pressure restoring force, while the electrons transmit the perturbation to the E-field.

1.1.7 Conclusion

We have seen most of the collective plasma parameters relevant for ultra-intense laser-plasma interaction, especially the Debye length and the plasma frequency. The plasma is essentially collisionless, leading to complex distribution functions. We derived the two-fluid model in non-magnetic non-relativistic conditions and showed the existence of two kinds of waves, at high and low frequency. The acoustic wave is the only one that assumes ion motion, and it is the type of wave that may degenerate into a soliton or a shock. The electronic plasma wave may be excited by an ultra-intense laser. The next section describe the propagation of an intense laser into a plasma.

1.2 Femtosecond Laser in plasma

1.2.1 Relativistic motion of a single electron in a plane wave

We start by introducing the basic picture of the motion of a single electron in a plane EM field. We will focus on the case where the motion is relativistic. These derivations are inspired by [Gibbon, 2005]. It is useful to define the dimensionless parameter a_0, related to the maximum momentum that an electron reaches in a field of amplitude E_0 and frequency ω (in linear polarization, in unit of m_ec^2):

$$a_0 = \frac{eE_0}{m_e\omega c} \tag{1.33}$$

The hypothesis $v \sim c$ where v is the electron speed translates in $a_0 >> 1$. a_0 is related to the intensity I by:

$$I = \langle|\mathbf{E} \times \mathbf{B}|\frac{1}{\mu_0}\rangle = \frac{c}{2\epsilon_0}\left(\frac{m_e\omega c a_0}{e}\right)^2 \tag{1.34}$$

where $\langle\rangle$ denotes the average over a duration greater than the laser period. In practical units:

$$a_0 = 0.85 \left(\frac{I(\lambda/[\mu\mathrm{m}])^2}{[10^{18}\,\mathrm{W}\cdot\mathrm{cm}^{-2}]} \right)^{1/2} \tag{1.35}$$

For instance, a Ti:Sa laser system ($\lambda = 0.8\,\mu\mathrm{m}$) and $I = 10^{20}\,\mathrm{W}\cdot\mathrm{cm}^{-2}$ give $a_0 = 7$. What is the motion of an electron in such field ? The relativistic equation for the electron position in a plane EM field propagating along x and polarized along y is

$$kx = \frac{a_0^2}{8\gamma_0^2}\sin 2\phi \qquad\qquad ky = -\frac{a_0}{\gamma_0}\sin\phi \tag{1.36}$$

with $\phi = kx - \omega t$, k the wave number $2\pi/\lambda$ and $\gamma_0 = \sqrt{1 + a_0^2/2}$.

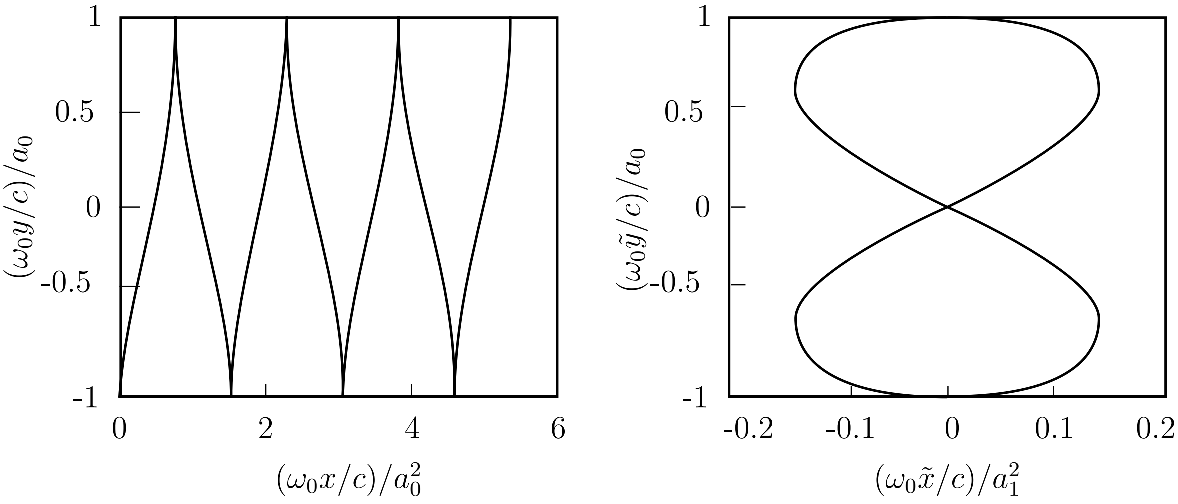

Figure 1.1 – Electron trajectory in a linearly polarized wave of amplitude a_0. (left) in the laboratory frame (right) in the drifting frame where the electron is in average immobile. In the last case $a_1 = a_0/\sqrt{1 + a_0^2/2}$.

When observed in a frame where the electron is *in average* immobile, the motion describes the so-called *figure of eight*, with significant movement in the propagation direction due to the magnetic term of the Lorentz force. The motion can be seen Fig. 1.1. The famous Lawson-Woodward theorem states that an electron in vacuum in an infinite (transversely) and plane EM wave cannot gain energy and momentum. But an electron can be accelerated by a laser field if these assumptions are violated, especially for a pulse of finite width in a plasma. In order to describe such pulse we introduce the slowly varying envelop of the fields $\mathbf{E} = \mathtt{Re}(\tilde{\mathbf{E}}(\mathbf{r}, t) \exp i\omega_t)$ which vary slowly with respect to the laser period $T = 2\pi/\omega$ (cycle-averaged). It possible to express the cycle-averaged motion of the electrons by:

$$m_e \frac{d^2\langle\mathbf{r}\rangle}{dt^2} = -\nabla \frac{e^2}{2m_e\omega^2}\langle\mathbf{E}^2\rangle \tag{1.37}$$

This secular effect is named $\mathbf{F}_p$ the *ponderomotive force* (PF). It repels charged particles from the regions of high intensity gradients. An approximate relativistic expression is $\mathbf{F}_p = -\nabla m_e c^2 \left(1 + \langle \mathbf{a}^2 \rangle\right)^{1/2}$, showing the relationship between a_0 and the PF.

1.2.2 Electromagnetic wave propagation in plasma

Let's write the propagation equation of the electric fields derived from Maxwell's equations, assuming (1) linear waves, (2) cold ions, (3) non-relativistic electron motion, (4) no magnetic fields:

$$\left(\nabla - \frac{1}{c^2}\partial_t^2\right)\mathbf{E} - \nabla(\nabla \cdot \mathbf{E}) = \mu_0 \partial_t \mathbf{J} \tag{1.38}$$

where $\mathbf{J} = e n_e \mathbf{u}_e$ is related to the electric field with Eq 1.23 : $\partial_t \mathbf{J} = -(e/m_e) n_e \mathbf{E}$. Lets express the equation with the envelop $\tilde{\mathbf{E}}$, which verifies $\mathbf{E} = \mathtt{Re}(\tilde{\mathbf{E}}(\mathbf{r}, t) \exp i\omega_t)$. The plasma frequency naturally appears:

$$\tilde{\mathbf{J}} = -i\epsilon_0 \frac{\omega_p}{\omega} \tilde{\mathbf{E}} \tag{1.39}$$

Introducing Eq.1.39 into Eq.1.38 we obtain the inhomogeneous Helmotz equation :

$$\left(\nabla^2 - \eta(\omega)\frac{\omega^2}{c^2}\right)\tilde{\mathbf{E}} - \nabla(\nabla \cdot \tilde{\mathbf{E}}) = 0 \tag{1.40}$$

with the expression for the dielectric function $\epsilon(\omega)$ and the refractive index $\eta(\omega)$ for cold plasmas:

$$\epsilon(\omega) = \eta^2(\omega) = 1 - \frac{\omega_p^2}{\omega^2} \tag{1.41}$$

For plane EM waves $\nabla \cdot \mathbf{E} = 0$ and $\tilde{\mathbf{E}}(\mathbf{r}) = \mathbf{E}_0 e^{i\mathbf{k}\cdot\mathbf{r}}$ and we obtain the classic dispersion relation:

$$\omega^2 - \omega_p^2 = k^2 c^2 \tag{1.42}$$

For $k = |\mathbf{k}|$ to be real, it is necessary that $\omega < \omega_p$. The plasma frequency is the maximum frequency that can propagate into a cold, linear, non-relativistic plasma model. For a given laser wavelength, this condition translates into a maximum electronic density into which the laser can propagate : we recall that $\omega_p^2 = n_e e^2 / m_e \epsilon_0$. This density is called the *critical density* n_c. $\omega < \omega_p$ translates in:

$$n_e < n_c = \frac{\epsilon_0 m_e \omega^2}{e^2} = \frac{1.1 \times 10^{21}\,\mathrm{cm}^{-3}}{\lambda^2[\mathrm{\mu m}]} \tag{1.43}$$

Typically gas targets are said under-dense ($n_e < n_c$) for 1 µm wavelength laser, while solid targets are over-dense ($n_e > 10 n_c$). We can see the interest of CO_2 lasers with wavelength ≈ 10.3 µm: It rises the ratio of the density over the critical density, and a gas target becomes a near critical-target (i.e. the range $n_e = 0.1$ to $10 n_c$), where absorption and propagation leads to the ion acceleration mechanisms of TNSA, CSA or MVA. If $\omega > \omega_p$, k is imaginary and the wave degenerates into a evanescent wave and is reflected by the *critical surface* where $n_e = n_c$. In a real plasma, depending of the plasma gradient, various absorption mechanisms can deplete the laser.

If the laser intensity is high enough to drive the electrons to relativistic speed, the relation between $\mathbf{u}_e$ and the fields is non-linear due the effect of the magnetic force and the relation $\mathbf{p}_e = m_e\gamma(|\mathbf{u}_e|)\mathbf{u}_e$. For circular polarization we can replace m_e by γm_e and :

$$\epsilon_{NL}(\omega) = \eta_{NL}^2(\omega) = 1 - \frac{\omega_p^2}{\gamma\omega^2} \tag{1.44}$$

This relationship is still true for linear polarization if one replaces $\gamma \to \langle\gamma\rangle$. We recall the relation between γ and a_0 : $\gamma = (1 + a_0^2/2)^{1/2}$. In relativistic condition, the refractive index depends from the intensity of the pulse, different parts of the pulse encounter different refractive index. It gives rise to a complex interplay between the pulse envelop, the pulse spectra, the refractive index, the electronic density. In the weakly relativistic regime with small perturbations and $kL << 1$ (where L is the pulse length), the refractive index can be put in a form making clearer its different components [Mori, 1997] :

$$\eta = 1 - \frac{\omega_p^2}{2\omega_0^2}\left[1 + \frac{\delta n}{n_0} - \frac{\langle a^2\rangle}{2} - 2\frac{\delta\omega}{\omega_0}\right] \tag{1.45}$$

The intensity gradient of the laser pulse will result in a central refractive index lower than on the edge. The ponderomotive force will also modify the electronic density. This gradient of η in the transverse direction results in Self-Focusing (SF), in longitudinal direction it provokes pulse shortening (Self-Compression SC), and phase modulation (sometime named photon acceleration or Self Phase Modulation (SMP)).

1.2.3 Relativistic Self-Focusing

We synthesize here the derivation by Sprangle [Sprangle et al., 1987]. In this treatment, the dominant term is the self-focusing induced by the relativistic mass increase alone (the $\langle a^2\rangle/2$ term in the η development Eq. 1.45). It occurs in a time comparable to ω^{-1} and electrons cannot reach local thermal equilibrium in such condition. Assuming propagation of a circular pulse in a cold collisionless plasma with $k_\perp^2 << k^2$. The dispersion relation 1.44 becomes :

$$\omega \approx ck + (c^2k_\perp^2 + \omega_p^2(r,z))/2ck \qquad\qquad \omega_p^2 = \frac{n}{n_0}\frac{\omega_{p0}^2}{\gamma_\perp} \tag{1.46}$$

The analysis starts with ray equations given by :

$$\frac{d}{dt}\mathbf{r}_\perp = \frac{\partial\omega}{\partial\mathbf{k}_\perp} \qquad\qquad \frac{d}{dt}\mathbf{k}_\perp = -\frac{\partial\omega}{\partial\mathbf{r}_\perp} \tag{1.47}$$

where $\mathbf{r}_\perp$ and $\mathbf{k}_\perp$ are the transverse position and wavenumber of a ray. Insertion of Eq. 1.46 in Eq. 1.47 gives:

$$\frac{d^2x}{dt^2} + \Omega^2(\mathbf{r}, z)x = 0 \tag{1.48}$$

$$\frac{d^2y}{dt^2} + \Omega^2(\mathbf{r}, z)y = 0 \tag{1.49}$$

$$\Omega^2(\mathbf{r}, z) = \frac{1}{2k^2r}\frac{\partial\omega_p(r, z)}{\partial r} \tag{1.50}$$

Where Ω is the oscillation frequency of ray in a plasma channel ($\partial\omega_p(r, z)\partial r > 0 \rightarrow n_e(r = 0) < n_e(r)$), which encodes all information on the plasma profile. We define the mean-square radius of the radiation beam envelop as:

$$R^2(z, t) = \langle r^2\rangle \tag{1.51}$$

By taking the moments of Eq. 1.50, it is possible to find a differential equation in r alone, derived along t. Assuming that $\Omega^2(\mathbf{r}, z)$ may be expanded in Taylor series, it comes an equation on R. The special case of a gaussian ray distribution in vacuum gives the correct integration constant and relates R to the spot size $w^2 = 2R^2$. It comes :

$$\frac{d^2w}{dz^2} + \frac{2\langle\Omega^2r^2\rangle}{wc^2} - \frac{(\lambda/\pi)^2}{w^2} = 0 \tag{1.52}$$

where $z = ct$ and λ/π an integration constant. The second term is the focusing relativistic effect, while the third term is always defocusing, and is due to refraction effect. Derivation of the term $\langle\Omega^2r^2\rangle$ is beyond the scope of this introduction, but Sprangle [Sprangle et al., 1987] shows that the spot size evolves like a pseudoparticle in a potential V. Using the normalized envelop radius $\tilde{w} = w/(a_0w_0)$:

$$\frac{d^2}{dt^2}\tilde{w} = -V_0\frac{\partial^2}{\partial t^2}V \tag{1.53}$$

with for weakly relativistic pulse :

$$\frac{\partial^2\tilde{w}}{\partial t^2} = V_0(\frac{1}{\tilde{w}^3} - 16\sqrt{2}\frac{P}{P_c}) \tag{1.54}$$

where $\tilde{w} = w/(w_0a_0)$, and $V_0 = [(c\lambda/(w_0a_0)^2]^2$ and P the laser power, and P_c a critical power, density-dependant, above which relativistic effects become important. They are expressed by:

$$P = \frac{(m_ec^2\omega a_0w_0)^2}{8ce^2} \qquad P_c = 2c\left(\frac{m_ec^2}{e}\right)^2\frac{\omega^2}{\omega_{p0}^2} = 17.3\frac{n_c}{n_e}\mathrm{GW} \tag{1.55}$$

The first term in Eq. 1.54 represents the vacuum diffraction, and the second the relativistic self-focusing. For $P > P_c$ and $\tilde{w} >> 1$ and the right initial slope, the spot size will oscillate in the pseudo-potential V between a minimal and a maximal pseudo-position. If the initial focusing $(d\tilde{w}/dt)$ is strong, the spot focuses and then diverges indefinitely, by the effect of diffraction. Shape of V is different for each P/P_c: for

$P > P_c$, V has a local minimum, whose depth increases and $\tilde{w}_m$ the position decreases as P/P_c increases. For the right initial condition, SF and diffraction may compensate exactly over propagation, and $d\tilde{w}/dt = 0$. The beam keeps the same radius, and this radius is named the *matched spot size* w_m [Sprangle et al., 1987; Thomas et al., 2007b; Lu et al., 2007]. It is expressed by [Bulanov et al., 2010]:

$$w_m = \frac{\lambda}{2^{1/2}\pi^{5/6}} \left(\frac{n_c}{n_e}\right)^{1/2} \left(\frac{P_0}{P_c}\right)^{1/6} \tag{1.56}$$

Or with another expression:

$$w_m = 2\left(0.25 P_0/P_c\right)^{1/6}/k_p \tag{1.57}$$

1.2.4 Self-steepening

The longitudinal modulation of the plasma density affects both the duration and chirp of the laser. Results at weak relativistic intensity ($a_0 \approx 1$) [Schreiber et al., 2010; Faure et al., 2005] describe self-pulse compression when the laser pulse sits in the first oscillation of the plasma wave. The refractive index is expressed for $n_e << n_c$ $\eta = 1 - n_e/2\gamma n_c$ where $\gamma^2 = 1 + a^2$. Both density and intensity gradients affect the pulse envelope via their contributions to η (see Eq 1.45). In intense case ($a >> 1$) the ponderomotive force drives a blow-out regime: the laser sits entirely into near vacuum and relative density variation are small compared to variation of γ. A simple model assuming a linear increase of the refractive index from $\eta_1 = 1 - n_e/2n_c$ (before the pulse) to $\eta_2 = 1$ (inside the pulse) is derived in [Schreiber et al., 2010] and gives the evolution of the laser duration τ:

$$\frac{\partial\tau}{\partial z} = -\frac{1}{2c}\frac{n_e(z)}{n_c} \tag{1.58}$$

This model gives a handy description of the pulse evolution, accurate for weakly relativistic pulses $a_0 \approx 1$ and for $n_e << n_c$ [Schreiber et al., 2010; Faure et al., 2005]. A more accurate description is called *self-steepening* and is presented by Vieira et al. [Vieira et al., 2010]. For $a_0 = 4$ and $n_e = 0.03 n_c$ it gives :

$$\frac{\partial L^2}{\partial t} = -0.12 L_0^2 \omega_p \left(\frac{k_p}{k_0}\right)^2 \tag{1.59}$$

This model does not account for transverse dynamic, and the resulting growth of the potential vector. Variation of the refractive index across the pulse has an effect on the laser envelope and the laser spectrum [Mori, 1997]. The laser frequency shift can be written as $\delta\omega = -\omega_0 \int \partial\eta/\partial\psi \mathrm{d}t$, causing the front of the pulse to redshift and the back to blushift [Faure et al., 2005], as observed Fig. 2.3a). Vieira et al. [Vieira et al., 2010] derivation shows that self-steepening occurs where the laser experiments a redshift, i.e. at the front of the pulse in our case. They derive a threshold for front self-steepening: $aL/(c/\omega_p) > 2.7$ where L is the longitudinal extent of the laser.

Ionization state	E_{ion}[eV]	$I_{ionization}\mathrm{W}\cdot\mathrm{cm}^{-2}$
H^{+}	13.6	$1.1\times10^{14}\,\mathrm{W}\cdot\mathrm{cm}^{-2}$
He^{+}	24.59	$1.4\times10^{15}\,\mathrm{W}\cdot\mathrm{cm}^{-2}$
He^{2+}	54.42	$8.8\times10^{15}\,\mathrm{W}\cdot\mathrm{cm}^{-2}$
Ar^{8+}	143.5	$5.2\times10^{15}\,\mathrm{W}\cdot\mathrm{cm}^{-2}$
Ar^{9+}	422.5	$3.9\times10^{17}\,\mathrm{W}\cdot\mathrm{cm}^{-2}$
Ar^{16+}	918.03	$8.8\times10^{18}\,\mathrm{W}\cdot\mathrm{cm}^{-2}$
Ar^{18+}	4426	$4.7\times10^{21}\,\mathrm{W}\cdot\mathrm{cm}^{-2}$

Table 1.1

1.2.5 Ionisation

Laser intensities used in intense laser-matter interaction have the ability to ionize the matter. We recall that the laser electric field is related to the normalized vector potential by:

$$E_{laser}[\mathrm{GV}\cdot\mathrm{m}^{-1}] = 1\times10^{9}\frac{m_e c}{e}\omega_0 a_0 \tag{1.60}$$

Two ionisation regimes exist, depending on the pulse intensity. The limit between these regime is given by the Keldysh parameter γ_k [Keldysh, 1965].

$$\gamma_k = \omega_0\sqrt{\frac{m_e c\epsilon_0}{e^2}}\sqrt{\frac{E_H}{I_0}} \tag{1.61}$$

where E_H is the binding electric field of an hydrogen atom $E_H = 13.6\,\mathrm{eV}$. For small laser intensities $\gamma_k > 1$, the laser electric field is not sufficient to disturb the atom binding potential and the energy of one photon alone is not sufficient for photo-ionization (At $800\,\mathrm{nm} : \hbar\omega_0 = 1.5\,\mathrm{eV} < 13.6\,\mathrm{eV}$). The ionization mechanism is called *multiphoton ionization* [Mainfray and Manus, 1991]. For large laser intensities $\gamma_k < 1$ relevant to our experiments, the electric field perturbs the binding potential between electrons and atoms, enabling the electrons to escape by tunnel ionization. The potential barrier can even be totally suppressed, and the electron is instantly freed. The threshold energy for this mechanism is given by [Gibbon, 2005]:

$$I_{ionization}[\mathrm{W}\cdot\mathrm{cm}^{-2}] = 4\times10^{9}\frac{(E_i[\mathrm{eV}])^4}{Z^2} \tag{1.62}$$

where Z is the atomic number and E_i the ionization energy of the considered electron. The Table 1.1 gives the intensity threshold for different ionization state of species used in our experiments.

For focused laser of intensity greater than $1\times10^{19}\,\mathrm{W}\cdot\mathrm{cm}^{-2}$, helium is completely ionized by the leading edge of the laser, and we assume that the laser propagates into a fully ionized plasma. For argon, the picture is more complex, and the maximum ionization state is not uniform along the pulse, and may vary as the laser self-focuses and self-compresses, with a maximum ionization sate of Ar^{16+}.

Tunnel ionization occurs before this threshold, and a more complete quantum model is required to describe the ionization of argon along the laser path. The so-called ADK analytical model [Ammosov et al., 1986] has been shown to describe correctly the effect of an external electric field on the binding atomic potential, and the resulting ionization rate. It is valid as long as the external field stay below the critical value:

$$E_{crit}[\mathrm{GV}\cdot\mathrm{m}^{-1}] = 213\left(\frac{E_i[\mathrm{eV}]}{27.2}\right)^{3/2} \tag{1.63}$$

For Ar^{9+} (Ar^{16+}) the critical E-field is respectively $1.3\times10^4\,\mathrm{GV}\cdot\mathrm{m}^{-1}$ ($4.1\times10^4\,\mathrm{GV}\cdot\mathrm{m}^{-1}$), or $a_0 = 3.2$ ($a_0 = 10.2$). The ADK model is therefore only approximately valid if the laser experiments self focusing. The ADK ionization probability rate for an electron depends on the amplitude of the laser E-field and the unperturbed ionization potential E_i of the considered state :

$$W[\mathrm{s}^{-1}] \approx 1.52\times10^{15}\frac{4^{n^*}E_i[\mathrm{eV}]}{n^*\Gamma(2n^*)}\left(20.5\frac{E_i^{3/2}[\mathrm{eV}]}{E[\mathrm{GV}\cdot\mathrm{m}^{-1}]}\right)^{2n^*-1}\exp\left(-6.83\frac{E_i^{3/2}[\mathrm{eV}]}{E[\mathrm{GV}\cdot\mathrm{m}^{-1}]}\right) \tag{1.64}$$

where $n^* \approx 3.69i/\sqrt{E_i}$ is the effective principal atomic number, i the ionization state level, and Γ the standard Gamma function. The fraction of species which is ionized during a time Δt is given by $W\Delta t$.

1.3 Ion acceleration mechanism in near-critical density gas

As seen in the introduction, ion acceleration in under-dense targets has been demonstrated both experimentally and numerically through various mechanisms : Collisionless Shock Acceleration [Silva et al., 2004; Macchi et al., 2012; Haberberger et al., 2012], Magnetic vortex acceleration [Fukuda et al., 2009; Nakamura et al., 2010; Bulanov and Esirkepov, 2007], Hole boring [Tresca et al., 2015], TNSA [Willingale et al., 2006; Palmer et al., 2011], Wakefield assisted Coulomb explosion Krushelnick et al. [1999]; Lifschitz et al. [2014]; Kahaly et al. [2016], or combination of these mechanisms. At the exception of the non-directive wakefield assisted coulomb explosion and MVA in clusters([Fukuda et al., 2009]), none of these mechanisms have yet been demonstrated with ultrashort femtosecond lasers. Transverse Coulomb explosion is observed in PIC simulations, and thus is described here. The properties of the today state-of-the-art gas targets are more adapted to CSA and MVA mechanisms. Still, respectively maximum density and gradient length achievable today by gas targets are at the edge of the parameters range required for CSA and MVA. The following sections describe the physics of these two mechanisms, and exhibit the parameters required to reach them.

1.3.1 Coulomb explosion in gas jet

The first ion accelerating mechanism described during the interaction of an ultra-intense laser with an underdense plasma is Coulomb explosion, as observed by Krushelnick et al. [Krushelnick et al., 1999]. Krushelnick et al. computed a simple model where the charge separation ($\nabla \cdot \mathbb{E} = -4\pi e \delta n_e$) is balanced by the ponderomotive force on the electron ($\mathbb{F} = -m_e c^2 \nabla(\gamma)$ during the long laser pulse duration (1 ps in their case). The maximum energy the ion can gain is linked to the relativistic ponderomotive energy:

$$U = Z m_e c^2 (\gamma - 1) \tag{1.65}$$

In their experiment, Helium ions are accelerated during the pulse duration up to 3.6 MeV from an helium plasma of electronic density $n_e = 1 \times 10^{19}\,\mathrm{cm}^{-3}$ ($n_e = 0.006 n_c$). In the case of femtosecond laser pulses, the ponderomotive force is too short-lived to sustain charge separation during the ion motion time, and the mean effect of the wakefield must be evaluated.

The laser ponderomotive force expels electrons along its path, driving a non-linear wakefield. The secular wakefield force expels electrons from a cylindrical surface at the radius $r > w/2$ where w is the laser spot size, while it pinches them on the axis for $r < w/2$ [Gorbunov et al., 2001]. Its results in a secular transverse wakefield pinching ions near the axis and expelling the others. The dense electron beam injected into the bubble enhances as well the pinching, resulting in an ion filament behind the laser. Ions on outer shells experience a transverse outwards momentum from the secular effect of the wakefield. After sufficient plasma periods, the electrons shield the field and a second phase begins : The ions evolve ballistically in a quasi-neutral plasma according to the momentum given by the wakefield. In *Coulomb explosion* of electron-stripped clusters or droplets, the space charge of the ion channel alone accelerate ions. In underdense gas jets, the secular effect of the wakefield and the central electron beam add an inward momentum component close to the axis, and an outward momentum component far from the axis.

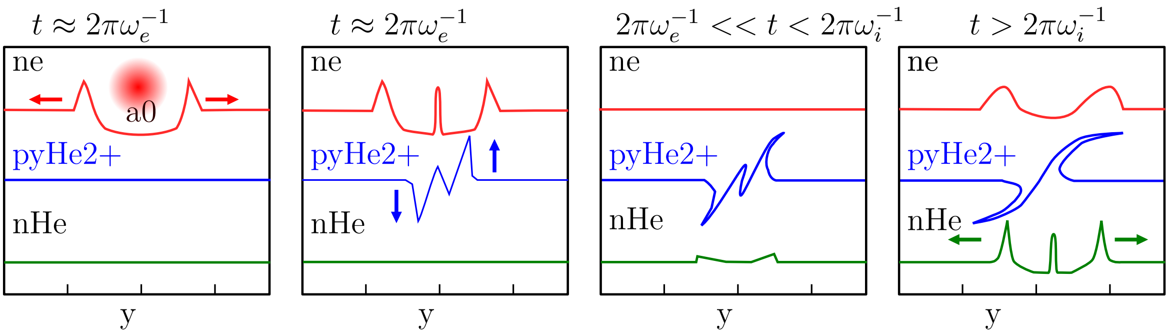

Figure 1.2 – Evolution of electronic density, ionic density, and transverse ion momentum at different characteristic times describing coulomb explosion. This simple case presents a pure helium plasma experiencing ponderomotive force from a short laser pulse $\tau_{laser} < \omega_{pe}^{-1}$, where $\omega_{pi}^{-1} >> \omega_{pe}^{-1}$, showing two distinct phases : 1) wakefield acceleration 2) ballistic expansion leading to a shock front.

The typical ion motion time is $\omega_{pi}^{-1} = \sqrt{\epsilon_0 m_i / Z e^2 n_e m_i}$ the ionic plasma period, where m_i the ion mass and Z the atomic number: for $n_e = 0.03n_c$ $2\pi\omega_{iHe^{2+}}^{-1} = 0.94\,\mathrm{ps}$ and $2\pi\omega_{iH^+}^{-1} = 0.66\,\mathrm{ps}$ for protons. Ions expand radially for the outter shells [Lifschitz et al., 2014]. The inner ion shells are faster than the outer ion shells, resulting in a front of piling-up ions i.e. a shock, or blastwave. The electrons move with the ions, but their temperature induces a charge field separation at the shock vicinity. This fields can be at the origin of a second acceleration stage, or of a spectrum modulation. A schematic representation of wakefield assisted coulomb explosion is described in Fig. 1.2.

1.3.2 Collisionless shock acceleration

In hydrodynamics, shocks are a discontinuous solution of fluid equations. Non-linearities of these equations allow small perturbations to grow into discontinuities, to propagate and to self-sustain. A *shock front* is a discontinuity surface crossed by the fluid, and then, one can define an *upstream* flow and a *downstream* flow. In gas, collisions dominate the other interactions, and the fluid distribution is maxwellian on both side of the shock. If the gas is made of several species, the constituents reach the same temperature. The downstream conditions are uniquely described by the upstream conditions, according to the flux conservation of mass, momentum and energy (these relations are given with more details in Chapter III). Dissipation processes are limited to collisions, and therefore the shock thickness is of the order of the mean free path. In contrast, plasmas created by intense short pulse laser are collisionless, and the energy and momentum can be transferred to the electromagnetic field. Electrons and ions are affected differently by the fields and thus do not share *a priori* the same velocity distribution. Without collisions and in the presence of fields, the temperatures are not isotropic either. These various non-linear interactions between the particules, the fields and the kinetic distribution yields a wealth of different shocks, transient state, and instabilities. Nonetheless, the effect of dissipation is necessary to shock formation, otherwise, equations exhibits soliton or waves solutions leaving the downstream fluid unchanged. This dissipation is given by turbulence trough the correlation function see Eq. 1.21

Electrostatic laminar fluid equations in the shock frame

We will restrain the analysis to steady shock in quasi-laminar conditions, i.e. ignoring turbulence of scale greater than the shock thickness. On scale much longer than these turbulences, they appear as solitons, but are shocks at the scale of interest. We will focus on the Electrostatic Shock (ES), (without magnetic field), as this kind of shock is observed in laser-plasma PIC simulation [Silva et al., 2004]. The collisionless electrostatic shock comes from the steepening of an ion acoustic wave, as this is the only ion wave that can propagate in such plasma. The following derivations are inspired by the classical reference of Tidman and Krall [Tidman and Krall, 1971], and by the Theory Introduction of Macchi [Macchi, 2013].

The shock front moves at a velocity V_s (the *shock velocity*). The shock is characterized by the potential $\mathit{\Phi}$ at the front of the shock, and its Mach number $M = V_s/c_s > 1$ where c_s is the speed of sound $c_s = \sqrt{ZT_e/m_i}$ where T_e is the electron temperature, m_i the ion mass and Z the ionization number. The concept of *speed of sound* may seem paradoxal in a medium unable to propagate compression waves by collision. Actually the ion compression waves are performed by the electric field. Interest in ES for ion acceleration comes from the ability of the shock potential to reflect upstream plasma ions (ahead of the shock). Ions at rest and reflected from the shock reach a final velocity of $2V_s$, and thus, and energy $m_i(2V_s)^2/2 = 2ZM^2T_h$. We see here the importance of temperature on the final ion energy, and we will see later the importance of the ion velocity distribution in the shock formation. Let's focus on the potential Φ, it obeys the Poisson equation given by:

$$\partial_x^2\Phi = \frac{e(n_e - Zn_i)}{\epsilon_0} \tag{1.66}$$

The first and second moment of the Vlasov equation give the continuity and momentum equations for all charged species a, assuming isotropic thermal velocities:

$$\partial_t n_a + \nabla\cdot(n_a u_a) = 0 \tag{1.67}$$

$$m_a n_a(\partial_t u_a + u_a\cdot\nabla u_a) = q_a n_a(\mathbf{E} + u_a\times\mathbf{B}/c) - \nabla P_a \tag{1.68}$$

In an unmagnetized plasma $\mathbf{B} = 0$ and $\mathbf{E} = -\nabla\Phi$. Lets look first at the electron distribution. We are interested in the phenomena at the time scale of the ion motion, we can neglect the inertia of electrons $m_a n_a(\partial_t u_a + u_a\cdot\nabla u_a) = 0$: they adapt instantly to the ion distribution. Finally eq. 1.68 yields:

$$en_e\nabla\Phi = \nabla P_e \tag{1.69}$$

And closing the Vlasov system with the perfect gas equation of state $P_e = n_eT_e$ and integrating:

$$n_e = n_0 \exp e\Phi/T_e \tag{1.70}$$

The quasi neutral assumption $n_e \approx Zn_i$ is broken as shock scale length reaches the same magnitude as the debye length λ_D. We search now the expression of Φ propagating with a constant wave velocity V in the laboratory frame. We write the equations 1.67 and 1.68 for ions in the frame where the shock is stationnary. We assume the ion pressure ∇P_i to be negligible in front of the coulomb potential. In the stationary frame $\partial_t n_i = 0$ and $\partial_t u_i = 0$ and thus :

$$\partial_x(n_iu_i) = 0 \qquad\qquad u_i\partial_x u_i = -(Ze/m_i)\partial_x\Phi \tag{1.71}$$

Ions upstream are in the region $x > 0$. Far ahead from the shock, their velocity is $-V$, and $\Phi = 0$, then integration of the previous equations yields:

$$n_iu_i = -(n_0/Z)V \qquad\qquad m_iu_i^2/2 + Ze\Phi = m_iV^2/2 \tag{1.72}$$

Eliminating u_i:

$$n_i = \frac{n_0}{Z}\frac{V}{(V^2 - 2Ze\Phi/m_i)^2} \tag{1.73}$$

We notice that n_i is real valued only if $m_i V^2/2 > Ze\Phi$, meaning that ions have enough kinetic energy to overcome the potential jump, and therefore are *not reflected*. Let's develop the soliton solution first, and we will see how a soliton can evolve in a shock. Let's introduce the dimensionless units : $\xi = x/\lambda_D$, $\phi = e\Phi/T_e$, and $M = V/c_s$. The soliton condition $m_i V^2/2 > Ze\Phi$ translates in $\phi < M^2/2 = \phi_{cr}$. Replacing n_i in the Poisson equation 1.26 yields:

$$\frac{\partial^2 \phi}{\partial \xi^2} = \left[e^{\phi} - \frac{M}{(M^2 - 2\phi)^{1/2}} \right] \tag{1.74}$$

Multiplying by $\partial\phi/\partial\xi$ and integrating, it possible to write the previous equation with the form $(\partial_{xi}\phi)^2/2 + U_1(\phi) = 0$ where :

$$U_1(\phi) = -\left[e^{\phi} + M(M^2 - 2\phi)^{1/2} \right] + 1 + M^2 \tag{1.75}$$

To study the solution of this equation we will represent it with the Sagdeev's *pseudopotential* method. This method draws an analogy between the trajectory of a particle $q(t)$ in motion in a potential U. The trajectory $q(t)$ is equivalent to $\phi(\xi)$. The integration constant in U_1 is chosen in order to have $U_1(0) = 0$. Such pseudopotential and the associated soliton solution $\phi(\xi)$ is given in Fig. 1.3

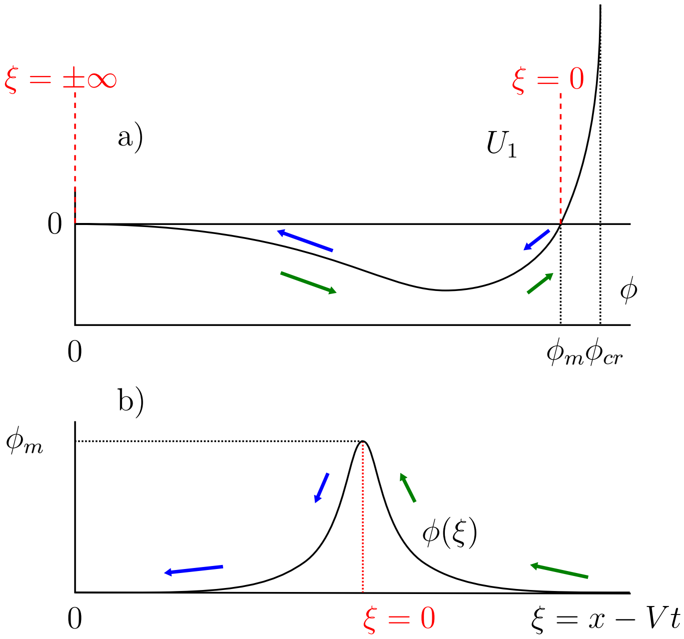

Figure 1.3 – (a) Pseudopotential U_1 and the associated soliton solution $\phi(\xi)$ (b). The pseudo-particle starts in $\phi = 0$, falls in the potential well, is reflected in ϕ_m then comes back at $\phi = 0$ in an infinite time. Arrows show the pseudo-particle path.

The pseudo-particle starts in $\phi = 0 (\xi = +\infty)$, falls in the potential well, is reflected in ϕ_m then comes back at $\phi = 0$ in an infinite time $(\xi = -\infty)$, performing a single oscillation. The soliton is symmetric in ξ, meaning that the plasma comes back to its initial conditions. The condition $\phi < \phi_{cr}$ translates in $M < 1.6$ [Tidman and Krall, 1971]. In short, an ionic acoustic soliton with velocity V cannot reflect cold ions if the threshold condition Eq. 1.76 is not met:

$$Ze\Phi_{max} > m_i V^2/2 \qquad\qquad M > 1.6 \tag{1.76}$$

.

For $Ze\Phi_{max} > m_i V^2/2$, all ions are reflected, and one would expect the shock to quickly loose its energy and collapse.

Symmetry breaking

Several effects can break the symmetry of the soliton solution, and give rise to a shock. All include kinetic effects due to the ion velocity distribution: ion reflection, Landau damping, and electron trapping. We will discuss the first condition. The reflection of ions enables to break this symmetry by changing the upstream and downstream densities. Lets assume that the ion population has a given distribution function $f(v)$ in the shock frame. In the soliton case, $f(v) = 0$ and all ions have a velocity V in the shock frame, sufficient to overcome ϕ_m. If $f(v) \neq 0$, some ions may be too slow to overcome ϕ_m and get reflected. The function $F(\phi)$ denotes the fraction unable to cross a potential ϕ, i.e ions with a velocity v in the shock frame such as $(v+V)^2 < 2Ze\Phi/m_i$.

The ion density need now to account for reflected ions, and this effect is opposite before and after the shock: $n(\xi = +\infty) = n_0[1 + F(\phi_m)]$ and $n(\xi = -\infty) = n_0[1 - F(\phi_m)]$. From Poisson equation again we obtain:

$$\frac{\partial^2 \phi}{\partial \xi^2} = \left[(1 + S(\xi)F(\phi_m))e^{\phi} - \frac{M(1 - F(\phi_m))}{(M^2 - 2\phi)^{1/2}} - 2\Theta(\xi)F(\phi)\right] \equiv -\frac{\partial U_2}{\partial \phi} \tag{1.77}$$

Where $S(\xi) = 1$, $\Theta(\xi) = 1$ for $\xi > 0$ and $S(\xi) = -1$, $\Theta(\xi) = 0$ for $\xi < 0$. These terms break the symmetry of ϕ and the potential oscillates between ϕ_m and ϕ_2 behind the shock, as shown Fig. 1.4.

Landau damping by the electrons may also transform a soliton acoustic wave into a shock. It gives a solution close to the one given by U_2, but the amplitude of the ϕ oscillation is dumped behind the shock, and stabilizes around a constant.

To conclude, we have seen that an ionic acoustic soliton with velocity V can not reflect cold ions if $Ze\Phi_{max} < m_i V^2/2$. For $e\Phi_{max} > m_i V^2/2$, all ions are reflected, and one would expect the shock to quickly loose its energy and collapse. Resolving the equation governing Φ, the reflection condition requires $M > 1.6$. But if the ion velocity distribution $f(v)$ allow some ions to have a velocity such as $(v+V)^2 < 2Ze\Phi/m_i$, then a shock is formed and ions get reflected at velocity $2(V+v)$. Two conditions may allow this effect :(1) if the ions have a sufficient temperature T_i, (2) if the ions move with a bulk velocity in the same direction than the shock, that helps to lower the relative velocity below the threshold. This second condition is of special interest in case of strong gradient target with hot electrons but cold ions. The vacuum expansion of the plasma due to thermal charge separation at the rear side of the target pulls the ions in the same direction as the shock. This "TNSA-like" pre acceleration enables the ions to be slow enough relatively to the shock to be reflected [Macchi et al., 2012]. We will see next how the shock is trigged in laser-plasma interaction, and how the model holds in 1D and 2D PIC simulation.

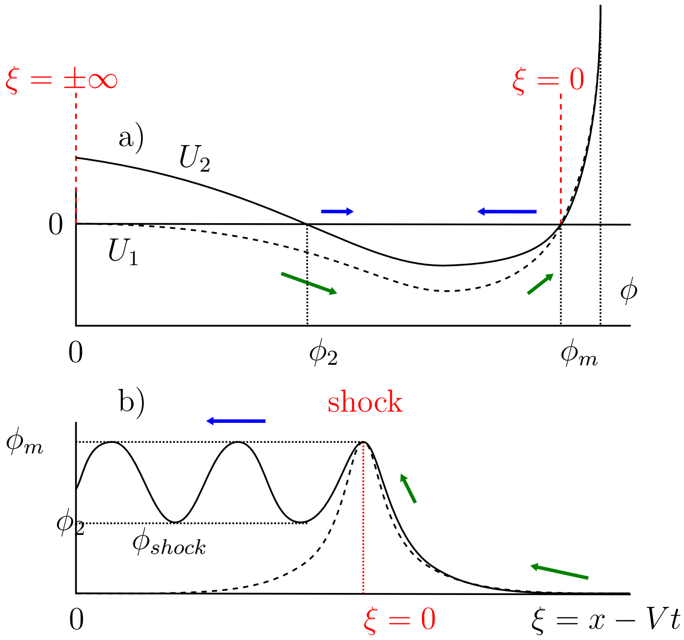

Figure 1.4 – Pseudopotential U_2 of a shock solution (a) and the associated $\phi(\xi)$ (b). The pseudo-particle starts in $\phi = 0$, falls in the U_1 potential well, then jumps into the U_2 potential at the reflection in ϕ_m. Then the pseudo-particule oscillates between ϕ_m and ϕ_2. The modulation of ϕ creates the necessary condition to trap ions behind the shock, who oscillate in the shock frame. Arrows show the pseudo-particle path.

Shock triggered by intense laser

PIC simulations of ES shocks are challenging, as the slow velocity tail of the distribution function must be accurately described. Furthermore, experimental demonstration of CSA obtained only a weak number of protons ($< 10^8$ [Haberberger et al., 2012]). Several teams [Esirkepov et al., 2004; Silva et al., 2004] showed in 2D PIC simulations that such a soliton could be launched by the piston action of intense laser radiation pressure. The observation of reflected ions demonstrate that the soliton evolves into a shock. The piston velocity u_p is derived from the flow momentum balance $m_i(n_i u_p)u_p \sim I/c$:

$$u_p = \left(\frac{Z}{A}\frac{m_e}{m_p}\frac{n_e}{n_c}\right)^{1/2} a_0 c \tag{1.78}$$

If $u_p > c_s$, this piston snowplow may generate a shock wave propagating at velocity $V_s \approx u_p$. Silva *et al.* observed few differences between 2D and 1D in the maximum ion energy. As the piston pressure depends of the inhomogenuous laser intensity, the shock front is bent. The effect on the shock propagation over few wavelengths is said to be weak, as long as $w_0 >> \lambda$. 1D simulation by Macchi *et al.* [Macchi et al., 2012] ($a_0 = 16$,$n_e = 20n_c$,10 fs,thickness of 15λ,gradient of 1λ) observed a density spike moving at $0.05c$, close to the Hole-boring velocity. In a cold ion plasma the soliton verified the full reflection condition 1.76 and indeed accelerated monoenergetic ion bunches. The bunching comes from oscillation of the hot electron cloud around the ion density spike. With a non-zero ion temperature of $T_i = 5\,\text{keV}$, and a shock velocity at the threshold limit, ions still are reflected as expected, and the shock slows down. The ion spectrum is nonetheless never mono-energetic. A longer pulse (170 fs) shows the creation of a train of shocks, from pulsed hole-boring. The first one accelerating ions with a broad spectrum up to 6 MeV, while other ions oscillate back and forth in the shock train.

1.3.3 Ion acceleration with dipole vortex in near critical plasma

The trigger of a collisionless shock with the ponderomotive force of the laser requires high density of several n_c to ensure $u_p > c_s$. Creation of a soliton has only been demontrasted with sharp gradients, both in simulations and experiments [Haberberger et al., 2012; Tresca et al., 2015]. Here I present another mechanism, achievable in plasma of electronic density between 0.1 and 1 n_c. This model makes use of a magnetic vortex, it has been proposed from simulations [Kuznetsov et al., 2001; Matsukado et al., 2003; Bulanov and Esirkepov, 2007; Yogo et al., 2008; Nakamura et al., 2010], and indirectly inferred from few experiments [Willingale et al., 2006, 2007; Fukuda et al., 2009]. Entering the near-critical plasma, the laser self-focuses, ideally in a single filament, and the target is thick enough that the laser is totally absorbed. The laser wakefield accelerates fast electrons. Together with the neutralizing cold electron return current, this current leads to the formation of a quasistatic magnetic field with magnitude:

$$|\mathbf{B}| = m_e c\omega_0/e \tag{1.79}$$

which can reach ≈ 100 MG. If the plasma gradient is steep (with respect to the self-focused spot size), the vortices expand perpendicularly to the plasma gradient, and the magnetic field disappears before accelerating ions. If the plasma gradient is more gentle, the vortices move along the plasma channel, and survive during the time necessary for the ion motion (few ps). Nakamura et al. find an optimal gradient length $l = |n/(dn/dx)| = c\tau_0 n_{min}/n_{max}$ where $n_{min}/n_max = 1/8$. The magnetic field gradient repels the electrons and maintain charge separation. The resulting E-field is roughly:

$$E \sim \nabla B^2 \epsilon_0/2\pi e n_e \tag{1.80}$$

Near the axis, the oscillations of the wakefield have an average (over several plasma period) focusing effect for ion near the axis [Gorbunov et al., 2001; Lifschitz et al., 2014]. This ion filament is accelerated by this long lived charge separation and pinched by the magnetic vortex. A density spike is formed at the ion filament extremity, which moves with the vortex expansion, at the Alfven velocity V_A: the characteristic velocity of ion-magnetic waves.

$$V_A = B_2/\sqrt{\mu_0 A m_p n_2} \tag{1.81}$$

Bulanov S.S. et al find by 2D parametric PIC simulation an optimal density $n_i > 1.6 n_c$ and a proton energy scaling of $E_{p,max} = a\gamma_e^2 m_e c^2$, reaching 1 GeV at 1 PW for an optimal density and target length of $n_i = 4n_c$ and $l = 50\lambda$.

Chapter 2

PIC simulation of laser-plasma interaction at near-critical density

Contents

2.1 Laser-plasma interaction in the near-critical regime : PIC simulation of the experimental conditions

Motivation

We compared laser-plasma interaction simulations on two massively parallel Particle-in-Cell (PIC) codes. The first one is OSIRIS [Fonseca et al., 2002] in cartesian 2D geometry, and the second one is CALDER-CIRC [Lifschitz et al., 2009] in quasi-cylindrical 3D geometry. 2D geometry simulations, while less computationally expensive, do not model accurately relativistic self-focusing, and heat dissipation processes, which are inherently 3D effects.

The simulations reproduce laser parameters of the SAPHIR Laser, and plasma profiles achieved with near-critical supersonic shocked nozzle made from a mixture of helium and 1 % hydrogen. It confirms the key features observed during the experiments : laser depletion and filamentation, electron acceleration mixing wakefield acceleration and direct acceleration, and the absence of collisionless plasma shock waves able to accelerate protons. The laser undergoes relativistic self-focusing (SF) down to the matched spot size [Sprangle et al., 1987], and is reduced to an ultra-intense single cycle pulse by self-compression (SC) with a growth rate close to the scaling derived by [Vieira et al., 2010]. Transverse ion acceleration by Coulomb explosion is observed in accordance with mechanisms described in[Lifschitz et al., 2014; Kahaly et al., 2016; Krushelnick et al., 1999], yielding up to 1.4 MeV protons. The cold electron return current in quasi-cylindrical 3D geometry is smaller ($(|p_{cold}/p_{hot} \approx 1/40)$) than the value observed in 1D simulation ($(|p_{cold} \sim p_{hot}|)$). In absence of two-stream mixing, the electronic heating is related to the ponderomotive scaling, and the electronic temperature is not sufficient to trigger a plasma shock wave.

2.1.1 Simulation Parameters

Normalized vector potential (a_0)	**Laser wavelength**	**Laser pulse length (FWHM)**	**Laser pulse radius**$(1/e^2)$	**Plasma composition**
4.0	0.8 µm	25 fs	10 µm	99 %He + 1 %H

Table 2.1 – Laser and plasma parameters for both CALDER-CIRC and OSIRIS simulations

Transverse box size	**Longitudinal box size**	**Trans. cell size**	**Long. cell size**	**Nb. of MP of protons and electrons per cell**	**Nb. of MP of helium ions per cell**
76 µm	1016 µm	47 nm	25.4 nm	16	3

Table 2.2 – Grid parameters for OSIRIS 2D simulation. MP stand for macro-particles

Grid parameters for OSIRIS and CALDER-CIRC are given Tab. 2.2 and 2.3 respectively. OSIRIS simulate the whole 2D plan, without reflection on the symmetry axis. No collisions nor ionization were included. The initial electron temperature is 3 keV. The input laser polarization is along the transverse direction of the box. The laser parameters are given in Tab. 2.1, the pulse is Gaussian with normalized potential at focus in vacuum $a_0 = E_x e/m_e c\omega_0 = 4$ (i.e. $\mathrm{I} = 3 \times 10^{19}\,\mathrm{W \cdot cm^{-2}}$). The plasma profile is a fit of actual gas jet experimental data: the supersonic shock nozzle profile is well described by the sum of two gaussians with characteristic lengths $(\lambda_1, \lambda_2) = (35\,\mu\mathrm{m}, 200\,\mu\mathrm{m})$ and maximal helium density $n_{at0} = 1.3 \times 10^{20}\,\mathrm{cm^{-3}}$. The plasma is made of 99 % He and 1 % H, both fully ionized prior to the simulation, with an initial temperature of zero. Protons being likely to be the accelerated particles, we set more hydrogen macro-particles than helium ones, but with a reduced weight, decreasing noise on the proton density. The maximum electronic density is $n_{e0} = 2.6 \times 10^{20}\,\mathrm{cm^{-3}} = 0.15 n_c$. The large size of the simulation box in the propagation direction z enables to monitor full laser propagation into the long low density tails of the density profile given by:

$$n_e(z) = n_{e0}\left(\frac{2}{3}\exp(-\frac{z^2}{2\lambda_1^2}) + \frac{1}{3}\exp(-\frac{z^2}{2\lambda_2^2})\right) \tag{2.1}$$

CALDER-CIRC is a quasi-cylindrical 3D PIC code with Fourier decomposition of the electromagnetic fields in the poloidal direction [Lifschitz et al., 2009]. We use only the two first poloidal transverse modes, laser and plasma parameters remain unchanged. Although reduced to two modes, the 3D geometry of CALDER-CIRC enables a better treatment of the long-term hot electron expansion and relaxation.

OSIRIS simulates the whole 2D plane (no reflection on the axis).

Transverse box size	**Longitudinal box size**	**Trans. cell size**	**Long. cell size**	**Nb. of MP of protons and electrons per cell**	**Nb. of MP of helium ions per cell**	**Transverse modes**
100 µm	1200 µm	47 nm	25.4 nm	25	3	0 and 1

Table 2.3 – Grid parameters for CALDER-CIRC simulation. MP stand for macro-particles

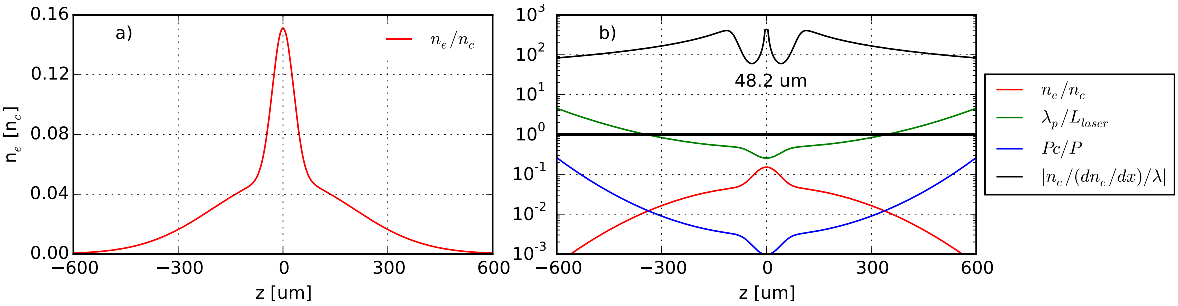

Figure 2.1 – (a) electronic density profile (b) Dimensionless parameters associated with the profile in log scale. $\lambda_p = 2\pi c/\omega_p$ is the plasma wavelength and L_{laser} the laser pulse length. P_c is the critical power defined Eq. 1.55, and P the power calculate for 1.5 J in the focal spot. The parameters $n_e/(\lambda \partial n_e/\partial z)$ is the gradient length expressed in λ. Its minimal value is given for $\lambda = 0.8\,\mu\text{m}$

2.1.2 Laser propagation

In a first phase, the laser propagates into a plasma ramp whose electron response time is longer than the pulse duration, or in other terms, the plasma wavelength is longer than the pulse. Considering a constant pulse duration, this regime holds while $n_e < 2 \times 10^{19}\,\text{cm}^{-3}$ ($n_e < 0.012 n_c$). The ponderomotive force drives a non-linear plasma wave and the refractive index is modulated by the density and intensity gradients. As the pulse propagates, these gradients focus and compress the laser, increasing its intensity. The ponderomotive potential is strong enough to leave a cavitation region behind the pulse, where all electrons are expelled from (referred to as the *blowout* regime[Pukhov and Meyer-ter Vehn, 2002; Lu et al., 2006, 2007]).

The spot size reduction is driven by the relativistic self-focusing. The laser power exceeds the critical power for relativistic self-focusing $P_c = 17.3(n_c/n_e)$GW when $n_e > 6 \times 10^{17}\,\text{cm}^{-3}$, as soon as the laser enters the simulation box. We assume than 50 % of the laser power is encircled into the $1/e^2$ spot size. When the laser reaches the region $n_e = 0.02 n_c$, self focusing and self compression lead to $a = 5.5$, and $c\tau_0/(c/\omega_p) = 5$, and the self-steepening conditions derived by Vieira et al [Vieira et al., 2010] Eq. 1.59 at the front are met.

Laser propagation: OSIRIS

The laser E-field and the electronic density are shown for three different time-steps Fig. 2.2. On the first picture, after the first 400 µm of propagation, the laser has experienced self-focusing. Reaching the position where $n_e = 0.04 n_c$ (middle picture) the laser transverse mode is degraded. It splits in several beams, each one with a size comparable to w_m, and the wakefield experiments transverse modulations leading to asymmetric plasma bubbles. It continues to break into several beams. The evolution of the laser spot size during propagation is illustrated in Fig.2.4a).

In the region of the peak density ($n_e = 0.15 n_c$) the laser is diffracted and depleted, its intensity dropping below the relativistic limit. Both the laser and energetic electron beams drive several wakefields. In accordance with the Vieira scaling for self-focusing, the laser front evolves to an optical shock: one cycle reaches $a = 7$ when the rest of the

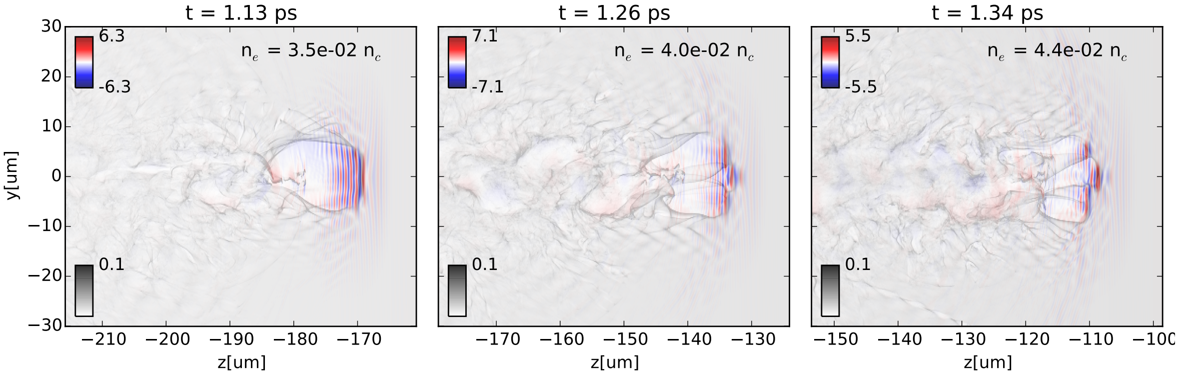

Figure 2.2 – Laser E_x field (in blue to red scale) and electronic density (gray) at various times during propagation. Field is given in normalized unit $a = E_x e/m_e c\omega_0$, and density in fraction of n_c. Peak density of the gas jet is located at $z = 0\,\mu\mathrm{m}$.

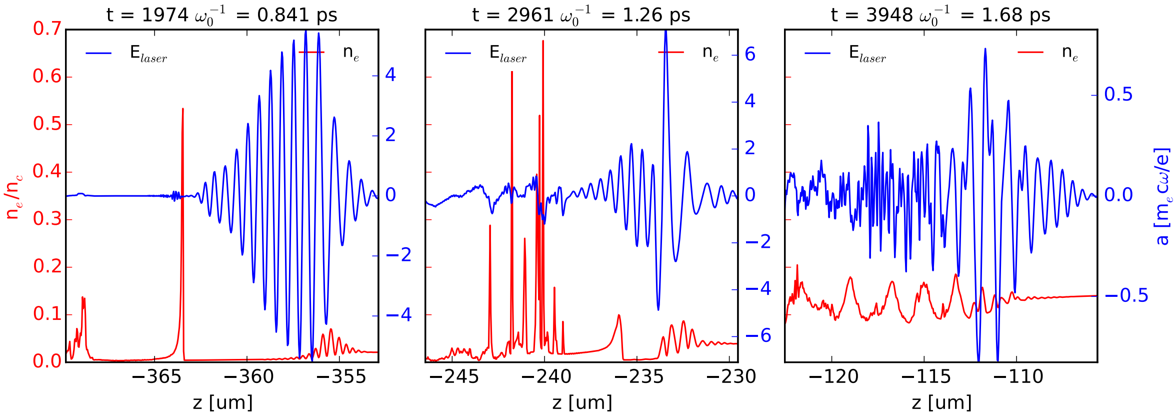

Figure 2.3 – Laser E_x field (blue) and electronic density (red) longitudinal lineouts at various times. Field is given in normalized unit $E_x e/m_e c\omega_0$, and density in fraction of n_c. Peak density of the gas jet is at $z = 0\,\mu\mathrm{m}$.

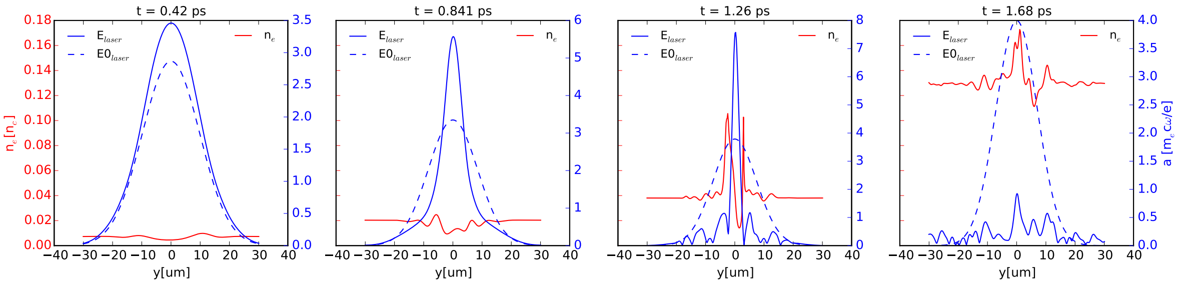

Figure 2.4 – Laser E_x field envelop (blue) and electronic density (red) transverse lineouts at various time. Field is given in normalized unit $E_x e/m_e c\omega_0$, and density in fraction of n_c. Dashed line shows the field envelope in vacuum.

pulse amplitude is below $a = 2$, as seen on Fig. 2.3. At this time, the laser is already broken in several beams, and collapses quickly. Evolution of pulse duration and spot size just before the collapse are plotted Fig. 2.5.

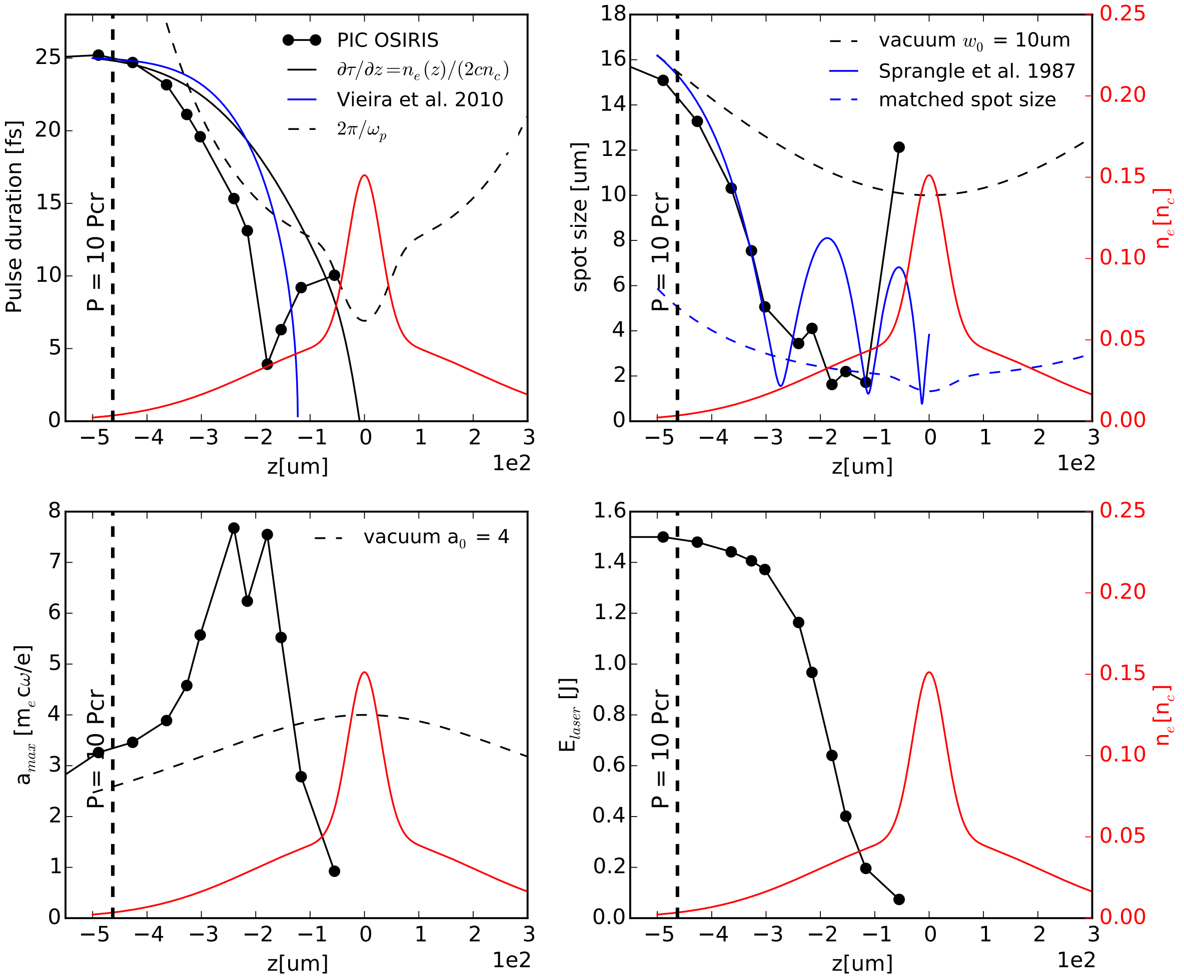

Figure 2.5 – 2D simulation: Evolution during propagation of a) pulse duration (FWHM) (b)laser spot radius (intensity level at $1/e^2$) c) the maximum normalized potential vector a (d) the relative variation of the laser energy. The electronic density profile is plotted (red line) on all figures. (a) Self-steepening Vieira et al. [Vieira et al., 2010] model for $a_0 = 4$ (dashed line), and self compression rate assuming linear refractive index (solid black line). The plasma response time $2\pi/\omega_p$ in blue line. (b) Spot size is compared with spot size for vacuum propagation (dashed line), and with the matched spot size, assuming actual self-compression but no energy loss(solid line). (c) $a(z)$ is compared with vacuum propagation for $a_0 = 4$ (dashed line).

Laser propagation: CALDER-CIRC

Self-focusing occurs at the same rate, and the laser spot size reduces eventually to the matched spot size after 350 µm of propagation. The laser E-field and the electronic density are shown beyond this point in Fig. 2.6. Self injection inside the bubble starts when the laser spot size reaches the resonant matched spot size w_m (Eq. 1.57) after 350 µm propagation. Electrons are accelerated into the bubble wakefield. Electrons are faster than the laser group velocity, thus after a distance called *dephasing length*, electrons reach the bubble center and enter in the decelerating part of the bubble. The laser envelop is modulated longitudinally (See Fig. 2.7) by the electron beam, and particle acceleration coincides with laser depletion. The electron beam eventually outruns the laser, reaches the front of the bubble, and drives its own wakefield. The code produces increased noise near the axis, due to the on-axis singularity in cylindrical Maxwell equation. After the peak of the gas jet, self focusing and laser depletion reduces the laser transverse extent to ≈ 10 simulation cells, and therefore, the laser behaviour must be cautiously interpreted. The relativistic self focusing rate is accurately described (see Fig. 2.9b)) by the envelope equations derived by Sprangle et al. [Sprangle et al., 1987] and recalled in Chapter I. Without laser energy loss and self compression, the spot size would oscillate, as the diffraction and the self focusing compete. The simulation doesn't feature such oscillations, but the complete electron blow-out limits the validity of Eq.1.54.

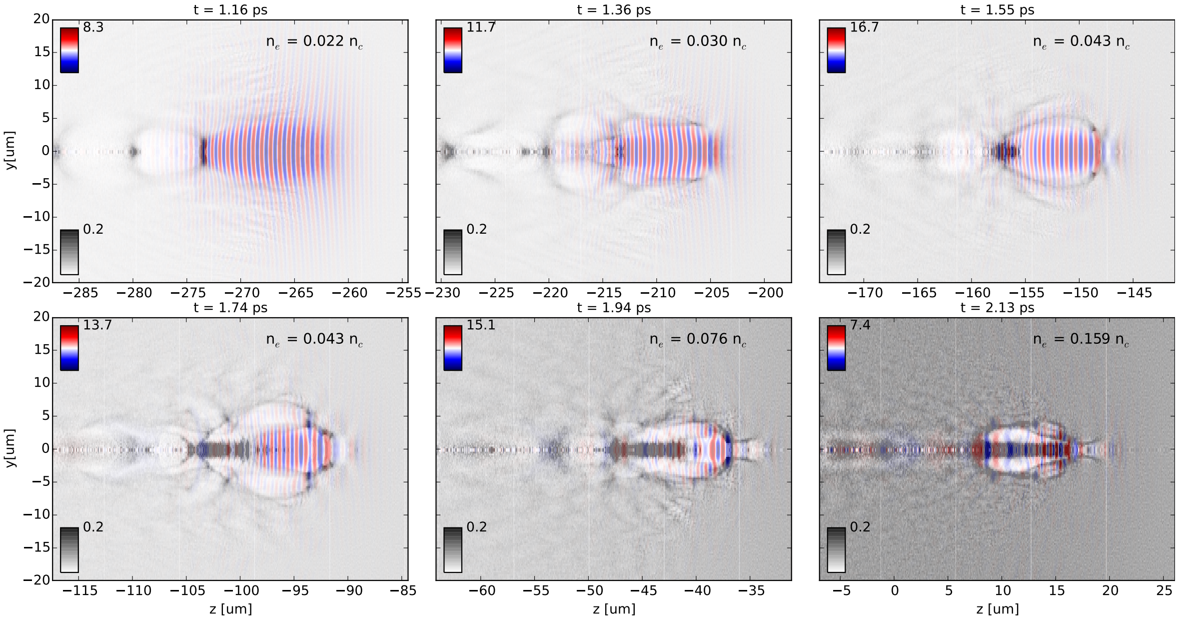

Figure 2.6 – Laser E_x field (in blue to red scale) and electronic density (gray) at various times during propagation. Field is given in normalized unit $a = E_x e/m_e c\omega_0$, and density in fraction of n_c. The thick black line is the length of the plasma wavelength of surrounding plasma, whose density is annotated. Peak density of the gas jet is located at $z = 600\,\mu\text{m}$.

Laser propagation in CALDER-CIRC features slower self-compression rate compared to the OSIRIS simulation. The optical shock occurs after 1.94 ps and 560 µm propagation (1.26 ps and 370 µm in OSIRIS). The results plotted in Fig. 2.9a) integrate Eq. 1.59 with local value of the initial electronic density profile. Nonetheless, it agrees quantitatively with the simulation, at the exception of early bouncing. The associated laser redshift is illustrated in Fig. 2.8 by the evolution of the local frequency normalized by the laser central frequency ω_0. The local frequency $w(\xi)$ across the pulse is derived by the help of the Hilbert Transform expressed as a Fourier operation:

$$\tilde{E} = E + i\mathrm{H}(E) = \mathrm{F}^{-1}\left(\mathrm{F}(E)2U\right) \tag{2.2}$$

Where H is the Hilbert Transform and F the Fourier Transform, and U the unit step function. From the complex value $\tilde{E}$ of the electric field E, it is possible to derive the en-

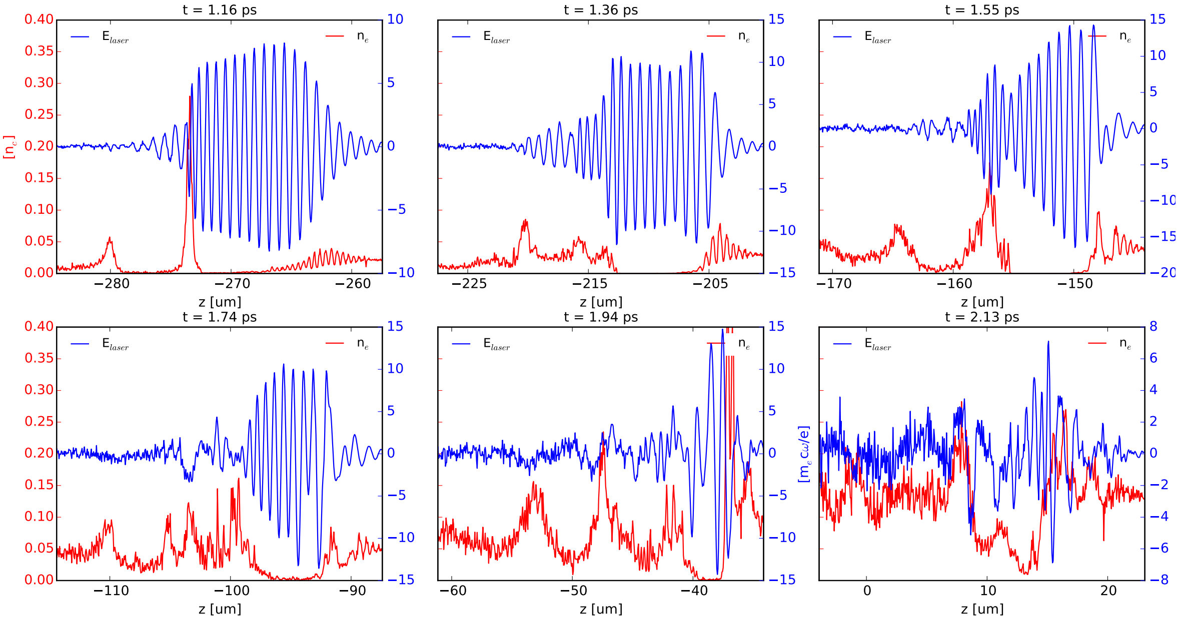

Figure 2.7 – Laser E_y field (blue) and electronic density (red) longitudinal lineouts at various times. Field is given in normalized unit $E_x e/m_e c\omega_0$, and density in fraction of n_c. Peak density of the gas jet is at $z = 0\,\mu\mathrm{m}$.

velop of the field ($|\tilde{E}|^2$), and its phase along $\xi = x - tc$ via its complex argument($\Phi(\xi) = \mathrm{Arg}(\tilde{E(\xi)})$). The local frequency is defined as $\omega(\xi) = (\partial\xi/\partial t)(\partial\Phi/\partial\xi) = -c(\partial\Phi/\partial\xi)$. The pulse is redshifted as the front and blue shifted at the back, with relative frequency variation reaching $d\omega/\omega_0 = \pm 0.4$. The peak density of the background plasma is $n_e = 0.15 n_c(\omega_0)$ but $n_e = 0.4 n_c(0.6\omega_0)$ and the laser absorption is enhanced.

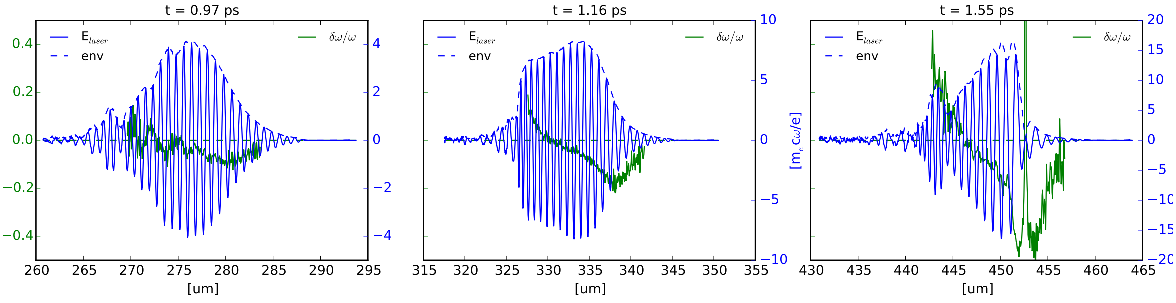

Figure 2.8 – Laser E_y field (blue) and $\delta\omega/\omega_0$ (green) the local frequency shift before the optical shock at various times during propagation.

The relative laser energy evolution is plotted in Fig. 2.9d). After 400 µm propagation, the laser energy drops drastically and the laser losses 90 % of its initial value in the 200 µm preceeding the peak density. The laser energy is lost generating the channel and accelerating electrons. The absorbed energy can then be linked to the average electron quiver motion in the laser field, which transmits its energy to other processes (wakefield, ion motions..):

$$n_e(\langle\gamma\rangle - 1)m_e c^2 = \frac{1}{2} n_e \langle a^2\rangle m_e c^2 \tag{2.3}$$

The laser energy is linked to $\langle a\rangle$ by $E_L = c\tau(\pi w_0^2)\epsilon_0(m_e c\omega_0/e)^2\langle a^2\rangle$. Producing a channel of length d requires $E_{channel} = \frac{1}{2} n_e \langle a^2\rangle m_e c^2 n_e d(\pi w_0^2)$. Equating the laser energy to $E_{channel}$ gives the depletion length d [Willingale et al., 2009]:

$$d = 2c\tau n_c/n_e \tag{2.4}$$

For $\tau = 25\,\mathrm{fs}$ and $n_c/n_e = 1/0.15$ it gives $d \approx 100\,\mathrm{\mu m}$. This length is in rough accordance with: (1) the depletion length observed Fig. 2.9(d) ($\approx 150\,\mathrm{\mu m}$), and (2) with the lineouts Fig. 2.7 showing the laser depletion at the rear side while the optical shock maximal amplitude is conserved.

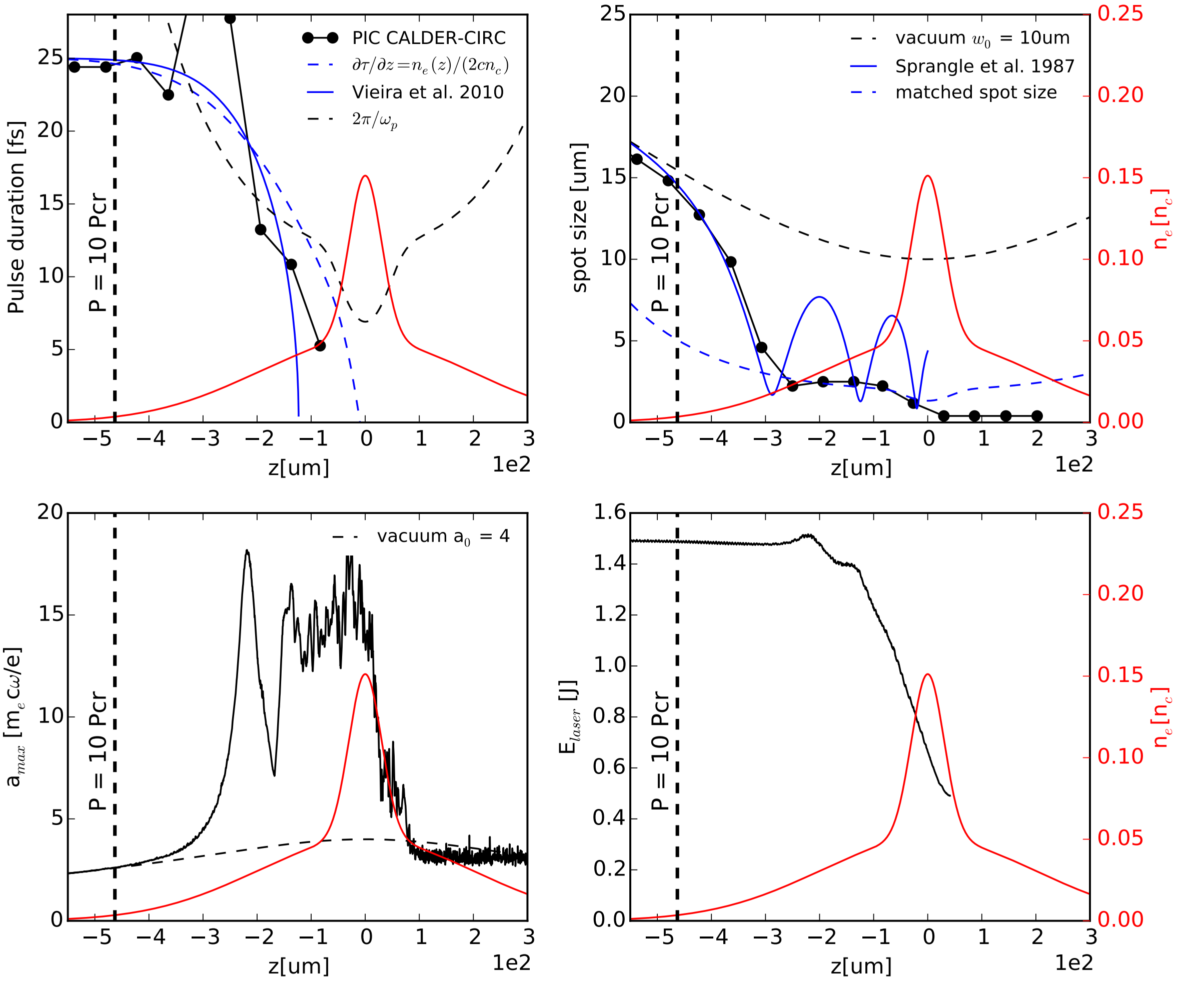

Figure 2.9 – Quasi-cylindrical 3D: Evolution during propagation of a) pulse duration (FWHM) (b)laser spot radius (intensity level at $1/e^2$) (c) the maximum normalized potential vector a d) the variable $\int |a|^2 dz$ compared to its initial value. The electronic density profile is plotted (red line) on all figures. (a) Self-steepening Vieira et al. [Vieira et al., 2010] model for $a_0 = 4$ (dashed line), and self compression rate assuming linear refractive index (solid black line). The plasma response time $2\pi/\omega_p$ in blue line. (b) Spot size is compared with spot size for vacuum propagation (dashed line), and with the matched spot size, assuming actual self-compression but no energy loss.(solid line). (c) $a(z)$ is compared with vacuum propagation for $a_0 = 4$ (dashed line).

2.1.3 Electron acceleration

During the first phase of the propagation ($n_e < 0.02 n_c$) the laser dimensions are close enough to the resonant parameters ($k_p w \approx \sqrt{2}a$ and $c\tau \approx 0.26\lambda_p$ [Lu et al., 2007] to enter the blow-out regime. Expelled electrons form a thin sheath around a cavity following the laser and ions do not move over this time scale due to their inertia. The cavity is a focusing and accelerating structure for trapped electrons. In the approximation of a perfectly spherical bubble the back of the bubble is accelerating electrons, while the front is decelerating them. The typical accelerating field for $a_0 >> 1$ is given by the cold relativistic wave breaking field $E_{WB} = \sqrt{2}(\gamma - 1)^{1/2} E_0$ where

$E_0 = cm_e\omega_p/e \approx 96\,\mathrm{GV}\cdot\mathrm{m}^{-1}\sqrt{2n_e 1\times 10^{18}\,\mathrm{cm}^{-3}}$. The transverse field is always focusing for electrons, and confines them into the bubble. Without specific conditions, no electrons are trapped into the wakefield, as the electron trajectories go around the cavity. But for $a_0 >> 1$ the longitudinal E-field may cross the wavebreaking limit: the velocity of some electrons becomes higher than the phase velocity of the wake and these electrons can be trapped into the bubble. In a 3D model, electron trajectories may cross transversely the rear side of the bubble, injecting electrons [Bulanov et al., 1997]. Laser self focusing, self-steepening, and non-uniform density, affect the size of the cavity. Electrons in the density peak following the cavity can be trapped by the evolving cavity [Kostyukov et al., 2010; Kalmykov et al., 2009]. The background electron temperature grows typically (from zero at our simulation start) to a few eV and increases in high density area [Schroeder et al., 2006]. This increased temperature can trigger self-trapping.

OSIRIS

In the OSIRIS PIC 2D simulation, no injection occurs for $n_e < 0.01 n_c$ i.e. before the relativistic self-focusing. When the bubble becomes unstable, self injection occurs and electrons are accelerated up to 135 MeV. As the laser collapses during propagation, these hot electrons drive wakefields into the dense part of the gas jet. The unstable nature of the injection induces a filamentation of the electron beam, a broad electron spectrum, and electrons in the energy range 5 to 30 MeV are longitudinally spread behind the laser over 10s of µm. The collapsed laser is stretched backwards, and electrons experience the depleted laser field $a \approx 0.1$ for the rest of the propagation.

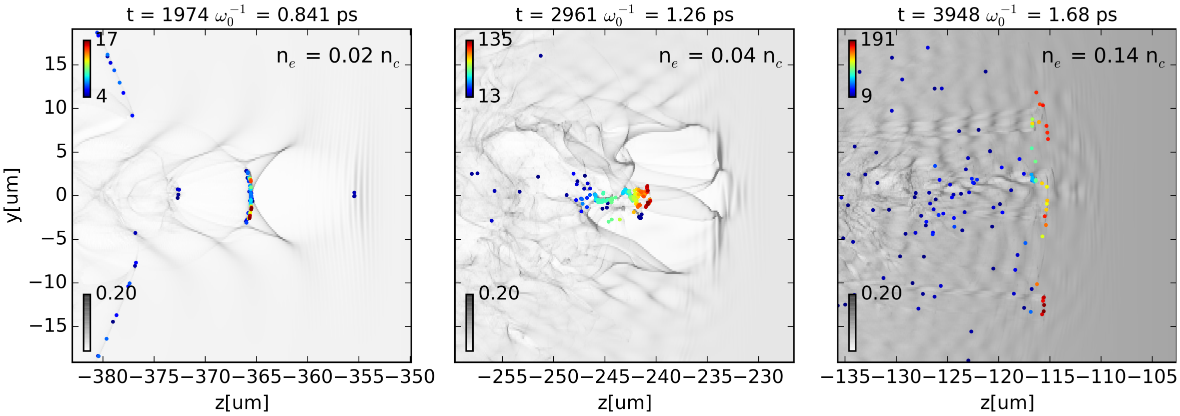

Figure 2.10 – Position and kinetic energy (upper color scale, in MeV) of randomly selected electrons at various times. The background density just before the pulse is indicated. Electronic density is in gray scale, in n_c unit.

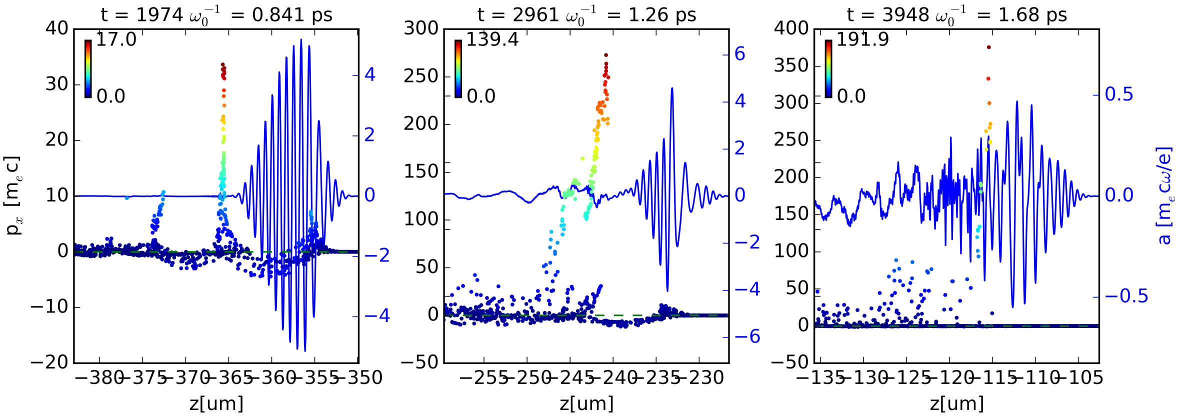

Figure 2.11 – Laser E_y field (blue) and electronic density (red) longitudinal lineouts at various times, averaged over 4 µm in transverse direction. Field is given in normalized unit $E_y e/m_e c\omega_0$, ($a_0 = 4$) and density in fraction of n_c. A random selection of electrons with energies in the 5 to 30 MeV range is plotted in z-p_z phase space, colored with energy (color scale in MeV)

CALDER

In the CALDER PIC simulation, injection occurs when the laser reaches the matched spot size at $z = 400$ µm. An intense electron beam is accelerated by the cavity wakefield up to hundreds of MeV as illustrated Fig. 2.12. At first the electron beam lies into the laser field (Fig. 2.12a)), as the cavity is smaller than the pulse length. The electron velocity is $\approx c$ while at the peak gas density the group velocity of the laser is as slow as $\approx v_g = 0.9c$, therefore the electrons quickly outrun the laser. The electronic density reflects the back of the laser which is depleted within $z = 200$ µm propagation. As the electron beam reaches the middle of the bubble, it experiences a decelerating wakefield, as illustrated in the phase space Fig. 2.13, where the longitudinal field is shown. This figure shows that the dense electron beams drives its own wakefield once the laser is depleted, a feature not observed in the OSIRIS simulation. The plasma channel extends beyond the laser depletion region, generated by the beam space field.

Electrons pile up in front of the laser due to the intense ponderomotive force associated with the optical shock. These electrons at the front of the laser pulse gain positive momentum up to $p_z = 40 m_e c$. Then they are pulled backwards by the conjonction of the wakefield and ponderomotive force with momentum down to $p_z = -15 m_e c$. Both backwards and forward current overlap in the bubble as shown Fig. 2.14. Backward current is neutralized after the first bubble. In the first Chapter section dedicated to electron heating, we described a mechanism where this two streams mixing enables electron heating above the ponderomotive scaling $<\gamma>= \sqrt{1 + a_0^2}$ (where $<\gamma>$ is the mean relativistic factor over all electrons). While effective in 1D, this mechanism drives a weaker back current in 3D, as the electrons escape the ponderomotive pressure transversally.

The divergence of the electron beam is measured at the end of the simulation, at the rear side of the simulation box (Fig. 2.16). The total charge above 4 MeV is 30 pC, and the beam FWHM is 0.15 rad. The beam is more dispersed along the polarization

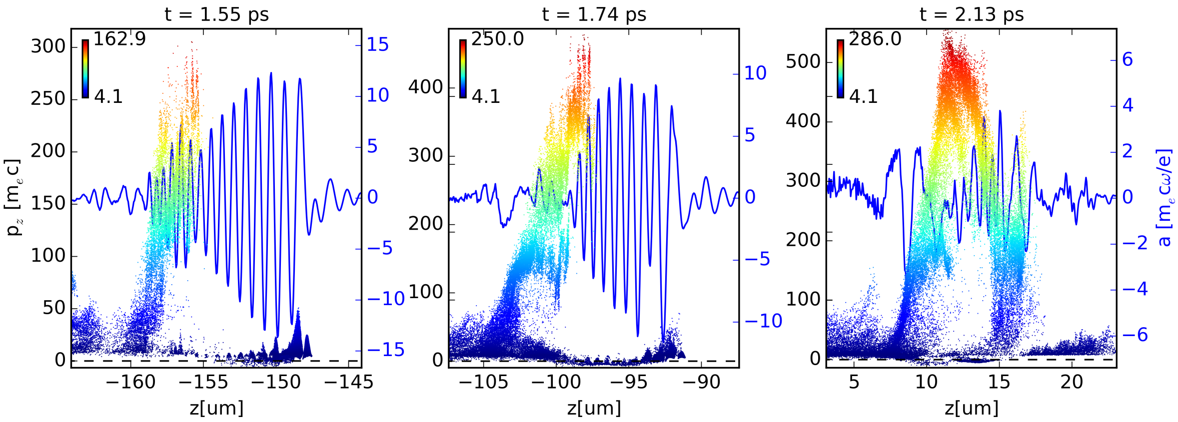

Figure 2.12 – Laser E_y field lineout (blue) and electronic phase space z-p$_z$ (colored dots) along propagation for electrons with energy above 4 MeV. Field is given in normalized unit $E_y e/m_e c\omega_0$, ($a_0 = 4$) and p$_z$ in $m_e c$. Phase space scatter is colored with energy (color scale in MeV).

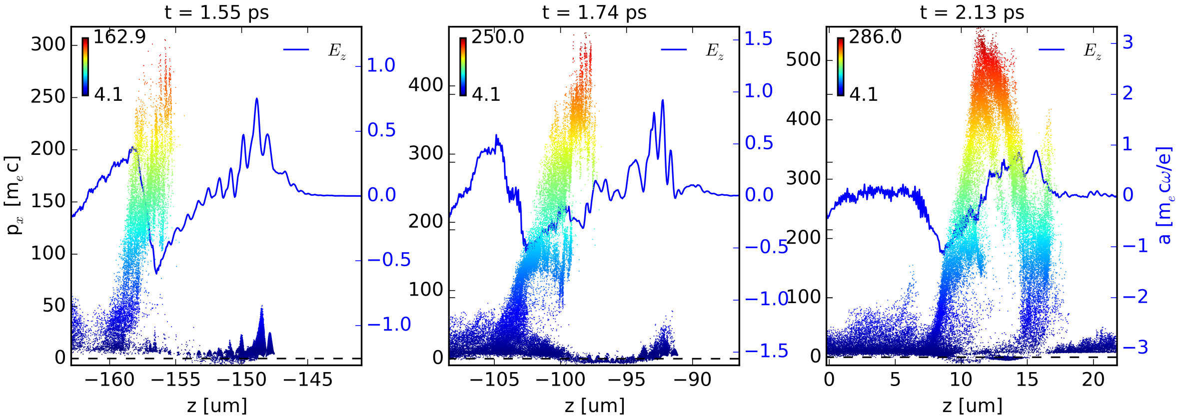

Figure 2.13 – Longitudinal laser E_z field (blue) and electronic phase space z-p$_z$ (colored dots) along propagation for electrons with energy above 4 MeV. Phase space scatter is colored with energy (color scale in MeV).

direction as expected.

The increased noise on the symmetry axis is not due to an equation singularity, but instead to the smaller volume of the simulation cells on the axis. At the beggining of the simulation, macro-particle are evenly scattered in the simulated volume. Eventually, all particles at similar radius mix up. The electric field is the integrate of the charge, and then is less sensible to noise, and it has a limited effect on the electron dynamic. The main effect of the axis-noise is the growing of the emittance.

The 2D OSIRIS simulation shows laser and electron beam filamentation, whereas CALDER-CIRC shows a clean electron beam. The limited number of transverse modes used in this CALDER-CIRC simulation (0 and 1) explains the symmetry of its solution. Higher order transverse modulations are better captured by OSIRIS 2D.

Electronic temperature is initially set to 0. This temperature increases during the simulation due to numerical heating, without impacting electron injection or acceleration. Initale temperature can be set to 100 eV without changes in the solution. Effects of numerical heating on ion acceleration were not investigated.

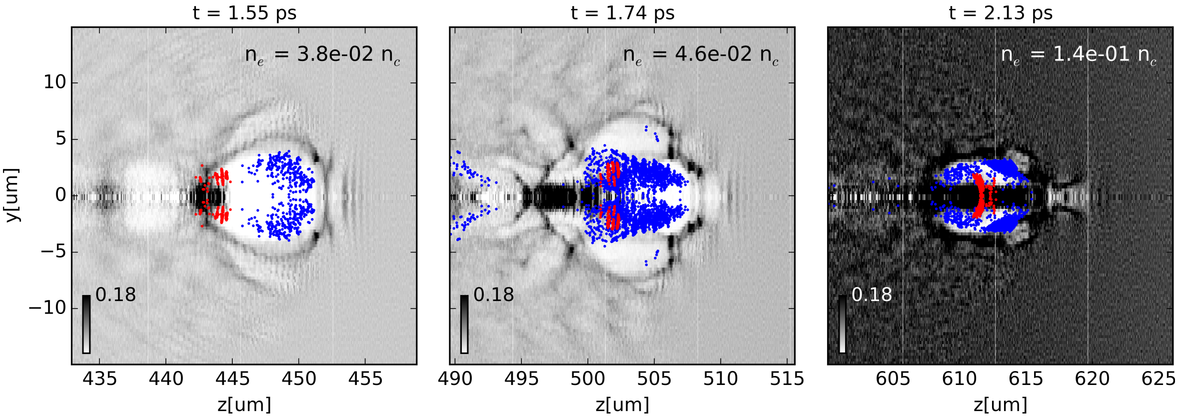

Figure 2.14 – Electronic density (gray scale) in n_c unit between the beginning of the injection and the peak position of the gas jet. Electrons with the higher momentum p_z are plotted in red, and electrons with negative p_z in blue, showing the overlap of the return current over the hot forward current.

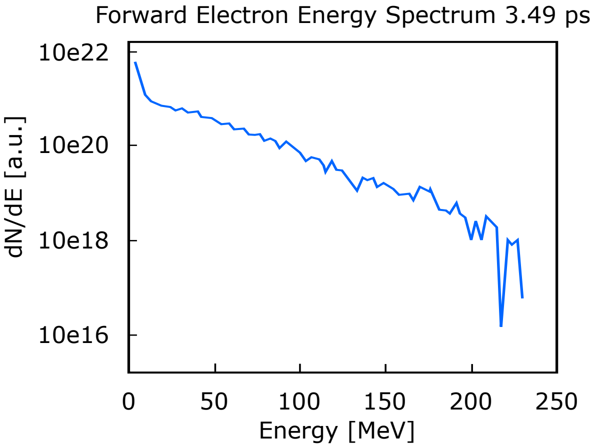

Figure 2.15 – Forward electronic spectrum for the CALDER simulation at the last timestep, within an half-angle of 5°

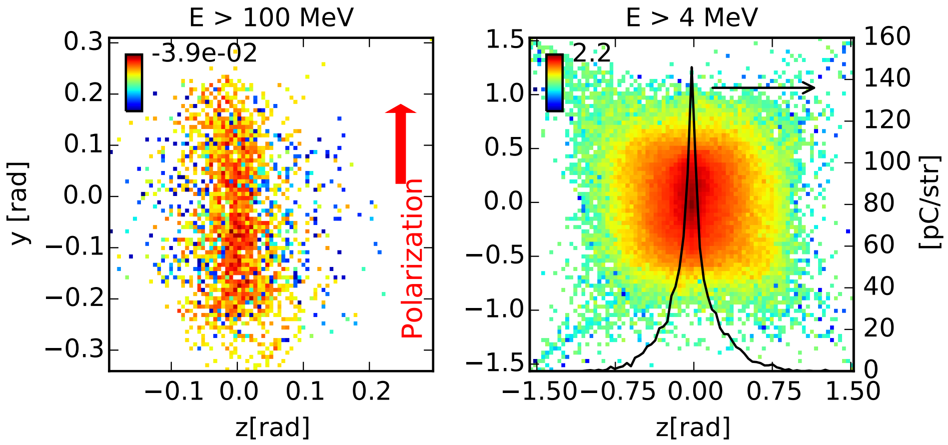

Figure 2.16 – Electron beam transverse size at the end of the simulation ($\approx 4\,\mathrm{ps}$). Colorscale in decimal log of $\mathrm{pC} \cdot \mathrm{sr}^{-1}$. (a) charge of electron $> 100\,\mathrm{MeV}$. (b) charge of electrons $> 4\,\mathrm{MeV}$. The total charge of electrons $> 4\,\mathrm{MeV}$ is $30\,\mathrm{pC}$, the beam FWHM is $0.15\,\mathrm{rad}$ or 9°

2.1.4 Transverse proton acceleration

The ion acceleration mechanism observed in both PIC simulations is transverse Coulomb explosion. In the region where self focusing increases the laser amplitude, the wakefield is intense enough to drive the background helium motion, as described in Chapter 1 section 1.3.1. Hydrogen ions are in too weak number to modify the density and fields, and their effect is negligible: they are test-particles. In a first stage they are accelerated from the mean wakefield (like Helium ions), in a second stage, they outrun the transverse helium blast-wave, and gain slightly more momentum in the transverse electric field preceeding the blastwave. The apparation of an ion filament, as described by [Gorbunov et al., 2001] is clearly visible in CALDER-CIRC simulation, but not in 2D OSIRIS, where the wakefield is turbulent and non-regular. The simulation geometry (2D versus axi-symmetric 3D) has a direct effect on the filament stability, and full 3D would be more relevant to derive its exact stability. No ion acceleration on the rear side, neither longitudinal shock formation could be observed. The laser lost its energy in the up-ramp instead of the down-ramp, and no CSA nor MVA can be triggered.

Coulomb explosion in 2D OSIRIS

In the OSIRIS 2D PIC simulation, transverse acceleration occurs predominantly in the region where self focusing has increased dramatically the field amplitude ($a > 5$ for $300\,\mu\mathrm{m} < z < 350\,\mu\mathrm{m}$). The high density in this region ($n_e = 0.03 n_c$) provokes a quick response of the ions, which start moving while the wakefield is still present. In this case, the two phases depicted in Fig. 1.2 overlap and the wakefield imprints the blastwave. The gas is an helium/hydrogen mixture, but only proton datas has been saved in this simulation. Nonetheless the transverse shock is clearly visible both with electronic density and the transverse field (Fig. 2.10b) and c), respectively 0.60 ps and 1 ps after the laser.). The shock geometry is not axi-symmetric and the ion momentum has a forward component, due to the "bubble-like" shock structure visible Fig. 2.18.

In the first phase, protons are accelerated transversely by the wakefield up to

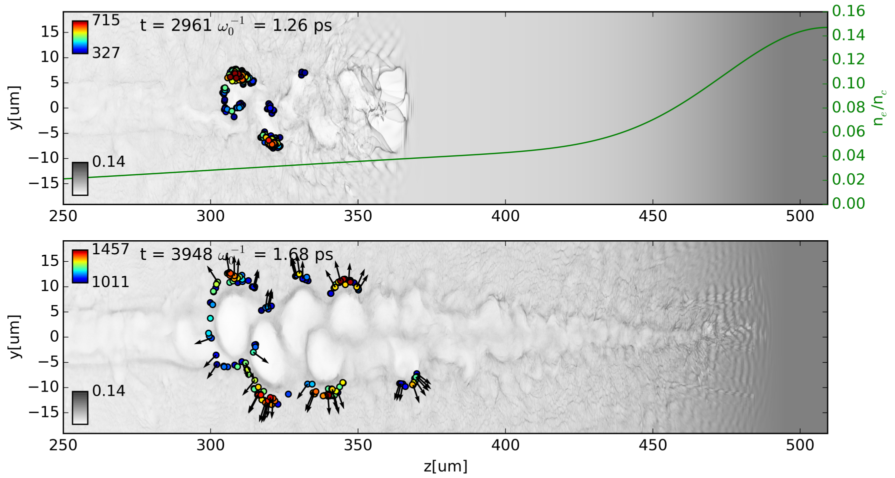

Figure 2.17 – Position and dynamic of the protons accelerated by coulomb explosion. Electronic density in gray scale in n_c unit. Only the 150 more energetic protons are plotted, colored by energy (colorscale in keV). The last image shows the quiver motion for some protons, given by the couples (p_z, p_y)

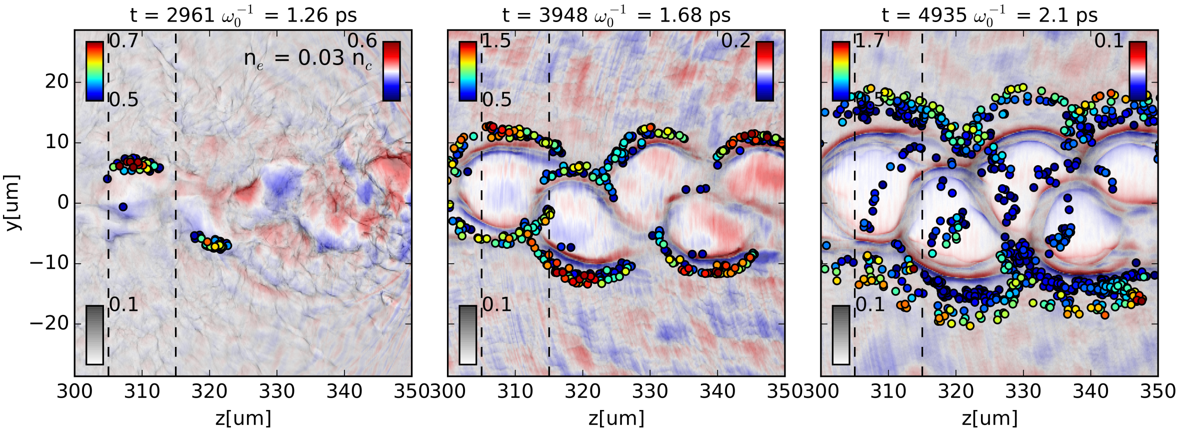

Figure 2.18 – Details of the positions and dynamics of protons accelerated by Coulomb explosion at various times, respectively 0.18 ps, 0.6 ps and 1 ps after the laser. At $t = 2961\omega_0^{-1}$(picture a)), the laser position is $z = 365\,\mu\mathrm{m}$. Electronic density in gray scale in n_c unit. Transverse field in blue to red colorscale, in normalized unit $E_y e/m_e c\omega_0$. The 300 more energetic protons are plotted, colored by energy (colorscale in MeV). Dashed lines delimit the lineout area plotted Fig.2.19

1.5 MeV. Due to their charge over mass ratio, protons are quicker by a factor $\sqrt{2}$ than He^{2+} ions. At 0.6 ps a spike is clearly visible in the electronic density, following the moving helium ions. Protons outrun the helium shock and a peaked field appears. At 1 ps the field is dominated by the field induced by charge separation near the shock, and some protons get marginal energy gain, while others are slowed down. Protons reach 2.5 MeV after 4.2 ps, essentially with transverse momentum (see Fig. 2.20b)). Forward protons reach 0.9 MeV after 4.2 ps (Fig. 2.20a)). Fig.2.19 shows a lineout of the expanding blastwaves and the corresponding proton phase space. Full proton phase-space is visible in Fig. 2.20, with a typical shock structure. It must be recalled that the real shock is sustained by the background helium ions, not shown here.

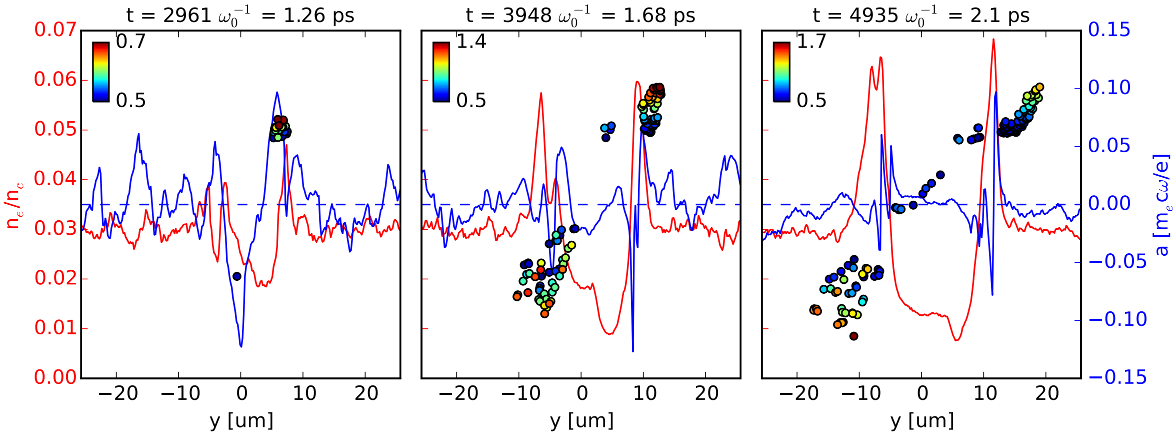

Figure 2.19 – Lineout of the transverse field (blue line) in normalized unit $E_y e/m_e c\omega_0$ and the electronic density (red line) in n_c unit during coulomb explosion. The data are averaged along z over the limits shown by the dashed line in Fig. 2.18. Protons in this area are plotted in phase space, the vertical axis is p$_y$ for scattered protons. Proton are colored by energy (colorbar in MeV). Dashed line shows the zero level of the transverse field

Transverse ion acceleration by Coulomb explosion had been demonstrated with ultra-short pulse in underdense plasma by Lifschitz et al. [Lifschitz et al., 2014]. He$^+$ and He^{2+} up to 200 keV were observed from an helium plasma of electronic density $n_e = 1 \times 10^{19}\,\mathrm{cm}^{-3}$ ($n_e = 0.006 n_c$), $a_0 = 2.5$ and $\tau = 35\,\mathrm{fs}$. They observed similar modulated spectrum as in Fig. 2.20.

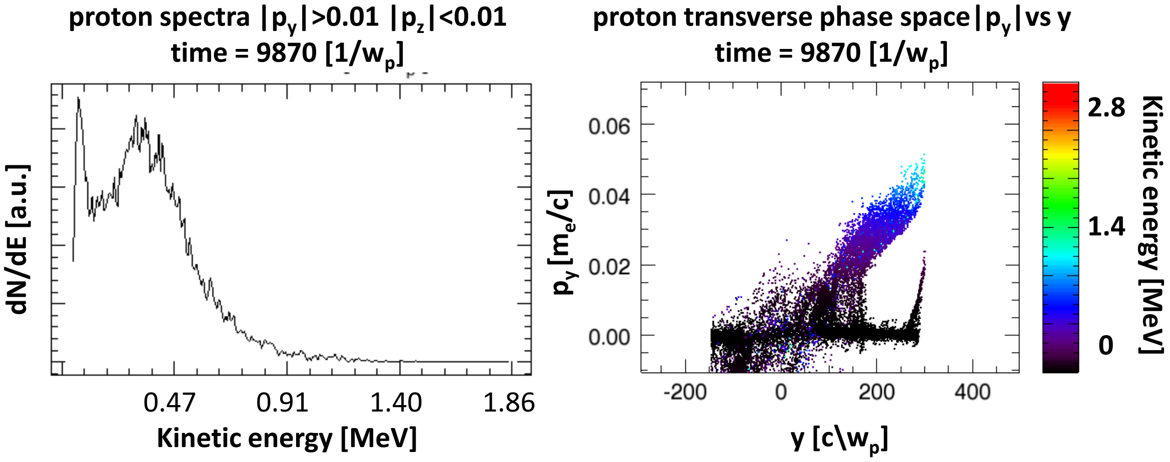

Figure 2.20 – Final proton transverse spectrum and phase space(p$_y$ vs. y) after 4.2 ps. a) The spectrum features a peak at 0.4 MeV b) the phase space features the shock structure of the expanding blastwave.

Coulomb explosion in quasi-cylindrical 3D CALDER-CIRC

In the CALDER simulation the secular effect of the wakefield over the ion population is more visible than in OSIRIS due to its cylindrical symmetry. Ions near the axis are pinched inward, while ions from outer shell are pulled outward by the secular wakefield effects, in accordance with the model of Gorbunov [Gorbunov et al., 2001]. Both effects are illustrated by Fig.2.21. At $t = 2.13\,\mathrm{ps}$ the laser reaches the gas peak density and transverse momentum distribution (on the bottom half of the figure) shows both the pinched and blastwave populations. At $t = 3.49\,\mathrm{ps}$, the protons outrun the transverse shock waves made from helium ions and the inner ion filament is exploded. The momentum is essentially transverse and $< p_z ><< p_\perp$. The maximum transverse energy is 1.5 MeV, and the forward only 120 keV. (See spectrum Fig. 2.22).

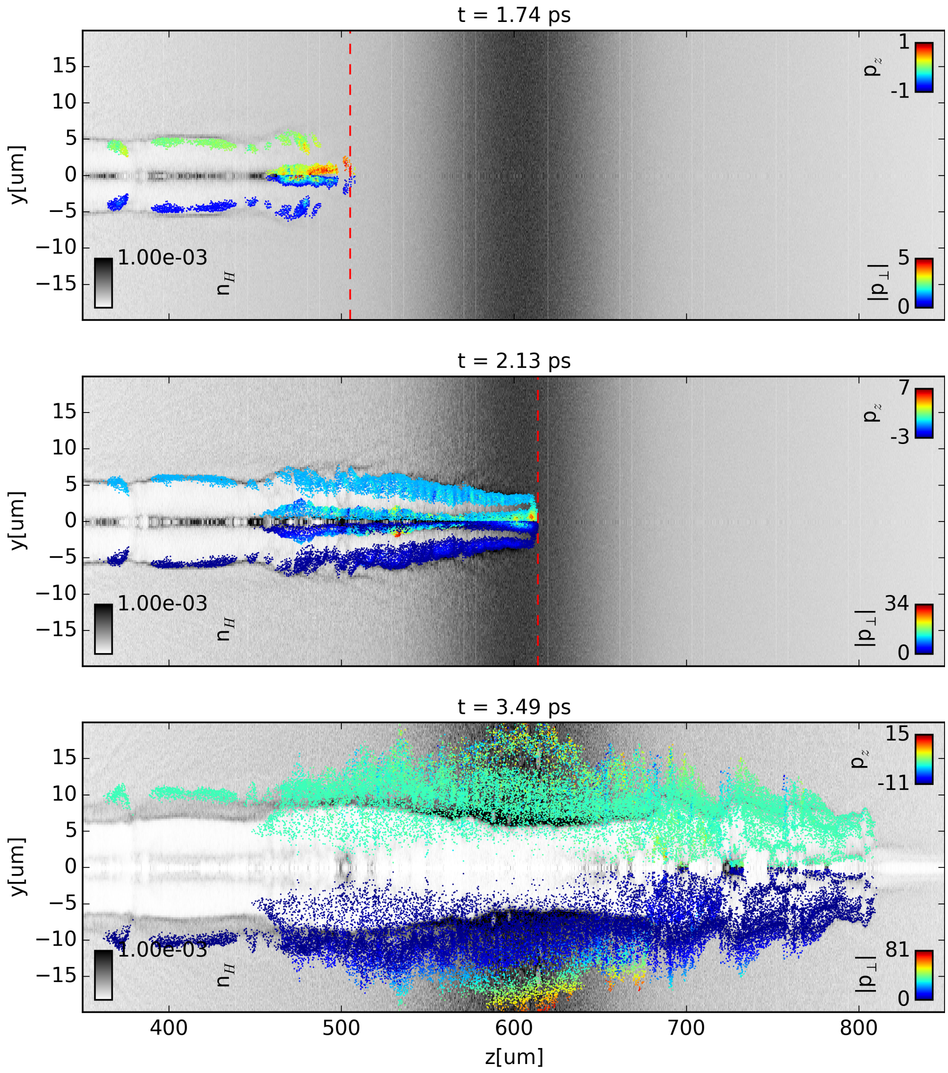

Figure 2.21 – Positions and dynamics of protons accelerated by coulomb explosion at various times from CALDER-CIRC simulation. Proton density is in gray scale, in n_c unit. y-z-p_z phase space is plotted on the top half of each picture, and y-z-$|\mathrm{p}_\perp|$ on the bottom half. The dashed red line denotes the peak laser position. The laser is outside the window on the last picture.

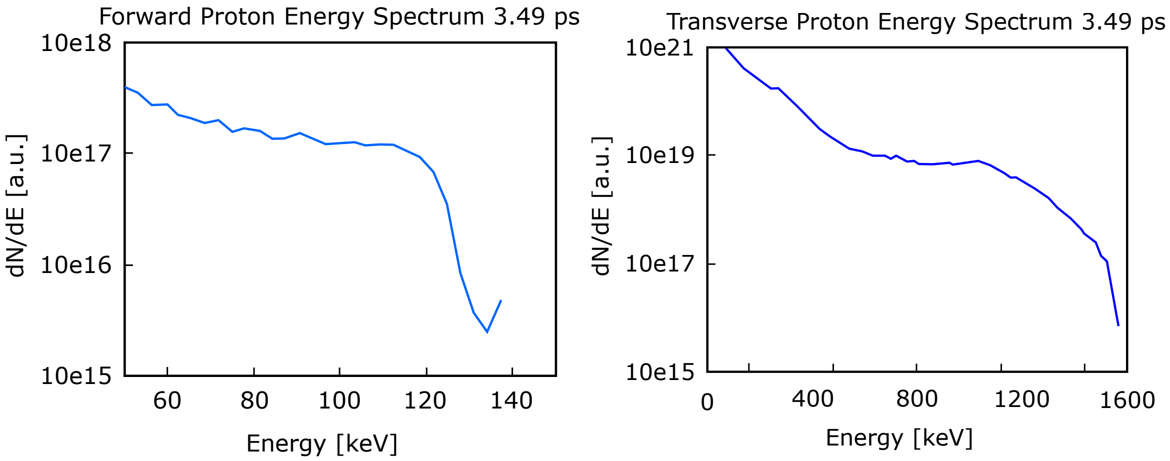

Figure 2.22 – a) Forward proton spectrum from the CALDER simulation within a half-angle of 5° b) Transverse proton spectrum within a half-angle of 5°

2.2 Electronic heating in the near-critical regime

2.2.1 Motivation

We present here an original mechanism of electron heating that develops when an ultra-intense laser pulse propagates into a high density plasma. The hot electrons following the laser are neutralized by a cold return current. In this regime, the combined action of the strong longitudinal ponderomotive laser field and the wakefield efficiently accelerates the cold electrons backwards to very high energies. The conversion from kinetic to thermal energy is achieved by a two-stream instability between the backward flowing cold electrons and the forward flowing hot electrons. Final mean energies well higher than the conventional ponderomotive scaling can be reached for high laser intensities ($> 1 \times 10^{21}\,\mathrm{W \cdot cm^{-2}}$) and gas density around 10 % the critical density.

This study is motivated by recent experiments of collisionless shock (CS) generation [Haberberger et al., 2012; Fiuza et al., 2012; Tresca et al., 2015]. Such experiments demonstrated mono-energetic forward ion acceleration (CSA), with ions being reflected by the positive potential barrier at the shock front. Shocks are experimentally created by successive impacts of "long" laser pulses (ps scale) onto near critical or critical targets, the first pulses heat the electrons who launch the collisionless shock. A shock may rise more generally from the expansion of an heated plasma population into a colder one [Sorasio et al., 2006], and significant electron heating from a single pulse may be sufficient to trigger CSA. We observed shock generation in 1D PIC simulation with a single ultrashort ultraintense ($a_0 = 19$) laser pulse impinging a $0.64 n_c$ target. While this specific target parameters is beyond experimental reach, identification and understanding of efficient heating mechanisms in the short pulse regime is critical for future CSA application with high repetition rate, table-top ultrashort laser.

2.2.2 Basic Mechanism

First, we observe the apparition of CSA in an illustrative 1D PIC simulation. The initial gas density profile, presented in Fig. 2.23a), is equal to $n_i = n_e = 0.64n_c$ over $10c/\omega_0$, surrounded by two exponential profiles, with the characteristic lengths of $\lambda_1 = 20\pi c/\omega_0$ and $\lambda_2 = 40\pi c/\omega_0$ at the front and rear side, respectively. Initial temperature for both ions and electrons is 10 eV . There is 100 macro-electrons and 100 macro-protons per cell. In absence of collision, all length are normalized at the laser wavelength.

Normalized vector potential (a_0)	**Laser pulse length (FWHM)**	**Plasma density**	**Time resolution**	**Space resolution**
19.0	$\omega_0\tau = 70(30\,\mathrm{fs})$	$n_i = n_e = 0.64n_c$	$\omega_0\Delta t = 0.0625$	$\omega_0\Delta x/c = 0.09375$

Table 2.4 – Simulation parameters for 1D CALDER PIC

Fig. 2.23b) shows the electron distribution function when the laser crossed the thin target. The laser (not shown) is followed by a hot electron beam trapped into the wakefield exited by the intense laser field. In the case of a single 1D cold electron fluid, the laser induces oscillations of the electron momentum around $p_x = 0$ [Bulanov et al., 1992; Teychenne et al., 1994], but here the cold current is neutralized by the hot forward current. This is illustrated by the electrostatic interaction potential $-e\phi/m_ec^2$ (white solid line on Fig.2.23b)). The hot electrons are confined behind the potential jump while the cold electrons are accelerated backwards along the potential drops. A two stream instability develops behind the laser pulse between the cold return current and the forward hot electrons. It converts the cold fluid momentum to thermal energy via phase mixing, resulting in a mean energy of $< \gamma - 1 > /m_ec^2 \approx 40$. In comparison, the ponderomotive scaling gives $< \gamma - 1 > /m_ec^2 \approx 18$. After the laser propagation, the ions start to expand by TNSA with a typical momentum scaling as $\sqrt{Zm_i < \gamma - 1 > /m_e}$ [Mora, 2003]. Fig. 2.24 shows the ion phase space at late time, here an electrostatic shock wave develops, due to the conjugate effect of the heating and steep plasma gradient [Fiuza et al., 2012].

As said before, the electron heating is triggered by the phase mixing in the wake of the laser field. This process can be explained with a simple 1D model, avoiding detailed kinetic description. We present first a 1D PIC simulation performed in constant plasma density $n_e = 0.032n_c$ with similar laser parameters. In these conditions the pulse length is large with respect to the plasma wavelength, and the laser pulse head is quickly depleted as it transfers its energy to the wakefield. It induces laser self-steepening at the front as seen in previous sections. The laser evolves into an optical shock (See Fig. 2.25) with a significantly increased longitudinal ponderomotive force. Fig. 2.25c and

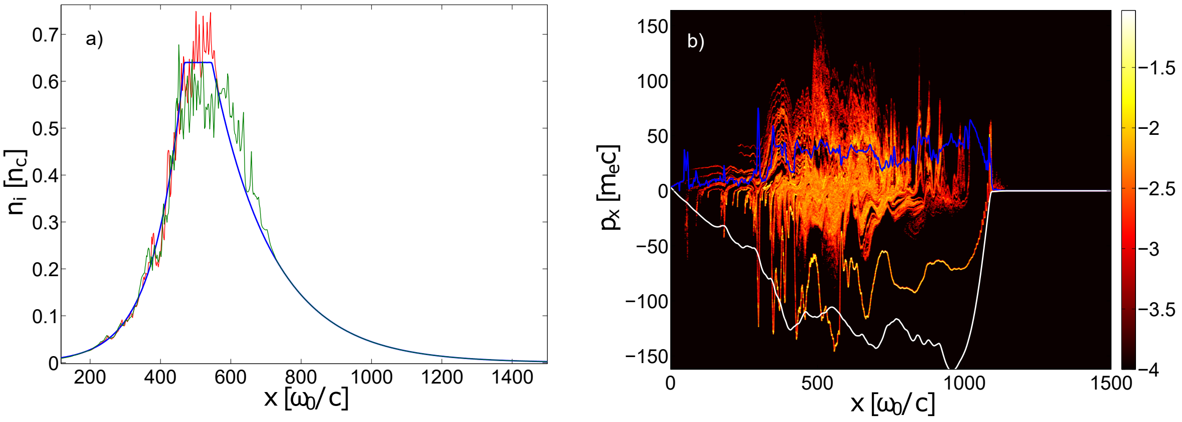

Figure 2.23 – a)Initial ion density profile of 1D PIC simulation b) Electron phase space x-p_x, mean energy $< \gamma - 1 > /m_e c^2$ (blue solid line), and potential $-e\phi/m_e c^2$ (white solid line) at time $\omega_0 t = 1250$

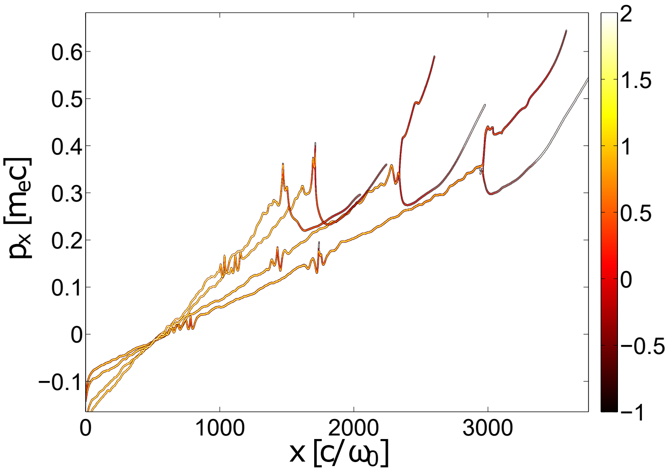

Figure 2.24 – Ion z-p_z phase space at time $\omega_0 t = 4375$, 5000, 6250 and 7500.

d),the optical shock is achieved and the electron momentum reaches $p_x \approx 40$ in front of the laser. The electrons are then repelled back by the ions and reach a negative momentum of similar amplitude $p_x \approx -40$, before coming back to rest (Fig. 2.25c). A new regime starts after $t\omega_0 > 1850$, when the beam loading and the associated phase mixing become significant. As in the 2D CALDER CIRC simulation, this marks the beginning of quick laser depletion, whereas laser energy loss was small for $t\omega_0 < 1850$. The cold current does not come back to rest and leave the interaction region with momentum up to $p_x \approx -100$

This work has been performed in collaboration with CEA-DAM at Bruyères-le-Chatel, and a publication by A. Debayle has been submitted : "*Electron heating by intense short-pulse lasers propagating through near-critical plasmas*"

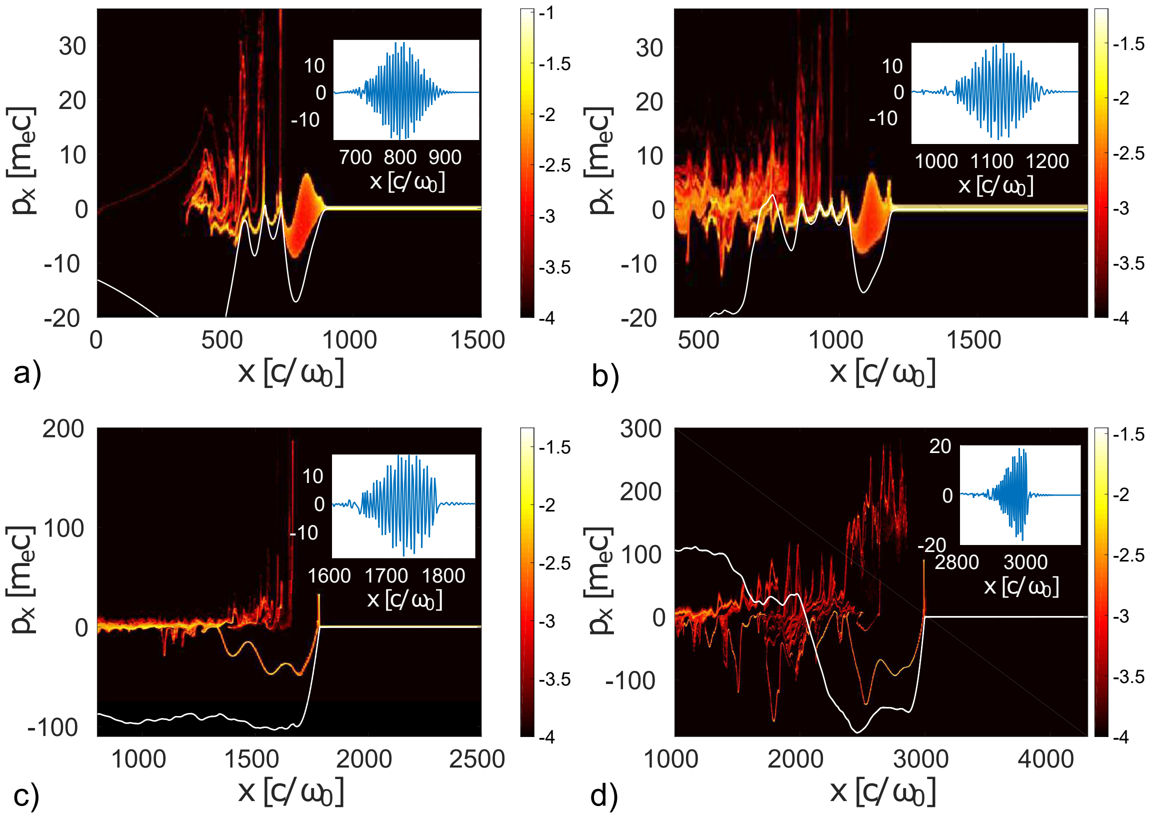

Figure 2.25 – 1D PIC simulation: Electron $x - p_x$ phase space at time $\omega_0 t = 937.5$ (a) $\omega_0 t = 1250$ (b) $\omega_0 t = 1875$ (c) and $\omega_0 t = 3125$ (d).Withe solid line plots the normalized electrostatic potential $-e\phi/m_ec^2$. The insert plot is the transverse normalized electric field a_y.

2.3 Conclusion

2.3.1 Laser propagation

By means of 2D and quasi-cylindrical 3D PIC simulations, we study the propagation of an intense ultrashort laser into a near critical target featuring experimentally relevant gradients and peak density. We explore first the interplay of self-focusing(SF), self-compression(SC) and the laser-wakefield interaction in a regime with $a_0 >> 1$, $P >> P_{cr}$, $w_0 > w_m$, and $w_p\tau > 2\sqrt{2}|a|^{-1}$. In a first phase, the laser excites a non-linear wakefield into the plasma, and experiments relativistic envelop (SF) and chirp (SC) variations. Self focusing obeys to the Sprangle's [Sprangle et al., 1987] scaling with great precision, until the beam reaches the matched spot size w_m. Self compression leads to an optical shock within the propagation time derived by Vieira et al. [Vieira et al., 2010]. Self compression and self-focusing lead to an adiabatic increase of the potential vector a, and drive an unstable blow-out regime, where all electrons are expelled from a cavity behind the laser.

2.3.2 Particle acceleration

Electrons injection starts when the matched spot size is reached: electrons are injected from the back of the cavity, into the stretched back of the laser pulse. A cold backward current overlaps with the hot forward current into the cavity, with $|p_{cold}/p_{hot}| \approx 1/40$. As the electrons quickly outrun the laser, they deplete the laser energy, and finally drive their own wakefield(s).

The plasma is a mixture of light atoms, with helium (99 %) and hydrogen (1 %), leading to a swift response to the wakefield. Secular ponderomotive force from the wakefield gives to ions transverse momentum. Within the characteristic time of the ion plasma frequency, helium evolves in a blastwave, while protons outrun the blastwave shock and get extra-momentum from the shock field.

2.3.3 Perspectives

During the time frame of the simulation, we could not observe energetic backward cold current ($p_{cold} \sim -p_{hot}$), neither any forward ion acceleration, neither collisionless shock waves. Nontheless, with the demonstrated understanding of the laser propagation and depletion, it is possible to tailor the gas profile and laser parameters to enable laser energy depletion at the rear side of the target, and charge-separation field formation. The chapter 3 will describe how to reach the plasma parameters used in the simulations. Both simulation parameters match the experimental conditions ($a_0 = 4$,$n_e = 0,15n_c$, realist gradients) of our experimental system. The results presented in this chapter show that increased laser power, and sharper targets, would be necessary to demonstrate the enhanced heating and CSA.

Chapter 3

High density targets: design and characterization

Contents

Target innovations has often been the key for unraveling new mechanisms of ultra-intense laser plasma interactions. For example, gas jet targets have shown their potential in the field of laser plasma interactions [Malk, 2006], in areas such as Laser Particle Acceleration (LPA), studies of parametric instabilities in Inertial Confinement Fusion (ICF), atomic physics of warm dense plasma, X-ray lasers and high harmonic generation. For example, in the context of ICF work, focusing a nanosecond laser pulse with a Random Phase Plate onto the gas jet provides large scale length (few mm), uniform, quasi-static and reproducible plasmas, whereas focusing the laser pulse with a spherical or an axicon lens can generate a preformed channel of relevance for X-ray lasers or LPA. Controlling the gas flow is essential to provide the desired interaction density. For example, using a sonic or a supersonic gas flow will provide a uniform or a parabolic neutral density profile. Changing the gas pressure will change the initial neutral density. Using a combination of gases will give plasmas with a mixture of different ions species. Changing the nozzle diameter allows the control of the plasma length. Recently, tailoring on the gas jet profile still drives new results in laser-driven electron acceleration [Schmid et al., 2010; Thaury et al., 2015a]. Compared to the thin exploding foil techniques, the use of a gas jet presents some interesting advantages. In the thin foil technique the laser beam heats the target, which explodes symmetrically. The density decreases rapidly from the solid density to the sub-critical desired density, giving a parabolic density profile. In the domain of laser ion acceleration, limitations of TNSA foster the study of various targets. Mass-Limited targets [Zeil et al., 2014; Buffechoux et al., 2010], nano-wire and micro-structured targets [Zigler et al., 2011; Schwoerer et al., 2006], droplet targets [Ter-Avetisyan et al., 2011, 2012], foam targets [Passoni et al., 2014; Willingale et al., 2009], grating targets[Ceccotti et al., 2013], conic solid targets [Gaillard et al., 2010], were all characterized by their increased ability to concentrate the laser energy or to optimise its absorption. Recently, the ability to produce and handle nm thick foils was critical for the experimental demonstration of the RPA regime, with a new record energy for laser-plasma ions [Kim et al., 2016]. Solid targets cannot yet scale the high repetition rate and reproducibility needed in industrial or medical applications, and self-healing targets, gaseous or liquid, got renewed attention.

In this context, this work focused on the design of a new gas jet target suitable for ion acceleration in the regime described in the introduction chapter: Collisonless Shock Acceleration (CSA), and Magnetic Vortex (MV) acceleration. CSA up to few MeV is observed in simulations [d'Humières et al., 2013b; Silva et al., 2004; Macchi et al., 2012] in plasma of $\approx 10n_c$. No parametric studies explored the effect of the front gradient, most simulation featuring squarelike plasma slabs of $\approx 10\lambda$ thickness. These simulations show ion acceleration starting after $\approx 5\lambda$ of propagation. Nonetheless, experimental demonstrations with exploded targets [Antici et al., 2009] and CO2 lasers [Haberberger et al., 2012] show the importance of plasma tailoring, producing a front gradients of $\partial(n_e/n_c)/\partial z = 0.3\,/\lambda$. Simulation in Chapter II section 2.2 shows that a gradient of $0.03\,/\lambda$ and peak density of $0.64n_c$ is sufficient to launch a shock if sufficient heating is achieved. In contrast Magnetic Vortex allows ion acceleration for broader conditions in term of maximum density ([Matsukado et al., 2003] from $0.1n_c$ to $10n_c$). One experiment claimed observing MVA ions [Willingale et al., 2006] in a plasma of $0.03n_c$ and gradient of $1.6 \times 10^{-4}\,/\lambda$ with significant laser energy (340 J). MVA simulation by [Nakamura et al., 2010] makes use of rear gradient of 0.15 $/\lambda$. Supersonic jets with backing pressure of 400 bar typically produce gradients of $4 \times 10^{-3}\,/\lambda$ (at 800 nm) but such jets have a width of several hundreds of microns. As shown in chapter I, the laser undergoes significant self-focusing, filamentation and depletion during propagation. Once at the matched spot size, the laser is depleted within $\approx$ 100 µm, and collapses. The target design has therefore to produce a density spike above $0.1 n_c$, with FWHM $<$ 100 µm, with gradients at least above 0.03 $/\lambda$.

A gas jet apparatus is basically made from a tank of gas compressed at the desired pressure, an electrovalve commanding the opening of this tank, and a nozzle, tailoring the gas jet. To reach the most suitable conditions we typically use a gas compressed up to 400 bar, an electrovalve able to open and close in 5 ms and a nozzle of diameter 400 µm. Technical difficulties arising from high pressure operation have been solved recently by patented electrovalve [Sylla et al., 2014]. This work focused on the tailoring of the density gradient by the design of a specific supersonic nozzle. The density is shaped by reproducible sharp shock waves provoked by the nozzle profile.

The first section presents the characterization of the shock nozzle and covers briefly the shearing interferometry diagnostic. The second section describes the basics of the well-known compressible fluid mechanics through a duct, and apply this model to the proper design of the nozzle. Third, we present a parametrial study by ANSYS fluid simulations, exploring the effect of fine nozzle geometrical features, and discuss its agreement with the compressible model and the experiments. These results are currently submitted to Review Of Scientific Instrument.

3.1 Characterization of supersonic shock gas jet

Compressible conditions are reached when the fluid velocity is higher than the velocity of compression waves: information on the upstream boundary condition cannot propagate backward to the flow, and the flow cannot homogenize itself to an uniform density. In case of molecule "traffic jam", the incoming molecules can only pile-up while slowing down and losing their energy by molecular friction: this is called a shock. The presented nozzle exploits the ability of supersonic flows to create shocks to adapt their properties to external constraints. Across a shock, density, pressure, temperature and fluid velocity experiment a brutal variation, leading to steep density gradients, dow to several 10's of nm [Mott-Smith, 1951; Greene et al., 1951]. The flow is accelerated to supersonic velocity by a Laval nozzle, also called "converging-diverging" nozzle. Then the flow undergoes an abrupt direction variation, imposed by the throat design. Adapting to these limit conditions, the flow gives rise to steady oblique shocks. In 3D axis-symmetric geometry, this shock geometry is a cone. At the top of it, the density peak can be as thin as 100 µm of FWHM. The following derivation quantifies these processes and gives an analytical tool to predict the shock position and strength.

3.1.1 Implementation

Despite simulation and analytical derivation, the exact flow and density of the gas is highly dependent from nozzle machining, electrovalve operation, turbulence and viscosity. It is necessary to characterize the flow carefully before using it in actual

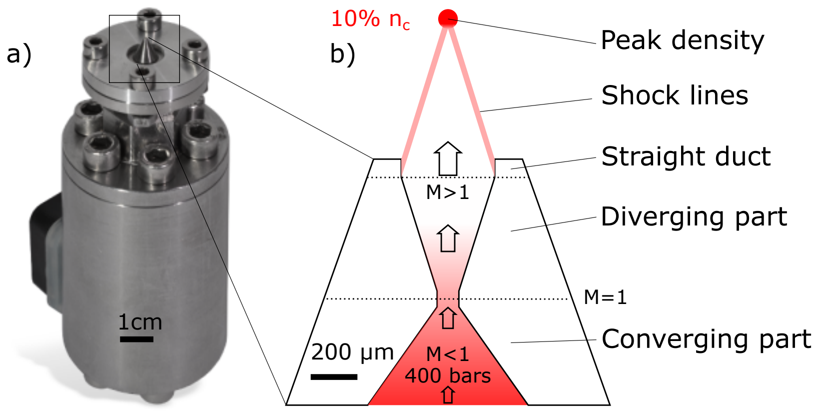

Figure 3.1 – a) Picture of the RRV237 Electrovalve from GSR Ventiltechnik, topped by the nozzle mount and the nozzle. b) Scheme of the nozzle lineout. The high pressure gas accelerates in a converging-diverging nozzle, then encounters a final straight duct at supersonic speed. The resulting shock lines cross into a high density area with sharp gradients.

experiment. Atomic density is characterized within a test vacuum chamber with a diagnostic named Quadri-Wave Shearing Interferometry (QWSLI), described thereafter (Fig. 3.2). We build the high pressure apparatus incrementally toward limited footprint and better reliability, monitoring, and safety. In the continuity of this dynamic, we designed and build with SourceLab S.A. prototypes of their SL-HP-10 product(Fig. 3.3).

Probing and imagery implementation

The flow evolves within the ms scale, we use the dynamic of the transient flow to tune the gas density. To describe this dynamic, it is necessary to use pulsed illumination. Flashed white LED delivers bursts of 100 µs. Its large bandwidth is not an issue because 1) gases we use (Ar, He,H) are weekly dispersive and 2) QWSLI is achromatic. Probing magnification is 4, and numeric aperture 0.13, giving resolution of 2.3 µm, far below the size of one pixel (7.4 µm×7.4 µm for the QWSLI camera Retiga 4000R from Qimaging).

High Pressure module

The High Pressure module was first designed by Sylla et al. in 2012 [Sylla et al., 2012b, 2014]. A new switching technology made possible quicker opening/closing of the electrovalve, with higher backing pressure. Previous technology features a plastic poppet loaded by a spring. A current runs through a solenoid and displaces axially a rod. But such technology cannot handle backing pressure above 80 bars. The chosen system is the RRV237 electrovalve from GSR Ventiltechnik GmbH. This new system uses a metallic ball, which seals the aperture of the valve, seating on a teflon joint. When current flows trough the coil, induced asymmetric magnetic field displaces the ball from its seating and lets the gaz flow out. Once the current is off, the ball goes back in its seat within 10's of ms, pushed back by the gas flow. Duration of the opening command is a critical parameter: too short, the ball may not have the time to leave the

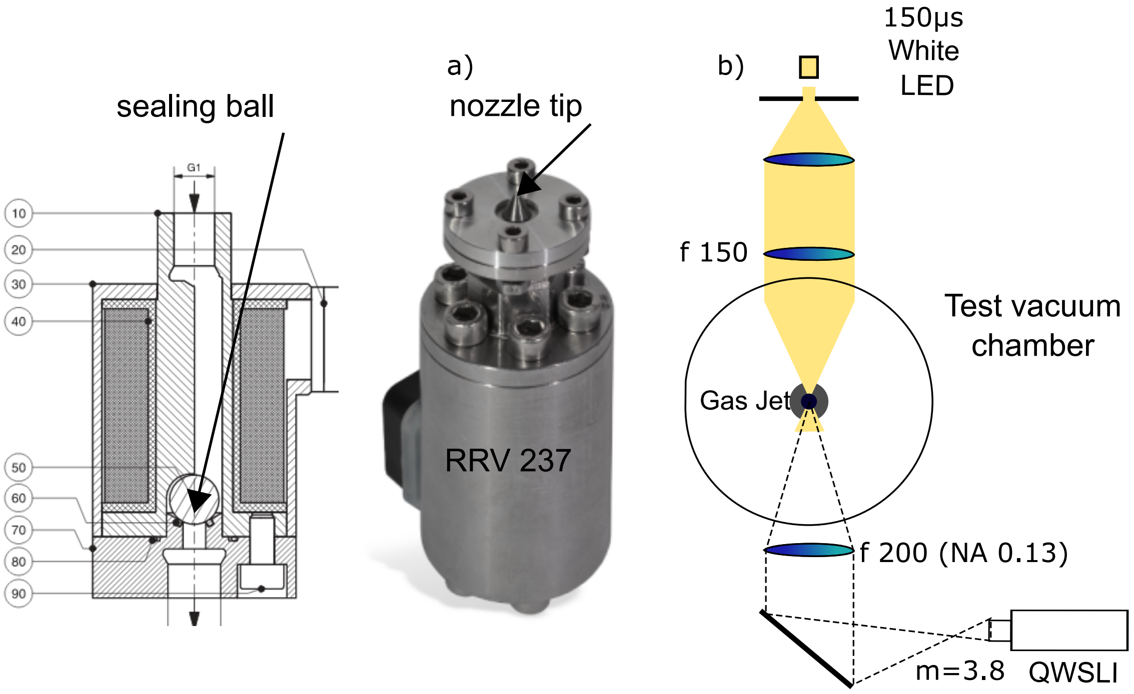

Figure 3.2 – a) RRV237 electrovalve, nozzle adaptor and nozzle. Scheme of the electrovalve on the left. b) Implementation set-up of the test stand, including the flashed LED, lenses,vacuum chamber and SID4-HR camera from Phasics.

teflon joint; too long and the ball may move too far from the joint and doesn't come back properly. At 400 bar, optimal current command duration for Helium is 2.8 ms. It should be noted than the dynamic of the ball is slower than the current command itself. Maximum valve opening for Helium typically occurs 13 ms after the command.

Several constraints applied to the valve operation:

- The RRV237 is a solenoid valve, normally-closed if the backing pressure is above ≈ 75 bar. But a debit too weak may prevent the ball to come back properly, and may break the vacuum by letting the high pressure gas to flow into the chamber. That's why nozzle diameter couldn't be decrease below 200 µm as smaller diameters constraint too much the debit. The security valve purpose is to close the high-pressure flow if the sealing ball doesn't come back correctly.

- Operation was stable for pressure above ≈ 100 bar up to 400 bar (the limit allowed for the valve and the tubing) depending of nozzle diameter. High pressure slows down the movement of the sealing ball, and valve power command must be adjusted accordingly. 400 bar is necessary to operate a 200 µm nozzles without risk for the sealing.

- In order to be able to change the density in our experiment, we change the delay between laser arrival and valve trigger. Therefore dynamic of the valve opening needs accurate characterization.

Figure 3.3 – 3D view of the SourceLab product SL-GT-10, presenting the high pressure control module, and the connection with the GSR Ventiltechnik Electrovalve

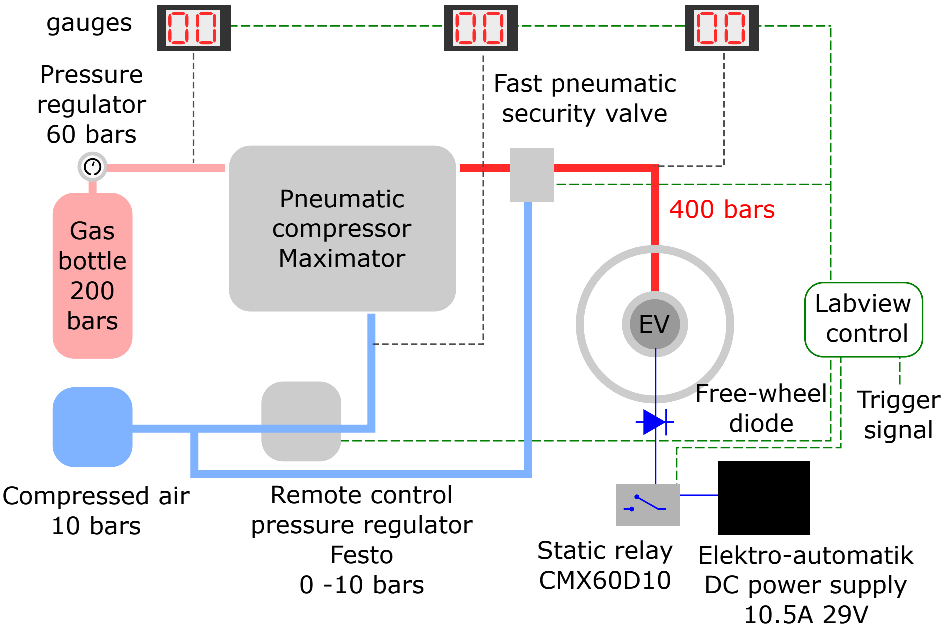

Figure 3.4 – High pressure apparatus. Automation, monitoring and safety had been improved by collaboration with SourceLab S.A. Pressure out of the compressor is × 75 the compressed air input pressure: pressure can rise up to 400 bar. Pressure is monitored in various locations and the safety valve closes automatically 1) if the pressure drops unexpectedly 2) if pressure is too low for proper operation.

3.1.2 Density probing by Quadri-Waves Lateral Shearing Interferometry

In order to retrieve density, we make use of the change of refractive index with density. By retrieving the phase front distortion of a probe light, we are able to measure the refractive index profile of the medium (assuming some symmetries, as discussed in the Annexes). Depending of the nature of the medium, we can link the refractive index to the density. Lorentz-Lorentz formula express relationship, in a gas, between the refractive index η, molar refractive index A, and atomic density n. A simplified expression yields (see Annexes):

$$n = (\eta^2 - 1)\frac{N_A}{3A} \tag{3.1}$$

Where $A_{\text{argon}} = 4.2\,\text{cm}^3/\text{mol}$ and $A_{\text{helium}} = 0.519\,\text{cm}^3/\text{mol}$. $N_A = 6.02 \times 10^{23}$ the Avogadro constant.

Phase-front measurements are usually made by a Mach–Zehnder interferometer (MZI), or by Normasky/DIC interferometry with a Wollaston prism. Nonetheless, such interferometers have some limitations: large footprint (MZI), missing fringes (Fig.3.5) for high gradients, need of complex unwrapping algorithms (Wavelet Packet Decomposition [Herráez et al., 2002]), non-physical discontinuities.

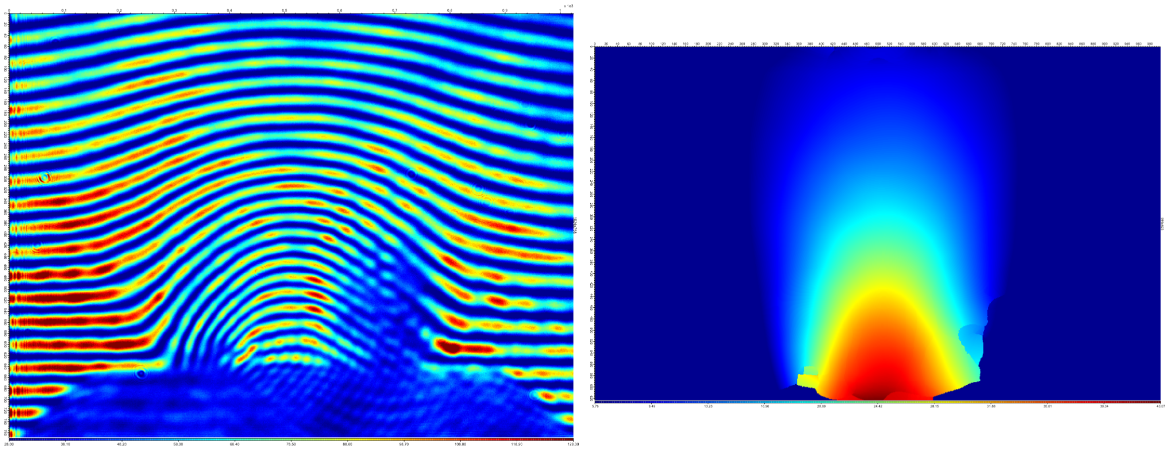

Figure 3.5 – a) MZI interferogram of a sonic nozzle with 400 µm diameter and 400 bar argon backing pressure. Missing fringes are visible in an area of strong gradient near the nozzle exit. b) Resulting discontinuity in the phase, unwrapped by Wavelet Packet Decomposition.

Considering those limitations, we decided to extensively use another phase front diagnostic, rarely used for density diagnostics (described in [Plateau et al., 2010]): Quadri-Wave Lateral Shearing Interferometry (QWLSI). QWLSI is a phase front measurement techniques which found successful applications in bio-imagery [Bon et al., 2009] and laser phase-front monitoring and correction [Wattellier et al., 2004]. Basically, instead of measuring the phase difference between the phase $\varPhi$ at position (x_0, y_0) and a reference $\varPhi_0(x_0, y_0)$ (MZI), QWLSI looks for phase difference between data $\varPhi(x_0, y_0)$ and $\varPhi(x_0 + dx, y_0 + dy)$, by making 4 shifted duplicates of the phase front interfere (two in each transverse directions).

The QWSLI is implemented with a Modified Hartmann Mask (see Annexes and Fig. 3.6). A grating is placed at a distance of $D_T/6$ from the CCD camera, where D_T is the Talbot distance. The grating has a hole size of $a = 66\,\mu\text{m}$, a pitch of $d = 100\,\mu\text{m}$ and Talbot distance:$D_T = 2d^2/\lambda = 40\,\mu\text{m}$. In addition a phase chessboard is superimposed: it has a pitch twice the pitch of the grating, and its phase shift is π over the visible and NIR light spectrum. This Modified Hartmann Mask (MHM)

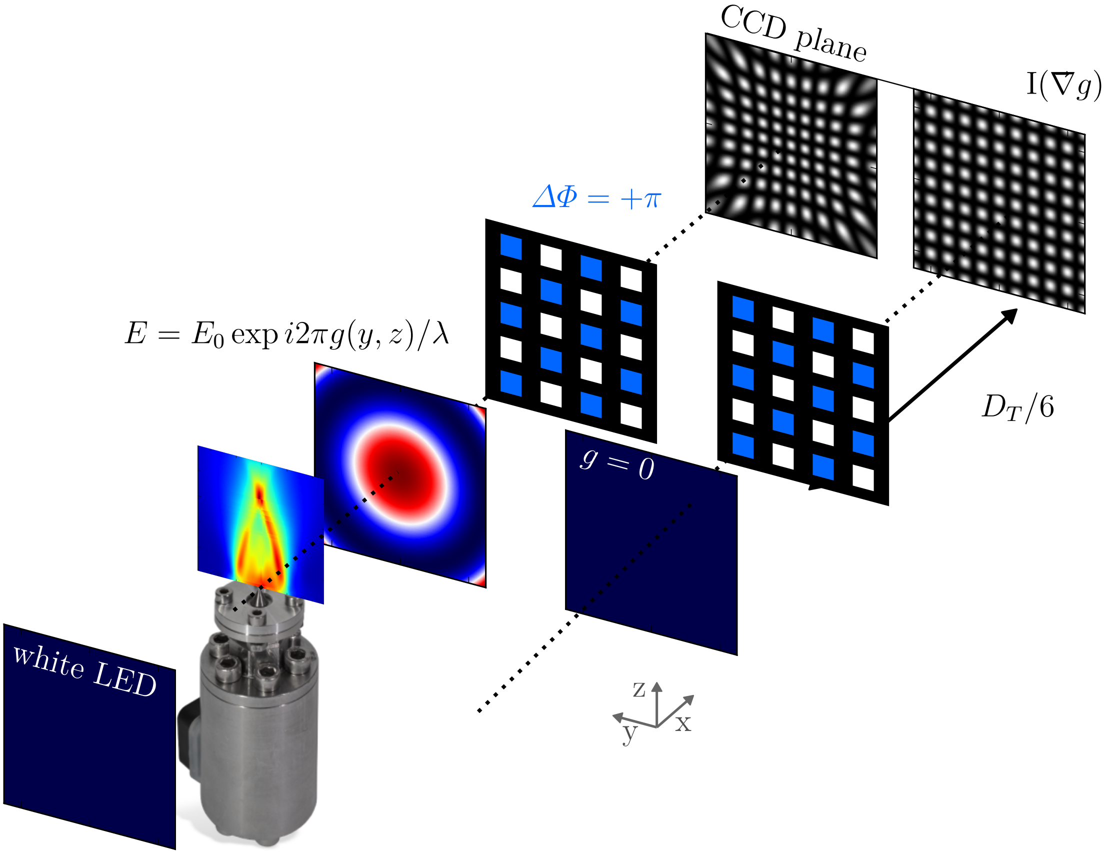

Figure 3.6 – Examples of interferometry pattern made by QWSLI's grating in the CCD plane, for a flat wavefront and for an aspheric aberration. Phase front is given by the phase $g(x, y)$. Hole size: $a = 66\,\mu\text{m}$, pitch: $d = 100\,\mu\text{m}$, Talbot distance: $D_T = 2d^2/\lambda = 40\,\mu\text{m}$. The intensity of interference pattern I is dependent only of ∇g, and Fourier analysis enables to reconstruct g from I within a constant. The QWSLI grating features a π phase chessboard, ensuring an achromatic response (calculation in Annexes).

enables compact, achromatic QWLSI. The MHM has been implemented by *Phasics S.A.* in France, and we used their system (SID4-HR) in order to retrieve probe beam phase fronts. It includes: a high-resolution camera, a MHM, and the analysis software.

Let's consider a 1D impinging wave on a 1D MHM with a scalar field:

$$E(x = 0, y) = E_0 e^{i2\pi g(y)/\lambda} \tag{3.2}$$

Then the intensity of the diffraction pattern visible on the CCD at distance z is given as a function of ∇g (Details in Annexe):

$$I(y, z) = I_0 \left\{ 1 + \cos\left[\frac{2\pi}{d} \left(y - z\frac{dg}{dy} \right) \right] \right\} \tag{3.3}$$

One can note that the contrast is achromatic, the MHM allows to analyse interferograms made with polychromatic illumination (within the bandwith of the π phase chessboard, which may be not exactly flat on the whole visible spectrum). Finally, derivative of the phase ∇g acts as a *frequency modulation* of a sinusoidal function.

With a proper demodulation algorithm, it is possible to retrieve the phase gradient of the incoming wave within a constant. By applying a low-pass filter, one can also retrieve the intensity map, which has considerable advantages over other wave-front sensor techniques like Normasky/DIC. Getting the two maps (phase and intensity) from a single interferogram has a price, which is a loss in resolution. The demodulation algorithm extracts a quarter (in both dimension) of the spectrum. If the interferogram had a dimension of $N_x \times N_y$ pixels, then the phase map is made of $N_x/4 \times N_y/4$ pixels.

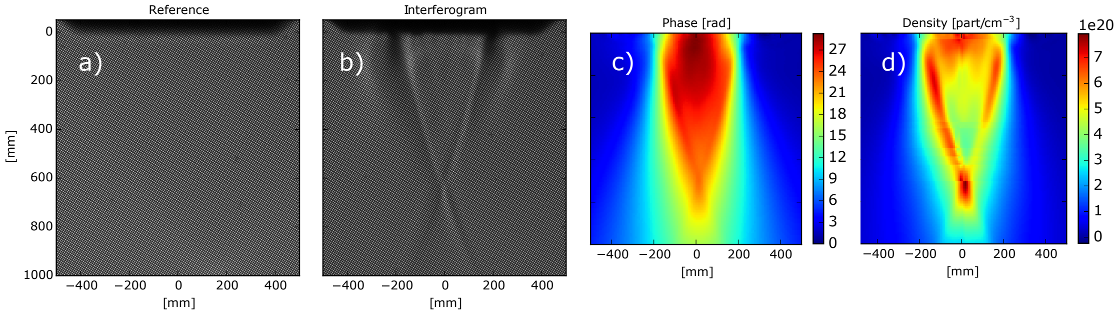

Figure 3.7 – a) Reference interferogram as seen on the SID4-HR without gas, nozzle tip is visible at the top b) Interferogram modified in presence of gas (gas flows from top to bottom) c) Phase reconstructed from the interferogram in "b)" d) Density derived by Abel inversion of phase "c)". Crossing shock lines are clearly visible

3.1.3 Density profiles

Effect of the expansion angle

Various nozzle geometries had been tried over this thesis work. The main challenge was to get the shock line crossing at the right position. Not too close from the nozzle, and not too far, in order to keep the peak density sufficiently high. This was achieved by tuning the length of the final straight collar of the nozzle. Optimal shock was achieved by the B20 geometry, with 20° expansion angle, shown in the layout in Fig. 3.8.

Machining of this 200 µm throat with half-angle of 10 deg was found to be challenging, even for high-precision providers from the automotive industry. Bad surface quality could lead to unwanted or asymmetric shock lines. Machining by electro-erosion was finally assessed as the most reliable technique, but providers for prototyping are in scarce supply. The B118 geometry is designed to ease the constraints for the precision machining providers, as the straight collar and the conical part are machined at the same time with a single drill. Length of the collar is choosed based on CFD simulations.

Fig. 3.9 shows density map for B118 and B20 nozzles (layout fig. 3.8), for 400 bar helium. General features are the same for both geometry: shock lines cross in a single peak of density. Density lineouts are shown Fig. 3.10. The profile peaks at $3 \times 10^{20}\,\mathrm{cm}^{-3}$ and the FWHM is down to 125 µm with B20 geometry, $4 \times 10^{20}\,\mathrm{cm}^{-3}$ and FWHM of 190 µm with B118 geometry. It appears that the shock position is too close from the B118 nozzle for safe operation, and more iterations on the collar length

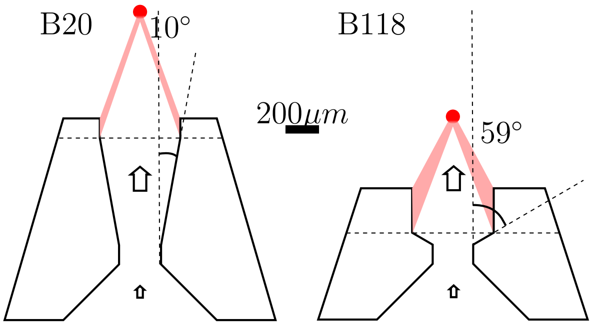

Figure 3.8 – B20: Shock nozzle layout with expansion angle of 10 deg and straight collar of length 100 µm. B118: Shock nozzle layout with expansion angle of 59 deg and straight collar of length 225 µm. This angle is equal to the standard angle of drills. This geometry is easier to machine for the precision machining providers, as the straight collar and the conical part are machined at the same time with a single drill.

are needed. Inaccuracy in the drilling cannot be excluded, as the provider has no diagnostics to check the compliance of his machining with the layout. Nevertheless, this simpler B118 design features very similar characteristic than the B20 design, making it a good candidate for future application.

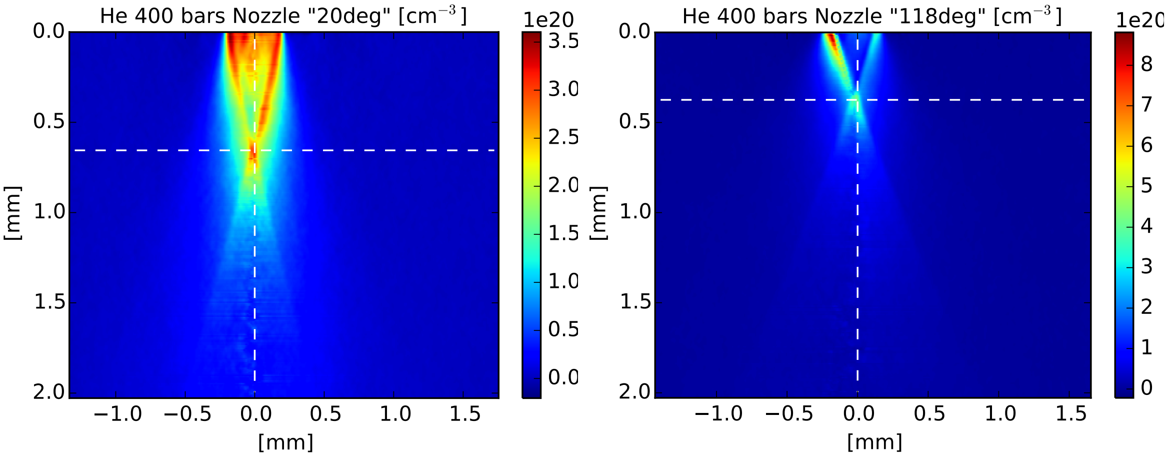

Figure 3.9 – Atomic density profile for shock nozzle "118 deg" (left) shown Fig. 3.8 compared with shock nozzle "20 deg" (right), with parameters optimized for maximum density. The nozzle is upside-down, the gas flows from the top. Helium, 400 bar, EV open time: 2.8 ms, delay after opening: 13 ms. The longer straight collar seems to place the peak density closer to the nozzle, but the overall density and shape is conserved.

Effect of the gas species

During experiments, we used both helium mixture and argon mixture. We assume that the dynamic and density is barely affected by the low fraction 1 % of hydrogen. Fig. 3.11 shows density map of from the B20 nozzle (layout fig. 3.8), for argon and helium. Shock lines are very similar. Density lineouts are shown Fig. 3.12. For helium the profile peaks at $3.5 \times 10^{20}\,\mathrm{cm}^{-3}$ with FWHM down to 170 µm, and for

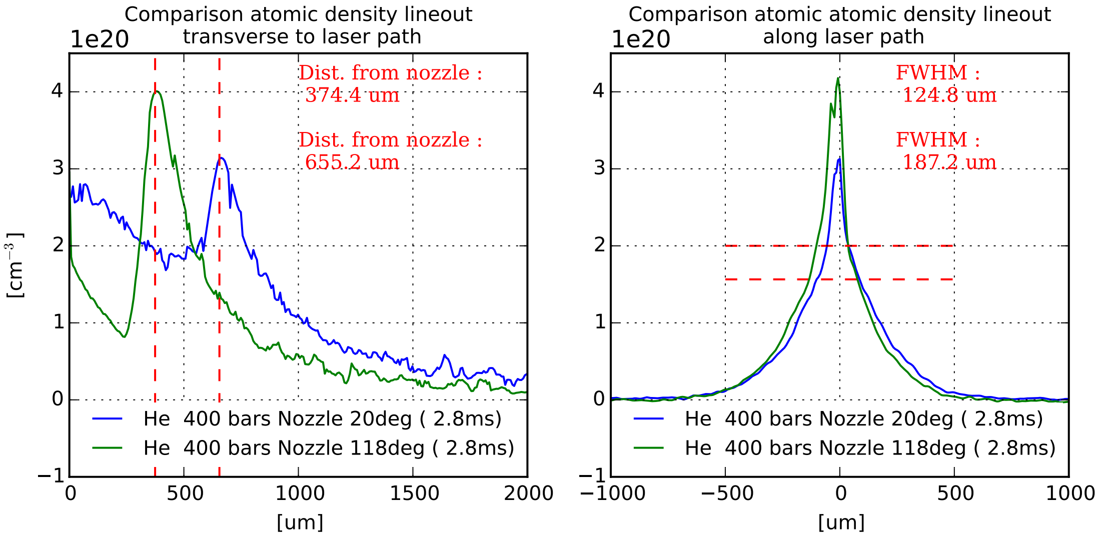

Figure 3.10 – Transverse (right) and longitudinal (left) density lineout at peak density for helium at 400 bar for both nozzles "20 deg" and "118 deg". Maximum density reaches $4 \times 10^{20}\,\mathrm{cm}^{-3}$ for "20 deg", and $3 \times 10^{20}\,\mathrm{cm}^{-3}$ for "118 deg", this difference is discussed in the text. Position of the shock is more favourable on the nozzle "20 deg".

argon $8 \times 10^{20}\,\mathrm{cm}^{-3}$ and FWHM of 140 µm. Nevertheless, dynamic for both species is very different (cf Fig. 3.13). Maximum opening command duration without leaking of the valve is 2.9 ms with Helium and 4.2 ms with Argon. For these parameters, maximum density is achieved respectively at 13 ms and 35 ms. In other words, the argon mixture takes more time to reach its maximum. For both gas composition, density is proportional to the backing pressure, but the ratio is more favourable to Argon. We observed also that the dynamic is independent from the backing pressure.

These differences between both gas compositions are not well explained. Molecular viscosity η of argon rises at low temperature: going from $2.3 \times 10^{-5}\,\mathrm{Pa \cdot s}$ at 300 K to $27.4 \times 10^{-5}\,\mathrm{Pa \cdot s}$ at 83 K, argon boiling point [Younglove and Hanley, 1986]. Helium viscosity is $1.9 \times 10^{-5}\,\mathrm{Pa \cdot s}$ at 300 K and $0.63 \times 10^{-5}\,\mathrm{Pa \cdot s}$ at 50 K [Jensen et al., 1980]. Reynold number of the flow is given by:

$$R_e = \frac{\rho u L}{\mu} \tag{3.4}$$

where ρ is the fluid density, u the fluid velocity, L the typical length of the flow (the hydraulic diameter in a duct), and μ the dynamic viscosity. Typically for an argon flow in out nozzle (see CFD section) $\rho = 50$ to $500\,\mathrm{kgm}^3$, $u = 500\,\mathrm{m/s}$, $L = 400\,\mu\mathrm{m}$, $\mu = 2.3 \times 10^{-5}$ to $27 \times 10^{-5}\,\mathrm{Pa \cdot s}$. Therefore R_e stays above 1×10^5 in all cases, and viscosity is unlikely to drive this dynamic change, in agreement with observation in CFD simulation. Higher ejection velocity with helium (see CFD section) at same pressure and temperature derives from the mass difference between argon and helium and may explains the faster dynamic for helium. The lower peak density for helium at same backpressure is due to the reduced valve opening time achievable (2.9 ms for Helium vs. 4.2 ms for Argon), preventing the flow to reach a full steady state.

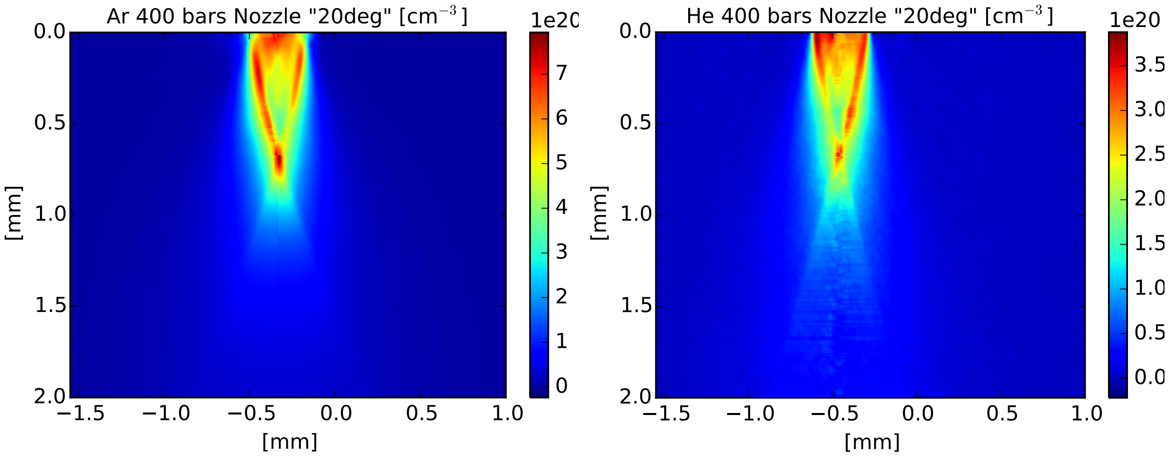

Figure 3.11 – Atomic density profile for shock nozzle "20 deg" shown Fig. 3.8, with parameters optimized for maximum density. The nozzle is upside-down, the gas flows from the top. Left) Argon, 400 bar, EV open time: 4.2 ms, delay after opening: 35 ms. Right) Helium, 400 bar, EV open time: 2.9 ms, delay after opening: 13 ms. Shock lines are clearly visible as well as the density peak where they cross. Helium and argon profile are very similar, see lineout Fig. 3.12, and similar to ANSYS fluent simulations as well.

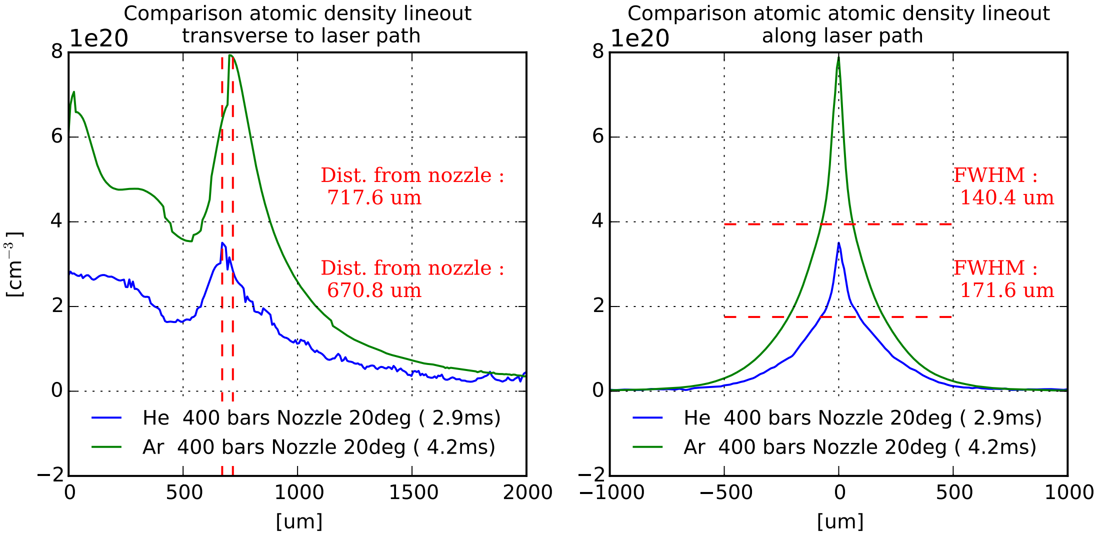

Figure 3.12 – Transverse (right) and longitudinal (left) density lineout at peak density for shock nozzle "20 deg" for both argon and helium. Maximum density reaches $8 \times 10^{20}\,\mathrm{cm}^{-3}$ for argon, and $3.5 \times 10^{20}\,\mathrm{cm}^{-3}$ for helium, this difference is discussed in the text. Position of the shock, shape of the profile, and full-width-half-max are similar for both gas mixture despite difference in atomic density.

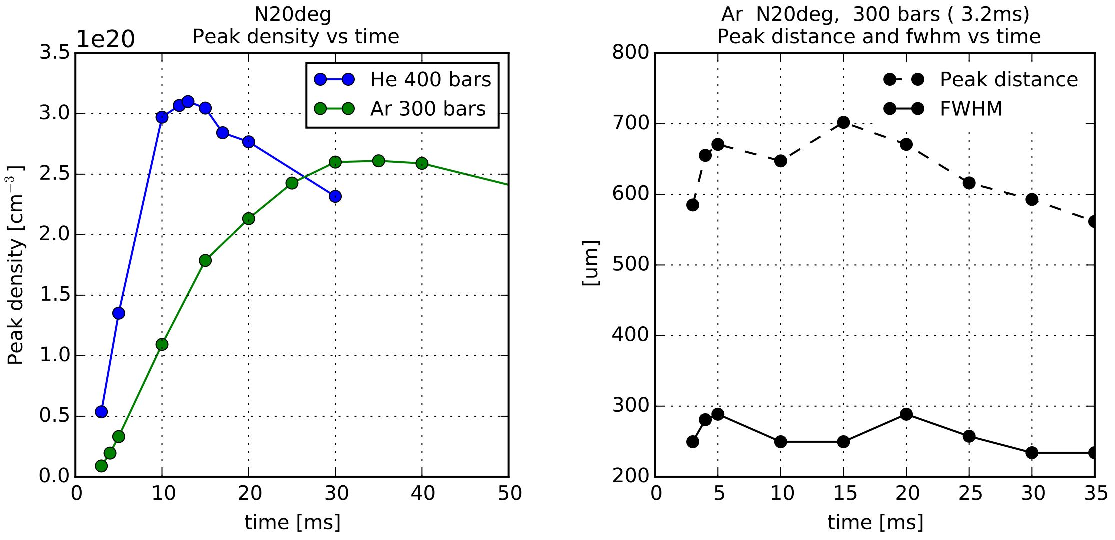

Figure 3.13 – Right) Evolution of atomic density at the peak position versus time. Here back-pressure of argon (green) is 300 bar, and valve is open 3.2 ms. Back-pressure of helium (green) is 400 bar, and valve is opened 2.9 ms. Dynamic of argon is slower than for helium. Left) Stability of the density profile over valve operation for shock nozzle "20 deg" shown Fig. 3.8, with argon, 300 bar, EV open time: 3.2 ms FWHM (plain line) of the peak and peak position over time (dashed line). These data are acquired over consecutive shots.

3.2 Supersonic gas jet and shock formation

3.2.1 Steady compressible flow

The fluid flow is described in steady state by a set of variables functions of the position $\vec{r}$: the velocity field $\vec{u}(\vec{r})$, the pressure $p(\vec{r})$, the density $\rho(\vec{r})$ and the temperature $T(\vec{r})$. Those 4 variables are linked through 4 equations:

- State equation
- Mass conservation
- Energy conservation
- Entropy conservation (isentropic process)

State equation

First, the equation of state in a fluid links the pressure to the density and temperature at local thermodynamic equilibrium. Pressure can be seen as a measure of volumetric kinetic energy along any 1D axis. The relationship between kinetic energy, total energy and temperature is determined by (1) the atom velocity distribution and (2) the number of degrees of freedom the energy can split in (evenly at equilibrium). In an ideal gas, atoms are considered as point masses who undergoes only elastic collisions, therefore degrees of freedom are limited to the 3 directions in space, and the velocity distribution obeys Maxwell-Boltzmann law, then the state equation is:

$$p = \frac{R}{M_m}\rho T \tag{3.5}$$

With M_m the molar mass of the fluid and $R = N_A k_b$ the gas constant $\approx 8.314\ \mathrm{J \cdot mol^{-1} \cdot K^{-1}}$.

Mass conservation

The mass conservation equation is written:

$$\frac{\partial \rho}{\partial t} + \nabla \cdot (\rho \vec{u}) = 0 \tag{3.6}$$

Let's consider a duct of slowly changing area $A(x)$ with a steady mass flow $\dot{m}$ all along the x-axis, and the fluid velocity in this direction noted u. With the hypothesis that u and ρ depend of x only it comes:

$$\rho(x)u(x)A(x) = \dot{m} = \mathrm{cst} \tag{3.7}$$

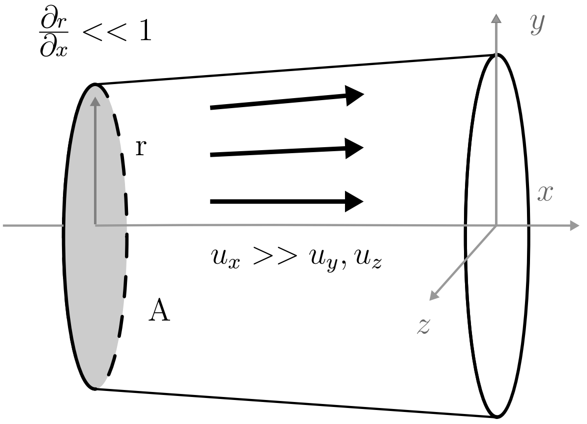

Figure 3.14 – Slowly changing area duct geometry

Energy conservation

The third relationship is obtained from energy conservation in a fixed control volume inside the flow (an *Eulerian* control volume). Using the first law of thermodynamic, the total energy of the fluid in the control volume $E_0 = E_{internal} + E_{kinetic}$ evolves as:

$$\frac{dE_0}{dt} = \dot{Q} + \dot{W} + \dot{E}_{in} - \dot{E}_{out} \tag{3.8}$$

Where E_0 is the sum of internal energy and kinetic energy. $\dot{E}_{in}$ ($\dot{E}_{out}$) stands for both the internal energy and kinetic energy that flows in (out of) the control volume. $\dot{W}$ is the work rate, and $\dot{Q}$ the heat transfert rate. Let's define the internal energy per unit of mass e (also called the specific internal energy), and the total specific internal energy $e_0 = e + \frac{1}{2}u^2$. Assuming:

- neither body work (negligible gravity) or viscous work
- no heating transfer at volume surface (adiabatic flow)
- no body heating

It comes:

$$\dot{E}_{in} - \dot{E}_{out} = \oiint_S (e + \frac{1}{2}u^2)\rho\vec{\mathbf{u}} \cdot \mathbf{d\vec{S}} \tag{3.9}$$

$$E_0 = \iiint_V (e + \frac{1}{2}u^2)\rho dV \tag{3.10}$$

$$\dot{Q} = 0 \tag{3.11}$$

$$\dot{W} = \oiint_S -p\vec{\mathbf{u}} \cdot \mathbf{d\vec{S}} \tag{3.12}$$

By introducing the specific enthalpy $h = e + \frac{p}{\rho}$ and total enthalpy $h_0 = h + \frac{1}{2}u^2$, it is possible to combine the two surface integrals and to convert them into a volume integral using the Gauss Therorem:

$$\dot{E}_{in} - \dot{E}_{out} + \dot{W} = -\oiint_S \rho h_0 \vec{\mathbf{u}} \cdot \mathbf{dS} \tag{3.13}$$

$$= \iiint_V \nabla \cdot (\rho \vec{\mathbf{u}} h_0) dV \tag{3.14}$$

Finally Eq. 3.8 is expressed as a volume integral, and holds for any control volume: therefore the integrated quantity is zero at every points:

$$\frac{\partial(\rho e_0)}{\partial t} + \nabla \cdot (\rho \vec{\mathbf{u}} h_0) = 0 \tag{3.15}$$

Adding to previous hypothesis the assumptions of:

- steady flow (i.e. $\frac{\partial}{\partial t} = 0$)
- conservation of the mass

Along streamlines, it gives:

$$h + \frac{1}{2}\rho u^2 = \text{cst} = h_0 \tag{3.16}$$

In the following, streamlines originate all from the same reservoir and then, h_0 is the same over the whole flow. The enthalpy is very simply linked to the temperature in a perfect gas by $h = c_p T$ where c_p is the specific heat capacity at constant pressure.

Entropy conservation

The last relationship is obtained by applying the first and second principle of thermodynamic to a control volume moving with the flow (a *Lagrangian* control volume). Internal specific energy evolves as:

$$de = \delta q + \delta w \tag{3.17}$$

We assume that no heat transfer occurs either internally or through the boundaries: $\delta q = 0$ and the process is called adiabatic. We assume also the process to be reversible, i.e. without dissipation or friction: $\delta w = -p\, dv$ where $v = 1/\rho$ is the specific volume. The process, both adiabatic and reversible is then isentropic and:

$$\begin{aligned} -pdv &= de \\ p\frac{d\rho}{\rho^2} &= de \end{aligned} \tag{3.18}$$

Using perfect gas relationship $p/\rho = RT$ and $de = c_v\, dT = R\, dT/(\gamma - 1)$ with $\gamma = c_p/c_v$ the ratio of specific heat and $R = c_p - c_v$ it comes:

$$\frac{d\rho}{\rho} = \frac{1}{\gamma - 1}\frac{dT}{T} \tag{3.19}$$

which can be expressed along streamlines with various combinations of p,ρ, and T, called isentropic relations:

$$\begin{aligned} \rho &= \text{cst} \times T^{1/(\gamma-1)} \\ p &= \text{cst} \times T^{\gamma/(\gamma-1)} \\ p &= \text{cst} \times \rho^{\gamma} \end{aligned} \tag{3.20}$$

Again, supposing a single reservoir for all streamlines, one can assume the constants to be equal between streamlines.

We will consider a flow coming from a reservoir where gas properties are ρ_0, p_0, T_0, h_0, and $u_0 = 0$. Other given properties of the problem are the slowly varying duct area A, and the mass flow $\dot{m}$, constant along the duct. Let's sum up in this table the relationships between the gas variables and the laws from which they derive.

Equation	**Variables**	**Relationship**
State equation	ρ,p,T	$p = \rho RT$
Mass Conservation	ρ,u	$\rho u A = \dot{m}$
Energy Conservation	T,u	$h_0 = \frac{\gamma}{\gamma-1}RT + \frac{u^2}{2}$
Entropy Conservation	ρ,T	$\frac{\rho}{\rho_0} = (\frac{T}{T_0})^{1/(\gamma-1)}$

3.2.2 Supersonic flow

In the description above, compression perturbations are missing a characteristic speed. It is called the "speed of sound". Let's consider the propagation of a small compression $\delta\rho$ at velocity a in a non-viscous media. Applying mass conservation equation and momentum conservation equation (equivalent to Navier-Stokes equation [Anderson et al., 2001]) and dropping high-order terms it comes:

$$a = \frac{\partial p}{\partial \rho} \tag{3.21}$$

In case of a perfect gas in isentropic flow it turns out that a depends of the temperature alone and can be expressed as:

$$a = \sqrt{\frac{\gamma p}{\rho}} \qquad a = \sqrt{\gamma RT} \qquad a = \sqrt{(\gamma-1)h} \tag{3.22}$$

This velocity appears naturally in the energy equation, giving the characteristic flow velocity at which a substantial part of the internal energy (measured with T) has been transferred to the kinetic energy (measured with u^2). Indeed, introducing the dimensionless Mach number $M = u/a(T)$ the energy equation can be re-written as:

$$h_0 = h + \frac{1}{2}u^2 = h\left(1 + \frac{1}{2}\left(\frac{u}{\sqrt{h}}\right)^2\right) = h\left(1 + \frac{\gamma-1}{2}M^2\right) \tag{3.23}$$

All variables can then be re-written in function of M alone:

$$\begin{aligned}
\frac{T}{T_0} &= (1+\frac{\gamma-1}{2}M^2)^{-1} \\
\frac{\rho}{\rho_0} &= (1+\frac{\gamma-1}{2}M^2)^{-1/(\gamma-1)} \\
\frac{p}{p_0} &= (1+\frac{\gamma-1}{2}M^2)^{-\gamma/(\gamma-1)} \\
\frac{u}{a_0} &= M(1+\frac{\gamma-1}{2}M^2)^{-1/2}
\end{aligned} \tag{3.24}$$

Linear development for $M << 1$ leads to $\rho = \rho_0 + \mathcal{O}(M^2)$ and $p + \rho u^2/2 = p_0 + \mathcal{O}(M^4)$: the fluid is called incompressible and obeys the Bernoulli's Law. As velocity increases along the flow and $M \approx 1$, the internal energy decreases in favour of the kinetic energy, leading to drop of pressure, density, and temperature and consequently, to an increase of the Mach number (which scales as $M = \mathcal{O}(u/\sqrt{T})$).

Finally, determination of fluid parameters along the flow is reduced to determination of the Mach-number M alone. The following derivations explain the origin of variations of M. The supersonic nozzle is described as a duct of slowly changing area $A(x)$ with a steady flow of given mass flow $\dot{m}$. Under condition of 3.7, mass conservation equation gives:

$$\rho u A = \dot{m} = \text{cst} \tag{3.25}$$

using 3.24:

$$\rho u = \rho_0 a_0 M(1+\frac{\gamma-1}{2}M^2)^{-(\gamma+1)/2(\gamma-1)} \tag{3.26}$$

Finally, ρu is a function of A the duct area and M. It is handy to define a new function of $f(M)$ and to study its behaviour:

$$\begin{aligned}
f(M) &= \frac{\rho u}{\rho_0 a_0} \\
&= M(1+\frac{\gamma-1}{2}M^2)^{-(\gamma+1)/2(\gamma-1)}
\end{aligned} \tag{3.27}$$

The mass flow per area unit ρu binds M with the nozzle profile $A(x)$. $f(M)$ exhibits a non-monotonic behaviour, with a maximum for $M = 1$, leading to major consequences. For a given mass flow and duct area, two Mach numbers can be sustained: one supersonic ($M > 1$), one sonic ($M < 1$). Assuming an isentropic flow, fluid variables cannot change abruptly, so we will assume the Mach number to be continuous and not jumping from supersonic to sonic solution, starting from $M_0 = 0$ in the reservoir. In sonic flows, a decrease of the area of the duct leads to an acceleration of the flow, but it is reversed in supersonic flows: the increase of the area leads to acceleration of the flow.

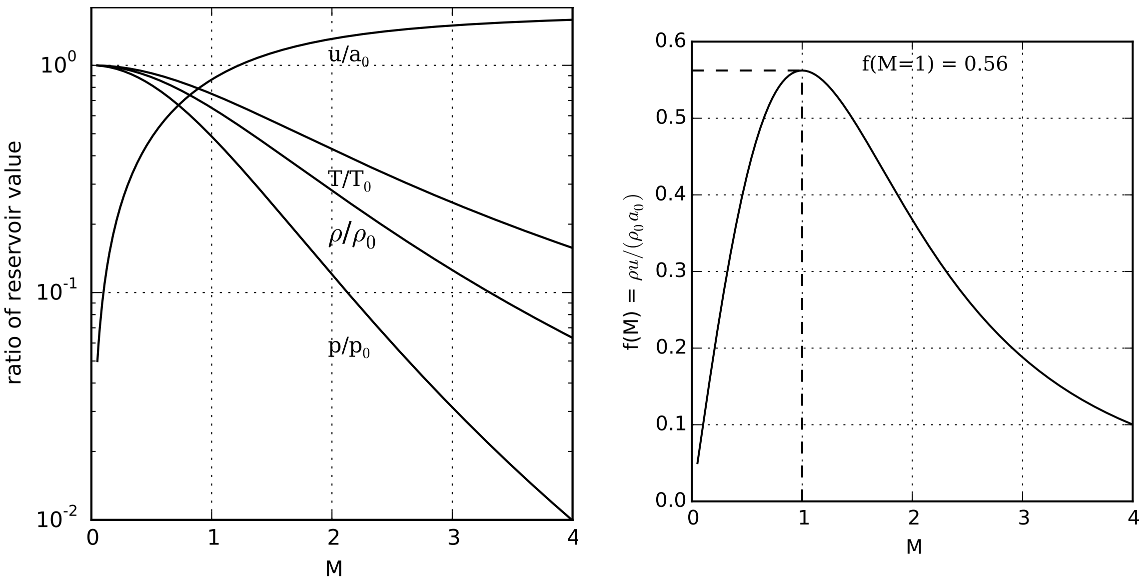

Figure 3.15 – Left: evolution of thermodynamic variables (normalized by reservoir values for p,T and ρ, and by reservoir sound speed for u) with the Mach-number M in an isentropic steady compressible flow of Argon or Helium (for both $\gamma = 1.67$). Right: profile of the areal mass flow $f(M) = \rho u/(\rho_0 a_0)$ with M. f is maximum in $M = 1$

Assuming that *somewhere along the duct* it exists x_1 such as $M(x_1) = 1$, then $\partial f/\partial M(x_1) = 0$ and:

$$\frac{\partial A}{\partial x}(x_1) = -\mathrm{cst}\frac{1}{M^2}\frac{\partial M}{\partial x}\frac{\partial f}{\partial M}(x_1) \tag{3.28}$$

$$\frac{\partial A}{\partial x}(x_1) = 0 \tag{3.29}$$

$$x_1 = x_{\mathrm{throat}} \tag{3.30}$$

If M reaches 1 in the duct, it is at the throat (of area A_t). Relationship binding $A(x)$ and M is used to solve the profile of M along the duct, and therefore, the profile of all thermodynamic variables:

$$\begin{aligned} \rho u A = \dot{m} = \mathrm{cst} \\ f(M)A = \mathrm{cst} \end{aligned} \tag{3.31}$$

Shape of $f(M)$ shows also that the fluid cannot sustain any given steady areal mass flow. For $\gamma = 1.67$ (mono-atomic heat capacity, like argon and helium), it is limited by $\rho u \leq 0.56\rho_0 a_0$. For a mass flow under this limit, the flow will be subsonic along the whole duct, reaching a maximum at the throat. If the mass flow reaches this limit, the flow is said to be *choked* and M reaches 1 at the throat. Such supersonic nozzle with converging then diverging duct is called a *Laval nozzle*.

What exactly imposes the mass flow ? Considering an isentropic flow and a given duct, the mass flow is constrained by the reservoir and exit parameters. Using the set of equation 3.24 at the duct exit for pressure:

$$\dot{m} = \rho_0 a_0 A_e f(M_e) \tag{3.32}$$

with:

$$M_e^2 = \frac{2}{\gamma - 1}[(\frac{p_e}{p_0})^{(1-\gamma)/\gamma} - 1] \tag{3.33}$$

but:

$$\begin{aligned} \dot{m}_{max} &= \rho_0 a_0 A_t f(M_t) \\ \dot{m}_{max} &= \rho_0 a_0 A_t f(1) \\ \dot{m}_{max} &= \dot{m}_{choked} = f(1)\rho_0 a_0 A_t \end{aligned} \tag{3.34}$$

Decrease of p_e/p_0 leads to an increase of the mass flow. The flow is chocked when the imposed mass flow gets equal to the maximum flow sustainable by the throat and reservoir, i.e when $\dot{m} = \dot{m}_{choked}$:

$$\begin{aligned} \dot{m} &= \dot{m}_{choked} \\ \rho_0 a_0 A_e f(M_e) &= f(1)\rho_0 a_0 A_t \\ f(M_e) &= f(1) A_t/A_e \end{aligned} \tag{3.35}$$

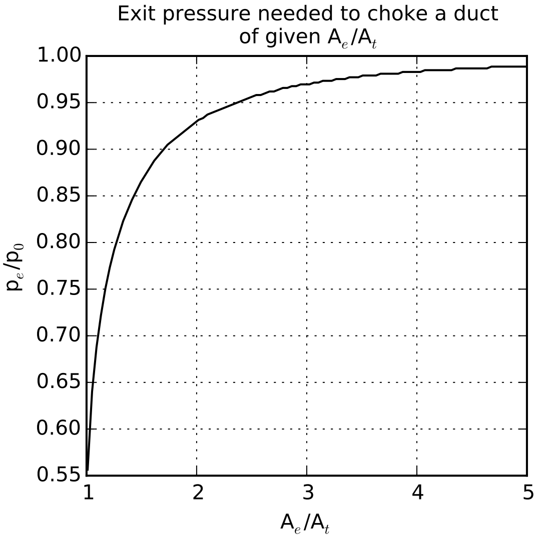

Figure 3.16 – Exit argon pressure p_e/p_0 needed to choke a duct of given ratio A_e/A_t. See Eq. 3.35. For $p_e/p_0 = 0$, the duct is always choked: M reaches 1 at the throat and the flow becomes supersonic after the throat

To conclude, if the exit boundary conditions (p_e,A_e) impose a subsonic flow, the mass flow is given by (p_e,A_e), and vary accordingly. If the exit boundary conditions imposes a supersonic flow, then $M = 1$ at the throat, and the flow and mass flow are determined only by the tank initial conditions: no information related to the exit can propagate backward. Relationship between A and M is illustrated in Fig. 3.17:

unchoked flow	**choked flow**
$\dot{m}$ depends from p_e	$\dot{m}$ constant
$f(M)A = f(M_e)A_e$	$f(M)A = f(1)A_t$

For a choked flow the relationship between the duct area A and M is eventually given by:

$$A = A_t f(1)\left[M(1+\frac{\gamma-1}{2}M^2)^{-(\gamma+1)/2(\gamma-1)}\right]^{-1} \tag{3.36}$$

Evolution of all variables along the duct can be obtained from these relationships, plotted in Fig. 3.18 for duct parameters with same ratio $A_e/A_t = 4$ as the shock nozzle presented in the previous section. Exit values for all variables are written in Fig. 3.18. It must be noted that the pressure of the exit reservoir needed to choke such a nozzle with $A_e/A_t = 4$ is only $p_e/p_0 < 0.98$. Here, p_e/p_0 reaches 0.02 at the exit, therefore the jet exit pressure may be lower than the pressure in the exit reservoir. This discrepancy is at the origin of shock waves that enable the flow to adapt to the boundary constraints. Those shock waves may or may not be located into the duct, depending on the pressure in the exit reservoir. In the next section we will introduce a formal description of a shock, before exploring the consequences for specific Laval nozzles.

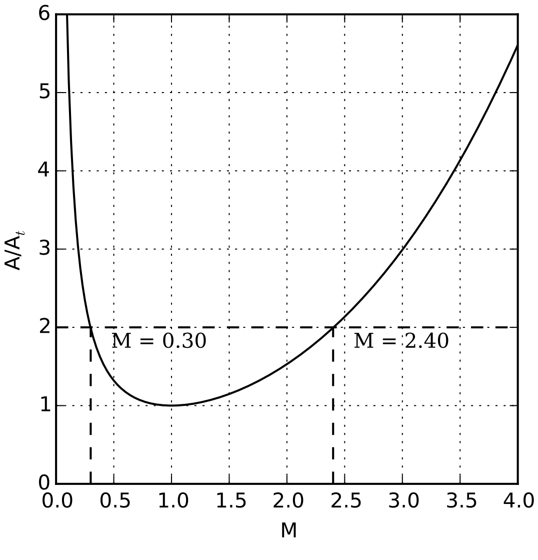

Figure 3.17 – Relationship between the normalized duct area A/A_t and the Mach-number M in case of a choked flow. See Eq. 3.31. A_t is the throat area. For a given area A, two solutions exist: one subsonic (or sonic) and one supersonic. Dotted lines show solutions for $A = 2A_t$. Reservoir conditions correspond to $M = 0$ and $A = +\infty$. Solution $M > 1$ are achievable only if the flow is choked, i.e. if the exit pressure is low enough (See 3.35)

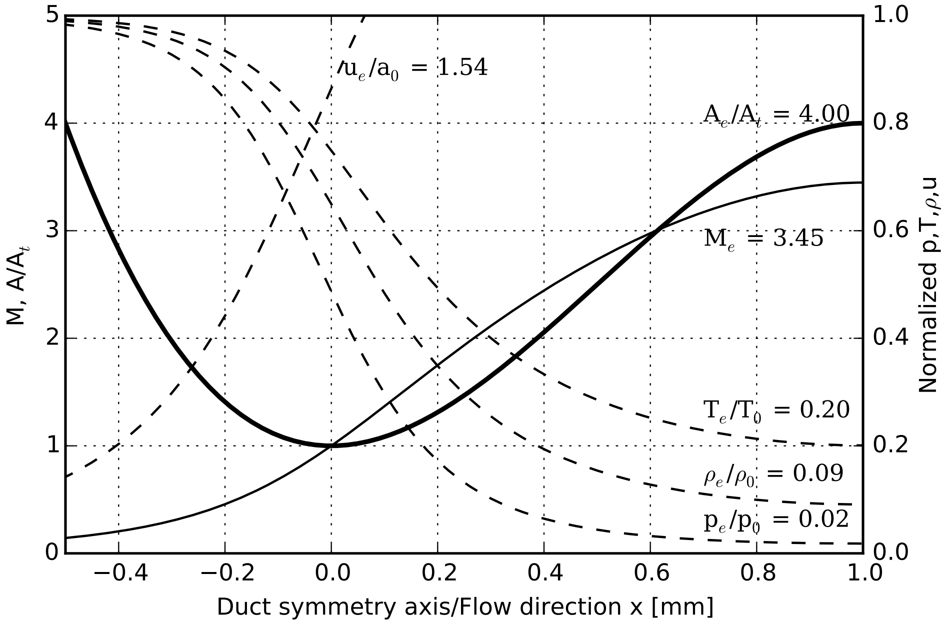

Figure 3.18 – Evolution of all fluid variables for a choked argon flow in a converging-diverging supersonic duct - so-called *Laval* nozzle - with $A_e/A_t = 4$, similar to the nozzle used in our experiments. A/A_t (thick line) and M (plain line) are read on the left y-axis. p/p_0, T/T_0, ρ/ρ_0, u/a_0 (dotted line) are read on the right y-axis. Values of all variables at the nozzle exit are written near the respective curves.

3.2.3 Shock waves from "de Laval" nozzles

A *shock front* is an abrupt and finite variation of temperature, pressure and velocity of a fluid. Linearisation of fluid dynamics equations shows that infinitesimal perturbations of density can propagate at speed of sound. But in a general case, non-linearity of these equations enables discontinuities to arise from smooth perturbations, and potentially to be self-sustained. A shock front is a discontinuity surface crossed by the fluid, and then, one can define an *upstream* flow and a *downstream* flow. Passing through the shock front, the gas experienced strong gradients in velocity and temperature. Hence, friction force and heat conduction are not negligible any more. These phenomena increase entropy of the flow. The process is still adiabatic, but not any more isentropic across the shock front.

Description

As the shock thickness is small compared to other duct dimensions ($<< 1\,\mu$m), we will describe it as a surface of zero thickness. Mass, momentum and energy are conserved through the shock, while entropy increases. We describe a shock occurring in a 1-D flow, where the subscripts 1 and 2 stand respectively for the upstream and downstream flows. The reference frame is the frame of the shock front.

Relationship between upstream and downstream variables are given by *Rankine-Hugoniot* equations, derived from conservation laws in a control volume surrounding the shock:

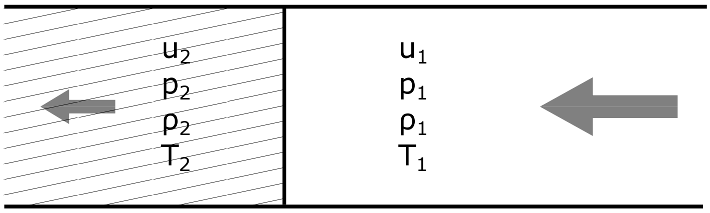

Figure 3.19 – Shock in 1-D representation. The subscripts 1 and 2 stand for respectively the upstream and downstream flow.

$\rho_1 u_1 = \rho_2 u_2$	Mass conservation
$\rho_1 u_1^2 + p_1 = \rho_2 u_2^2 + p_2$	Momentum conservation
$\rho_1 u_1 (h_1 + \frac{1}{2} u_1^2) = \rho_2 u_2 (h_2 + \frac{1}{2} u_2^2)$	Energy conservation
$p_2 = \frac{\gamma}{\gamma - 1} \rho_2 h_2$	State equation

Table 3.1 – Conservation Equations in compressible fluid

Variation of specific entropy across the shock being positive, the density and temperature across the shock can only increase. Indeed, specific entropy can be written from the first law of thermodynamic and the state equation:

$$\begin{aligned} ds &= c_v \frac{dT}{T} - \frac{p}{T} d\left(\frac{1}{\rho}\right) \\ ds &= c_v \frac{dT}{T} + (\gamma - 1)\frac{d\rho}{\rho} \end{aligned} \tag{3.37}$$

Let's express the second term. Energy conservation and mass conservation can be combined in:

$$\begin{aligned} dh + udu &= 0 \\ \frac{\gamma}{\gamma - 1} RdT + udu &= 0 \\ (\gamma - 1)\frac{d\rho}{\rho} &= \frac{\gamma R}{u^2} dT \end{aligned} \tag{3.38}$$

and then:

$$ds = c_v dT \left(\frac{1}{T} + \frac{\gamma R}{u^2}\right) \tag{3.39}$$

Specific entropy varies in the same direction as density and temperature. This result has for consequence that gaining entropy by passing through the shock front, the fluid can only increase its temperature and density. A *rarefaction* shock is then forbidden. What does it imply for both up- and downstream flow velocities ? As we did for the compressible flow, it is more convenient to express the downstream properties of the shock as a function of the upstream properties, and specifically, as a function of M_1 alone, where $M_1 = u_1/a_1$ is the upstream Mach number, and $a = \sqrt{\gamma p/\rho}$ the sound speed. Solving the system 3.1, one gets (plotted Fig 3.20)

$$\begin{aligned} M_2^2 &= \frac{1+\frac{\gamma-1}{2}M_1^2}{\gamma M_1^2 - \frac{\gamma-1}{2}} \\ \frac{\rho_2}{\rho_1} &= \frac{(\gamma+1)M_1^2}{2+(\gamma-1)M_1^2} \\ \frac{p_2}{p_1} &= 1+\frac{2\gamma}{\gamma+1}(M_1^2-1) \\ \frac{u_2}{u_1} &= \frac{\rho_1}{\rho_2} \\ \frac{T_2}{T_1} &= \frac{p_2}{p_1}\frac{\rho_1}{\rho_2} \end{aligned} \tag{3.40}$$

To ensure increasing entropy across the shock, equations system 3.40 shows that M_1 must be greater than 1 therefore $M_2 < 1$. In the shock frame, the upstream flow is always supersonic, and the downstream flow is sonic, while $u_2 < u_1$, p_2/p_1, T_2/T_1 and ρ_2/ρ_1 are greater than 1. Furthermore, ρ_2/ρ_1 is limited by $(\gamma+1)/(\gamma-1)$, meaning that there is a limit in the density jump of the shock, with $\rho_2/\rho_1 < (\gamma+1)/(\gamma-1) = 3.985$ in argon.

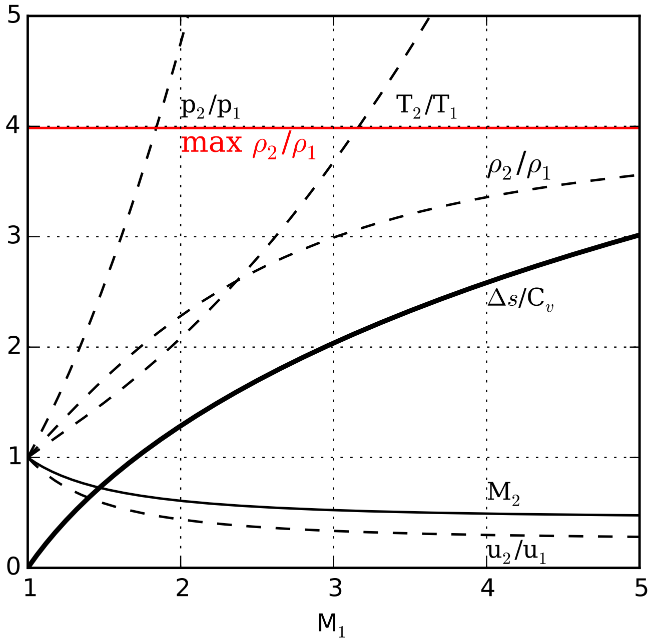

Figure 3.20 – Downstream variable as a function of upstream flow parameters. M_2 is the downstream Mach number (solid line). Δs is the specific entropy variation across the shock, and c_v the specific heat capacity at constant volume. A positive variation of entropy imposes $M_1 > 1$ and $M_2 < 1$

Oblique Shock

A shock typically arises from supersonic flows adjusting to external constraints. We will focus on how the flow adapts to a velocity constraint set by walls. When a supersonic flow undergoes a sudden variation of direction, conservation equations 3.1 impose the presence of a shock front, oblique to the flow. These oblique shocks are of great interest for density tailoring, and are used in our nozzles. I introduce here a description of these shocks adapted from Anderson, *Fundamentals of Aerodynamics* [Anderson, 2001].

In order to calculate 1) the downstream properties of the flow, and 2) the angle β formed by the shock, we need to apply the Rankine-Hugoniot shock relations 3.1 to the flow normal to the shock, and conservation laws for the flow parallel to it. The velocities V_i of the up- and downstream flows are split in a normal component u_i, and a parallel component w_i:

$$u_i = V_i \sin\beta \qquad\qquad w_i = V_i \cos\beta \tag{3.41}$$

Mach numbers in the normal (meaning: normal to the shock) direction are given by:

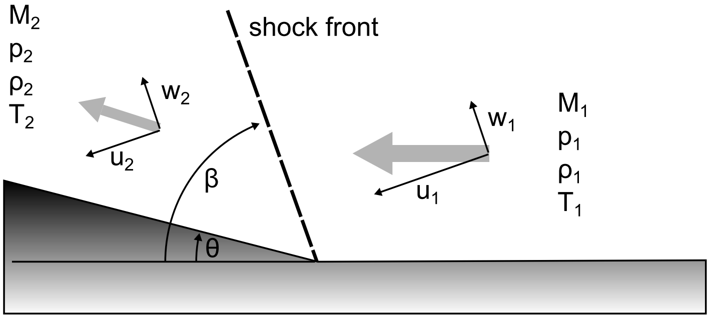

Figure 3.21 – Oblique shock schematic description for a concave corner. The subscripts 1 and 2 stand for respectively the upstream and downstream flows. The upstream flow, parallel to the wall, undergoes a sudden change in direction of an angle θ. Conservation laws impose the presence of a shock at an angle β. This angle depends of θ and M_1 alone, and is derived in this section. The velocities V_i are decomposed into two perpendicular components: u_i normal to the shock front, and w_i parallel to it.

$$M_{n1} = \frac{u_1}{a_1} \qquad M_{n2} = \frac{u_2}{a_2} \tag{3.42}$$

$$M_{n1} = \frac{V_1 \sin\beta}{a_1} \qquad M_{n2} = \frac{V_2 \sin(\beta-\theta)}{a_2} \tag{3.43}$$

$$M_{n1} = M_1 \sin\beta \qquad M_{n2} = M_2 \sin(\beta-\theta) \tag{3.44}$$

Making the substitutions $M_1 \to M_{n1}$, $M_2 \to M_{n1}$ into the Rankine-Hugoniot system 3.1, it comes:

$$M_{n2}^2 = \frac{1 + \frac{\gamma-1}{2} M_{n1}^2}{\gamma M_{n1}^2 - \frac{\gamma-1}{2}} \tag{3.45}$$

Using the relation $w_1 = w_2$, it is now possible to derive the angle β. Indeed:

$$\frac{\tan(\beta-\theta)}{\tan\beta} = \frac{u_2}{u_1} = \frac{\rho_1}{\rho_2} = \frac{2 + (\gamma-1)M_1^2 \sin^2\beta}{(\gamma+1)M_1^2 \sin^2\beta} \tag{3.46}$$

Isolating θ it comes:

$$\tan\theta = \frac{2}{\tan\beta} \frac{M_1^2 \sin^2\beta - 1}{M_1^2(\gamma + \cos 2\beta) + 2} \tag{3.47}$$

It is now possible to infer β from M_1 and θ with graphical resolution. The graph $\beta(\theta, M_1)$ is plotted Fig 3.22. Solution doesn't exist for all couple (θ, M_1). For a given M_1, there is a maximum θ_{max} allowing for β solution. For $\theta < \theta_{max}$, two solutions exist: one with $M_2 > 1$, called weak shock, and one with $M_2 < 1$, called strong shock. As only the normal velocity M_{n2} is reduced below 1, the total post-shock Mach number M_2 can still be supersonic without contradiction with the entropy increase. For $\theta > \theta_{max}$ a *detached bow shock* is formed, disconnected from the flow's inflection point. The presence of weak or strong shock will depend on the downstream pressure constraints. Fig 3.22 shows shock angle β for parameters close to those of our nozzles with argon

($\theta = 10^o$,$M = 3.45$). Variables evolution from both cases are summed up in the table 3.2.

Argon,$\theta = 10^o$,M = 3.45

	Strong shock	Weak shock
$\beta(^o)$	85.5	25.5
M_2	0.52	2.71
p_2/p_1	14.5	2.5
ρ_2/ρ_1	3.18	1.69

Table 3.2 – Shock parameters for strong and weak shocks, in the case of a wall angle of 10 deg and M = 3.45. These conditions are typical of gas jet designs used in experiments.

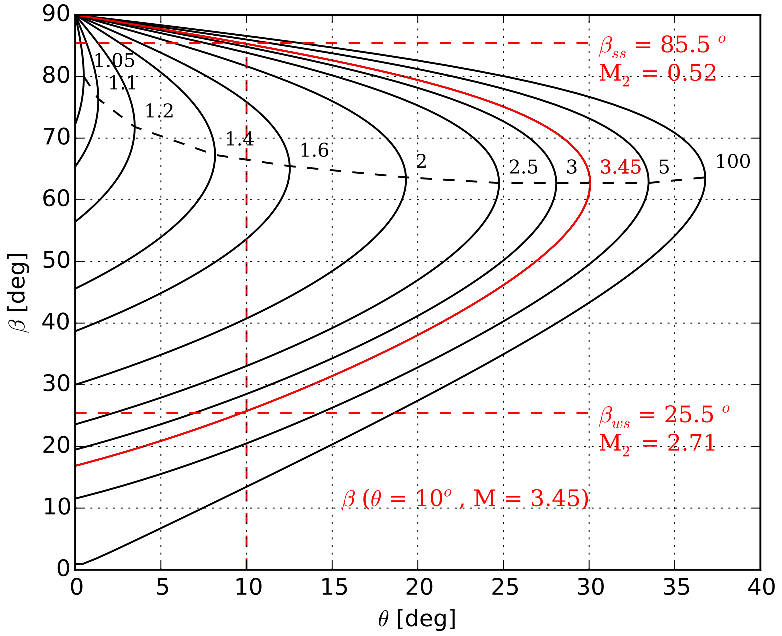

Figure 3.22 – Shock angle β vs. deflection angle θ (black line), in argon, for given upstream Mach-numbers. Each Mach-number is noted besides its curve. Curves feature a θ_{max}: 1) for $\theta > \theta_{max}$, a *bow shock* is formed, detached from the walls. Dotted line shows evolution of θ_{max} with M. 2) for $\theta < \theta_{max}$ shock angle β can take 2 values, leading to a strong shock case, and a weak shock case. Variables for both cases are plotted in red for flow parameters close to those of our nozzles ($\theta = 10^o$, $M = 3.45$)

3.3 Computational Fluid Dynamics simulation with ANSYS Fluent

3.3.1 Motivation

Analytical derivation of the shock waves properties enable us to identify the relevant parameters and their relationship. Other parameters may affect the shock density and position:

- Effect of the length of the final straight part of the duct
- Effect of the angle of the diverging part.
- Effect of the turbulence and dissipation

To explore various nozzle designs, we used CFD simulation with ANSYS Fluent Release 16., with 2D axis-symmetric geometry in steady flow.

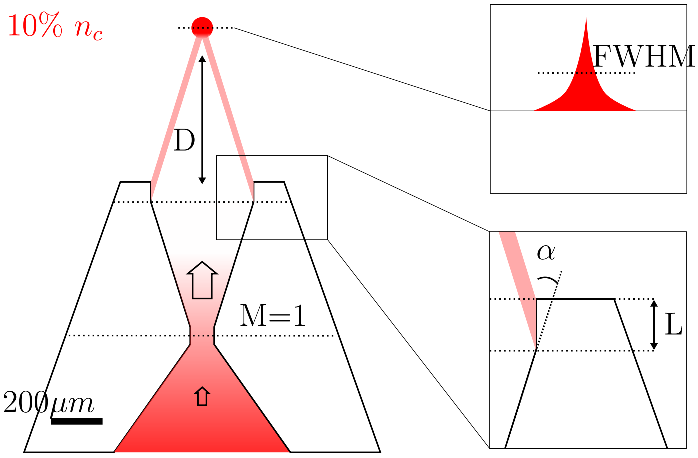

Figure 3.23 – Details on the nozzle geometry investigated by ANSYS simulation: influence of the straight duct length L and the angle α on the shock density and distance D.

3.3.2 Fluent Model

The flow is simulated in 2D-axis-symmetric geometry, with compressible Helium, ideal gas law, and the following boudary conditions:

- **inlet:** Total pressure 400 bar, $T = 300\,\mathrm{K}$
- **outlet:** Total pressure 0 bar, $T = 300\,\mathrm{K}$
- **wall** No-slip condition, $T = 300\,\mathrm{K}$

ANSYS Fluent solves simultaneously conservation equations for mass, momentum, and energy (for compressible flows), with a density-based solver [Inc., 2013].

3.3.3 Mesh

Mesh should accurately resolve the strong gradients risen by the shocks, and enable correct convergence of the simulation. We observed that a triangular mesh (called also *unstructured* mesh) was more robust than a rectangular mesh (*structured* mesh). Especially situations where angles between nodes are too small must be avoided. In areas close to the outlet and inlet of the simulation, the mesh size is set to 100 µm. In the part of the flow with high density gradients, the mesh size is reduced to 7 µm. A growth rate of 1.15 ensures smooth transition between these two cases. The number of nodes reaches roughly 12 000. Increasing the number of nodes to 160 000 by setting a fine mesh size of only 1 µm and a coarse mesh of 5 µm didn't change significantly the density profile once the convergence is reached. This analysis ensures that our mesh size is relevant.

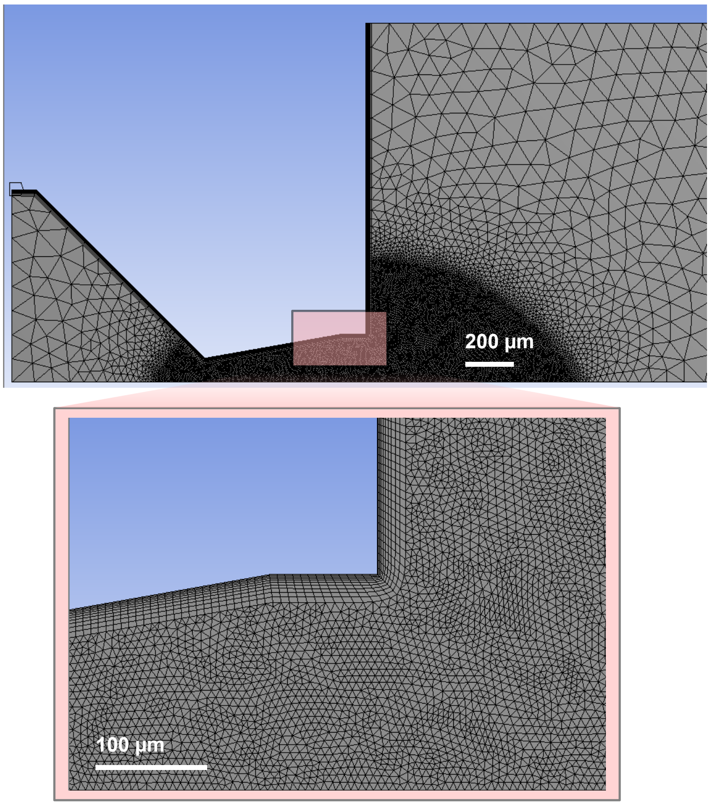

Figure 3.24 – Top) View of the whole domain with mesh size from 7 µm to 100 µm, Bottom) Details of the area with fine mesh, with the expansion layers resolving the viscous layer near the wall.

Meshing near walls deserves a specific treatment because, assuming no-slip boundary conditions, the velocity is zero at the wall. The layer between the viscous flow (low Reynolds, near the wall) and the free flow (high Reynolds, far from the walls) features strong velocity gradients, and needs to be accurately resolved. Correct wall treatment is critical for turbulent flow, as this layer features interplay between the slow mean flow and the turbulence viscosity. This layer is called *boundary layer*. Theodore von Kármán introduced the *Law of the Wall* [von Karman, 1934] describing the evolution of the parallel velocity with the wall distance, this law is shown in Fig. 3.25. He introduced the parameters y^+ (dimensionless wall distance) and U^+ (dimensionless parallel velocity) defined as:

$$y^+ = \frac{y u_\tau \rho}{\mu} \qquad U^+ = \frac{u}{u_\tau} \qquad u_\tau = \sqrt{\frac{\mu}{\rho}\frac{\partial u}{\partial y}} \tag{3.48}$$

Where y is the distance to the wall, u the velocity parallel to the wall, u_τ is the shear velocity, ρ the fluid density and μ the dynamic viscosity.

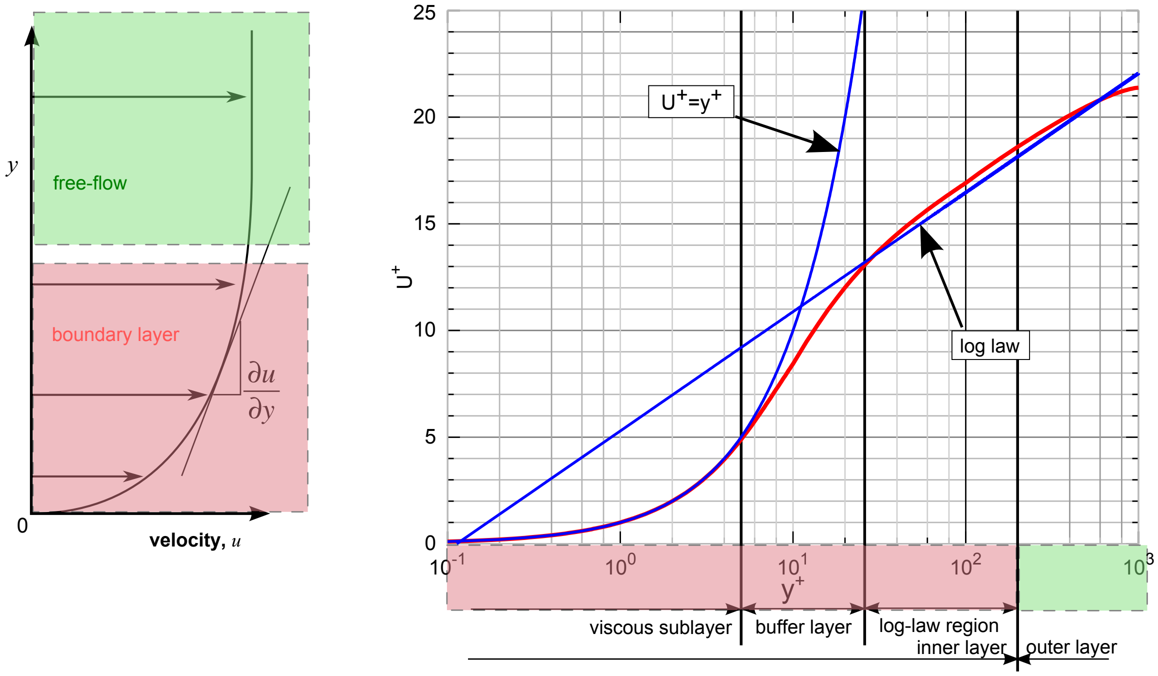

Figure 3.25 – Left) Schematic description of the velocity near the walls ($y = 0$) Right) Law of the wall in the dimensionless unit y^+ and U^+, showing the 3 regions of the boundary layer, extract from [Nezu and W.Rodi, 1986]

The first layer, where $y^+ < 5$, is called the *viscous layer* or *laminar layer*, because in this layer, viscosity effects are dominant, typically when the transverse Reynolds number $Re_y = \rho y u/\mu$ is below 200. In the viscous layer, the flow obeys simply to:

$$U^+ = y^+ \tag{3.49}$$

The third layer, where $y^+ > 30$, is the *log-law region.* In this layer the flow experiments constant shear-stress and negligible viscosity, which translates into a log law:

$$U^+ = \frac{1}{\kappa}\log y^+ + C^+ \tag{3.50}$$

Various log laws can be applied depending of the surface roughness and Reynolds number. The layer in between is the buffer layer, where none of the previous laws

Parameters	Value	y^+	Wall distance y
ρ	$10\,\mathrm{kg\cdot m^{-3}}$		
u_∞	$1500\,\mathrm{m\cdot s^{-1}}$		
μ	$1.9\times10^{-5}\,\mathrm{Pa\cdot s}$		
Re_∞	1.6×10^{5}		
		5	120 nm
		30	710 nm

Table 3.3 – Parameters relevant for wall functions near the exit for 400 bar Helium out of a B20 nozzle (layout Fig. 3.8)

applied. The first cell should avoid to lie in this region, as no law can describe accurately the velocity boundary condition onto the wall. CFD best practices advice to set either:

- The first cell at $y^+ > 30$ and to use the log-law Eq. 3.50 as boundary condition. Ansys FLUENT calls it "standard wall function" and use the values $\kappa = 0.4$ and $C^+ = 5.6$.
- The first cell at $y^+ < 1$ and resolving the viscous layer with at least 10 cells. Ansys FLUENT calls it "Enhanced wall function" and uses both Eq. 3.49 and Eq. 3.50.

3.3.4 Laminar CFD

The model of compressible supersonic flow described earlier (Eq. 3.24) had been tested against the CFD simulation inside a B20 nozzle with 440 bar of Helium at the inlet. This model assumes an isentropic flow in a duct of slowly varying area. The simulated nozzle has brusque area variations, leading in CFD simulation to inner shocks. Inner shocks (breaking the isentropy) and brusque area variations may limit the validity of this model. At the nozzle exit, the duct area becomes infinite, and the model is not relevant anymore, nonetheless, by assuming a virtual duct in continuation of the diverging part (of half-angle 10 deg) results show a very good agreement between the model and the CFD simulations. (Fig. 3.26). This virtual duct translates the fact that before the shock, the supersonic flow continues to expand straight in vacuum as it did into the duct. The compressible model is associated with the oblique shock model 3.45 to derive shock angle in Fig. 3.22 (and thus position of the crossing of shock lines) and thermodynamics variables after the shock 3.40. The shock position is accurately described (roughly 600 µm from the nozzle) by the weak shock case. In the weak shock case, the downstream flow is still supersonic. Downstream variables from compressible model only roughly match values from CFD laminar simulation. Density and pressure are underestimated, because the analytic model doesn't describe two intersecting shocks, but only a single one.

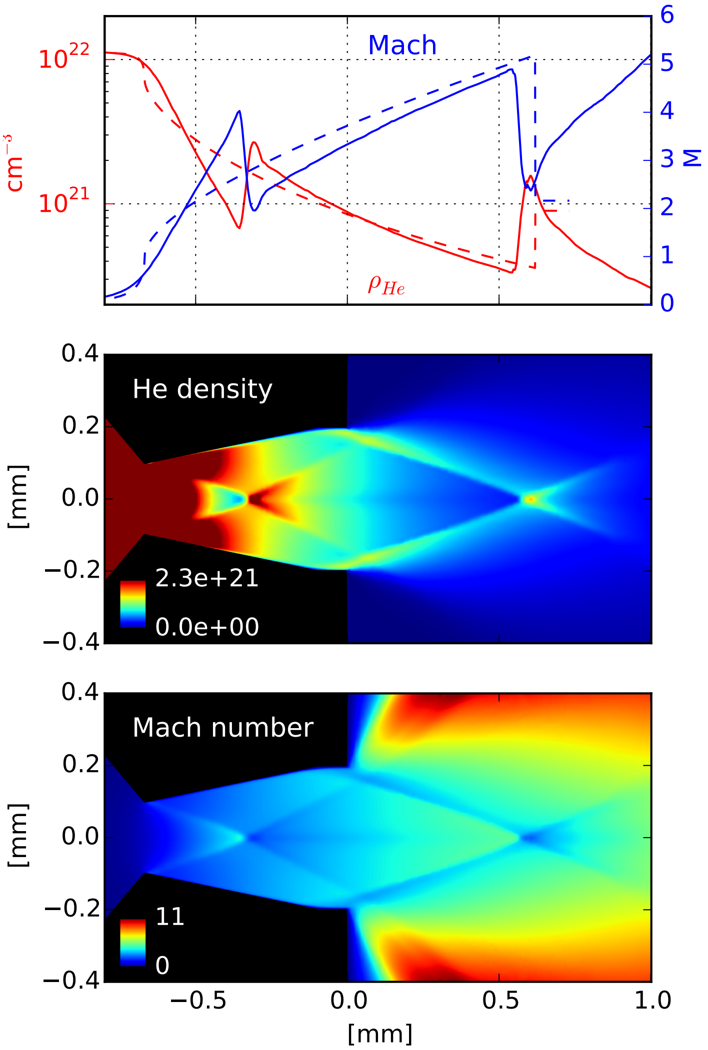

Figure 3.26 – Top: Evolution of the helium density (red,left scale) and Mach number (blue,right scale) along the nozzle axis from laminar CFD simulation (solid line) and compressible flow model (dashed line). Middle and bottom: Helium density (in cm^{-3}) and Mach number at the nozzle exit. The nozzle expansion half-angle is 10 deg, inlet pressure is 440 bars.

In Laminar CFD results, another shock lay within the nozzle. It rises from the abrupt angle of the throat. This inner shock breaks the condition of isentropy assumed for the compressible model. Nonetheless the agreement between the analytic model and the CFD simulation is fairly good, both for thermodynamic parameters and shock properties.

Fig. 3.27 compares the laminar CFD simulation with the experimental results. Shock position is well reproduced, as well as the low density wings. Gradients are not accurate, while the laminar CFD features a shock transverse dimension of FWHM 48 µm, experimental characterisation yields 187 µm. This difference may come from inaccurate drilling and electro-erosion of the nozzle, as the flow is very sensible to any defect in shape or surface roughness of the nozzle. A second criteria is investigated in the next subsection: the effect of turbulence. The Reynolds number is above 1×10^5 in the free-flow, and turbulence effects are present in these conditions.

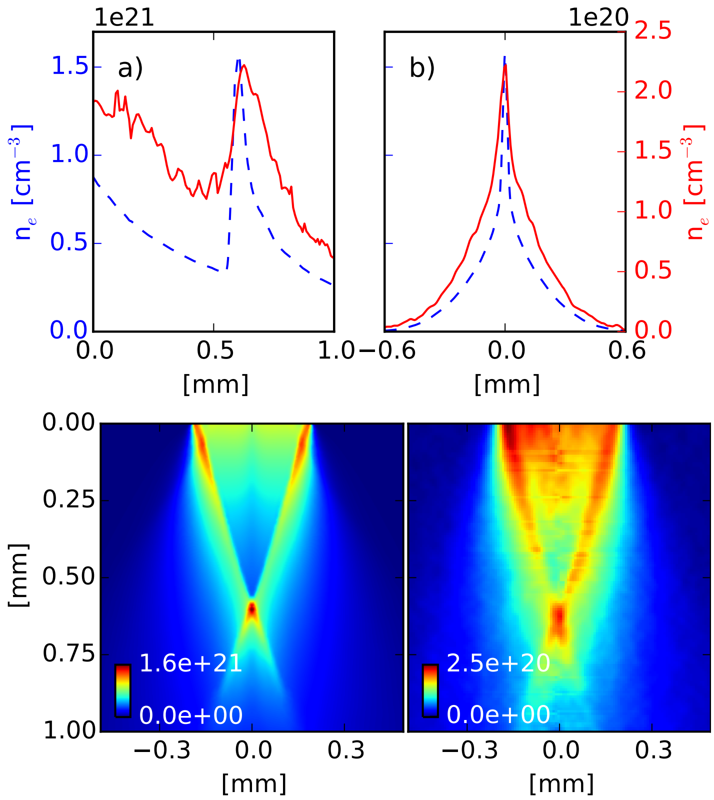

Figure 3.27 – Density lineouts (a) along the nozzle axis (b) across the shock. Helium with 400 bars at the inlet of B20 geometry for Laminar CFD (blue line, left scale), and experimental results (red line, right scale). Bottom, density map in the same conditions for Laminar CFD (left), and experimental results (right)

3.3.5 Turbulent CFD

Turbulence models

Reynolds averaging denotes the separation in the Navier-Stokes equations of the mean flow $\langle u \rangle$ from the turbulent one u' for each axis i:

$$u_i = \langle u_i \rangle + u'_i \tag{3.51}$$

In case of compressible flow the averaging is meant over mass, and is defined the same way for pressure and energy. It yields the ensemble-averaged momentum equations. A new term appears: the *Reynolds Stress* tensor given by $-\rho\langle u'_i u'_j \rangle$. The closing of the averaged equations requires the modelisation of this term, and numerous model has been proposed. Turbulence has a strong influence on shock gradient, and may explain the discrepancy between the CFD laminar case and the experimental results. We compared three turbulence models:

- The standard and broadly used K-ϵ model [Launder and Sharma, 1974]
- The improved K-ϵ RNG model [Orszag et al., 1993]
- The Reynold Stress Model [Launder, 1989]

The K-ϵ model has a low computational cost, and is suitable for supersonic High Reynolds flow in ducts. [Viegas and Horstman, 1979]. The K-ϵ model is named a *two equation model*, because it includes two extra transport equations to represent the convection and diffusion of turbulent energy. The two extra variables transported by the K-ϵ model are the turbulent kinetic energy k, and the turbulent dissipation ϵ. ϵ determines the scale of the turbulence, and k is the energy in the turbulence. The RNG model adds an analytic expression for the Prandtl number, and is derived from group renormalization of the momentum and mass equations. The Reynold Stress Model is the most complete model of RANS type (Reynolds-Average Navier-Stokes), and features less user-determined constants. Turbulence models require an extra inlet boundary condition: the turbulence energy, expressed as a fraction of the kinetic energy, and given in CFD best practices by:

$$I = 0.16 R_e^{-1/6} D[\mathrm{m}] \tag{3.52}$$

Where $R_e \approx 5 \times 10^5$ is the Reynold number, and $D = 200\,\mu\mathrm{m}$ the throat diameter. It yields $I \approx 1\,\%$.

Effect on shock gradients

These models give the same shock position (Fig. 3.28a), but show a large discrepancy in the shock gradient (Fig. 3.28b). The standard K-ϵ model features large gradient heavily dependent of the inlet turbulence boundary condition. Compared with the laminar case, shock position is unchanged, gradients are $\approx 5\times$ larger, and density value just after the shock is reduced by $\approx 30\,\%$. Other models display gradients closer to the laminar case, even sharper.

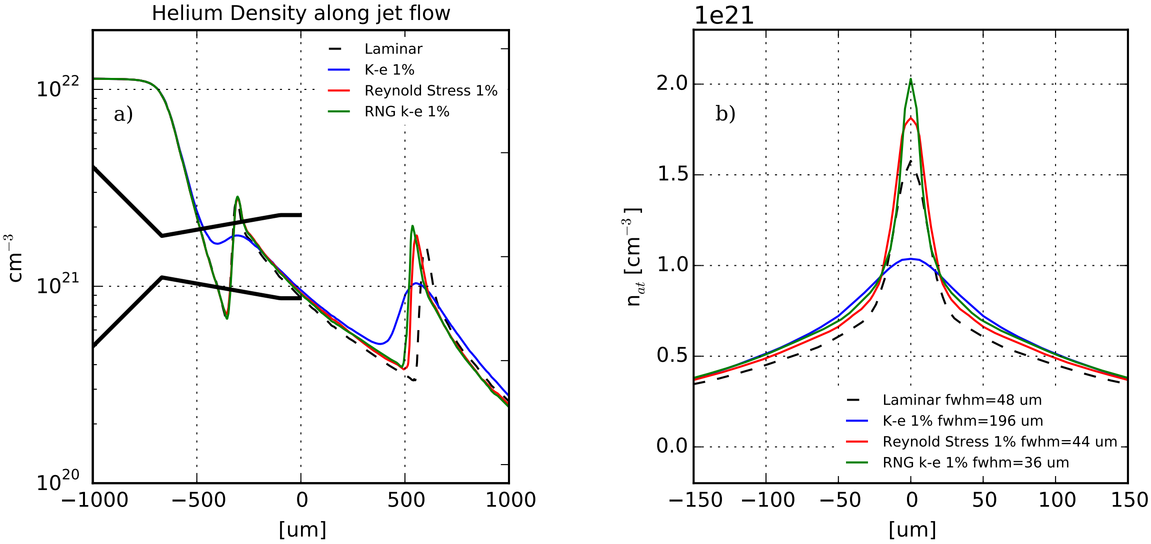

Figure 3.28 – a) Lineout of density along the nozzle axis for Helium with 440 bars, 300 K at the inlet, for various turbulence models. Nozzle profile is drawn with thick black line, gas comes from left to right. The 0 µm position denotes the nozzle exit. b) Transverse lineout at the peak position. Laminar model (dashed line), Standard K-ϵ model with $I = 1\,\%$ (blue), RNG K-ϵ model with $I = 1\,\%$ (green), RANS-RSM model (red)

Turbulence and experimental data

The standard K-ϵ model with $I = 1\,\%$ is closer to the experimental observations (Fig. 3.29). The transverse FWHM is 200 µm, similar to the experimental characterization of 187 µm. Absolute values of density cannot be compared, as the simulation assumes a steady flow, whereas in experimental conditions, the fast opening/closing of the valve allows only transient flow.

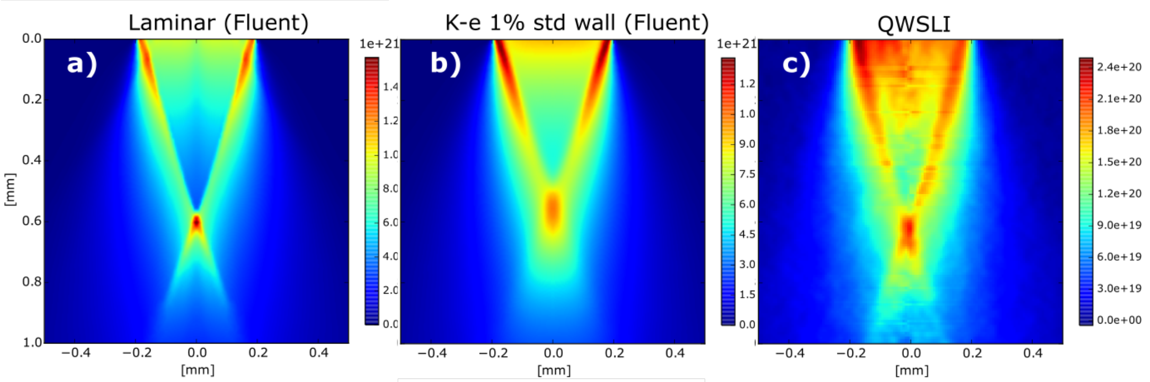

Figure 3.29 – Atomic density maps for helium with 400 bar backing pressure and B20 nozzle geometry (Fig. 3.8). (a) Solution from ANSYS Fluent simulation without turbulence (laminar flow). (b) Solution from ANSYS Fluent simulation with k-ϵ model, standard wall treatment (first layer at $y^+ = 45$), and inlet turbulent kinetic energy of 1 % of total kinetic energy. (c) Characterization by QWSLI of an actual B20 nozzle. It should be noted that the colorbars (in cm^{-3}) do not share the same scale.

Turbulence and boundary layer

Two mesh configurations have been tested in order to account for the turbulence creation near the wall in the boundary layer:

Standard Wall function The first cell near the walls is at $y^+ = 45$ and the CFD simulation uses the log-law as boundary condition, without resolving the viscous layer mentioned above.

Enhanced Wall function The first cell near the walls is at $y^+ = 0.7$ and the mesh resolves the viscous layer. Turbulence and velocity in the viscous and transition layer are described by the 1-D incompressible model of Wolfshtein [Wolfshtein, 1969].

Resolving the viscous layers (blue in Fig. 3.30) do not provide significant modification of the density and Mach profiles.

Improving the shock gradient would require to limit the production of turbulence. CFD simulation enables to monitor the areas of large k production. Fig. 3.31 shows the areas of large k production for Helium with 400 bar backing pressure and B20 nozzle geometry. Most of the turbulence production occurs at the throat and just before, on the diverging walls, and when the flow crosses the oblique shock. The production term in the equation of turbulent kinetic energy is given by [Delarue and Pope, 1997]:

$$P = -\langle\rho\rangle_t \sum_{i,j} \langle u_i' u_j' \rangle_\rho \frac{\partial \langle u_i \rangle_{\rho,t}}{\partial x_j} \qquad (3.53)$$

Where u denotes the velocity, ρ the density, the brackets $\langle\dot{}\rangle_t$ and $\langle\dot{}\rangle_\rho$ denote respectively time averaging and density averaging (sometime called respectively *Reynolds averaging* and *Favre averaging*). u' denotes the turbulent velocity given by $u = \langle u \rangle_t + u'$.

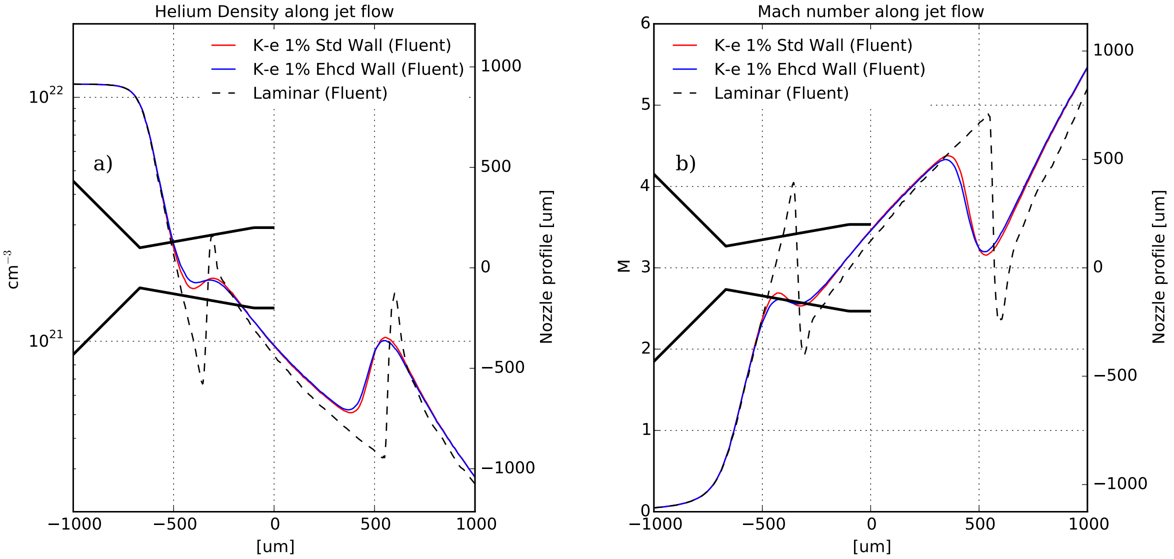

Figure 3.30 – a) Lineout of density along the nozzle axis for Helium with 440 bars, 300 K at the inlet, for various boundary layers models. Nozzle profile is drawn with thick black line, gas comes from left to right. The 0 µm position denotes the nozzle exit. b) Lineout of the Mach number in same conditions. Laminar model (dashed line), Standard Wall function (red), Enhanced Wall function(blue)

Unravelling the complexity of turbulence equations is beyond the scope of this work, but Eq. 3.53 shows that turbulence rises in areas of large density, large mean shear stress and large velocity gradient in general. This typically occurs at the throat, near the walls and across the shock. A path to increase the shock gradient could be to explore nozzle designs that limit production of turbulence energy. For instance by reducing velocity gradients and shear stress, or by moving them in areas of lower density.

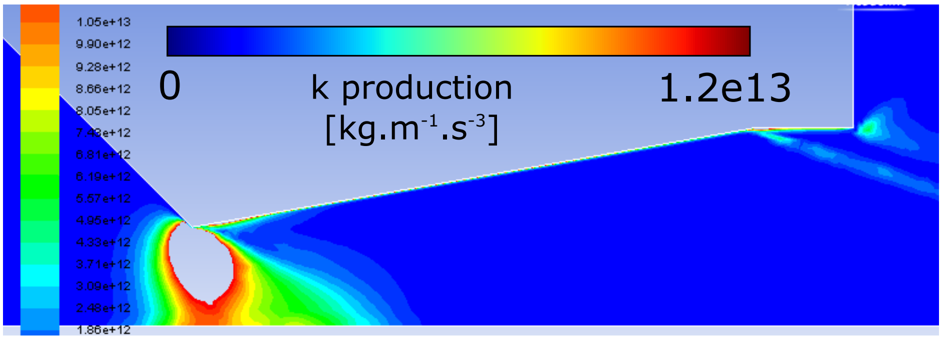

Figure 3.31 – Map of turbulent kinetic energy k production inside a B20 nozzle with helium at 400 bar backing pressure. Computed by CFD simulation using standard k-ϵ model, Enhanced Wall function, and inlet turbulent kinetic energy of 1 % of total kinetic energy. Turbulence is increased at the throat, near the walls and across the shock.

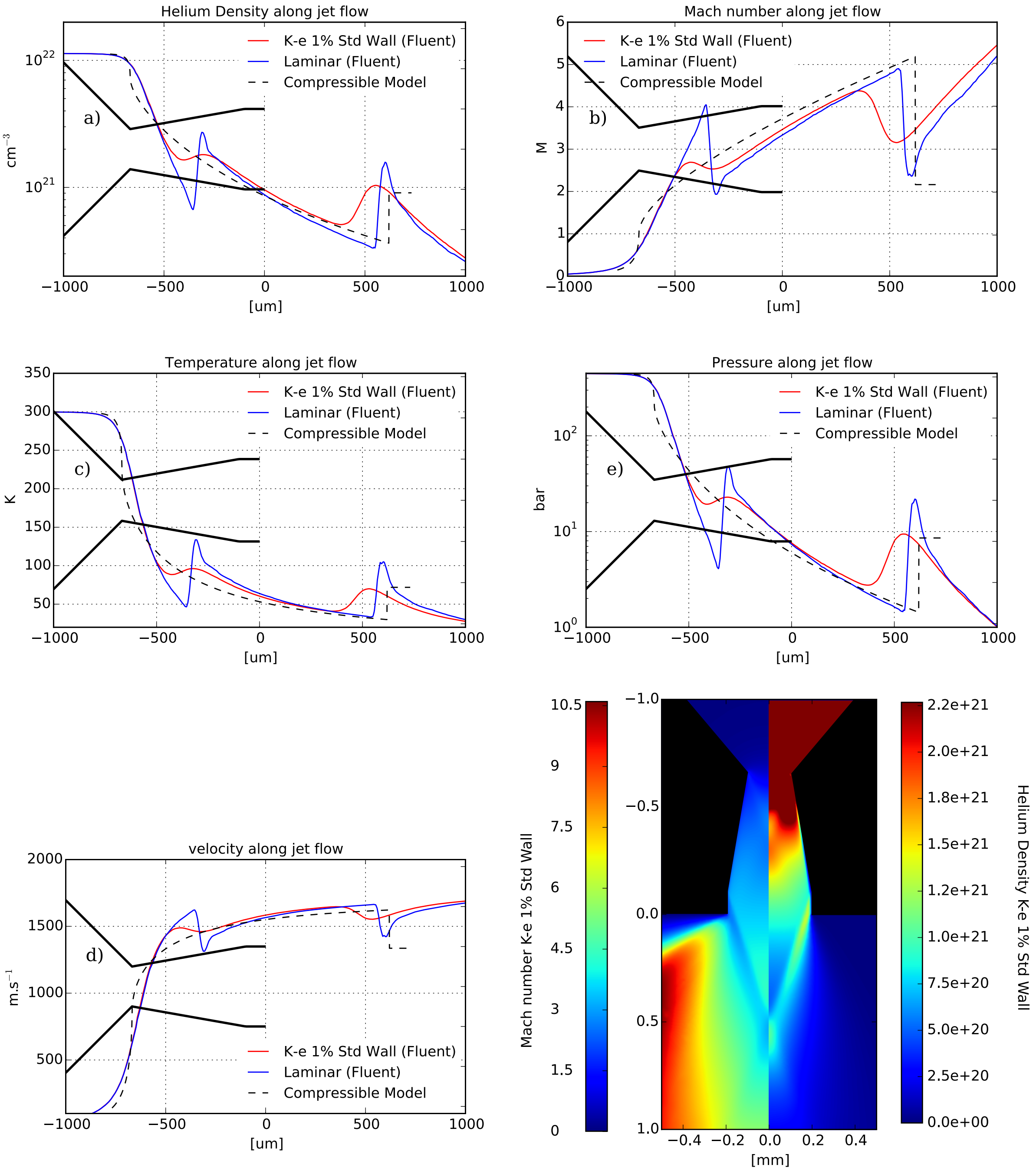

Figure 3.32 – Lineout of thermodynamics variables along the nozzle axis for Helium with 440 bars at the inlet. Nozzle profile is drawn with thick black line, gas come from left to right. The 0 µm position denotes the nozzle exit. Dotted line show the profile derived from the analytic model of supersonic compressible fluid. Solid lines are variables computed by CFD simulation (ANSYS Fluent). Blue: Laminar model. Red: Standard Turbulence k-ϵ model with 1 % of turbulent energy.

3.4 Length of the final straight duct

Modelisation of the oblique shock assumes an upstream flow parallel to the wall. In this configuration, the length of the final straigth part of the duct has no influence over the oblique shock angle. Nonetheless, in the diverging part of the nozzle, the flow is not parallel to the wall over the whole section of the duct, especially if the diverging angle is large. For a diverging angle of 10° (in the B20 geometry see Fig. 3.8), changing the length from 100 µm to 200 µm makes barely any changes in the shock structure, because the flow angle of incidence is almost unchanged over the 200 µm straight part of the duct. But in the case of a strong diverging angle of 59 deg (in the B118 geometry see Fig. 3.8), the assumption of a parallel flow doesn't hold anymore. The flow will form shock line with very low angle for small collar length, and a Mach disk for long collar. Different configurations have been tested by CFD simulations in the laminar case for 300 bar of argon on B118 geometry. Results are shown in Fig. 3.33: a length 225 µm provides an of optimal geometry for both shock position and gradient. For a short collar length, the shock lines are not able to cross, while with a long collar, a shock-disk appears.

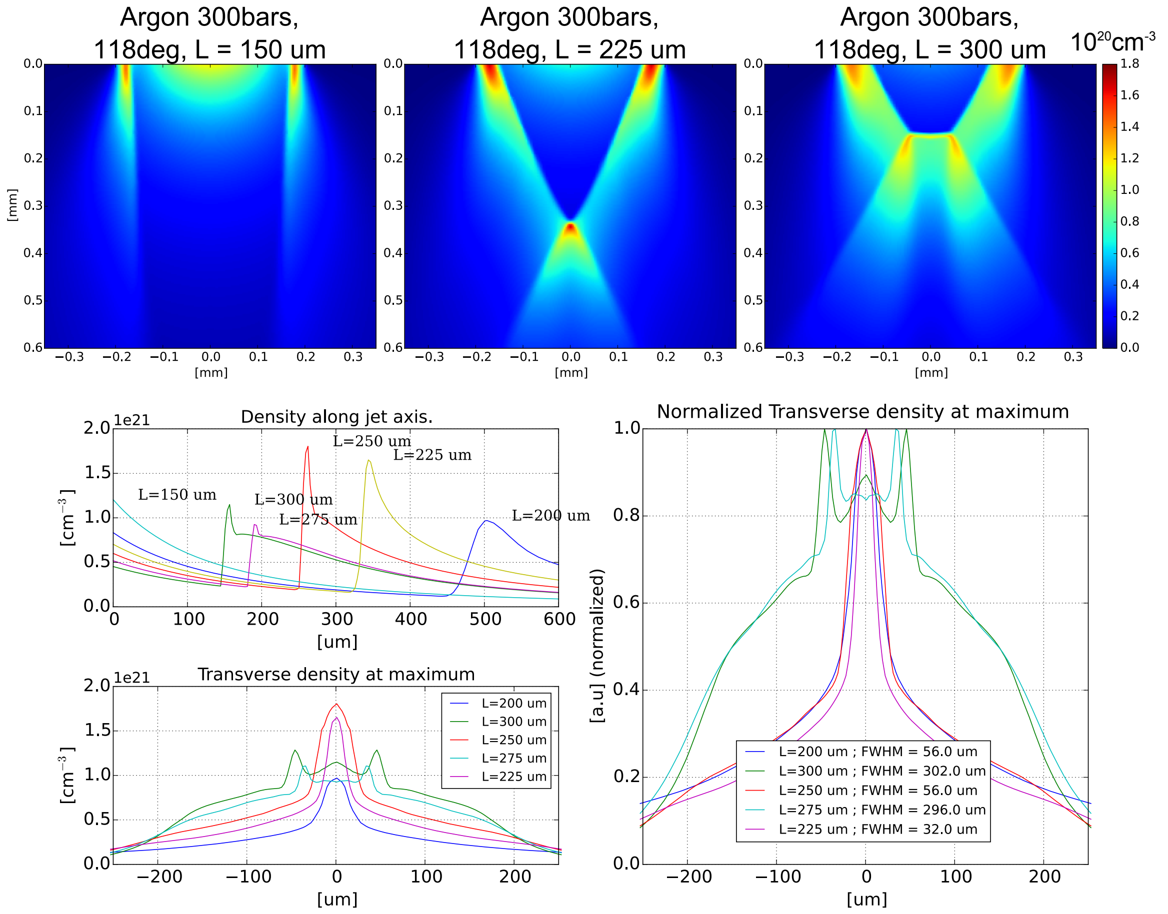

Figure 3.33 – a) b) c) Atomic density map computed in laminar CFD simulation for argon with 300 bar backing pressure and B118 nozzle geometry (Fig. 3.8) for different lengths L of the final straight part of the nozzle. a) $L = 150\,\mu m$, shock lines do not cross. b) $L = 225\,\mu m$ optimal geometry. c) $L = 300\,\mu m$. Mach disk formation. d) Density profile along the nozzle symmetry axis (gas come from the left) for various L. d) Transverse density profile at the peak e) Normalized transverse density profile at the peak.

3.5 Conclusion and Perspective

We demonstrate the possibility to tailor the density profile of a supersonic gas jet by superposition of shock waves, using a compact nozzle design. The shock waves rise from the design of the inner part of the nozzle, rather than from the addition of blade. We demonstrate that the shock line position can be predicted with accuracy for flow with small expansion angle. Our nozzle achieved an atomic density of helium of $3.5 \times 10^{20}\,\text{cm}^{-3}$ ($n_e = 0.4 n_c$) with a peaked density profile of FWHM $120\,\mu m$ at safe distance from the nozzle ($600\,\mu m$). The gradient of $\approx 50\lambda$ is better than conditions explored in other publications [Willingale et al., 2006] featuring TNSA enhanced by magnetic field at the rear side of a gas target. The thickness of the shock is affected by the quality of the nozzle machining, especially its surface quality, and by turbulence. The standard K-ϵ model reproduces well the actual shock gradients and the lower density wings far from the shock. The electrovalve operation still limits the maximum density achievable. With an electrovalve design ensuring proper valve sealing, it would be possible to increase the atomic density up to the critical density. The turbulence production arises at the nozzle throat, where high density and shear flow co-exist. A slowly varying throat could reduce the shearing gradient and its overlap with the high density area, and therefore decrease the turbulence production and the shock gradient.

Chapter 4

Intense laser-plasma interaction at near critical density

Contents

In the third chapter we demonstrated the creation of a supersonic gas targets with density and gradient close to the conditions required for Magnetic Vortex acceleration (MVA) and Collisionless shock acceleration (CSA). Yet the rear gradient is still longer than what has been used in the few experimental and computational MVA demonstrations. CSA had been experimentally demonstrated with laser and targets conditions far from our apparatus, but 2D PIC simulations from chapter II exhibits CSA for our target class, albeit with 3 times more laser energy.

In the first chapter we saw how the laser undergoes relativistic self-focusing (SF) and self-compression (SC) during its propagation into a plasma of near critical density. We show how the laser depletion coincides with the onset of electron acceleration. 2D and quasi 3D poloidal PIC simulations show differences in the depletion region and in the laser evolution. SF, SC and depletion occur at the same rate, but in 2D geometry the laser pulse starts depleting sooner, and collapses in multiple beams, leading to a significant difference in the laser energy deposition area. The plasma channel is severely affected by these instabilities in 2D, and looses its symmetry. Another open question is the actual properties of the hot electrons, and their ability to drive a toroidal magnetic field or to launch a CS.

Experiments presented in this chapter explore these questions by the use of targets of rising complexity. They were performed in the SAPHIR experimental area at LOA and span over 3 experimental campaigns in 2014,2015 and 2016. The first campaign was dedicated to the test of the laser and experimental apparatus in simple conditions. Our team previously explored thick (800 µm fwhm) supersonic gas jets[Sylla et al., 2012a; Kahaly et al., 2016] with a less energetic laser. We used simple sonic jets, with a reduced target thickness (500 µm FWHM), at the cost of smoother gradients. Second we explored the use of an asymmetric target, with a smooth front gradient to ease propagation and a sharp rear gradient to meet MVA conditions. This target was achieved by the mean of a blade inserted in a supersonic flow. Finally we present the laser-plasma interaction with the supersonic shock target described chapter II. Exploration campaign was also performed on supersonic jet in GIST Petawatt Laser (Gwangju, S. Korea) in 2013 and 2016 but results are not mentioned here.

SAPHIR laser underwent a major contrast upgrade in summer 2015. The first section describes, the laser in both contrast configuration (Sonic jet and blade shocks experiments at low contrast, supersonic shock nozzle experiments at high contrast). Then I describe the ion detection diagnostics and plasma diagnostics. The experimental set-up is presented in each case.

Figure 4.1 – 200 TW *SAPHIR* laser system in upgraded contrast configuration in 2016

4.1 Experimental methods

4.1.1 SAPHIR Laser system

SAPHIR laser system is a 200 TW CPA (Chirp-Pulse-Amplification) Ti:Sapphire laser, with central wavelength of 810 nm. Pulse duration is 25 fs, energy before compression is 6 J, leading to an energy on target of 3 J. I will first present the laser used for the sonic jets and blade shock campaigns.

Laser chain in medium contrast configuration

The laser layout in low contrast configuration is shown Fig. 4.2. It is made from a single CPA stage. A saturable absorber improves the contrast down to 1×10^8 10 ps before the main pulse (Fig. 4.5). Laser layout is illustrated Fig. 4.2.

The probe beam is split from the main beam before the last amplification stage by a beam splitter. The probe beam is compressed in a second compressor in air, then travels across a delay line to compensate its path relatively to the main beam. Probe beam reaches 20 mJ per pulse of 30 fs. In the last amplification stage the Ti:Sa crystal is cooled by liquid nitrogen at 100 K in ultra high vacuum. The crystal is pumped by 4 Titan lasers (Nd:YAG flash pumped, doubled at 532 nm, 4 J each at 5 Hz). The pulse reaches 6 J at 5 Hz.

The SAPHIR experimental area is located in a pit near the laser area, separated by a 1 m thick concrete wall ensuring proper radiation protection of the laser area during operation. The laser is transported in vacuum from the last compressor to the pit. Wave front correction is performed by reflection onto a deformable mirror from Imaging Optics with 52 actuators. A leak on a mirror is sent onto an "Haso" Shack-Hartmann camera (made with an array of micro-lenses) from Imaging Optics, imaging the phase front at the deformable mirror position. Aberration due to the imaging line is characterized by propagating back and forth laser diode light filtered into a gaussian

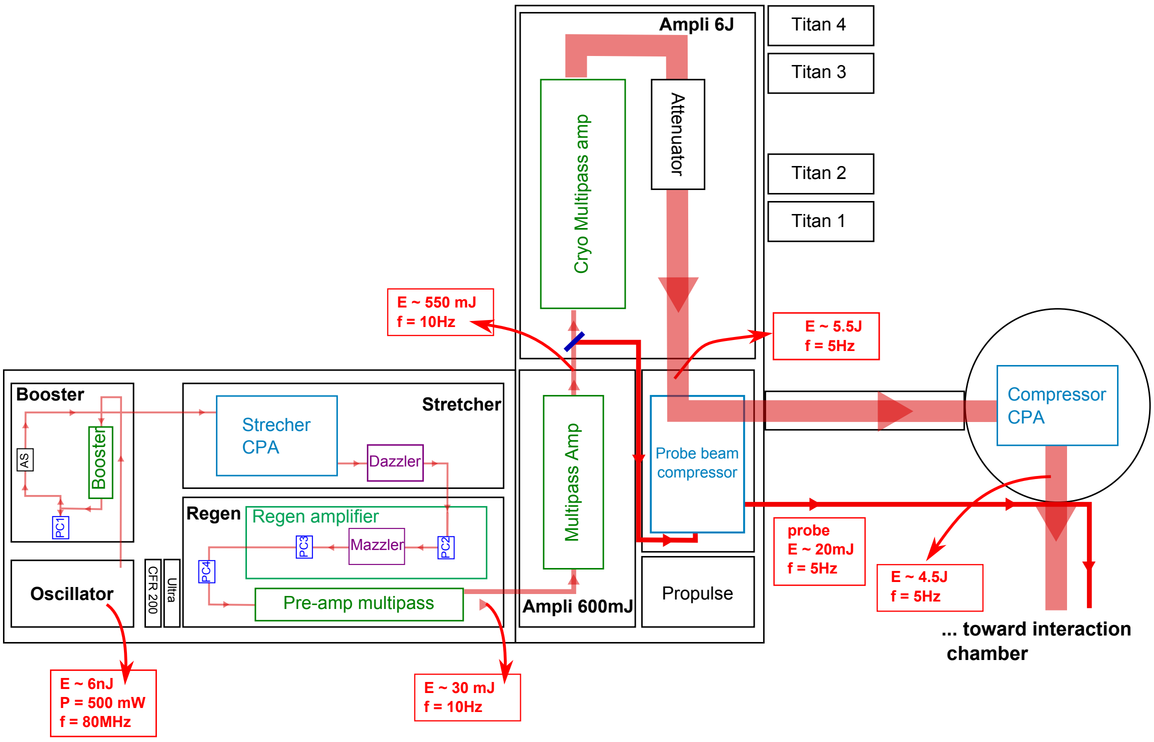

Figure 4.2 – 200 TW *SAPHIR* laser system in summer 2014.

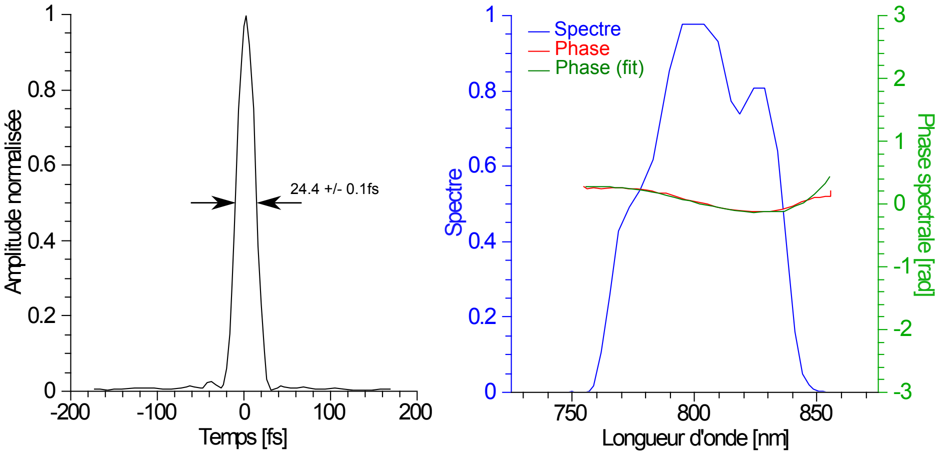

Figure 4.3 – a) Temporal profile of the pulse reconstructed from the laser spectrum and spectral phase shown in b). b) Spectrum and spectral phase of the SAPHIR laser as measured by Self-Referenced Spectral Interferometry (Wizzler from Fastlite). The spectral phase is corrected by a Dazzler placed after the CPA strecher.

mode by a monomode optical fiber.

Main laser beam (flat top, diameter 100 mm) is transported to an Off-Axis Parabola (OAP) with diameter 101 mm, angle 30° and effective focal length (EFL) 326 mm (#f/3.2). Focal spot has a half-width at $1/e^2$ of $w_0 = (4.5 \pm 0.1)\,\mu\mathrm{m}$. 66 % of the energy lays inside the encircled $1/e^2$ level. Resulting in a peak intensity at focus of $I = 1.2 \times 10^{20}\,\mathrm{W \cdot cm^{-2}}$ $(a_0 = 7.4)$.

Laser chain in high contrast configuration

The laser system underwent a major upgrade in Summer 2015 in order to improve its contrast, the quality of the spatial profile and to get rid of pre-pulses (Fig. 4.4). A contrast cleaning device based on cross-polarized wave (XPW) generation is installed into the laser chain. Named "XPW", it uses third order nonlinear properties of BaF2 cubic crystal to improve the temporal contrast of femtosecond laser pulses [Jullien et al., 2005]. This non-linear regime is accessible only at high intensity, therefore a second CPA stage, as well as a pre-amplifier is added to the chain prior to the XPW. A beam stabilization adjusts the compressed beam from the first CPA stage (0.95 mJ, 40 fs) into the XPW fiber. The contrast gain at the end of the chain is in the order of two decades(Fig. 4.5). Other improvements are performed:

- A cleaning Pockel cell (not shown on the scheme) is added after the second regenerative amplifier, cleaning pre-pulses at the nanosecond level.
- Beam diameter is decreased to 80 mm, in order to prevent clipping in the CPA2 compressor.
- CPA2 Compressor chamber is mounted on vibration proof table.
- The probe beam is expended, spatially filtered, and travel in air prior to its compression, improving its spatial quality.
- In order to reduce the laser peak density, we implement an off-axis parabola of 15° angle, with a longer focal length of 508 mm, (#f/6.3). Focal spot has a half-width at $1/e^2$ of $w_0 = (10 \pm 1)\,\mu\text{m}$. 55 % of the energy lays inside the encircled $1/e^2$ level. Peak intensity at focus is $I = 2.4 \times 10^{19}\,\text{W} \cdot \text{cm}^{-2}$ ($a_0 = 3.3$).

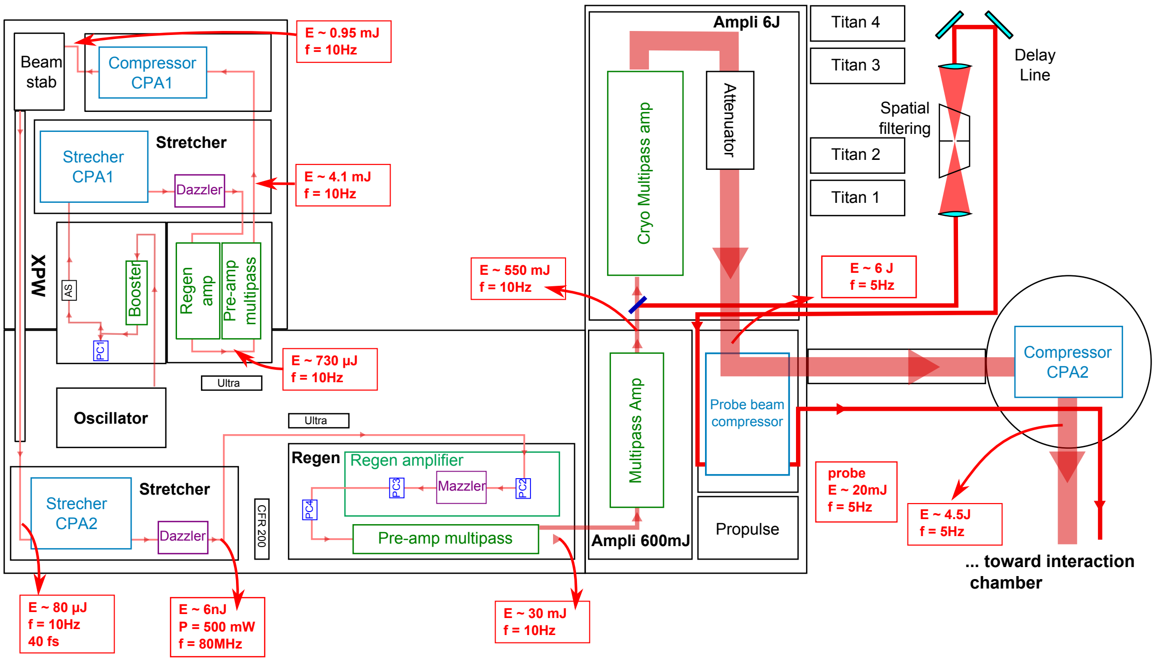

Figure 4.4 – 200 TW *SAPHIR* laser system after XPW upgrade in summer 2016.

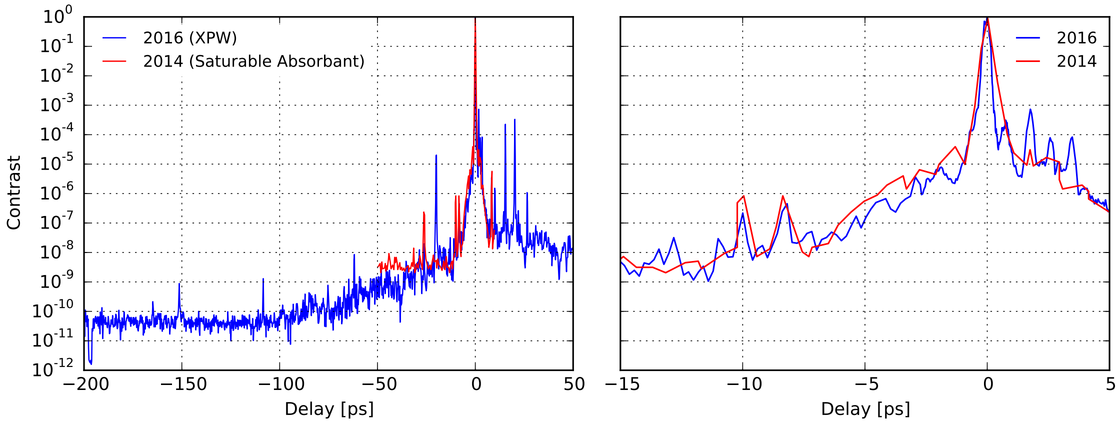

Figure 4.5 – Laser contrast before and after the XPW contrast upgrade. Negative delay denotes laser intensity before the main pulse. The contrast gain is ≈2 order of magnitudes. On the right, contrast at the picosecond range.

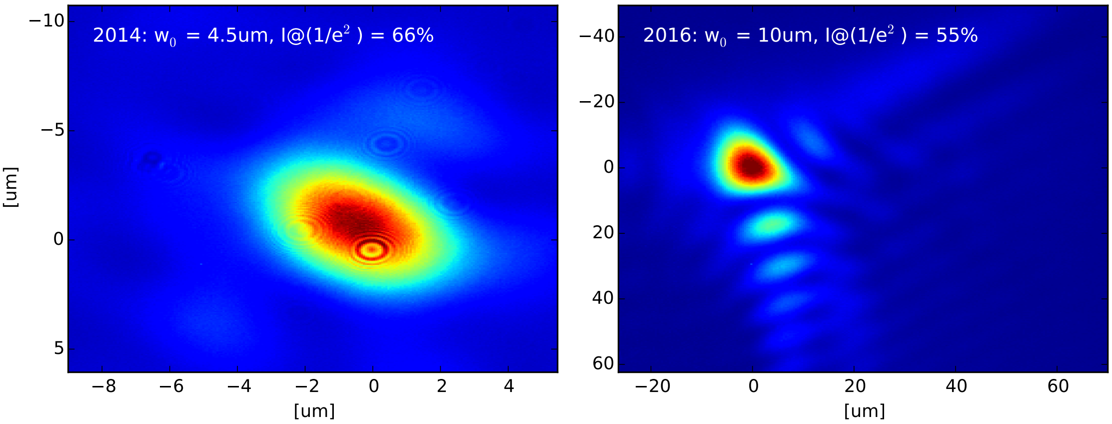

Figure 4.6 – (a) Focal spot for sonic jet and blade shock experiment: $w_0 = (4.5 \pm 0.5)\,\mu\text{m}$ (b) Focal spot for supersonic shock jet nozzle experiment: $w_0 = (10 \pm 1)\,\mu\text{m}$. Scale is different for each figure.

4.1.2 Ion detection method

Several methods can be used to detect energetic ions, each adapted to specific energy range and total charge. The total number of ions accelerated from a gas jet are expected to be in the range of 1×10^8 to 1×10^{10} [Willingale et al., 2006; Haberberger et al., 2012], with energies between 500 keV and 5 MeV. I introduce here the ion detection methods we used.

Radiochromic films

Radiochromic films (RCF) are used in medical dosimetry application, and have good spatial resolution. They need to be taken out of the vacuum chamber and to be scanned for analysis. RCF cannot detect protons below 1 MeV as they are stopped in the first inactive layer. Ions with more energy alter the inner layer, which becomes opaque after analysis. The net change in RCF optical density (OD, red channel) for 5 MeV protons is related with the total dose D in Gray by [Borca et al., 2013]:

$$OD = 9 \times 10^{-4} D^3 - 9 \times 10^{-4} D^3 - 2 \times 10^{-2} D^2 + 1.4 \times 10^{-1} D + 3.9 \times 10^{-3} \tag{4.1}$$

while it is convenient to note that in a RCF the dose in gray can be linked with the proton fluence F and the stopping power (SP) by [Belli et al., 1987]:

$$D/\mathrm{Gy} = 1.6 \times 10^{-10} (F/\mathrm{cm}^2)(SP/\mathrm{MeV} \cdot \mathrm{cm}^2 \cdot \mathrm{g}^{-1}) \tag{4.2}$$

The stopping power is $77\,\mathrm{MeV} \cdot \mathrm{cm}^2 \cdot \mathrm{g}^{-1}$ in the active layer [Borca et al., 2013]. A minimal detection threshold of $OD = 0.1$ leads to a fluence detection threshold of $F > 3 \times 10^7\,\mathrm{cm}^{-2}$. If the RCF is placed at 50 cm from the source, the minimal detected fluence is therfore $\approx 10^{11}$ protons of 5 MeV per steradian. This is the order of magnitude of fluence demonstrated up to now for MVA with kiloJoule lasers ([Willingale et al., 2006] 10^{11} to $10^{13}\,\mathrm{MeV}^{-1} \cdot \mathrm{sr}^{-1}$), whereas the SAPHIR laser deliver 3 J on target . Because of the 1 MeV detection threshold and the high fluence threshold, we didn't use RCF during our experiments.

CR39 plastick nuclear track detector

CR39 are plastic polymer detectors, available as pieces of dimension $50 \times 50 \times 1\mathrm{mm}^3$. Impinging ions create damaged tracks in the CR39 at the 1 µm scale, along the whole ion propagation. A single foil has a detection range of 0.1 to 7 MeV. Ions damage the polymer dominantly at the end of their trajectory, for protons above 7 MeV, the damage on the front surface is too faint to be detected. A solution of NaOH etches the CR39 at a rate depending of the concentration (molarity typically between 3 and 6) and depending of the temperature of the solution (typically 80 °C). The damaged tracks become visible, and by measuring etch pits diameter, it is possible to infer the energy of the impinging particles. Actually, the relation is non reciprocal, so only dynamic of the pits radius during etching can be linked to proton energy [Kanasaki et al., 2013; Fromm et al., 1993]. Nonetheless a CR39 is able to detect single particles tracks, and a counting procedure can give therefore an absolute number of detected particles.

Emission from laser-plasma interaction in gas may include other damaging radiations or particles: energetic electrons, X-ray, non-linear scattering of the laser light. It is important to acknowledge the effect of these irradiations on the CR39 detection ability. Recent work shows the variability of the etching rate after irradiation of CR39 by pulsed 1024 nm laser at $8\,\mathrm{J\cdot cm^{-2}}$ [Saffarini et al., 2012], without mention of the intensity. The effect of high intensity laser on CR39 is still unknown. Irradiation by large X-Ray dose (>200 Gy from ≈1 MeV Cobalt source [Thabayneh and Shoeib, 2016]) has been shown to increase the bulk etch rate, while irradiation by X-Rays from laser plasma interaction sources (γ in 1 to 30 keV range, for dose <30 Gy [Rojas-Herrera et al., 2015]) shows a reduction of the etch rate, and no incidence of photons energy. X-ray has not been shown in both work to increase the track counts. Dose rate emitted from femtosecond laser pulses interacting with gas is well below 1 Gy ([Rousse et al., 2004]). Previous works show that electron irradiation both in the 10 keV range and MeV range [Charvát and Spurný, 1988; Wahl and McLean, 2005] modifies significantly the etch rate, but does not result in extra tracks.

In conclusion, the combined effects of electron and X-Ray irradiation prevents from deriving any reliable relationship between pit diameter and particle kinetic energy. Caution must be taken in interpretation of CR39 pits irradiated directly by intense 100 TW class lasers, as no calibration has so far ruled out laser effects on the track creation, or on the etching process. Nonetheless, CR39 can be used to assess the presence of ions even in low numbers.

Thomson ion mass spectrometer

Thomson spectrometers are made from parallel electric and magnetic fields, perpendicular to the particle trajectories, deviating particle according to their energy, charge and mass. Ions are distributed by their energy along parabola traces given by their charge to mass ratio. Ions are selected at the entrance of the spectrometer by a pinhole, between 100 µm and 500 µm in our experiment. Ions propagating on a z-axis, of charge q, mass m_i, velocity v, experiment acceleration in the E-field direction given by $a_x = qE/m_i$ and in the perpendicular direction by $a_y = qvB/m_i$. Assuming small deviations from the z-axis, the deviation from the balistic direction is given by:

$$\Delta X = \frac{qEL^2}{2m_i v^2} \qquad \Delta Y = \frac{qBL^2}{2m_i v} \tag{4.3}$$

Combining both equations shows the quadratic relationship between ΔX and ΔY: particles from a given species distribute along a parabola given by q/m_i.

$$\Delta X = \Delta Y^2 \frac{q}{m_i} \frac{2E}{L^2 B^2} \tag{4.4}$$

The spot given by the ballistic direction is the combination of neutral and X-ray signal. It gives the origin for the curvilinear coordinate of each parabola.

Particles impact a MicroChannel Plate (MCP) perpendicular to the balistic path. An MCP is an electron multiplier made from a ceramic disk of 40 mm diameter with aspect ratio of 1:60. The disk is pierced with an array of channels of 8 µm diameter and a pitch angle (angle between the MCP surface and the hole axis) of 12°. MCP

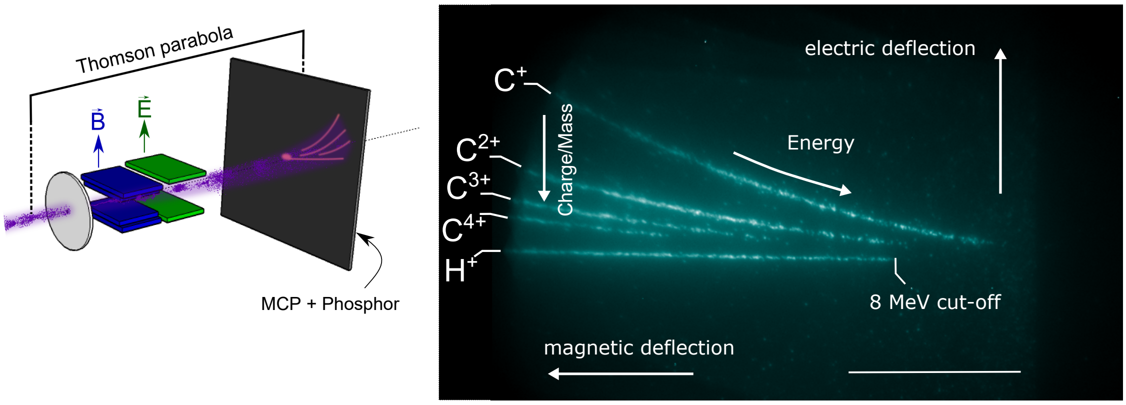

Figure 4.7 – (a) Scheme of the Thomson parabola apparatus. (b) Typical parabola tracks for severals ion species separated by their mass over charge ratio, as visible on the MCP. These tracks were obtained with solid target on SAPHIR in spring 2014, on 6 µm thick aluminium foil.

are also sensitive to ions, UV rays, X-rays and gamma rays. Impinging particles or radiation strike the inner walls of the channels and trigger an electron cascade. We use two stacked MCP in "Chevron" geometry, increasing the secondary electron yields to $\approx 1 \times 10^6$. The electron cascade is driven by high voltage (1.4 kV) applied between each side of the MCP. Electron detection at the rear side of the MCP is achieved by a phosphorus screen (P43), emitting light at 540 nm with a decay time in the few ms scale. Another High voltage (3.5 kV) is applied to the phosphorus screen to prevent secondary electrons from scattering once they exit the MCP. The parabolic traces appearing on the MCP are then imaged by a high dynamic, low noise ICCD camera, electronically cooled (Clara or Istar from Andor). High voltage applied between the components of the MCP reaches $2.8\,\mathrm{kV} \cdot \mathrm{mm}^{-1}$. Theses devices require low background pressure levels insuring isolating condition between electrodes. Otherwise, arcing may damage the MCP. Typical operating conditions are 5×10^{-7} mbar. The pinhole at the entrance of the Thomson parabola enables to create a pressure differential between the TP chamber and the main chamber. Pressure is kept under 5×10^{-5} mbar during gas shots, and no MCP damage occurs in normal operation condition. A picture of one of the TP is shown in Fig. 4.8

A Thomson spectrometer, called also *Thomson parabola* (TP) is a pertinent diagnostic for determination of accelerated species. The transverse properties of the beam are lost and no absolute count can be measured without *ad-hoc* calibration [Prasad et al., 2010], as the phosphorus response can be non-linear at high flux.

Time of Flight spectrometer

A time of flight (ToF) spectrometer measures the time of arrival of particles impinging on a fast MCP. Secondary electrons impact the anode of the MCP and the resulting current is measured by a fast numerical oscilloscope: a Picoscope with 2 GHz sampling rate. Temporal resolution is down to 0.5 ns, and resolution in energy is increased with distance. In our case, the ToF MCP is placed at 1.5 m from the target, a pinhole of

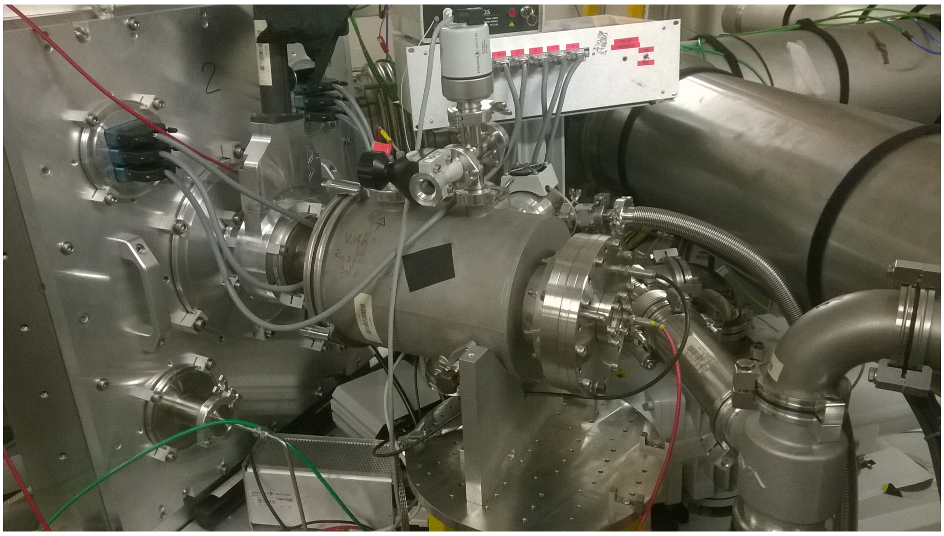

Figure 4.8 – Thomson Parabola. Beam enters the TP vacuum chamber from the gate valve at the left, and phosphorus light exits from the window on the right.

5 mm selects a solid angle of 0.2 sr. The bright flash light produced by the interaction triggers the MCP signal acquisition, and sets the origin of the time axis (soustracting the light propagation time). The contrast between the photon peak signal (which can damage the oscilloscope if not attenuated properly) and the signal at later time results in poor dynamic range for the particles below $1\,\mathrm{MeV}\cdot\mathrm{u}^{-1}$. Strong oscillation of the signal occurs after the photon peak, the ringing amplitude decays with a characteristic time of $\approx 100\,\mathrm{ns}$, perturbing the measure.

Time of flight cannot give information on the transverse properties of the beam. The arrival time is linked to the ratio E_c/A where A is the nucleon number and E_c the kinetic energy. Therefore it is then not possible to discriminate between several ion or atomic species with ToF signal alone. On the other hand, ToF can measure the energy of neutral particles, and the ion(atom) signal is clearly separated in time from electron and photon signals.

Plastic scintillator

BC-404 scintillator is made from a fluorescent emmiter suspended in a vinyltoluene plastic polymer. It is used in numerous applications: calorimeters, time of flight detectors, nuclear gauging and large area contamination monitors. Ionizing radiation and secondary electrons activate this emitter, which has a decay time of 1.8 ns and radiate at 408 nm. They can detect electrons, X-Rays, ions, with light outputs in same order of magnitude for radiation of equal energy. Early work by Becchetti et al. [Becchetti et al., 1976] shows that the light output L is highly non-linear with the ion kinetic energy: scaling as $L = f(Z,A)E^{1.6}$ for $E/A < 15\,\mathrm{MeV}\cdot\mathrm{u}^{-1}$ where A,Z are the nucleon number and the proton number respectively. The light output scales with the depth range of the impinging particle. For 5 MeV protons, the required energy per scintillator photon is 5 keV. Or 1000 photons per 5 MeV protons. [Saraf et al., 1990] confirms this result for He and H ion at energy $< 5\,\mathrm{MeV}\cdot\mathrm{u}^{-1}$, closer to our parameters. At 1 MeV, only 75 photons per proton are expected due to the non-linear scaling.

Experiments and Monte Carlo simulations for electrons in the 1 to 12 MeV range show emission of 2000 photons per MeV loss. [Beaudoin et al., 1986]. In vinyltoluene-based plastic, the total stopping power of electrons in the range 1 to 100 MeV is ≈ $2\,\mathrm{MeV} \cdot \mathrm{cm}^2 \cdot \mathrm{g}^{-1}$. Considering a plastic thickness and density of respectively 5 mm and $1.032\,\mathrm{g} \cdot \mathrm{cm}^{-3}$, it yields 2000 photons per incident electron. Therefore, ion detection requires shielding and deflection of electrons. Considering the light collection efficiency (#f/6, Istar ICCD Quantum efficiency (QE = 20 %) and Istar readout noise, it could be possible to detect single protons and electrons of 5 MeV. Nonetheless significant scattered light in the chamber decreases this sensitivity. Furthemore, low energy protons are stopped within the few first 10s of µm, and this layer can be inactivated if the scintillator is old [Becchetti et al., 1976], preventing fluorescence of low energy protons.

In conclusion, plastic scintillator are valuables for their price and their large size. It gives the possibility to have an in-line diagnostic of the transverse property of the electron and proton beam. The photon yields is roughly linear for a large range of electron energy, but not for ions: plastic scintillator are not suited for quantitative ion spectrometry.

4.1.3 Probe beam

The probe beam is used for target alignment, and for the study of the plasma dynamic. The extreme plasma conditions encountered in these experiments impose strict requirements on the probe beam quality and plasma imaging. First of all, smaller wavelengths are best suited to probe high density plasma, as the critical probe density is higher. Second, the use of a wavelength different from the main pulse enables the use of filtering optics. Coloured-glass filters and interferometric filters isolate the probe light from the diffuse 800 nm light due to the main pulse interaction. The probe beam is then doubled at 400 nm.

Various modifications of the probe beam implementation have been made over the time covered by this work, so we will present the last, and best suited configuration. This is the result of numerous iterative effort:

The probe beam is split from the main beam before the last amplification stage. Its energy is 20 mJ per pulse. Before probe compression, an afocal telescope of magnification unity enables to correct collimation and astigmatism aberrations (monitored with QWSLI phase front measurement with Phasics SID4-HR). Then the beam is transported through a coarse delay line, adjusting the synchronisation with the main pulse on target to the nanosecond level. The long (18 m) propagation in air degrades the intensity profile of the beam, so the beam undergoes spatial filtering in vacuum through a pinhole of 150 µm.

Second Harmonic Generation

After compression down to 30 fs, the probe beam is transported into vacuum to the main chamber. Its energy is 7 mJ into the chamber. It goes through a Beta Barium Borate (BBO) crystal for SHG (Second Harmonic generation), of 200 µm thickness and 10 mm diameter. Thin BBO are preferable, as Group Velocity Dispersion (GVD) and velocity mismatch (between fundamental and harmonic pulse) stretch the impulsion. A pulse of 30 fs at 800 nm is streched to 35 fs by a 200 µm thick BBO [Liu et al., 1994]. We optimized the probe compression in order to maximize the 400 nm output from the BBO. The probe beam is send collimated into the BBO, illumination is $I_{BBO} = 1.2 \times 10^8\,\mathrm{W \cdot cm^{-2}}$, and conversion efficiency in SHG reaches ≈20 %. Residual fondamental at 800 nm is filtered out by dichroic mirrors reflecting only 400 nm. An implementation is shown Fig. 4.9.

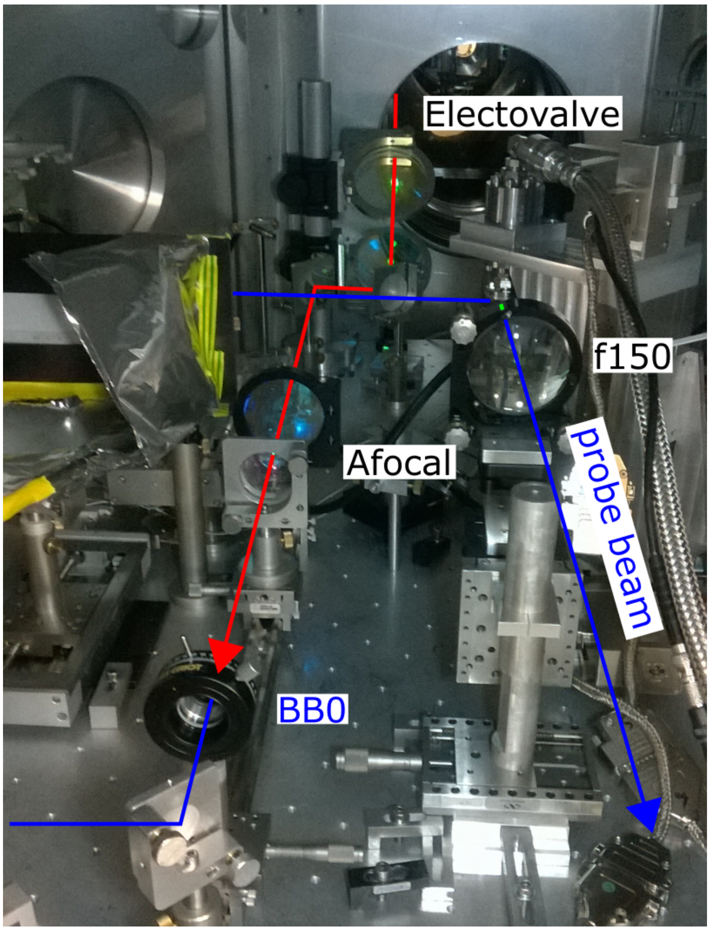

Figure 4.9 – Second Harmonic Generation apparatus, implemented with an afocal telescope here prior to the BBO. The lens imaging the plasma tip is visible on the right, near the electrovalve, oriented downwards.

Imaging and filtering

Synchronisation is adjusted at the femtosecond level by a delay line on precision translation stage. Fine synchronisation with the main pulse is made easy by looking, at low intensity for the main laser, into the gas. Interaction is imaged by an achromatic doublet ($\Phi = 75\,\mathrm{mm}$, $f = 150\,\mathrm{mm}$) ensuring a large numerical aperture ($NA = 0.24$) and a resolution of 1 µm. Imaging magnification is ≈ 9, and the SID4-HR camera (a QImaging Retiga-4000) has pixels of size 7.4 × 7.4 µm, therefore, the imaging is not diffraction limited. Outside the chamber, another dichroic mirror filters out fundamental light at 800 nm (Reflectivity 2.9 %) coming either from the interaction point or from the probe beam, and reflects the 400 nm harmonic (Reflectivity 95.3 %). Further filtering is done with 2 Schott's BG39 coloured glass filter (See curve Fig. 4.10) and an interferometric filter (IF) at 410 µm. Emission visible on sideviews is then 1) second harmonic of the probe beam, or 2) second harmonic from the main laser, potentially harmonic from Raman side-scatter ([Thomas et al., 2007a]Fig.2).

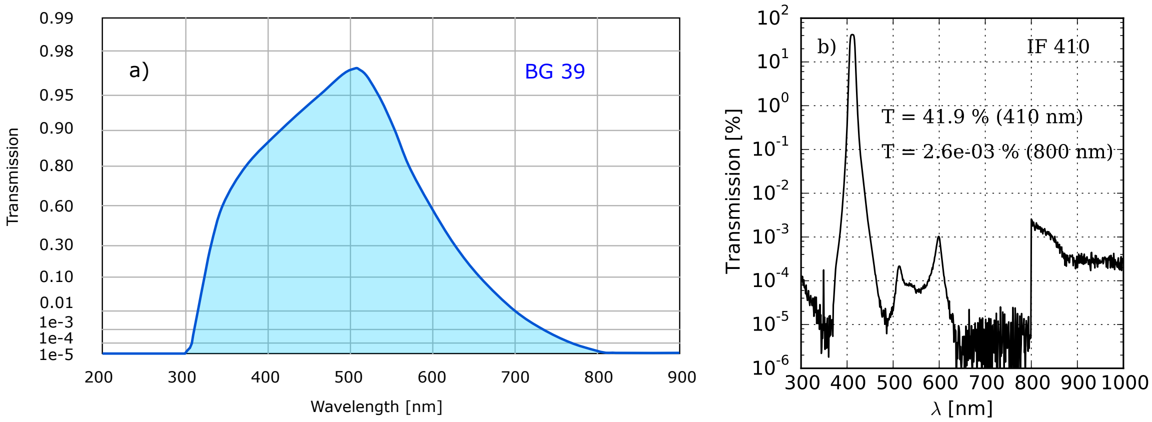

Figure 4.10 – a) Transmission of 1mm thick BG39 coloured-glass filter from Schott b) Transmission from 410 nm interferential filter (IF410), with transmission value at 410 nm and 800 nm. *(data from Thorlabs specifications).* IF410 extinction ratio 400 nm/800 nm is lower than the BG39 one, but IF enables to filter out other broadband light between 400 nm and 800 nm due to electron injection. ([Thomas et al., 2007a]Fig.2c)

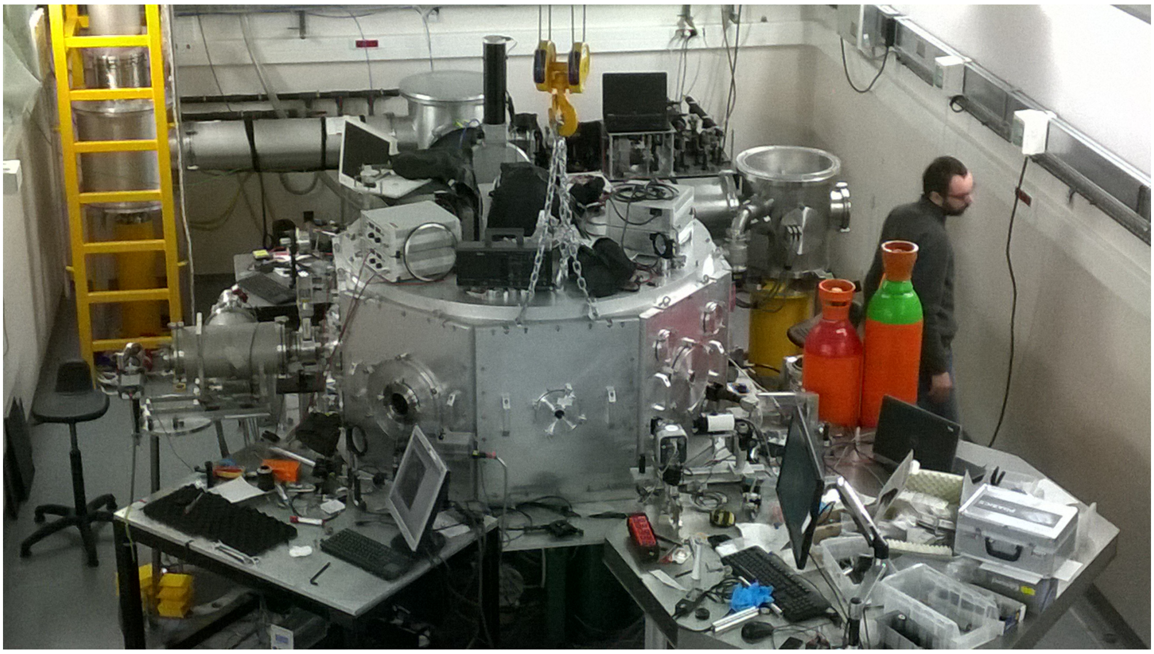

Figure 4.11 – SAPHIR Experimental chamber. The main beam arrives from the tubes beside the chamber. The rightmost turning box host the deformable mirror. A Thomson Parabola is installed on the left side of the chamber. Co-director A. Flacco gives the scale.

4.2 Sonic target

The objective of this campaign is to test the laser system and the diagnostics by using similar targets as Lifschitz and Sylla [Lifschitz et al., 2014; Sylla et al., 2012a], with reduced thickness in order to let the laser propagate to the rear side. Plasma gradients achievable with a sonic jet are not sufficient to trigger shock waves, but this experiment explores the suitability of the diagnostics, and the laser propagation in a rather simple plasma geometry.

4.2.1 Target and apparatus

We installed a sonic jet of 500 µm diameter, and we use two different gases: helium and argon mixtures with 1 % hydrogen. The density map is given in Fig. 4.12. The density decreases with distance z from the nozzle, following a law $n_0/(1+(y/y_0)^2)$ with $n_0 = 1.4\times10^{21}\,\mathrm{cm^{-3}}$ at 200 bar of helium, and $y_0 = 185\,\mu\mathrm{m}$. For argon, the same profile is found, with $n_0 = 8.5\times10^{20}\,\mathrm{cm^{-3}}$ at 300 bar. Relation between the back pressure and the maximum density is linear as shown in Fig. 4.12(d)

Laser is focused on a focal spot of $\omega_0 = 4.5\,\mu\mathrm{m}$, with 66 % of the 3 J on target inside the focal spot (at $1/e^2$ level) by an Off-Axis Parabola (OAP) f/# 3. The peak intensity reaches $I = 2.5\times10^{20}\,\mathrm{W\cdot cm^{-2}}$ ($a_0 = 10$). The laser (25 fs) is focused at 600 µm from the nozzle, where the atomic gas profile has a broad gaussian profile with Full-width Half-Max of 500 µm. The peak atomic density n_{e0} is changed by adjusting the delay between the valve opening and the main pulse arrival. It typically takes values in the range 5×10^{19} to $1\times10^{20}\,\mathrm{cm^{-3}}$. At this laser intensity, helium

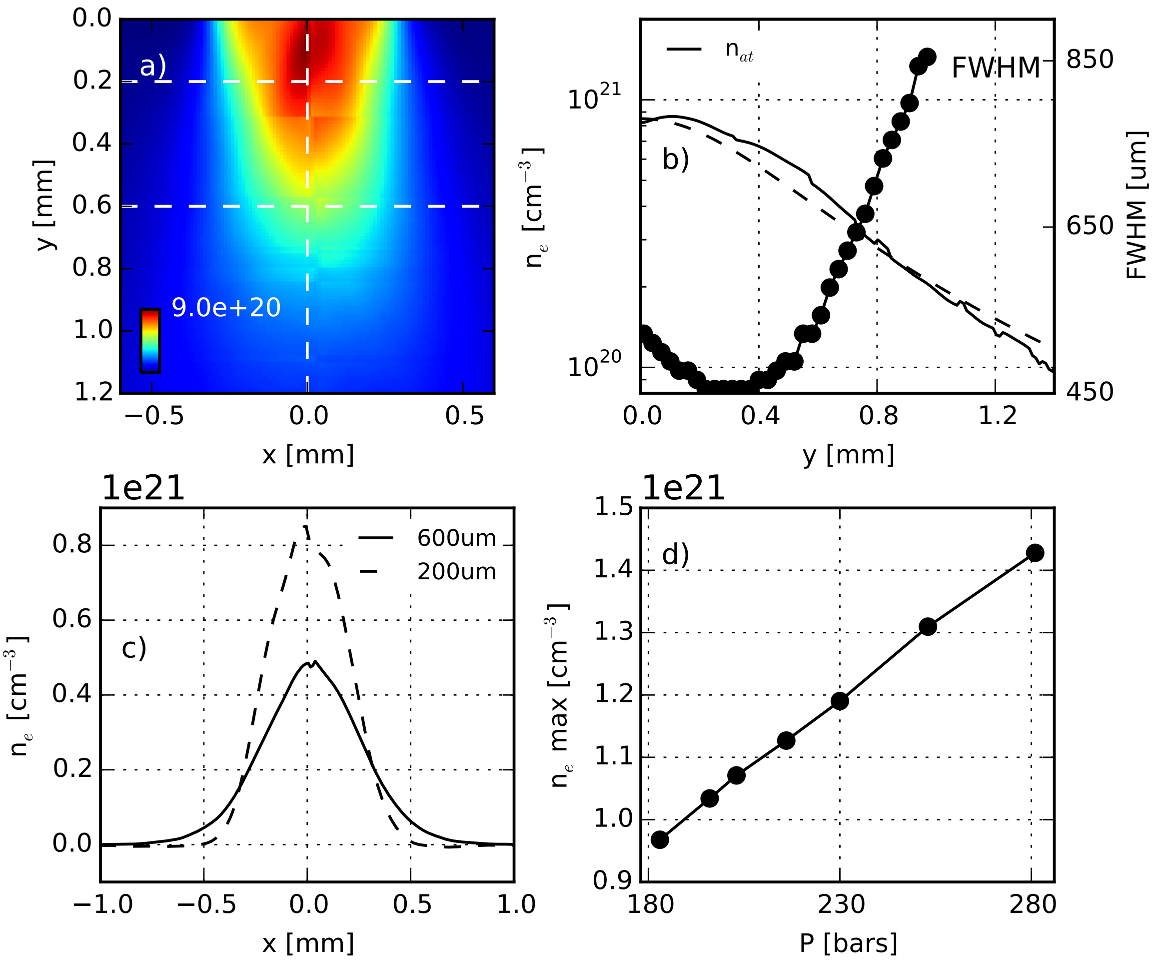

Figure 4.12 – (a) Atomic density map of a sonic gas jet of diameter 500 µm with a backpressure of 180 bar of helium. (gas flows from top to bottom) the vertical dashed line is the lineout in (b), and both dashed horizontal lines are the lineouts in (c). (b) Atomic density profile along the jet axis (solid line) and the fit with $n_{at} = n_0/(1 + (y/y_0)^2)$ (dashed line). Full width half max. (solid line with dots) (c) Lineout of the gas jet along the laser path at two distances from the nozzle tip. (d) Maximum atomic density against backpressure.

is totally ionized (See Chapter I), and $n_{e0} = 1 \times 10^{20}$ to $2 \times 10^{20}\,\mathrm{cm}^{-3}$ (0.06-0.12n_c). Argon in the same conditions is expected to be stripped of 16 electrons, and $n_{e0} = 8 \times 10^{20}$ to $1.6 \times 10^{21}\,\mathrm{cm}^{-3}$ (0.5-1n_c).

We use the following diagnostics:

- QWSLI sideview at 400 nm
- Standard sideview imaging at 400 nm
- Bottom view (Thomson scattering imaging)
- Thomson parabola
- Plastic scintillator BC404

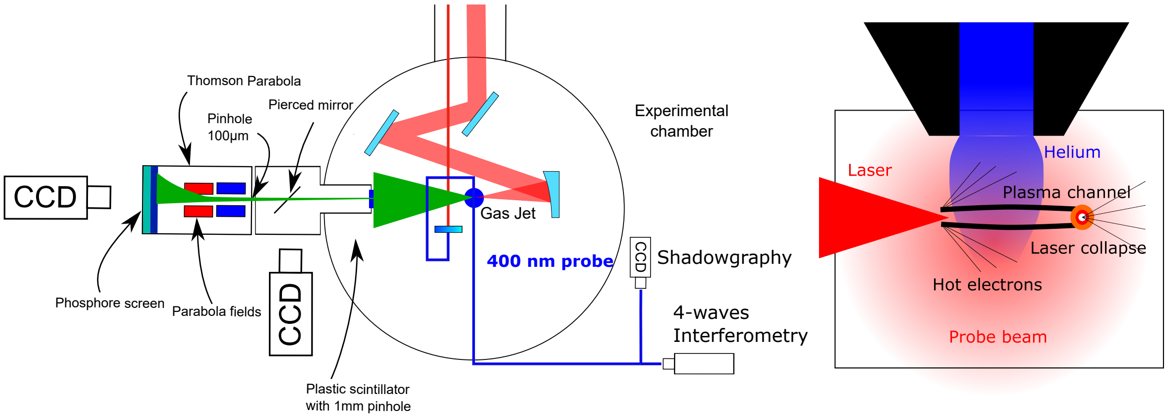

Figure 4.13 – Left: Layout of the experimental chamber for the sonic nozzle campaign. The diagnostics include a Thomson parabola, a plastic scintillator B404, with or without a pinhole of 1mm, protected by Aluminium foil. The scintillator is imaged by a high dynamic range MCP + CCD camera. A magnet and a slit, and CR39s are possibly inserted on the laser axis. The sideviews imaging includes QWSLI and shadowgraphy by a probe beam doubled at 400 nm. Right: Scheme of the apparatus as seen on sideview images. The laser irradiates the sonic gas target from the left. The thick opaque lines are the edge of the plasma channel, which stops where the laser collapse. Hot electrons are ejected from the laser axis and their tracks are visible on shadowgrams.

The Thomson parabola (TP) mass spectrometer aperture is a 200 µm pinhole. Such limited aperture is necessary to 1) ensure correct resolution in the measured spectrums, 2) prevent damages and saturation of the MCP. Any mismatch between the TP alignement, the main beam axis, and the gas target may result in emission outside the acceptance angle of the TP. To ensure collection of the beams over a broad solid angle, we used a combination of a plastic scintillator pierced with a hole in its center and a TP on the forward laser axis. A plastic (BC-404) scintillator disc of 90 mm diameter, 5 mm thick, is placed at 103 mm from the target. A hole of 1 mm is drilled in its center, in order to let the part of the beam on the laser axis to enter into the Thomson parabola. The scintillator is protected from laser light by a 15 µm thick aluminium foil then imaged by a high dynamic 16bits Istar ICCD camera from ANDOR, electronically cooled.

4.2.2 Laser propagation

Helium

Fig. 4.14 shows the plasma channel for different focal positions. The channel extent is compared with the spot size evolution. We have seen in Chapter II that self focusing and self compression rates in PIC simulation are given by [Sprangle et al., 1987] et [Vieira et al., 2010]. In PIC simulations, the spot size bouncing is not observed, and the laser propagates at the matched spot size w_m, given by:

$$w_m = 2\left(0.25P/P_c\right)^{1/6}/k_p \tag{4.5}$$

where P is the laser power, $P_c = 17.3(\omega_0/\omega_p)^2\text{GW}$ is the critical power [Esarey et al., 1996], and k_p the plasma wave-number. Our system delivers $P = 120\,\mathrm{TW}$, at $n_e = 0.01n_c$ and $n_e = 0.1n_c$, w_m is respectively $4.5\,\mu\mathrm{m}$ and $1.8\,\mu\mathrm{m}$. In PIC simulations the laser starts to deplete once it reaches the matched spot size. Here the laser pulse is able to propagate over much greater distance (1 mm). If the focal position is adjusted at the beginning of the jet most of the laser energy is guided, reaching the rear side of the target (Fig. 4.14(middle)). If the focal position is adjusted to the gas center, a part of the laser energy is not guided and the laser ionized the plasma outside the channel (Fig. 4.14(left)). If the focal position is before the jet, the laser collapses before reaching the rear side. After the laser collapse positions, the shadowgram shows a perturbated region caused by laser filaments and hot electrons, present also in PIC simulations. The optical shock position inferred from the Vieira scaling, in agreement with PIC simulation is not related to the position where the laser collapse.

Finally, it is possible to guide the laser across a thick target with peak density of $0.12n_c$. The guided mode is sensitive to laser conditions, and could not be reproduced every day, despite a controlled focal spot.

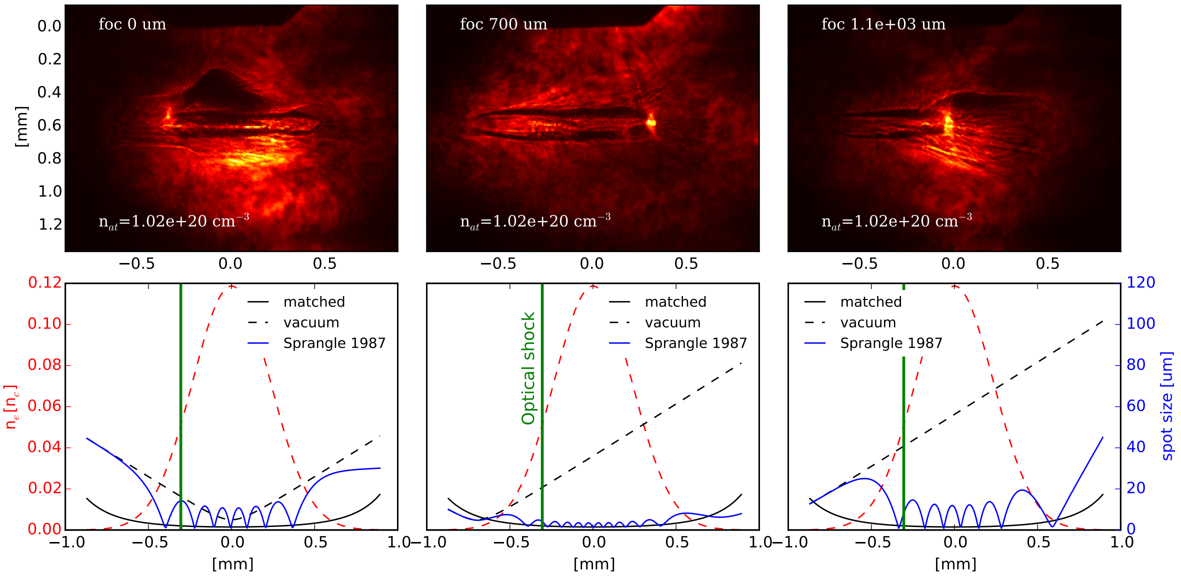

Figure 4.14 – (Top) Plasma channels 8.3 ps after the pulse arrival at different focal positions. Plasma from an helium sonic jet of peak density $1 \times 10^{20}\,\mathrm{cm}^{-3}$ ($0.12n_c$). (Bottom) Initial electronic density (dashed red line, left scale), spot size in vacuum (dashed black line), matched spot size (solid black line), oscillation of the laser spot size due to self-focusing as derived by [Sprangle et al., 1987] (blue line). Onset of the optical shock derived according to [Vieira et al., 2010] (green line)

Argon-Hydrogen mixture

Argon as a background gas is necessary to reach the critical density, but argon ions inertia prevent them to accelerate in phase with a collisionless shock. The addition of light ions has been proposed to act as "test particles" [Sahai et al., 2013] in CSA regimes. Fig. 4.15 shows the laser propagation into near-critical argon plasma ($n_{at} = 5.7 \times 10^{19}\,\mathrm{cm}^{-3}$, $n_{e0} = 0.5n_c$) with 1 % of hydrogen. The laser beam creates a channel comparable to the helium case, but we observe a pre-pulse up to 6 ps before the main pulse. We observe also the propagation of an opaque ionization front, and a large opaque plasma region. An intense light is emitted at the position where the laser collapses. It is likely related to a combination of wave breaking radiation, non linear Thomson scattering, and Raman scattering [Thomas et al., 2007a]. Assuming a total stripping of argon atom ($Z = 18$) leads to a peak plasma density of $n_e = 1 \times 10^{21}\,\mathrm{cm}^{-3}$, well below the critical density for the probe beam $n_{c400nm} = 6.8 \times 10^{21}\,\mathrm{cm}^{-3}$. A part of argon atoms is actually present in cluster form (see discussion at the end of the section) [Hagena, 1981] and clusters are not visible by standard interferometry characterization. The final plasma electronic density is underestimated by a factor 1.5 to 2, but still not above the probe critical density. Imaging aperture cut-off or absorption by the warm plasma may also explain this opacity.

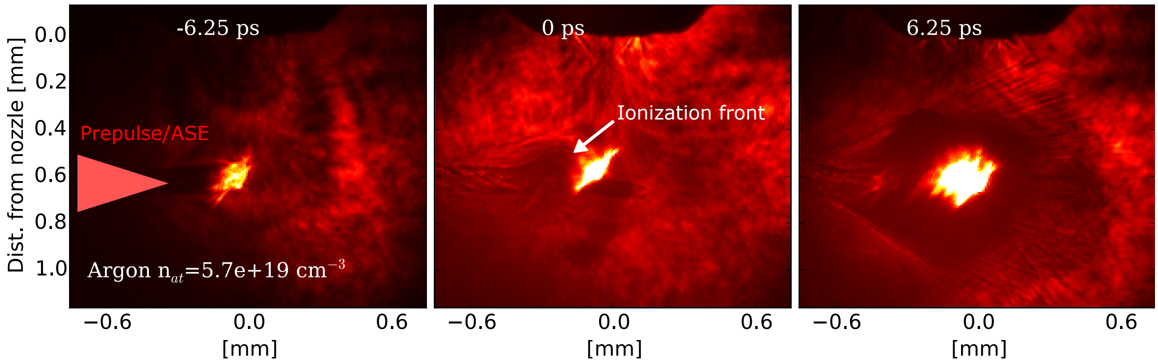

Figure 4.15 – Plasma Shadowgraphy at different delays (-6.25 ps,0 ps,6.25 ps)for near-critical argon plasma ($n_{at} = 5.7 \times 10^{19}\,\mathrm{cm}^{-3}$) irradiated at $I = 2.5 \times 10^{20}\,\mathrm{W \cdot cm}^{-2}$. Nozzle is visible at the top of each picture. Intense scattering blinds the camera at the position where the laser collapses and filaments. Filaments are visible at later time. A plasma is visible picoseconds before the main pulse (first picture), unveiling the presence of unwanted prepulses or ASE, pre-ionizing the target.

Fig. 4.15 shows the plasma evolution in the case of an helium target, the atomic density profile is gaussian with FWHM = 500 µm and peak density $n_{at} = 1.1 \times 10^{20}\,\mathrm{cm}^{-3}$. The laser beam is able to cross the plasma, and the expansion of the plasma channel is clearly visible at later time (200 ps). Large part of the gas is ionized outside of this channel by the wings of the focal spot. Transverse gas gradients explain the asymmetry in the plasma shadowgraphy. Plasma is going inside the nozzle, damaging it. Plasma density is derived by QWSLI and Abel inversion for the first time steps, and shown Fig. 4.16 and Fig. 4.17(a) but resolution is too low to resolve the plasma channel here. Fig. 4.17(b) shows evolution of plasma density, whose profile follows the atomic density profile. Ionization front position and plasma diameter are shown in Fig. 4.17, right graph. Ionization front velocity is $(2.7 \pm 0.1) \times 10^8\,\mathrm{m \cdot s}^{-1}$. Laser group velocity can be more conveniently expressed as: $1 - v_g/c$. In our case the measured confidence range is 0.08 ± 0.02. Group velocity for plane electromagnetic waves in homogeneous plasma is given by $v_g = c\sqrt{(1 - n_e/n_c)}$ where c is the light velocity in vacuum, n_e electronic density, and n_c the critical density. For a plasma with $n_e = 2.2 \times 10^{20}\,\mathrm{cm}^{-3}$, $1 - v_g/c = 0.0669$. A more accurate description of group velocity of a relativistic ultra-short laser at focus is given by Esarey et al. [Esarey et al., 1995], Eq. 4.6:

$$1 - \frac{v_g}{c} = \frac{1}{k_0^2 r_0^2}\left(1 + \frac{k_p^2 r_0^2}{2} - \frac{5}{k_0^2 L^2}\right) \tag{4.6}$$

Where k_0 is the laser wavenumber, L is the pulse length assuming $k_0^2 L^2 >> 1$, r_0 is the minimum spot size of the pulse at focus, assuming $k_0^2 r_0^2 >> 1$, and $k_p = \omega_p/c = k_0\sqrt{n_e/n_c}$ the plasma wavenumber. Correction to the linear case is minor and $1 - v_g/c = 0.0655$. Velocity measurement is then coherent with full ionization of the helium gas.

In the denser case plasma filaments are visible after few ps (Fig. 4.15 at 6.25 ps). They are emitted in the region where the laser enters the plasma, not at the end of the plasma channel. Such behaviour may be due to laser filamentation, or relativistic electrons ejected by the laser fields, ionizing the gas along their paths.

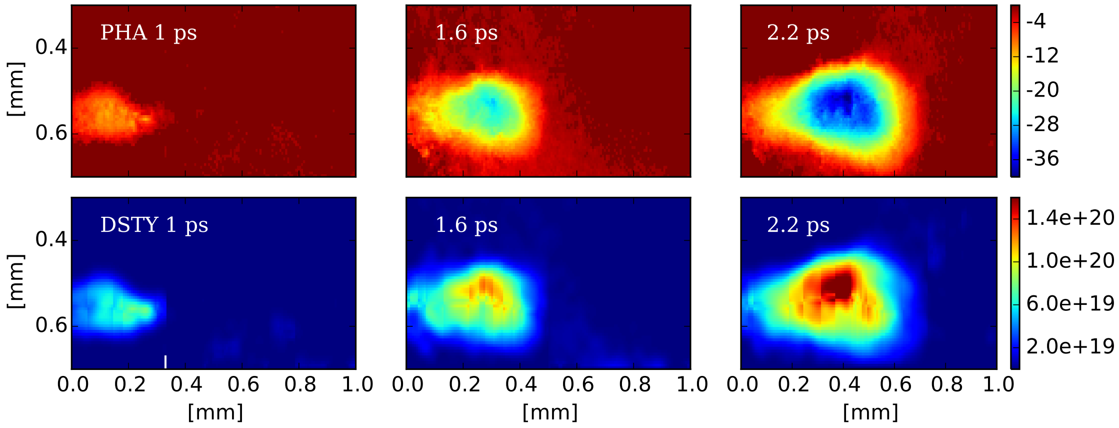

Figure 4.16 – (Top) Phase shift (in radian) measured from QWSLI. (Bottom) Plasma density map (in cm^{-3}) derived from Abel inversion at various delays between the main pulse and the probe beam. $I = 1.2 \times 10^{20}\,\mathrm{W \cdot cm^{-2}}$ and peak electronic density is $2.2 \times 10^{20}\,\mathrm{cm^{-3}}$, in helium.

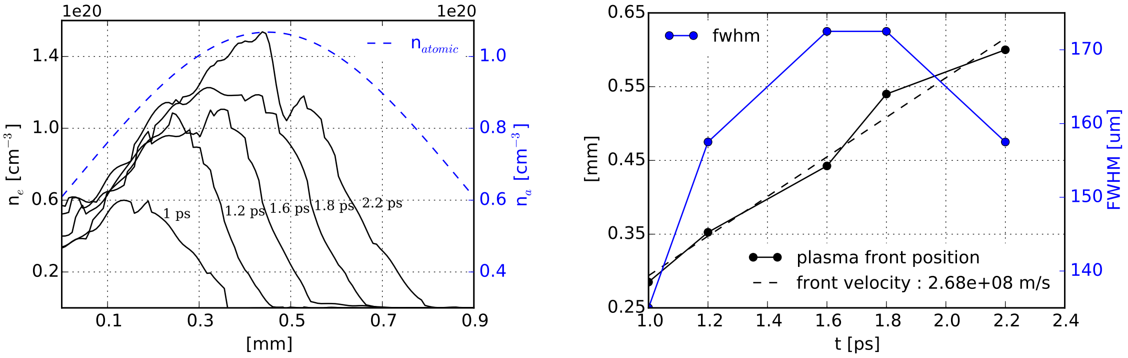

Figure 4.17 – Left) Plasma density longitudinal lineouts (solid lines) derived from QWSLI and Abel inversion at various delays between the main pulse and the probe beam (same as Fig. 4.16). $I = 1.2 \times 10^{20}\,\mathrm{W \cdot cm^{-2}}$ and peak electronic density is $2 \times 10^{20}\,\mathrm{cm^{-3}}$. Atomic density (dashed blue line) before interaction is read on the right scale. Ionization of helium is not complete. Right) Evolution of the transverse size of the plasma (blue line), and evolution of the ionisation front position (solid black line). Ionization front evolves with a constant velocity (fitted in dashed line) of $2.7 \times 10^{8}\,\mathrm{m \cdot s^{-1}}$.

Aperture limitation and shadowgram

Fig. 4.18 shows the shadowgram of a plasma channel from an helium sonic jet of peak density $1 \times 10^{20}\,\mathrm{cm^{-3}}$ $(0.12 n_c)$. The probe beam wavelength is 400 nm, therefore the critical density for the probe beam is $6.9 \times 10^{21}\,\mathrm{cm^{-3}}$. The picture shows that the probe may appear opaque, even in under-dense conditions. We show here that this effect comes from limitations of the imaging aperture. Propagating through the plasma the probe beam experienced a deflection whose angle θ with the propagation axis y is given by:

$$\tan(\theta) = \frac{k_x}{k_y} \qquad = \frac{\partial \mathit{\Phi}}{\partial x} \Big/ \frac{\partial \mathit{\Phi}}{\partial y} = \frac{\lambda}{2\pi} \frac{\partial \mathit{\Phi}}{\partial x} \tag{4.7}$$

where y is the propagation direction of the probe beam, and x the direction normal to y and to the plasma channel, and $\mathit{\Phi}$ the phase of the probe field. The probe phase after the plasma is related to the plasma profile (ignoring the contribution of the neutral gas) by:

$$\mathit{\Phi} = \mathit{\Phi}_0 + \frac{2\pi}{\lambda} \int_{-\infty}^{\infty} (\eta(x,y) - 1) dy \tag{4.8}$$

$$= \mathit{\Phi}_0 + \frac{2\pi}{\lambda} \int_{-\infty}^{\infty} \sqrt{1 - n_e(x,y)/n_c} - 1 dy \tag{4.9}$$

If the imaging numerical aperture is not sufficient to capture such propagation angle, the area appears black on the cameras, as illustrated Fig. 4.18. This example shows in (b, thick black line) a realistic plasma channel profile, with thickness 30 µm, shock compression $n_{shell}/n_{e0} = 2$ and middle density $0.5 n_{e0}$, similar to Chapter II simulation and to experimental references [Osterhoff et al., 2009]. The shaded region appears dark on the imaging due to high plasma gradient deflecting the probe beam.

In conclusion, dark region in the shadowgram should be interpreted in general as an aperture cut-off, and probe diffraction over micrometric size perturbations. In near-critical plasma, shadowgrams can give only qualitative information, given the complexity of the structures observed.

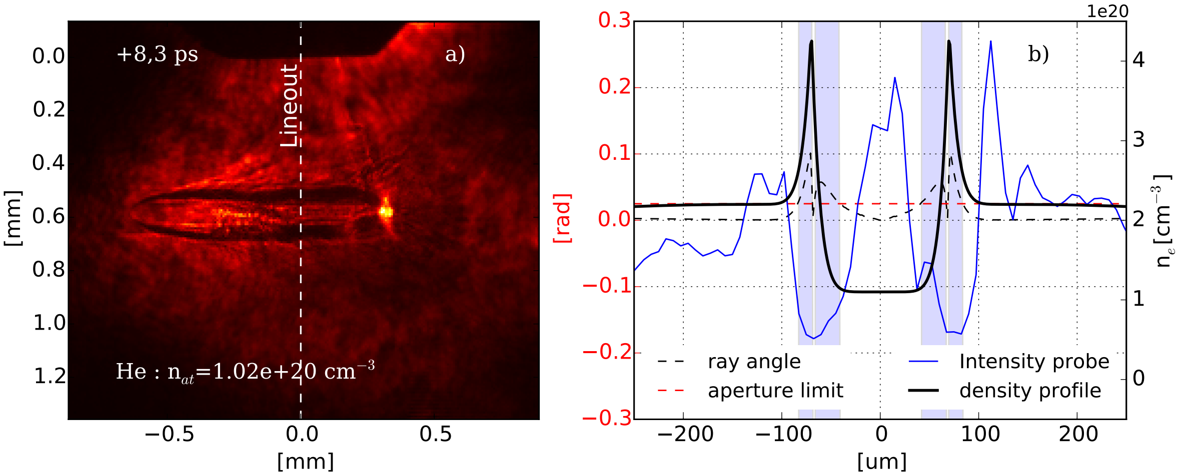

Figure 4.18 – a) Plasma channel 8.3 ps after the pulse arrival in the plasma from the left. Plasma from an helium sonic jet of peak density $1 \times 10^{20}\,\mathrm{cm}^{-3}$ ($0.12 n_c$). The parallel black lines are regions of gradient sufficient to deflect the probe beam from the collection angle of the imaging lens. Lineout of the probe intensity (dashed line in (a)) is shown in (b) (blue line). (b) black line: proposed channel density profile whose proportions are derived from Chapter II simulations and [Osterhoff et al., 2009]. Dashed red line: collection angle limit of the imaging lens. Dashed black line: deflection angle induced by the proposed density profile. Shaded region: area where the imaging aperture limits the probe transmission.

4.2.3 Scintillator detection

In first place, a grill is placed in front of the scintillator to ensure that the signal is coming from a source inside the gas jet, and is not a reflection from the thomson parabola's MCP, or light coming from somewhere else in the chamber. The laser pulse is focused on a gas target made from a mixture of argon and 1 % hydrogen, expelled by a sonic nozzle of diameter 300 µm. The gas has a peak atomic density of $8.7 \times 10^{19}\,\mathrm{cm}^{-3}$, and a FWHM of 500 µm. We observe an ionizing radiation coming from the jet within a solid angle bigger than the 0.52 sr collected by the scintillator (see Fig.4.19(a). A magnet of length 50 mm and of field 0.28 T is inserted in the laser axis, between the scintillator and the gas jet. The limits of the energy detection due to magnetic deflection is 4.3 MeV for electron, and 20 keV for proton. But the protecting 15 µm thick aluminium foil scatters electrons below 40 keV and protons below 1 MeV, according to projected range in aluminium from NIST database ESTAR, PASTAR and ASTAR [Berger et al., 2005]. Therefore this configuration was most suited to measure electronic spectrum. We observe a deflection of the signal towards the negative charge direction (Fig.4.19(b)). Spectrum lineout is given Fig.4.19(c) in $\mathrm{MeV}^{-1} \cdot \mathrm{sr}^{-1}$ after taking into account the background signal. The spectrum presents two distinct temperatures: at 1.2 MeV and 5.6 MeV . In this set-up, resolution is limited by the transverse magnet airgap aperture of 0.35 rad, and the collection of electrons is limited by the vertical aperture of 0.1 rad. As the full angular extension of the electron beam is not captured by the magnet aperture, and considering that slower electrons have bigger divergence, it leads to an underestimation of the number of low energy electrons.

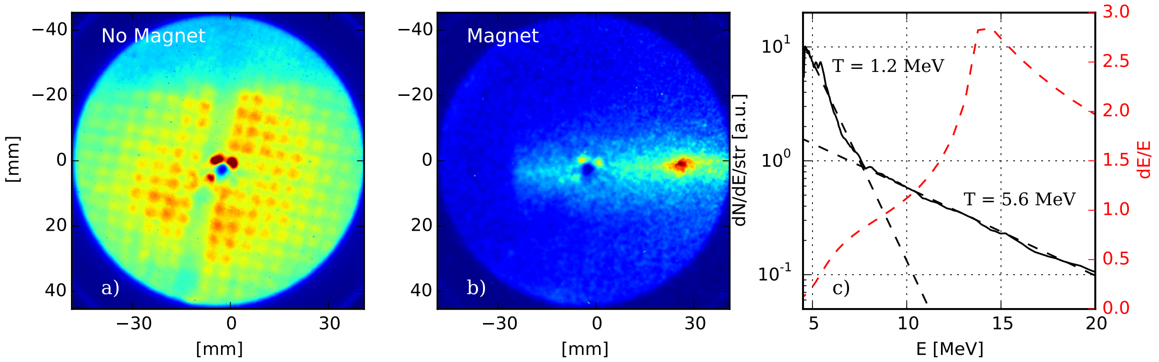

Figure 4.19 – (a)Scintillator image of electron beam produced by the laser impinging on a target of Ar/H(1 %) gas, with atomic density $8.7 \times 10^{19}\,\mathrm{cm}^{-3}$ and FWHM of 500 µm. Electronic density of $50\,\% n_c$. A grill is inserted to ensure that the signal comes from the target. Half-angle of collection: 0.41 rad. Center of the camera is damaged.(b) Insertion of a magnet, deflecting electrons, selecting emission inside a vertical half-angle of 0.1 rad (c) Spectrum derived from image (b), in arbitrary unit proportional to particles per MeV per steradian. Detection range of the set-up is 5 to 20 MeV. Right scale in red shows error ratio on energy determination, limited by the absence of pinhole or slit.

A vertical slit of 0.5 mm is installed to improve spectrum resolution. Results are given in Fig.4.20a-c) for peak atomic density of $1.1 \times 10^{20}\,\mathrm{cm}^{-3}$ in Ar/H(1 %). Spectrum in Fig.4.20d) shows similar electronic spectrum than at $8.7 \times 10^{19}\,\mathrm{cm}^{-3}$.

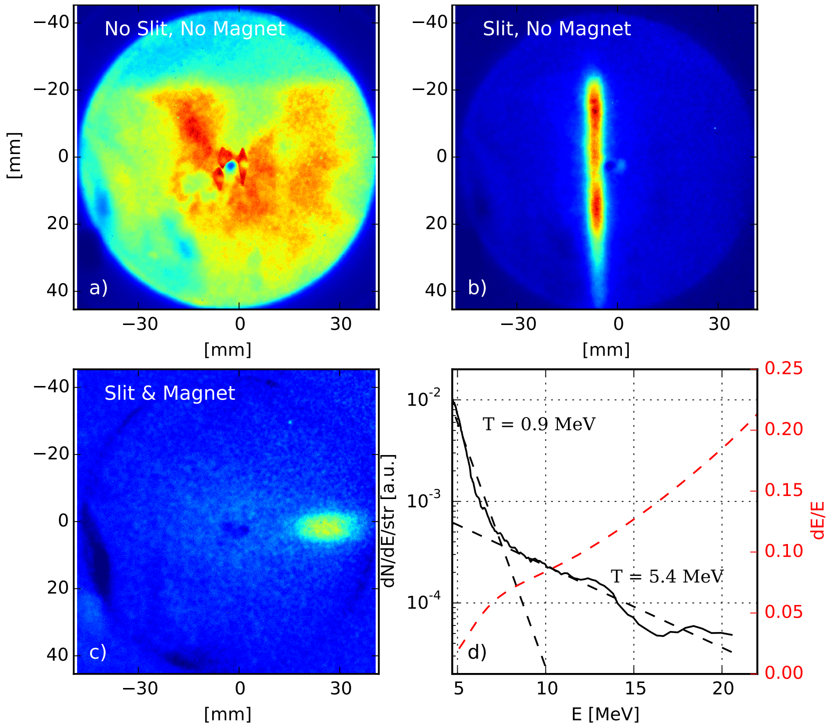

Figure 4.20 – (a) Scintillator image of electron beam produced by the laser impinging on a target of Ar/H(1 %) gas, with atomic density $1.1 \times 10^{20}\,\mathrm{cm}^{-3}$ and FWHM of 500 µm. Electronic density of 65 %n_c. Half-angle of collection: 0.41 rad. Center of the camera is damaged. (b) Insertion of a vertical slit of 0.5 mm. Cut-off signal at the top of the image is due to the nozzle apparatus. The signal FWHM is included in a cone of half-angle 0.33 rad (c) Insertion of a magnet, deflecting electrons, selecting emission inside a vertical half-angle of 0.1 rad (d) Spectrum derived from Fig 4.20b), in arbitrary unit proportional to particles per MeV per steradian. Detection range of the set-up is 5 to 20 MeV. Spectrum structure is similar to the case with less gas (50 %n_c) and no slit. Right scale in red shows error ratio on energy determination.

4.2.4 Accelerated protons

The geometry and field of the set-up is modified in order to improve proton detection limit on the scintillator. Aluminum foil thickness is reduced to 10 µm, scattering protons above 750 keV. The scintillator is moved further away from the magnet, at 11 mm and magnet strength is increased at 0.55 T. 750 keV protons should impact the scintillator 20 mm from the axis, within an error due to the slit aperture of 15 %. In this configuration, we use sonic target of diameter 300 µm, expelling Ar/H(1 %) gas with atomic density ranging from 2.5×10^{19} to $1.1 \times 10^{20}\,\mathrm{cm}^{-3}$ (≈20 to 64 %n_c once ionized). Gas profile is gaussian with a full width half max of 500 µm. No clear positive ion signal is detected in those conditions. Thomson parabola spectrometer detection limit is 300 keV, and protective Aluminium foil is pierced at the scintillator center, in order to let ions on the axis travel to the MCP. No ion signal could be detected on the TP.

In order to have definite confirmation on the presence or not of protons, we install CR39 plastic detectors at 30 mm from the target, covering any angle from 0° (forward direction, on axis) to 90°(transverse direction). We protect them with an Al foil 10 µm thick, in order to prevent damage from the laser, that may be mistaken for ion impacts. We performed a series of 60 shots in 3 conditions (20 shots each): atomic density $3.4 \times 10^{19}\,\mathrm{cm}^{-3}$ and normal contrast, argon mixture atomic density $2.5 \times 10^{19}\,\mathrm{cm}^{-3}$, normal contrast and degraded contrast. The contrast was degraded by removing the saturable absorber present in the CPA laser chain, reducing the contrast to $\approx 1 \times 10^6$ 10 ps before the pulse, resulting in large pre-ionized plasma channels. We observed damages on the CR39 in the forward direction, on the axis (see Fig. 4.21). An area of $(38 \pm 1)\,\mathrm{mm}^2$ revealed, after etching, etch pits absent from other area of the CR39.

Etching was performed once, with a solution of NaOH of Molarity 9.8 (250 g diluted in 750 mL of water) for 3 h at 85 °C.

The various inclinations of some pits relatively to the normal (see Fig. 4.21c) enforce the hypothesis of damages initially done by scattered particles. Laser light is blocked by the aluminium foil, which was intact after irradiation. In conclusion, it is unlikely that these etch pits come from electron or X-ray damages. The aluminium foil prevents laser and protons below 750 keV to create tracks in the CR39.

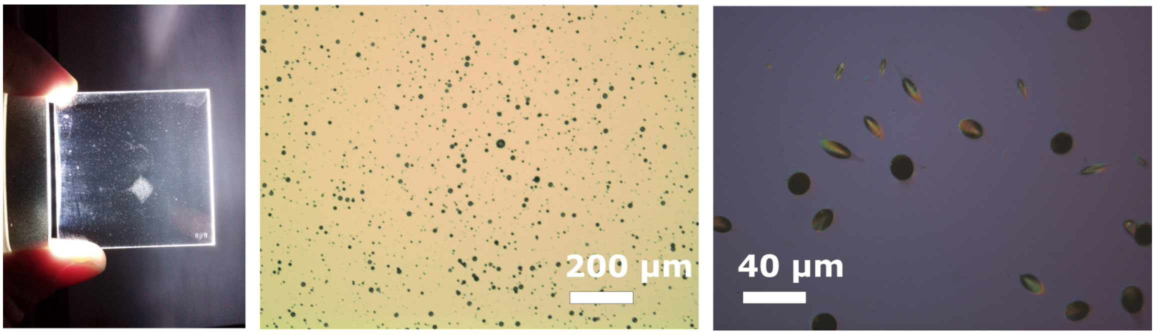

Figure 4.21 – (a) Impact area on CR39 (b) Optical Microscope image at ×10 magnification, showing spatial and size distribution of etch pits after CR39 etching. c) Close view of etch pits. The varied angle of incidence of protons scattered by the aluminium foil can explain the angle of proton tracks inside the CR39. These tracks are etched into pits conserving the same angle. Bigger pits have a radius of ≈ 10 µm.

From a picture at ×10 magnification (Fig. 4.21b) we count 680 ± 10 pits per mm^2, so a total of 2.6×10^4 pits, or $6.2 \times 10^5\,\mathrm{sr}^{-1}$ over a maximum of 60 shots. This is order of magnitudes below what as been measured from other experiments of laser accelerated ions in gas (protons $> 1 \times 10^{10}\,\mathrm{sr}^{-1}$ [Palmer et al., 2011], Helium ions $> 1 \times 10^{12}\,\mathrm{sr}^{-1}$ [Willingale et al., 2006]). It should be noted that Hydrogen is only a test particle in our experiment, with a density of $2.5 \times 10^{17}\,\mathrm{cm}^{-3}$, 100 and 1000 times less than in Willingale's work and Palmer's work respectively. Despite numerous reproduction of the various conditions tested, we couldn't reproduce this result on CR39. We stay critic relatively to its interpretation.

4.2.5 Ionization degrees and argon clusters

Argon is used to reach near-critical conditions, unachievable with helium alone. Argon atoms are too heavy to be in phase with a plasma shock wave during a sufficient time to gain momentum. Lighter ions, like protons or helium, may be reflected by shock waves and gain momentum. The protons in the plasma act as test particles. Plasma density profiles of argon gas targets are less controllable for two reasons. First, ionization degree of argon atoms is not homogeneous along the transverse direction: the plasma density is higher at the center of the pulse, and the pulse experiences a defocusing effect. In our nozzle, argon gas isentropic expansion results in the crossing of the surface vapor pressure line, in the *p*-*T* graph. Gas continues to follow the isentropic line and becomes *supersaturated*, until sufficient collisions results in clusterization. The gas return then to the surface vapor line condition. The kinetics of nucleation growth, especially combined with time dependency of the gas expansion, are poorly described, and give only rough estimations. Scaling laws derived by Hagena et al. [Hagena, 1981] give such estimation of the cluster size and mass produced by supersonic jets, Hagena's dimensionless parameter is given by:

$$\Lambda^* = k_h \left(\frac{0.74d}{\tan\alpha}\right)^{0.85} P_0 T_0^{-2.29} \tag{4.10}$$

Where d is the nozzle throat diameter, $k_h = 1650$ for argon, P_0, T_0 are initial pressure and temperature in the gas reservoir, and α the nozzle expanding half-angle. The number of atoms per cluster $< N >$ is then given by (the corrected expression):

$$< N >= 100 \left(\frac{\Lambda^*}{1000}\right)^{1.8} \tag{4.11}$$

Parameter β is the *dryness parameter*: the mass fraction in the gas phase. For supersonic nozzles with duct half-angle of 10°, Hagena's formulas and tables give:

$$\Lambda^* = 3.2 \times 10^5 \qquad < N > = 3.2 \times 10^6 \qquad 0.65 < \beta < 0.90 \tag{4.12}$$

Gas expansion in the vacuum leaving a sonic nozzle (straight duct), may be supersonic too if the exit velocity reaches $M = 1$, as explained by Hagena [Hagena, 1981]. Finally,the β value show that between 10 and 40 % of the argon mass is initially clustered, and is not measured by interferometry characterisation.

4.3 Blade shock target

4.3.1 Motivation

Sharp gradients made from hydrodynamic shock have been used recently with succes in the field of electrons accelerated by laser [Thaury et al., 2015b; Schmid et al., 2010]. A sharp down-gradient is tailored into the plasma, resulting in brutal modification of the wakefield. The non-linear wakefield bubble expands and electrons are injected into the accelerating part of the wakefield. Shock lines are made by insertion of a blade into a supersonic jet: from the modification of the direction of a supersonic flow rises an oblique shock described chapter II. Blade shocks are interesting also for the asymmetry of the gas profile. It is then possible to design a profile with a low gradient up-ramp, preserving the laser from filamenting before the density peak. By carefully adjusting the laser focalisation position, we expect to deposit the laser energy in the down-ramp, triggering a plasma shock wave. We expect also TNSA-like acceleration of protons in the down-ramp [Willingale et al., 2006].

4.3.2 Gas density

The supersonic jet is provided by a Laval nozzle of throat diameter 200 µm and exit diameter 400 µm, supplied with argon/hydrogen mixture (10 % hydrogen) at 300 bar. Exit Mach number is expected to reach $M \approx 4$. The blade is a 300 µm thin silicium shard, whose position relatively to the jet is adjustable in both vertical and longitudinal direction. Width of the shock in [Schmid et al., 2010] was as sharp as 5 µm. Reference work from Mott-Smith [Mott-Smith, 1951] derived shock thickness from kinetic theory and relates it to the molecular mean free path l before the shock:

$$X = 4 * l/B \tag{4.13}$$

with:

$$l = \frac{1}{\sqrt{2}\pi \rho d_m^2} \tag{4.14}$$

Where d_m is the molecular diameter (Argon: $d_m = 0.4\,\mathrm{nm}$, Helium: $d_m = 0.2\,\mathrm{nm}$). B is a parameter dependant from the Mach-number and from the heat capacity ratio γ. For $\gamma = 5/3$ and $M = 5$, Mott-Smith gives $B = 2.1$ and it comes $X = 18\,\mathrm{nm}$ for argon and $X = 5\,\mathrm{nm}$ for helium.

In our case, the shock width is below 100 µm, which is an upper limit, as the angle between the blade and the imaging axis limits the resolution of the measure. Density profiles for various blade positions are given Fig. 4.23. The lack of symmetry prevents from using Abel inversion, but the transverse (toward the reader) profile of the gas is unlikely to be different in term of shape and full-width-half-max, relatively to the un-shocked flow. Assuming same transverse gaussian profile, we are able to roughly derive plasma density through the shock. In plasma, the relationship between the probe phase shift $\Delta\Phi$ and the surfacic density (in cm^{-2}) is given by:

$$\Delta\Phi = \frac{2\pi}{\lambda}\int_x (\eta - 1)dx \tag{4.15}$$

$$\Delta\Phi = \frac{2\pi}{\lambda}\int_x ((1 - n_e/n_c)^{1/2} - 1)dx \tag{4.16}$$

where x is the QWSLI imaging axis. For peak densities where $n_{e0} << n_c$, one can link the phase shift to the surfacic density $n_{se} = \int_x n_e(x)dx$:

$$\Delta\Phi = -\frac{\pi}{n_c\lambda}\int_x n_e dx \tag{4.17}$$

$$\Delta\Phi/\mathrm{rad} \approx -5.7 n_{se}/10^{18}\,\mathrm{cm}^{-2} \tag{4.18}$$

A rough derivation of the peak plasma density can be done for Fig. 4.24(b-d), assuming a gaussian profile in the imaging direction of FWHM 300 µm, it yields $n_{e0} \approx 3 \times 10^{20}\,\mathrm{cm}^{-3} = 0.15 n_c$.

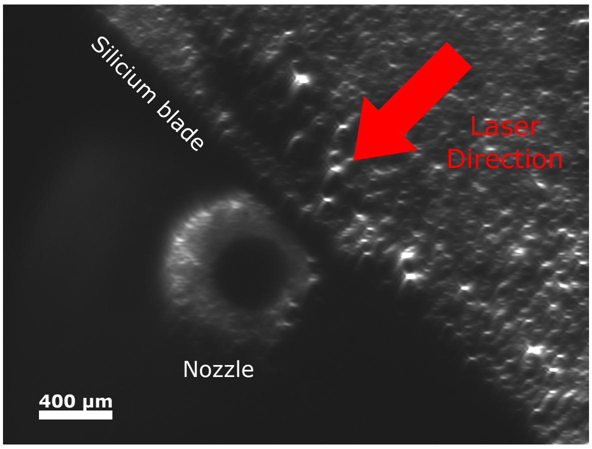

Figure 4.22 – Bottom view of the supersonic nozzle and the blade

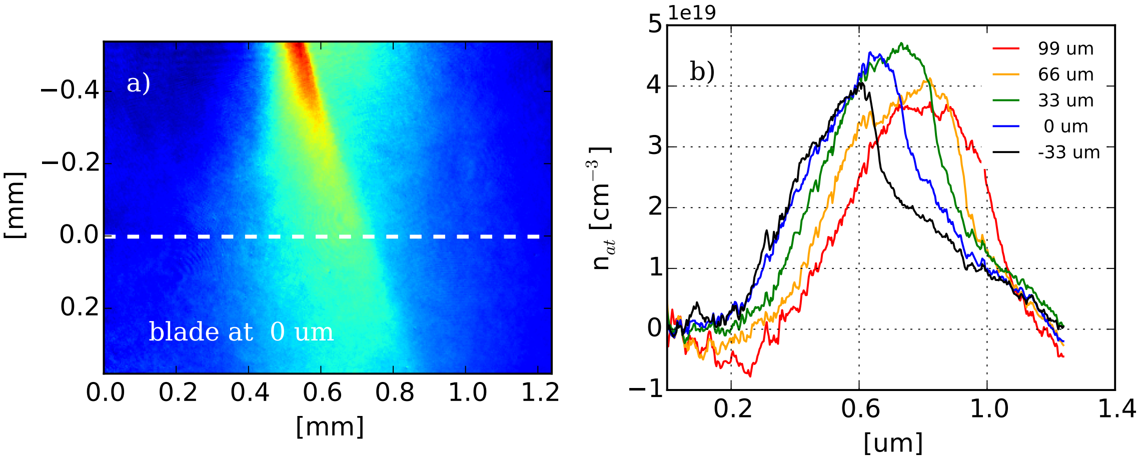

Figure 4.23 – (a) Projection of atomic density of a supersonic flow tailored by the blade (not visible, on top). The supersonic nozzle expels Ar/H(10 %) mixture at 300 bar, at Mach 3.5, from the top. Dashed white line shows the position of the lineouts visible in (b). (b) Atomic density lineout for various blade position, "0 µm" denoting the central position. Shock angle also changes with blade position. Absolute density values are derived with assumption that the gas extension is the same in every direction perpendicular to the flow direction, about 500 µm FWHM.

Electronic spectrum is measured for similar peak density of $n_{e0} = 4 \times 10^{20}\,\mathrm{cm}^{-3}$ in case of a blade shock, or without blade. The laser arrives through the smooth gas slope (blade side) Fig. 4.25. Electrons up to 100 MeV are observed, with no differences in the spectrum between both cases. Spectra are too unstable shot to shot to derive relationship with gas density or laser energy, despite the stability of the atomic gas profile.

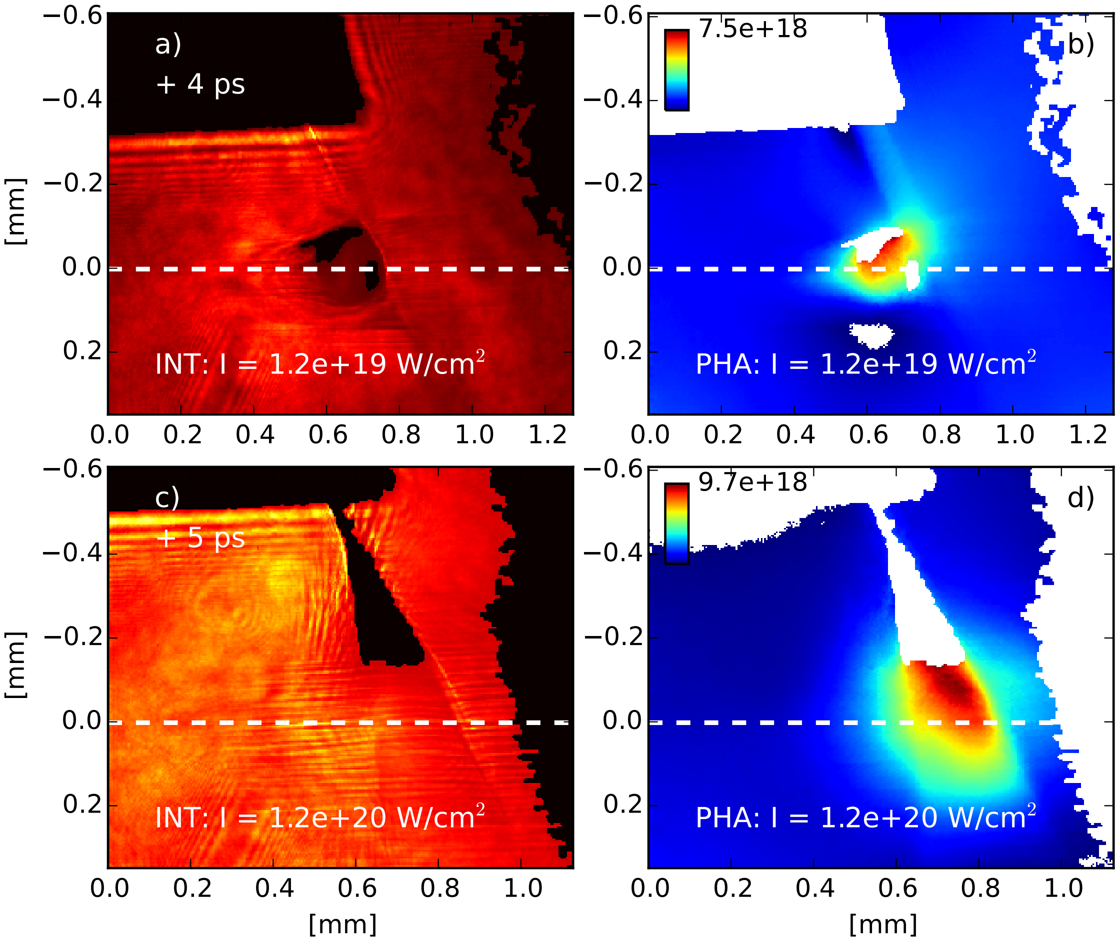

Figure 4.24 – Laser plasma interaction with a shock made from supersonic flow. Peak atomic density along laser path is $(5 \pm 1) \times 10^{19}\,\mathrm{cm}^{-3}$. The gas is a mixture of argon/hydrogen(10 %), the laser comes from the left, the gas from the top. Top row: intensity $1.2 \times 10^{19}\,\mathrm{W \cdot cm^{-2}}$, bottom row: $1.2 \times 10^{20}\,\mathrm{W \cdot cm^{-2}}$. (a-c) Shadowgraphy, the blade is visible at the top. Opaque area denotes high density or high probe deflection. (b-d) Projected density in cm^{-2} derived from the probe phase measured by QWSLI. Opaque areas cannot be reconstructed. Lack of symmetry prevent from using Abel inversion. Higher ionization is likely near the laser axis, but the plasma channel is not resolved on these pictures.

4.3.3 Conclusion

No forward accelerated ions are detected with neither scintillator nor the Thomson parabola. We couldn't shot the laser in the area where the shock is well-defined and where the density gradient is sharper, because in this case the blade explodes. Shadowgraphy shows well delimited opaque regions around the shock line, as far as hundred of micron from the laser beam path. Electron spectrum is qualitatively unchanged in Fig. 4.25 by the blade addition. Difficulties lie in (1) characterising the blade shock density and in (2) operation of the blade apparatus. A more straightforward device is required to build strong gradients. Tailoring sharp gradients requires thin blades with

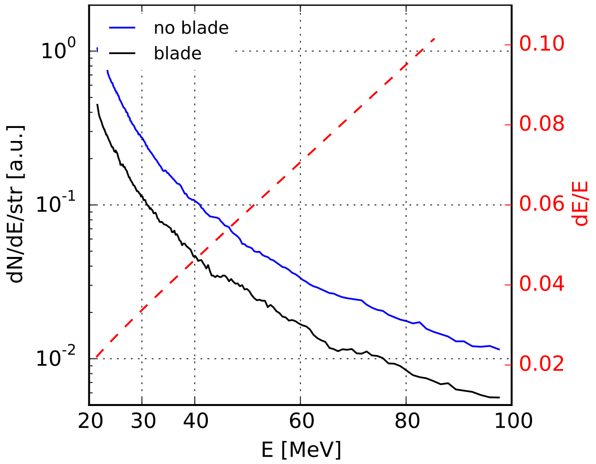

Figure 4.25 – Forward electronic spectrum measured on the scintillator in the presence of a blade (black line), and without blade (blue line) for a laser focus at $1.2 \times 10^{20}\,\mathrm{W \cdot cm^{-2}}$ into an argon/hydrogen(10 %) mixture with maximum density $n_{e0} = 4 \times 10^{20}\,\mathrm{cm^{-3}}$. Dashed red line shows resolution of the spectrometer

sharp edges, close to the nozzle and to the laser. This is detrimental to the durability, the robustness, and finally the reproducibility of the apparatus, because of damages from the laser, the plasma, and the high pressure jet. These limitations explains our work toward an all-inclusive nozzle, able to reliably deliver a well characterized density gradient at safe distance from the nozzle.

4.4 Supersonic steep-gradient target

4.4.1 Motivation

During previous experiments we encountered several obstacles summerized below:

- Experiments and simulations show that the laser cannot propagate in our target through plasma of electronic density higher than $\approx 15\,\% n_c$. This is due to strong self focusing and filamentation of the laser. We also observed constant pre-ionization of the target, due to pre-pulses visible on contrast diagnostics. Shadowgraphy of the interaction was quantitatively different day to day, despite stability of the target gas profile, and despite careful monitoring of the compression and focal spot of the main beam.

- Argon as a background gas was necessary to reach an electronic density of about n_c, but non homogeneous ionization level and clusterisation make the control of the plasma profile challenging. Opaque plasma prevented also plasma density analysis by interferometry measurement (QWSLI).

- Shock creation by a blade apparatus was found difficult to characterize due to its large transverse extent, and lacked of reliability and reproducibility, even when motorized with fine translation stages.

The Laser system was upgraded in summer 2015 into its high contrast configuration to prevent pre-pulses and to improve the beam quality. In order to reduce self focusing and prevent the collapse of the main beam before the peak density, we implement an off-axis parabola with longer focal length: 508 mm, giving $w_0 = (10 \pm 1)\,\mu\text{m}$ and peak intensity $I = 2.4 \times 10^{19}\,\text{W} \cdot \text{cm}^{-2}$ ($a_0 = 3.3$).

Supersonic Shock Gas Jet

To overcome limitation of argon mixtures, we use also a mixture of helium and hydrogen (1 %). The sharp gradient is made from a supersonic nozzle with a built-in shock design (See Chapter III), able to build a peak density up to $\approx 0.15 n_c$ once ionized, at safe distance from the nozzle. We achieved gradients lengths as short as 50 µm. At $0.15 n_c$, the laser is unable to propagate through the plasma, so the reduced peak density of helium jet (compare to an argon jet) is not a limit. The gas jet density profile is recalled Fig. 4.26. The apparatus is shown Fig. 4.27.

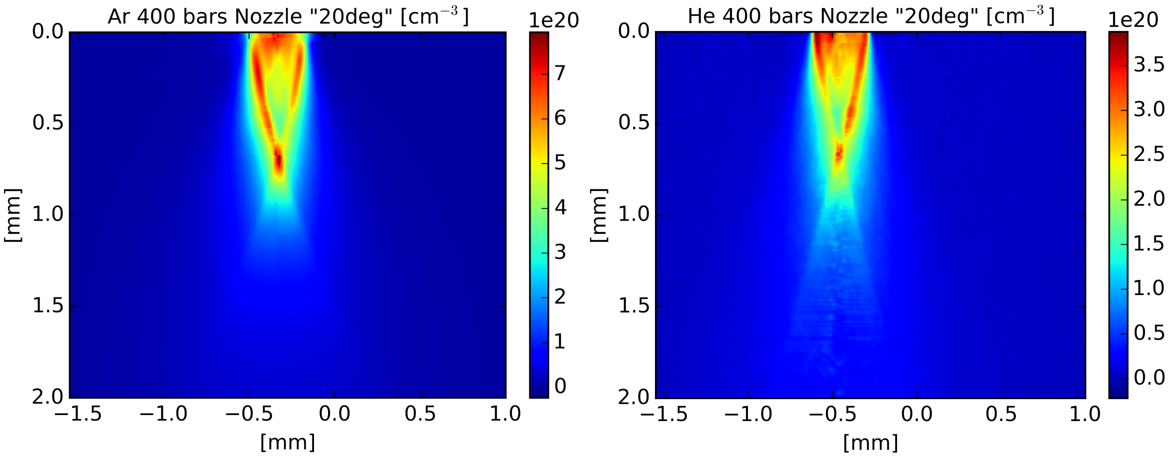

Figure 4.26 – Atomic density profile for shock nozzle "20 deg" shown Chapter III, with parameters optimized for maximum density. The nozzle is upside-down, the gas flows from the top. Left) Argon, 400 bar, electrovalve (EV) open time: 4.2 ms, delay after opening: 35 ms. Right) Helium, 400 bar, EV open time: 2.9 ms, delay after opening: 13 ms. Shock lines are clearly visible as well as the density peak where they cross. Helium and argon profiles are homothetic, the density difference comes from different operation parameters of the electrovalve.

4.4.2 Plasma dynamic

The improved quality of the probe beam enables quantitative analysis of the plasma channel, and of the plasma dynamic, both from shadowgraphy and QWSLI. With careful alignement, it is possible to focus the laser exactly on the peak density area. See Fig. 4.28. The peak density position can be easily spotted in shadowgrams, as the brusque changes in the plasma density at shock lines position appear as thin opaque lines. Plasma channel longitudinal extent shows where the laser collapses and we observe intense non-linear wavebreaking radiation at the channel's end. We were able to make the emission coincidental with the peak position. See Fig. 4.29, 4.30.

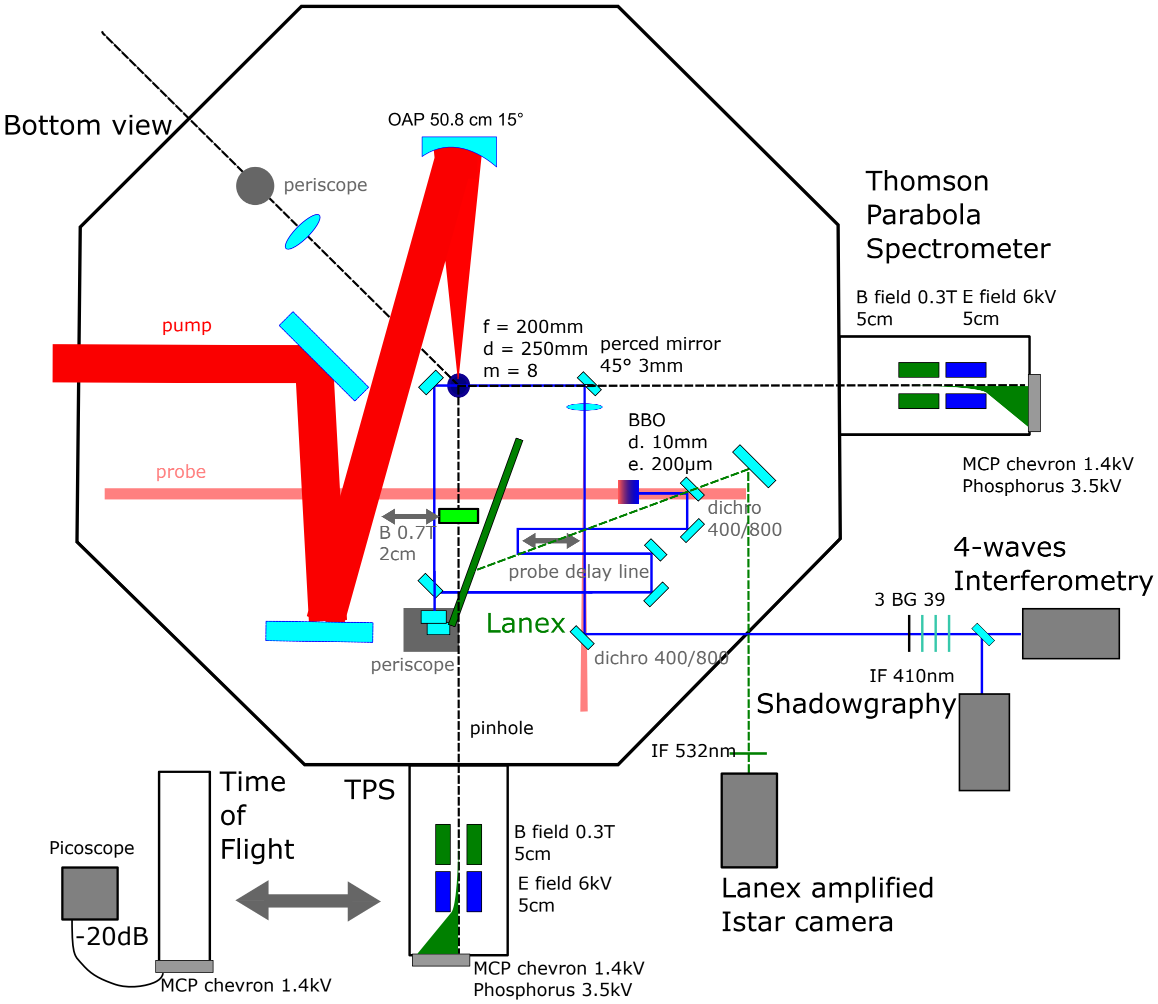

Figure 4.27 – Layout of the experimental chamber for the shock nozzle campaign. The diagnostics include a thomson parabola in forward direction, eventually switched with a Time of Flight MCP. In TP configuration the low energy detection limit is 600 keV. Another Thomson parabola is installed in the transverse direction. The electron spectrometer is made from a mobile Lanex screen associated with a static magnetic field of 0.7 T. The sideviews imaging includes QWSLI and shadowgraphy made by a probe laser doubled at 400 nm by a thin BBO crystal. The probe laser is cleaned from any remaining fundamental wavelength by dichroic mirrors, coloured glass filters and an interferometric filter.

Shadowgrams feature also multiple and thin tracks in forward direction within a half angle up to 75° (He/H(1 % $n_{at} = 1.3 \times 10^{20}\,\mathrm{cm}^{-3}$) and up to 55° (Ar/H(10 % $n_{at} = 2.8 \times 10^{19}\,\mathrm{cm}^{-3}$). These tracks are emitted at the beginning of the interaction and propagate at $\approx c$ velocity. According to simulations (Chapter II), no laser filamentation occurs at this position or at this angle. Similar tracks were seen in PIC simulations, in the wakefields of energetic electron beams expelled from the high laser intensity region. It is likely that the tracks observed in experiments are as well ionized path of energetic electron beams. The slight plasma gradient modulations resulting from this tracks are clearly visible in shadowgrams, and also with the interferometry (QWSLI), albeit less clearly.

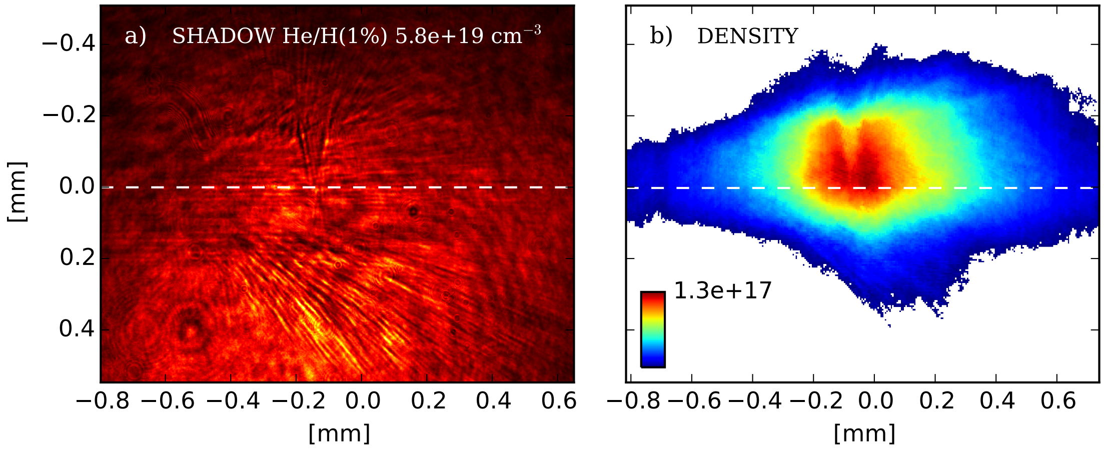

Figure 4.28 – a) Shadowgram of the interaction for a supersonic shocked jet (see Fig. 3.11) with He/H(1 %) mixture with peak plasma density of $5.8 \times 10^{19}\,\mathrm{cm}^{-3}$. The laser comes from the left, and the gas from the top. The shock lines from the atomic gas profile are visible. b) Plasma areal density for the same shot, expressed in cm^{-2}. No Abel inversion has been performed due to the lack of symmetry of the plasma profile, only an estimation assuming an axis-symmetric gaussian transverse profile with $\sigma = 150\,\mu\mathrm{m}$. The white dashed line denotes the laser axis.

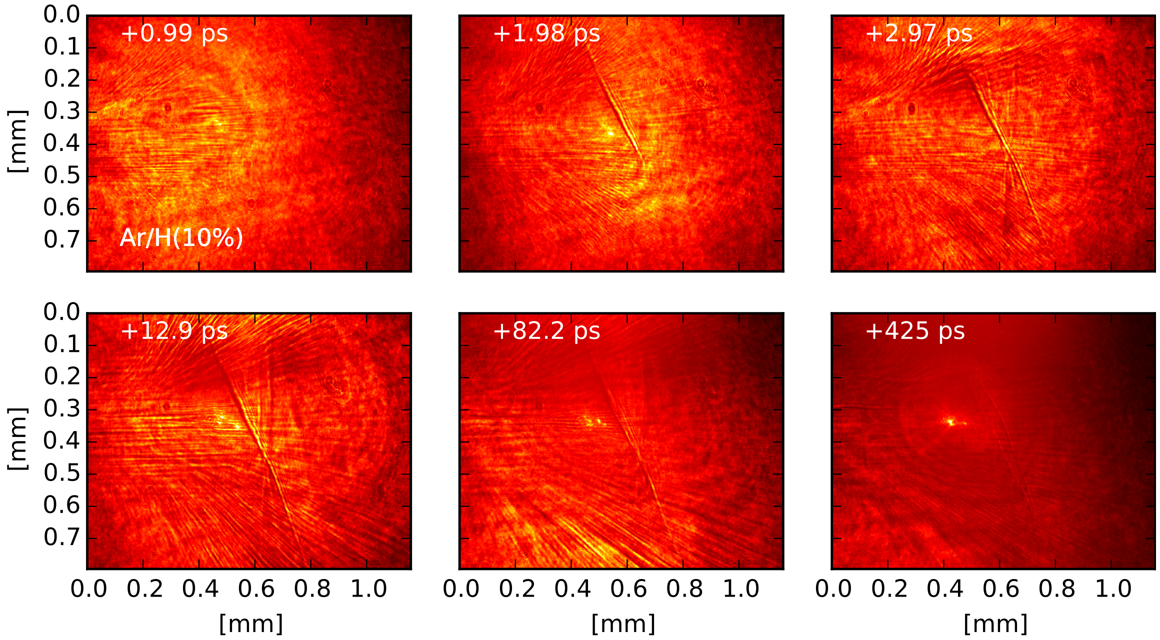

Figure 4.29 – Shadowgrams at different timesteps showing evolution of the interaction between the laser of intensity $2.4 \times 10^{19}\,\mathrm{W} \cdot \mathrm{cm}^{-2}$ and the supersonic shocked jet (see Fig. 3.11) with argon/hydrogen(10 %) mixture with top peak atomic density of $2.8 \times 10^{19}\,\mathrm{cm}^{-3}$. Crossing shock lines are clearly visible. The laser goes from left to right and the gas comes from the top.

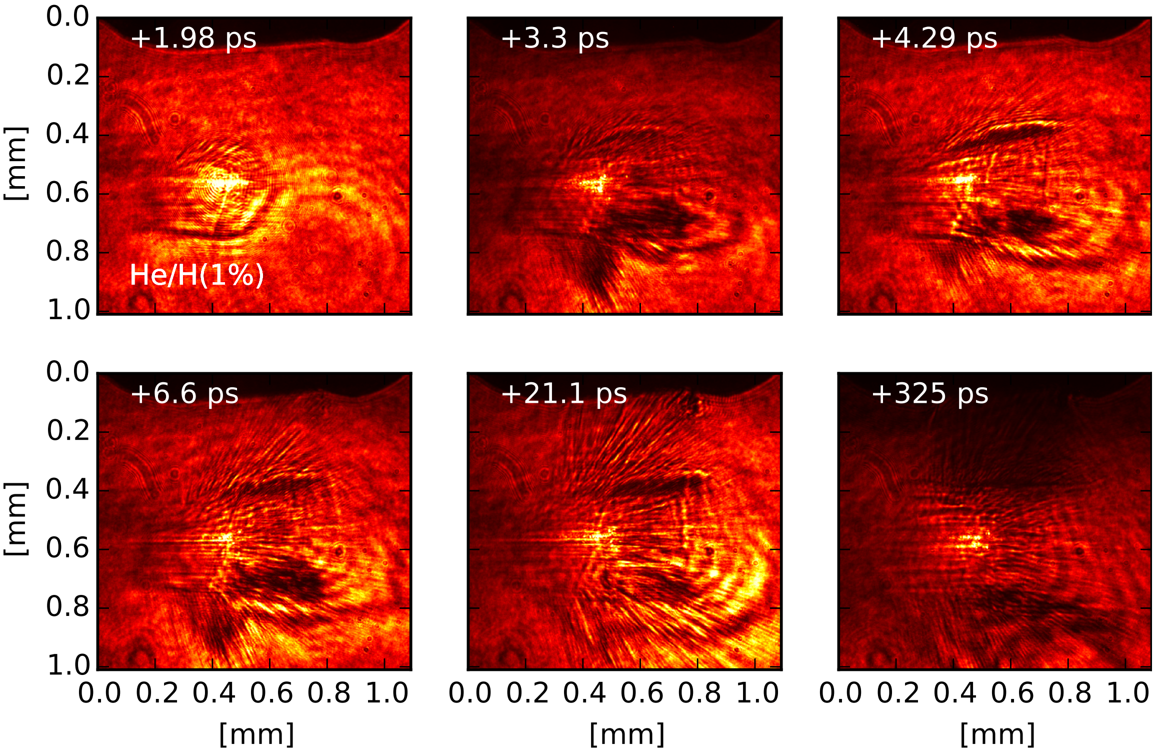

Figure 4.30 – Shadowgrams at different timesteps showing evolution of the interaction between the laser of intensity $2.4 \times 10^{19}\,\mathrm{W \cdot cm^{-2}}$ and the supersonic shocked jet (see Fig. 3.11) with helium/hydrogen(1 %) mixture with top peak atomic density of $1.3 \times 10^{20}\,\mathrm{cm^{-3}}$. Crossing shock lines are less visible than in Fig. 4.29 due to damage of the nozzle, and change in the imaging (less numerical aperture). The laser goes from left to right and the gas comes from the top.

Expansion of the plasma channel is visible in range of 100 to 450 ps in the argon mixture (see Fig. 4.31), and between 20 to 250 ps in the helium mixture. An expanding high electronic density shell surrounds the channel, where electronic density is depleted. The density modulation of this shell is clearly visible in shadowgrams, and on the QWSLI. In the smooth up-gradient of the plasma, the geometry is symmetric along the laser axis, and therefore, it is relevant to perform an Abel inversion in this area to derive the plasma channel electronic density evolution. Near the peak density, the density profile is not axis-symmetric, and Abel inversion can give only rough estimate of the electronic density. Fig. 4.31 shows density map in a) and shadowgram in b) of the plasma channel in argon mixture of maximum atomic density $n_{at} = 2.8 \times 10^{19}\,\mathrm{cm^{-3}}$. The lineouts Fig. 4.31c) show the transverse electronic density profile at different times. Canal size is derived from the distance between two consecutive maximums of the density along the transverse direction.

If the density is low enough the laser beam crosses the plasma in roughly 3 ps. The laser ponderomotive force expels electrons from the laser beam axis, and build a channel as described in section 1.3.1. This channel is made from a high electronic density shell surrounding a central cylinder of lower electronic density, typically $n_{e0}/2$ in simulations. Ion filaments observed in quasi 3D PIC simulations are not observed

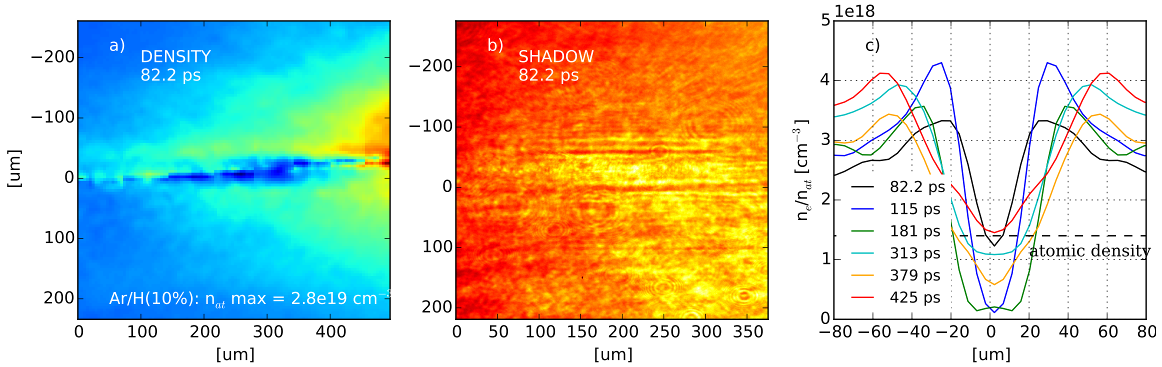

Figure 4.31 – a) Electronic density map and b) shadowgram of the plasma channel in argon mixture of maximum atomic density $n_{at} = 2.8 \times 10^{19}\,\mathrm{cm}^{-3}$. The delay between the probe beam and the main beam is 82.2 ps. c) The lineouts Fig. 4.31c) show the transverse electronic density profile at different times. They are derived by Abel inversion of a symmetrized profile of the phase measured by QWSLI.

here, but imaging resolution is $\approx 4\,\mu\mathrm{m}$ per pixel, which is roughly the size of such filament. This structure expands radially, its a collisional blast wave. Study of such blast-waves can be found in [Edwards et al., 2001; Osterhoff et al., 2009]. The Taylor-Sedov analytical class of solution describes the expansion of non-radiating shock waves (energy conserving shock) in non-resistant medium. The solution is self-consistent and can be written as:

$$R(E,t) = \beta \mathit{\Delta}_t^{\alpha} \tag{4.19}$$

where R is the radius of the shock wave at time t after the explosion, E the total energy of the system, $\mathit{\Delta}_t$ the time since the shock formation, and α the deceleration parameter (given alternatively by $\alpha = Rt/V$ where V is the shock velocity). In the case of a cylindrical, non-radiative shock wave, $\alpha = 0.5$, and the wave features a high pressure, low density core pushing a thin shell. There are two radiative regimes: the *radiative flux regime* and the *radiation dominated regime*. In the first one the radiative energy flux is greater than the convection energy flux, and it occurs at lower temperature than the second regime. In the *Radiation dominated regime* the radiation pressure exceeds the material pressure. Radiation is emitted either by bremsstrahlung, or by electronic level decay of excited high-Z materials. We measure the density of the surrounding plasma where the channel expansion has been measured ($9.3 \times 10^{-5}\,\mathrm{g \cdot mol}$ for argon and $4.3 \times 10^{-5}\,\mathrm{g \cdot mol}$ for helium). Assuming a temperature $\approx 10\,\mathrm{eV}$), the blast wave is well into the *radiative flux regime* [Symes et al., 2010]. In this regime, $\alpha = 1/3$.

Such regime has been investigated by Edwards et al.[Edwards et al., 2001]. Their work exhibits radiative regime in the case of cylindrical blast wave made in clustered gas (xenon) by femtosecond laser, where $\alpha < 0.5$. In argon they do not observe such radiative regime, but they explain the low α in xenon by its higher clusterisation. At early time, the surrounding medium is heated by the laser energy present in the wings, while the main part of the laser energy triggers a blast wave. During a second phase, the blast wave expands and looses its energy by radiation, a part of it is absorbed by the surrounding medium creating a shock precursor: an area prior to the shock with increased temperature. Both shock radiation and laser irradiation heat the plasma before the shock, thereby decreasing the shock Mach number and the density jump. In later time, the surrounding medium radiates more energy inside the shock than the shock loses energy by radiation, and the deceleration parameter may exceed $\alpha = 0.5$. [Edwards et al., 2001].

We measure a deceleration parameter $\alpha = 0.35$ in argon mixture, and $\alpha = 0.64$ in the helium mixture. The shock velocities are respectively $110\,\mathrm{km}\cdot\mathrm{s}^{-1}$ and $320\,\mathrm{km}\cdot\mathrm{s}^{-1}$. Work from Michault et al. [Michaut et al., 2004] shows that for these velocities and for precursor temperature of 10 eV, the density jump ρ_2/ρ_1 before and after the shock should reach ≈ 6 for argon and ≈ 4 for helium. In our case the density data give $\rho_2/\rho_1 \approx 4/3$.

We should conclude that our system is far from Local Thermodynamic equilibrium, either because the precursor features temperatures that are above 10 eV, or because the non-LTE changes the value of the heat capacity ratio, due to energy loss in radiation or ionization [Symes et al., 2010]. Both effects diminish the blast Mach number. The expansion of the argon channel seems linked to a strongly radiative shock, while the high deceleration parameter α in helium blast wave could come from energy recovered from an highly radiative precursor.

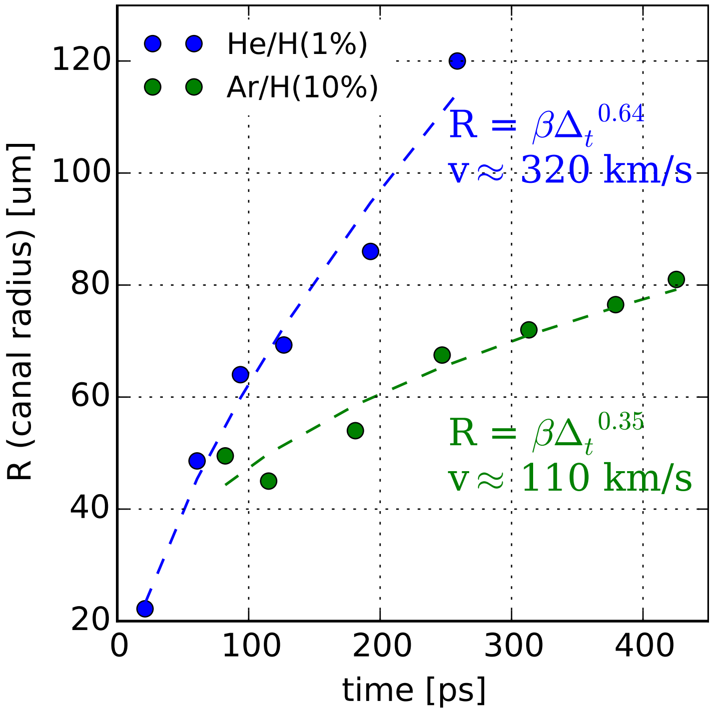

Figure 4.32 – Channel diameter evolution versus time since the laser entered the plasma, for argon and helium mixtures (respectively $n_{at} = 2.8 \times 10^{19}\,\mathrm{cm}^{-3}$ and $n_{at} = 1.3 \times 10^{20}\,\mathrm{cm}^{-3}$). In dotted line the fitted self-similar expansion with Taylor-Sedov parameters. The deceleration parameter α is 0.35 in argon mixture, and 0.64 in the helium mixture.

4.4.3 Effect of the laser chirp

Travelling through the dense plasma, the laser undergoes relativistic self-focusing, self-phase modulation and pulse shortening, as succinctly described in Chapter I section 1.2.4. We have seen in chapter II Fig. 2.8 that the pulse undergoes significant chirp during propagation, the larger wavelengths moving in front of the pulse. We introduced negative chirp in the pulse by changing the compressor separation. In peak helium plasma density with $n_e = 1.3 \times 10^{20}\,\mathrm{cm}^{-3} = 15\,\% n_c$ we could demonstrate that negative chirp increases the ability of the laser to cross a dense plasma. (See 4.33)At optimal compression, the laser collapses before exiting the plasma. With a negative chirp of -700 fs^2 the laser pulse is streched to 65 fs instead of the optimal 25 fs compression. The normalized amplitude is therefore reduced to $a_0 = 2.5$. These variations do not affect significantly the self-focusing nor the optical shock position (whose scaling is in $(a_0^2 L_0)^{-1}$, which is related to the fluence, [Vieira et al., 2010] Eq.(8)).

Nonetheless, introducing a positive (negative) chirp compresses (streches) the laser pulse as it propagates through the plasma [Pathak et al., 2012]. A positive chirp (large wavelength ahead) increases the absorption of the front of the pulse, and the laser is etched. Its envelope becomes sharper at the pulse front. It has been demonstrated, for laser with $\omega_p \tau \sim 10$ [Leemans et al., 2002] that an asymmetric profile with a fast rising front increases the amplitude of the wakefield, and the charge and energy of accelerated electrons. This effect is due to the asymmetric profile, rather than to the chirp in itself, and decreases for $\omega_p \tau \sim 20$ [Leemans et al., 2002]. Control of the laser chirp can be a tool to control laser propagation in such near-critical plasma, where self-focusing and self-steepening prevent laser propagation. Further studies are needed to observe the laser chirp at the plasma exit in such conditions. Such studies should be inspired by similar works performed with less density [Faure et al., 2005; Schreiber et al., 2010] .

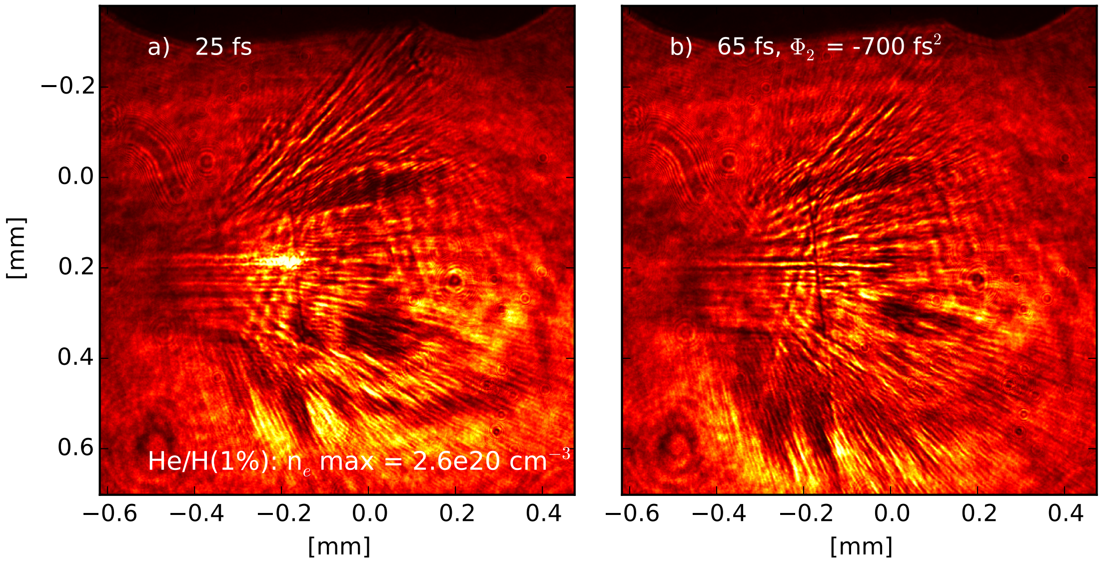

Figure 4.33 – Shadowgraphy of He/H(1 %) plasma at $2.6 \times 10^{20}\,\text{cm}^{-3}$, or $15\,\%n_c$, with $\omega_p\tau = 20$ at the peak. a) Optimal compression 25 fs, with interruption of the plasma channel on the peak density. b) Compression degraded to 65 fs ($a_0 = 2.5$), showing the clear plasma channel across the peak density.

4.4.4 Electron beam properties

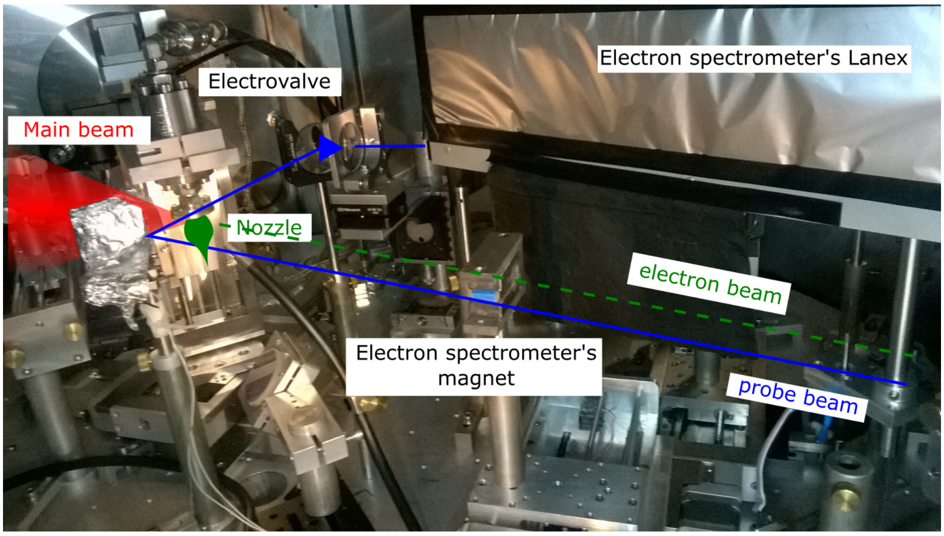

Figure 4.34 – Electron spectrometer apparatus. The lanex and the magnet are motorized and can be removed from the laser axis. To retrieve the electron beam transverse profile, a lanex screen is put in place of the magnet, but is not shown here.

Transverse profile

Electron beam transverse profile is measured by placing a Lanex screen in the laser axis, 20 cm after the target. The lanex is protected from the laser by a 10 µm thick aluminium foil. It is imaged with a 30° angle by electronically cooled high dynamic Istar ICCD. Light is filtered by an interferometric filter at 532 nm, close to the maximum of emission of the lanex. Beam distribution is shown in Fig. 4.35. For $n_e < 1.5 \times 10^{20}\,\mathrm{cm}^{-3}$ (i.e $n_e < 9\,\% n_c$) in helium mixture He/H(1 %), the beam presents an asymmetry, the part of the beam with the most charge has an angle of ≈ 50 mrad in vertical direction *below* the laser axis (dashed white line on Fig. 4.35). The laser polarization is horizontal. A weaker electrons background is emitted with a large divergence, bigger than the solid angle visible on the forward lanex screen. On the laser axis, the lanex screen features a region depleted from electrons. This feature disappears for density above $10\,\% n_c$, which can explain why it is not seen in PIC simulations Chapter II.

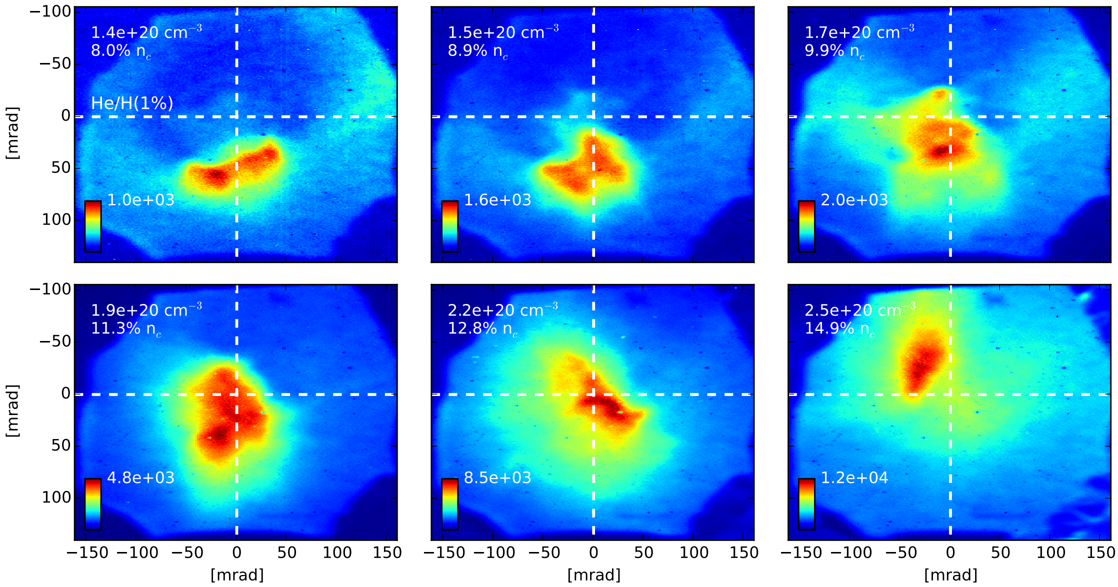

Figure 4.35 – Transverse distribution of electrons emitted in forward direction, measured with a lanex screen at 20 cm from the target. $I = 2.8 \times 10^{19}\,\mathrm{W \cdot cm^{-2}}$, in shocked nozzle, with peak plasma density ranging from $8.0\,\% n_c$ to $14.9\,\% n_c$. The color scale is different for each image, the signal being stronger at higher density. The laser axis is localized by the white dashed lines. A hole in the electron emission is seen at densities $n_e < 9\,\% n_c$, due to the ponderomotive effect of the laser on the electron beam during vacuum propagation after the target.

In a recent work [Thevenet et al., 2016], Thevenet & Leblanc used a plasma mirror to inject an electron beam from a solid target into an ultra-intense field. The electron beam features the same broad emission cone, with a hole on the laser axis. In this work as in the experimental results presented here, the hole cone is oriented along the laser propagation and its full angular width is comparable to the laser divergence (Here ≈ 150 mrad). The electron energy is also similar: in the range 4 to 20 MeV. The electrons from the large emission cone experienced isotropic ponderomotive scattering, leading to this symmetric hole. In Thevenet's work the bright off-axis spot are electrons who gained energy by Vacuum Laser Acceleration (VLA). Such electrons stay in phase with the laser as they propagate into vacuum. The laser being faster than the electrons in vacuum, these electrons drift backward relatively to the laser, staying in a region of constant E-field sign, before exiting the laser field. Therefore VLA electron bunches can be found on both sides of the hole in the polarisation direction, depending of the injection region. VLA was either observed after the interaction of ultra intense pulse with a solid target [Thevenet et al., 2016], or in gas at lower density ($0.01\,\%n_c$)

In our experiment, the main laser crosses the plasma only for plasma density lower than $0.1n_c$. Scattering by the ponderomotive potential could therefore explain the central hole in the emission. But the laser polarisation is horizontal, in contradiction with bunches from VLA. This hypothesis needs further investigation.

Electron spectrum

Electrons up to (100 ± 25) MeV are accelerated in shock gas target, with plasma density of $10\,\%n_c$. Electron spectrum may vary shot to shot at high energy, but present a maxwellian spectrum at low energy, of temperature (15 ± 1) MeV. This temperature does not change significantly by changing the plasma density. The total charge rises with density as illustrated in Fig. 4.36. Above $10\,\%n_c$, a bright forward X-Ray emission blinds the high energy region of the lanex, preventing analysis above 36 MeV. In this regime two mechanisms may explain the electron acceleration, either an acceleration by the laser field itself, or by the plasma wakefield.

In the work of Gahn et al [Gahn et al., 1999], a relativistic 200 fs laser of intensity $4 \times 10^{18}\,\mathrm{W \cdot cm^{-2}}$ is focused in a non uniform helium plasma of length 500 µm and density ranging from 3×10^{19} to $4 \times 10^{20}\,\mathrm{cm^{-3}}$. They observed a maxwellian electronic spectrum, with charge and temperature increasing with plasma density, and with better collimation for high energy electrons. Above $2 \times 10^{20}\,\mathrm{cm^{-3}}$ they do not observe any increase in the charge. By PIC simulation of their experiment, they monitor the relative contribution of the terms:

$$\mathit{\Gamma}_z = -\int_0^t \frac{2eE_z p_z}{(m_e c)^2} dt \qquad\qquad \mathit{\Gamma}_\perp = -\int_0^t \frac{2eE_\perp p_\perp}{(m_e c)^2} dt \tag{4.20}$$

which are related to the relativistic kinetic energy of each electron by:

$$\gamma^2 = 1 + \mathit{\Gamma}_z + \mathit{\Gamma}_\perp \tag{4.21}$$

where γ is the relativistic factor, E_z the longitudinal field. Relativistic electrons gaining energy from the laser field $E_\perp$ are moving in the forward direction because of the $v \times B$ term of the Lorentz force. They observe that the term $\mathit{\Gamma}_\perp$ is dominant, and electrons are experiencing Direct Laser Acceleration (DLA). The plasma wakefield contribution $\mathit{\Gamma}_z$ is even negative, slowing down the electrons. They explain the increase in electron temperature with density by the increase in the ratio P/P_{RSF} (laser power over relativistic self-focusing threshold $P_{RSF} \approx 17(n_c/n_e)$GW). This increased ratio leads to longer channels, with more laser energy trapped inside, therefore leading to longer and stronger DLA.

In the work of Malka et al. [Malka et al., 2001], a relativistic 30 fs laser of intensity $8 \times 10^{18}\,\mathrm{W \cdot cm^{-2}}$ is focused in a uniform helium plasma of length 2 mm and density from $1.5 \times 10^{19}\,\mathrm{cm^{-3}}$ to $1.5 \times 10^{20}\,\mathrm{cm^{-3}}$. They observe electrons with a maxwellian spectrum in the forward direction. In contrast with the results of Gahn et al.[Gahn et al., 1999], the electron temperature, the maximum energy, and the charge of electron of high energy, all decrease with increased density. Electron temperature and maximum energy scale also with the square root of the laser intensity. The decrease of the plasma wavelength at high density is responsible for a shorter dephasing length between electrons and the wakefield. Numerical PIC simulation shows that for moderate density ($2 \times 10^{19}\,\mathrm{cm^{-3}}$) the wakefield acceleration is dominant over DLA. As the pulse propagation is longer than the dephasing length, the wake may slowdown energetic electrons. The authors acknowledge the possibility of DLA at higher density in the self-modulated regime ($\omega_p \tau > 2$) where τ is the laser pulse duration.

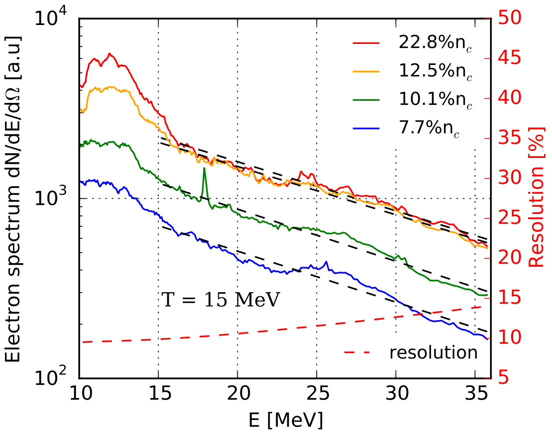

Figure 4.36 – Electron spectrum (in a.u./MeV/steradian) measured in mixture He/H(1 %) expelled by a shock nozzle, for different plasma densities. On the right red scale: resolution of the measured energy. The part of the spectrum above 15 MeV features a maxwellian distribution of temperature (15 ± 1) MeV, for every density

In our experiment, the charge rises with higher density. As in Gahn's work, we observe a maximum in the charge of energetic electron for density $> 2 \times 10^{20}\,\mathrm{cm^{-3}} (12\,\% n_c)$. Our plasma features a short longitudinal extent (140 µm) with no plateau and sharp gradient. The relativistic wakefield has a wavelength linked to the plasma wavelength λ_p, shrinking as the laser propagates in the up-ramp. Self-injected electrons may be dephased relatively to the accelerating wakefield, and cannot gain efficiently energy. If the plasma wavelength becomes smaller than the laser longitudinal extent: $\omega_p \tau > 2$ and self-modulation of the laser envelope occurs. In Gahn's work demonstrating DLA, $\omega_p \tau_{laser}$ ranges from 60 to 250. In our experiment, at peak density $\omega_p \tau \approx 20$. These arguments support the hypothesis of a DLA. In later time, if the density is low enough to enable the laser to cross the plasma, the electrons accelerated in a large cone are scattered on laser axis by the ponderomotive potential. This mechanism is preceded by self injection in the bubble in the low density plasma up-ramp, resulting in unstable high energy bunches for some shots (See Fig. 4.37b)).

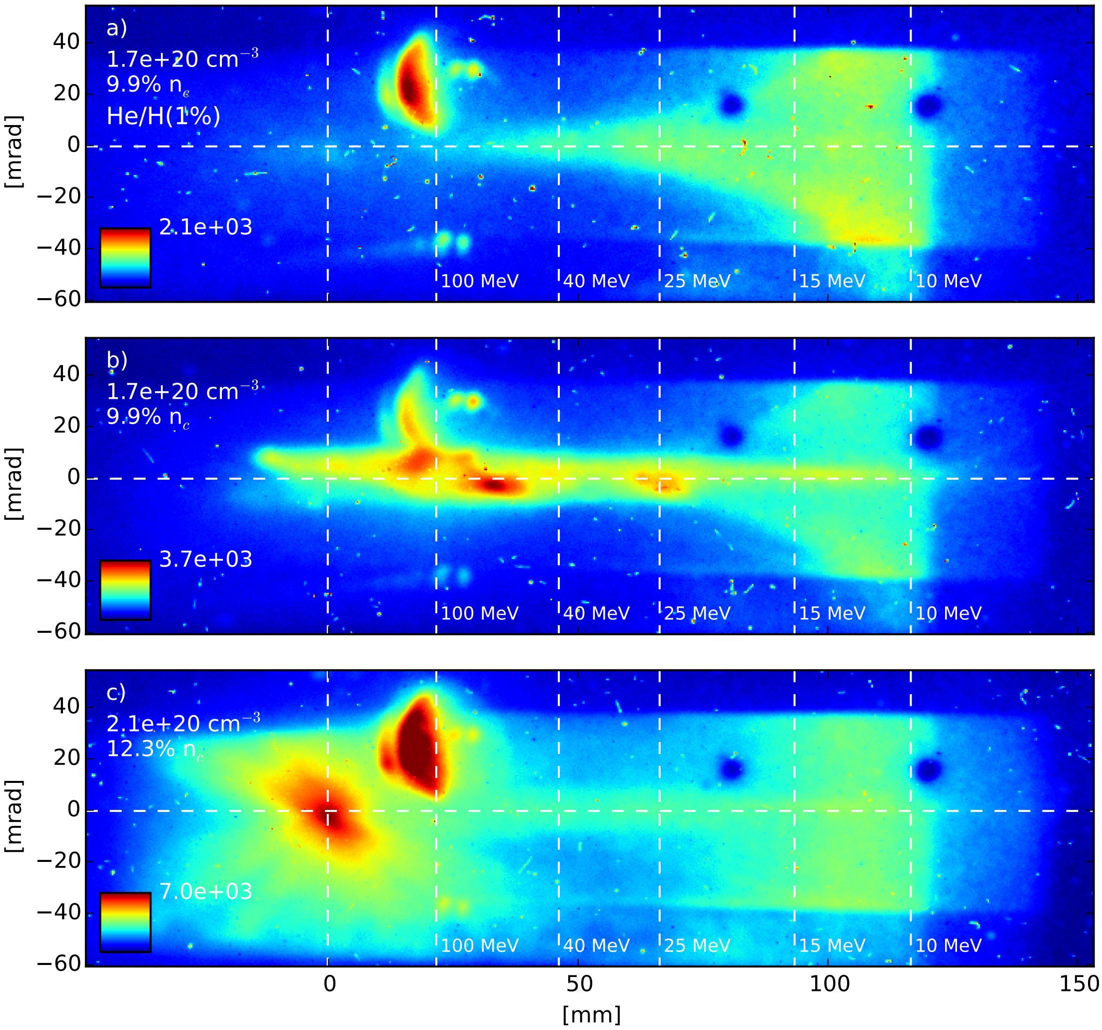

Figure 4.37 – Lanex traces at various plasma densities. The gas is a mixture He/H(1 %) expelled by a shock nozzle. The horizontal white dashed line and the leftmost line denote the laser axis. The other white dashed lines show the expected electron positions at various energies. a) and b) show electron traces in same condition ($n_e = 9.9\,\%n_c$) featuring in a) the electron maxwellian distribution, and in b) an unstable electron bunch of energy above 100 MeV. The spectrometer broad acceptance angle (50 mrad) explains the signal at the left of the laser axis. c) Interaction at $n_e = 12.3\,\%n_c$, featuring bright X-ray spot of (16 ± 2) mrad on the laser axis. The electron counts in the spectrometer acceptance angle is increased.

Betatron emission

The lanex screen of the electron spectrometer intersects the laser axis 43.7 cm after the target. This configuration enables to monitor the forward emission profile when the deflecting magnet is removed. For densities $n_e > 10\,\%n_c$, a bright signal is seen in forward direction, rising in intensity with the laser energy. This signal is shown Fig. 4.38. Insertion of the deflecting magnet into the laser axis does not spread the signal. Deflection would be negligible for mono-energetic electrons of energy > 200 MeV, but such beam has never beam demonstrated at such plasma density. The signal disappears for $n_e < 10\,\% n_c$. Its divergence is unchanged by change in the density or by the laser energy, and is $(16 \pm 2)\,\mathrm{mrad}$, well below the laser divergence ($(155 \pm 5)\,\mathrm{mrad}$). This emission is likely to be betatron emission coming from electrons oscillating in the wakefield.

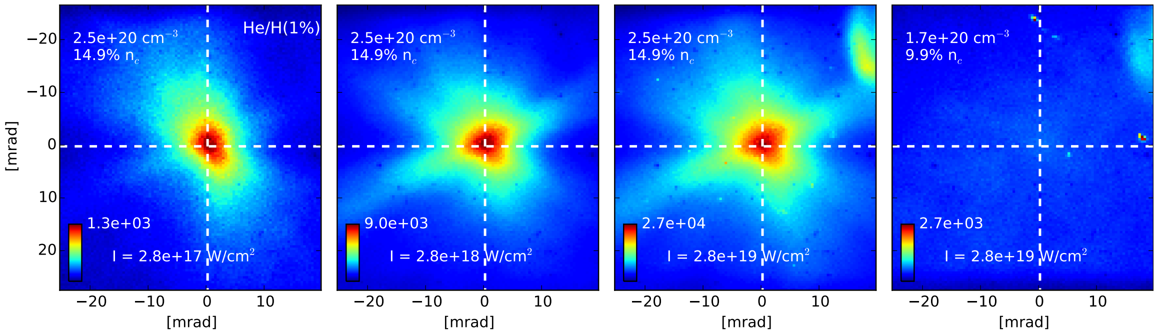

Figure 4.38 – Forward X-Ray emission measured on the lanex screen at 43.7 cm from the target, for various conditions of laser energy and plasma density. Color scale in arbitrary unit, is different for each pictures. The X-ray light output rises with laser intensity. The white dashed lines denote the laser axis position.

4.5 Conclusions

In conclusion, we studied the relativistice laser-plasma interaction on three different gas targets:

- Sonic gas jet targets (helium plasma with $n_{e0} = 0.06\text{-}0.12 n_c$. Argon/hydrogen plasma with $1\,\%$ of hydrogen and $n_{e0} = 0.5\text{-}1 n_c$. The gas FWHM was $500\,\mu\mathrm{m}$. The peak laser intensity reaches $I = 2.5 \times 10^{20}\,\mathrm{W} \cdot \mathrm{cm}^{-2}$ ($a_0 = 10$).
- Shock blade targets with Argon/hydrogen plasma with $10\,\%$ of hydrogen and $n_{e0} = 0.15 n_c$, and a rear gradient below 100 um, illuminated by a peak laser intensity of $I = 1.2 \times 10^{20}\,\mathrm{W} \cdot \mathrm{cm}^{-2}$ ($a_0 = 7.4$).
- Supersonic shock gas jet with Argon/hydrogen plasma with $10\,\%$ of hydrogen and Helium/hydrogen plasma with $1\,\%$ of hydrogen with densities up to $n_{e0} = 0.15 n_c$, FWHM of 50 um, illuminated by a peak laser intensity of $I = 2.4 \times 10^{19}\,\mathrm{W} \cdot \mathrm{cm}^{-2}$ ($a_0 = 3.3$) with improve contrast of 1×10^{10} (from 1×10^{8}).

We observed that in the smooth gradient of an helium sonic target at $0.1 n_c$, we were able to propagate the laser to the target rear side. With shock targets at the same density, the laser could not cross the gas, and collapsed at the density peak position. The self-similar expansion of the plasma channel was observed on shock targets at sub-nanosecond timescale, and it shows evidence of a strong radiative shock in argon, while fast canal expansion in helium may be explained by the heating of the surrounding medium, radiating energy into the transverse shock wave. Forward electrons acceleration up to $(100 \pm 25)\,\mathrm{MeV}$ is observed for all targets, with a rising charge for higher plasma density, up to $0.3n_c$. We observed also the modulation of the electron beam in the transverse direction. These properties suggest a different acceleration regime than the bubble regime, and are potential evidences of Direct Laser Acceleration. Collimated, unstable electron beams could be seen at lower density, in accordance with PIC simulations, where acceleration in the cavity could occur at early stage of the propagation. We observed forward accelerated protons above 1 MeV with the sonic jet, but we couldn't identify the correct conditions to reproduce this result.

Chapter 5

Efficient laser production of energetic neutral beams

We demonstrate the production of a neutral and directional beam of hydrogen and carbon atoms up to 200 keV per nucleon, with a peak rate of 2.7×10^{13} atom/s. Laser accelerated ions are neutralized in a pulsed, supersonic argon jet with tunable density between $1.5 \times 10^{17}\,\mathrm{cm}^{-3}$ and $6 \times 10^{18}\,\mathrm{cm}^{-3}$. The neutralization efficiency has been measured by a time-of-flight detector for different argon densities. An optimum is found, for which complete neutralization occurs. The neutralization rate can be explained only at high areal densities ($>1 \times 10^{17}\,\mathrm{cm}^{-2}$) by single electron charge transfer processes. These results suggest new perspective for the study of neutral production and open discussion of neutralization at lower density. This work has been published in Plasma Physics and Controlled Fusion [Mollica et al., 2016].

Contents

5.1 Introduction

Laser-driven ion acceleration by intense, ultra-short, laser pulse has been experiencing numerous innovations in the past few years, new acceleration schemes have been proposed [Ter-Avetisyan et al., 2011; Silva et al., 2004; Esirkepov et al., 2004; Sylla et al., 2012a; Haberberger et al., 2012; d'Humières et al., 2013a], the development of large dedicated facilities around the world [Danson et al., 2015], and new proton energy records [Kim et al., 2013] have been obtained, which makes laser accelerated beams even closer to their applications. Less attention has been dedicated to neutral particles production with lasers, with nevertheless a recent regain in interest [Ter-Avetisyan et al., 2011; Schnürer et al., 2013; Rajeev et al., 2013]. Unaffected by electro-magnetic fields, neutral particles can penetrate deeper than ions into targets, and a compact laser-driven energetic neutral source could be of high-interest for research and industry, complementary to charged particles [Wolfe and Craver, 2008].

Neutral beams are usually created from negative ion beams, because their neutralization efficiency is high (electron stripping) even at high energy; while for positive ions (electron capture) it drops drastically above 200 keV/u. However the ease of stripping negative ions makes it difficult to conserve their charge during the acceleration process. The main neutralization paths [Wells, 1982] involve either recombination by electron capture of a positive ion beam passed through a vapor target or volume production by discharge of excited neutrals and electrons, a filter selecting only cold electrons and neutrals, that easily recombine in negative ions. A variant of the last mechanism is currently under development for ITER in Garching, Germany [Franzen et al., 2007]. The production of negative ions by laser-plasma interaction has been demonstrated with various mechanisms: by Coulomb explosion of CO_2 clusters with CO_2 lasers [Nakamura et al., 2009], by recombination in the cooling plasma created by a moderately intense femtosecond pulse impinging a solid target [Volkov et al., 2002] and by irradiation of water droplets with ultra-intense, ultra-short laser pulse [Ter-Avetisyan et al., 2011]. In recent developments, droplets as neutralizer medium have been used with success [Abicht et al., 2013; Schnürer et al., 2013].

5.2 Experimental set-up and results

In the present experiment, a laser-accelerated ion beam is neutralized during its interaction with a gas jet. Ions are accelerated by Target Normal Sheath Acceleration (TNSA) [Mora, 2005]. The high reliability of TNSA, compared to other laser-driven ion acceleration mechanisms, makes it an ideal source for neutralization experiments. In this regime hot electrons from the front (i.e. irradiated) surface of a solid target heat and ionize the rear surface, producing a plasma where charge separation induces a strong accelerating field. Hydrogen and carbon atoms, initially adsorbed at the target rear surface, are ionized and accelerated in this field to the MeV range. The resulting ion beam contains mainly protons and multi-ionized carbon atoms, it features a broad angular distribution ($\sim 20°$ for parameters close to our experiment [Lindau et al., 2005]) and a quasi-Maxwellian energy spectrum. The choice of neutralization by charge exchange is motivated by its robustness and reproducibility. Experimental data of charge transfer cross sections through noble gas are available, whereas interactions with more complex neutralizers, like clusters [Rajeev et al., 2013] or droplets [Ter-Avetisyan et al., 2011] are less documented.

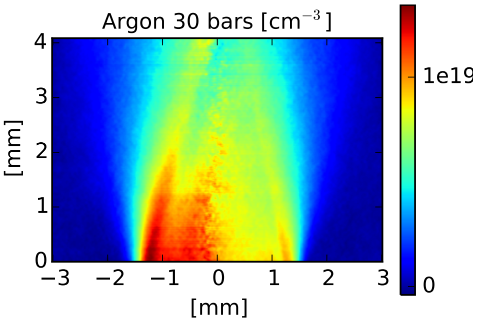

Figure 5.1 – (b) Density profile of the gas jet used for ion neutralisation. It is made from argon with backing pressure of 30 bars ($1.1 \times 10^{18}\,\mathrm{cm}^{-2}$ at beam height) measured by interferometry and reconstructed from Abel back-transform

In the proposed scheme (Figure 5.2), a Ti:Sapphire laser pulse (35 fs, 1.7 J) is focused at normal incidence on a 5 µm thick titanium foil with an Off-Axis Parabola ($f/\# = 2.5$, $I \approx 3 \times 10^{19}\,\mathrm{W/cm^2}$). The ion beam is neutralized by a pulsed, millimetric argon gas jet located on the ion beam trajectory at 16 cm from the source. The nozzle is supersonic (conical throat) with half-angle 10°, inner diameter 0.5 mm, outer diameter 2 mm. The back-pressure of argon is tunable from 0.1 to 40 bar and the argon density encountered by the ions ranges from 1.5×10^{17} to $6 \times 10^{18}\,\mathrm{cm}^{-3}$. A typical density map is shown Fig. 5.1. Surfacic (or areal) density is more relevant than density to describe charge transfer processes, and scales linearly with back-pressure and with distance from the nozzle (see Fig. 5.3) . This quantity is directly derived from gas jet characterization by wave-front sensor based interferometry [Plateau et al., 2010], it ranges from 3×10^{15} to $10^{18}\,\mathrm{cm}^{-2}$. In order to filter out the non-neutralized ions from the neutral beam, a filtering magnet is mounted after the gas jet. This magnet allows to get rid of any remaining charged particle in the beam after the neutralizer. The scattering due to the gas can also bend particles trajectories and limit the filtering magnet efficiency. To avoid this, a lead pinhole of 200 µm diameter is inserted between the foil target and the gas jet, selecting then a solid angle of 2×10^{-6} sr. The thickness of the pinhole enables to stop any particle outside the acceptance angle. A Thomson parabola spectrometer (TP) is used to measure the spectrum of the accelerated ions. The TP pinhole is set to select a solid angle of 5.3×10^{-7} sr. In order to estimate the amount and the energy distribution of the neutral particles, the TP spectrometer can be replaced by a time-of-flight (ToF) detector. A micro-channel plate (MCP) is mounted several meters away from the interaction point and the phosphor screen is replaced by an anode. Two distances D from the interaction point have been tested: 1.09 m and 2.61 m, without noticeable influence on the neutralization. The time-of-flight MCP selects a solid angle of 1×10^{-3} sr, which is much broader than the surfacic aperture of the first lead pinhole. The direct beam illumination area on the MCP detector is $24\,\mathrm{mm}^2$ when it is located at 2.61 m from the source. Electrons extracted by incoming particles on the MCP reach the anode and flow to the ground through a resistor. Measured with an oscilloscope, the current evolution in time gives the amount of incoming particles on the MCP, with a gain factor that can reach $\approx 1 \times 10^4$. Arrival time is related to the kinetic energy per nucleon of the particles.

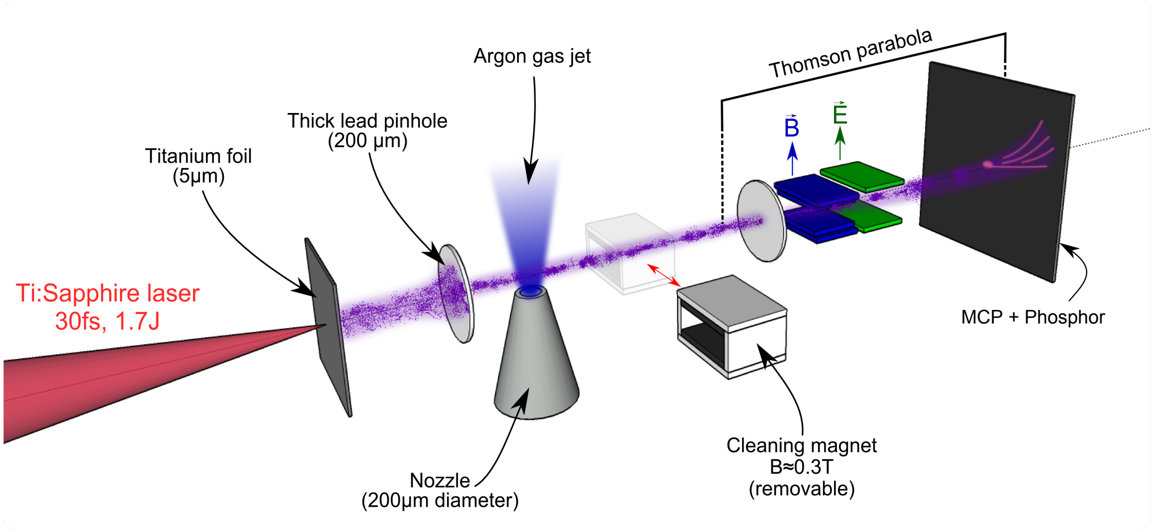

Figure 5.2 – Experimental set-up in Thomson parabola configuration, measuring ion spectra. To measure neutral spectrum the Micro Channel Plate (MCP) with phosphor is replaced by an MCP with anode, used as time-of-flight (ToF) diagnostic.

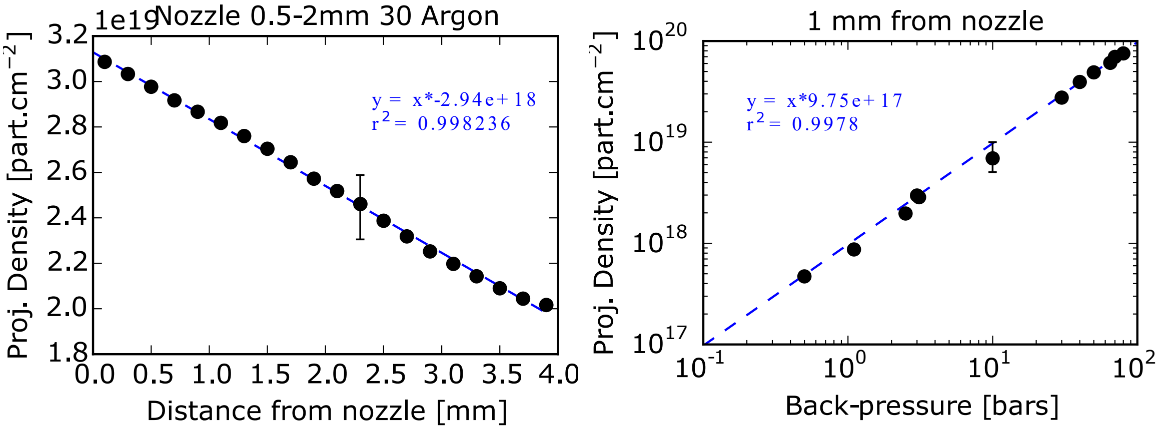

Figure 5.3 – (a) Projected (surfacic) density versus the distance from the nozzle tip for argon with 30 bar backing pressure. (b) Effect of the backing pressure on the projected density

5.2.1 Ions spectra

In a configuration without gas and without filtering magnet, the TP shows that the ion beam contains carbon ions with charge states from +1 to +5, with energies up to 500 keV/u, and protons with energies up to 3.8 MeV (Figure 5.4c). All ion populations present the same thermal-like spectrum profile with a cut-off. We assume a linear response of the detector, steady in time and free of saturation phenomena. In the Thomson Parabola, the MCP is coupled with a phosphor screen, imaged by a CCD. Absolute calibration has not been performed for this specific set-up, but calibration with CR39 can be found in Prasad *et al.* [Prasad et al., 2010, 2013] for comparable MCP and beam properties. MCP signal is shown to be ≈10 times higher with C^{6+} than with proton in the energy range of our experiment, and MCP response is roughly independent from the charge of the incident particle. We deduced that protons are predominant, with ≈ 2 times more protons than all carbon ions at 80 keV/u. When the gas jet is triggered, carbon signal and the lower energy part of the proton spectrum disappears (Figure 5.4b). Remaining protons, and the on-axis spot (i.e neutral particles and photons) get broadened, leading to the hypothesis that low energy ions had been either scattered or neutralized. Comparison between the proton signal with and without gas jet crossing is illustrated on Figure 5.4d). Protons above 500 keV are scattered but not neutralized. A part of protons below 500 keV are not detected in the TP spectrometer either because they are scattered or neutralized. This ambiguity motivates the use of a Time-of-flight detector.

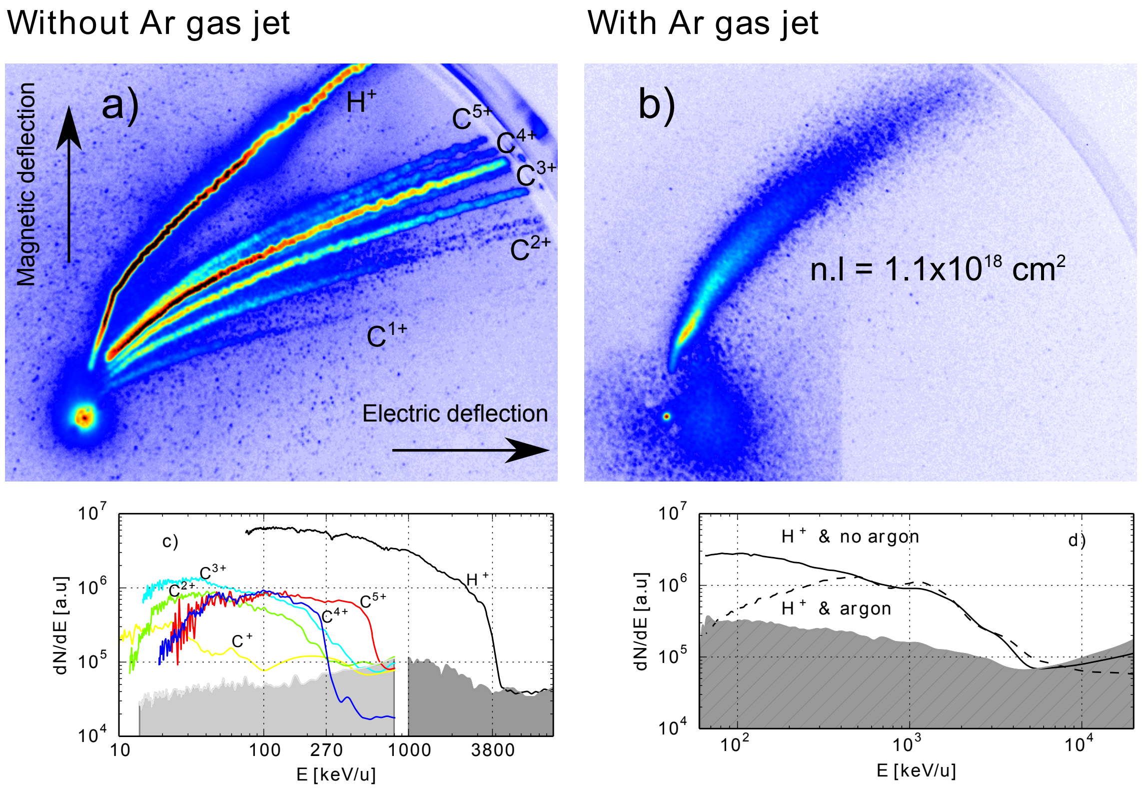

Figure 5.4 – (a) Thomson parabola traces obtained from set-up figure 5.2 without filtering magnet nor gas jet, and (b) with gas jet of areal density $1.1 \times 10^{18}\,\mathrm{cm}^{-2}$). (c) Spectra of protons and carbon ions accelerated by TNSA from a typical beam, same setup as a) showing the predominance of protons over carbon ions in the range 60-100 keV/u. d) Spectra of protons from b) (dashed line) compared with spectra in the same experimental set-up, but without gas jet. The proton amount above 500 keV stays unchanged. In both c)and d) light gray areas define the detection limit for carbon, dark gray areas the detection limit for proton.

5.2.2 Neutral spectrum

The ion ToF signal (blue curve on Figure 5.5a) shows three distinct features: 1) The photon peak coming from the laser-target interaction (used as a reference for time vs. energy calibration). This peak is stable shot to shot and is visible in all gas and magnet configurations. 2) Peaks of the incoming protons at 125 ns and 260 ns, corresponding to energies of respectively 2.2 MeV/u and 530 keV/u. The Thomson parabola does not show traces of carbon ions at these energies and so these particles can only be protons. 3) Trace of slower ions, both protons and carbons, after 400 ns (i.e. <200 keV/u).

In absence of gas, the filtering magnet removes all charged particles, and the MCP signal is reduced to noise (green curve in figure 5.5a), showing the absence of neutrals in the TNSA beam. Finally, the addition of gas between the target and the filtering magnet induces an increase in current above noise-level on the ToF MCP for particles with energy up to 200 keV per nucleon (red curve in figure 5.5a-b). The first lead pinhole selects a narrow solid angle, ensuring that all scattered ions are cleaned by the magnet and the ToF signal contains only neutral atoms. This is confirmed in TP configuration, where no ions are detected. The neutral flow peaks at 2.7×10^{13} atom/s for 1 bar Argon and improved laser conditions, different than those of Figure 5.5a). The overall efficiency of neutralization of the ions is covered in the next section.

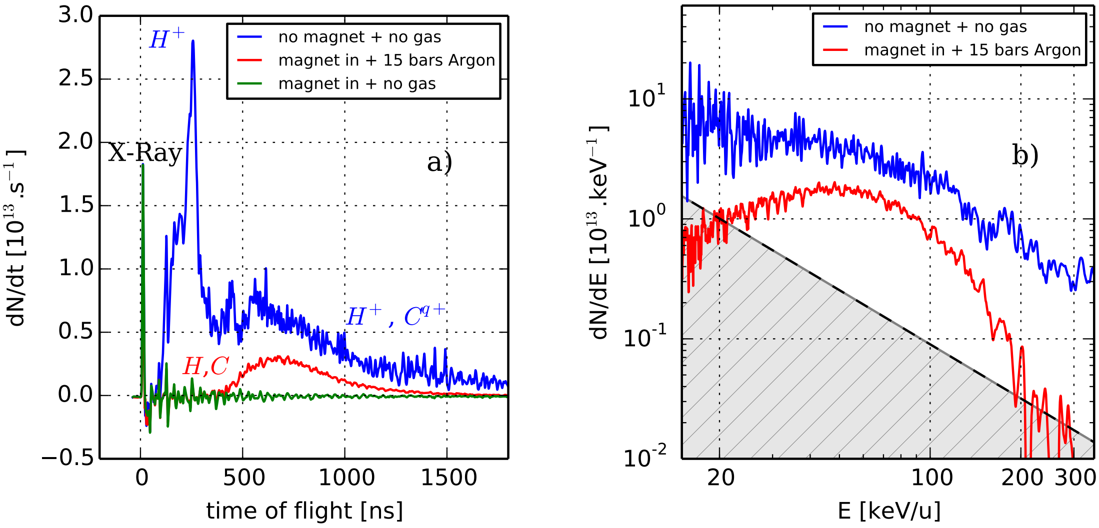

Figure 5.5 – (a) ToF signal as a function of time of arrival, for a flight distance of 2.61 meters. It features: 1) the photon peak at t= 8.7 ns, similar for the three curves, 2) (blue) TNSA ion flow, without filtering magnet nor neutralizer, 3) (green) cleaned signal by the filtering magnet and without gas: no remaining ions can reach the ToF detector, 4) (red) neutral signal after ion propagation through 2 mm of argon at 15 bar (i.e 5.5×10^{17} cm^{-2} in areal density), with filtering magnet in place, ensuring the red signal to be actually neutral particles. (b) Same ToF signal as function of energy, same color as (a), hatched area below detection level.

5.3 Neutral beam composition

Charge transfer model, detailed in this section, predicts the nature and spectrum of the neutral beam for argon surfacic density higher than 10^{17} cm^{-2}. Considering that 1) protons are predominant over carbon ions in the incident beam (Figure 5.4c) 2) Electron capture is more likely for proton than carbon during the propagation, it comes that the neutral beam is made predominantly of hydrogen.

5.3.1 Charge transfer model

Propagating through the gas, the ion beam undergoes two antagonist processes, single-electron capture and loss, whose competition sets the overall neutralization efficiency. The single-electron capture process of a projectile P of charge q impinging argon is quantified by the cross section $\sigma^{j}_{P:q,q-1}$, where j is the final charge state of the argon target. It can be represented as:

$$\mathrm{P^{q+}} + \mathrm{Ar^{0}} \xrightarrow{\sigma^{j}_{P:q,q-1}} \mathrm{P^{(q-1)+}} + \mathrm{Ar^{j+}}$$

and the single-electron loss process as:

$$\mathrm{P^{q+}} + \mathrm{Ar^{0}} \xrightarrow{\sigma^{j}_{P:q,q+1}} \mathrm{P^{(q+1)+}} + \mathrm{Ar^{j+}}$$

Only the total cross sections are relevant to derive the overall neutralization efficiency: $\sigma_{P:q,q\pm1} = \sum_j \sigma^{j}_{P:q,q\pm1}$. Collision of a moderately energetic ion (10 keV/u to 1 MeV/u) with an inert gas target triggers indeed more complex mechanisms than those described above: double- and triple-electron capture and loss mechanisms can occur, but their cross sections in the energy range of our experiment are one to two orders of magnitude smaller than their single-process counterparts [Graham et al., 1984] and will be discarded in the following analysis. The relative ions populations of charge q, named N_q, with q ranging from 0 to 6 in carbon case, evolve along propagation length l with the set of differential equations:

$$\frac{\partial N_q}{\partial l} = n_{Ar}(N_{q+1}\sigma_{q+1,q} + N_{q-1}\sigma_{q-1,q} - N_q\sigma_{q,q+1} - N_q\sigma_{q,q-1}) \tag{5.1}$$

where n_{Ar} is the argon density. It is interesting to note that in the case where $n_{Ar}l\sigma \gg 1$ (i.e the surfacic density is bigger than the inverse cross section) the left derivative gets close to zero and the relative populations stabilize such as for all q:

$$\frac{N_q}{N_{q-1}} = \frac{\sigma_{q-1,q}}{\sigma_{q,q-1}} \tag{5.2}$$

Computation of all population ratios requires the knowledge of all cross sections for hydrogen, proton and carbon ions. The charge capture and loss cross sections for these particles in argon are in the range 10^{-16} to $10^{-15}\,\mathrm{cm}^2$ and the surfacic density of our experiment ranges from 3×10^{15} to $10^{18}\,\mathrm{cm}^{-2}$. Above $10^{16}\,\mathrm{cm}^{-2}$, the population ratios derived from equation (5.2) are a good approximation of the equation system 5.1.

Charge transfers between projectile ions and inert gas target involve several competing mechanisms of equal magnitude, especially for projectile ions at intermediate velocity [Bohr and Lindhard, 1954], i.e. velocity close to v_0 (atomic velocity unit: electron velocity on first Bohr radius $v_0 = \alpha c$ with α the fine structure constant and c the speed of light). To compare with ion velocities in our experiment, a 100 keV/u ion has a velocity of $2v_0$, and capture and loss processes are then expected to be of the same order of magnitude. Cross sections of single-electron capture and loss in such conditions have been extensively measured during the last decades [Betz, 1972; Phaneuf et al., 1978; Graham et al., 1984], especially for protons in collision with argon

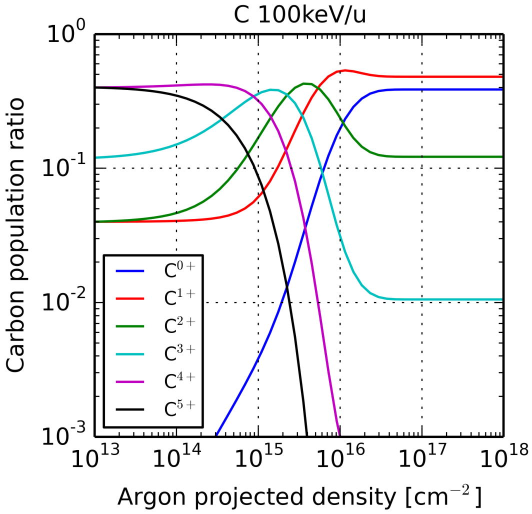

Figure 5.6 – Evolution of relative carbon population with the surfacic density. We used here the initial relative population of carbon derived from TP data (Fig. 5.4. carbon population is derived from Eq. 5.1 with cross section data shown in fig. 5.7).

target [Toburen et al., 1968; Allison, 1958].

Data for carbon ion projectiles are more scarce, with the exception of Melo *et al.* [Melo et al., 1999] for C^{3+} in argon in the range of 80 to 290 keV/u and a comprehensive data set by Dmitriev [Dmitriev et al., 2008] for a wide range of carbon species crossing inert gas in the range of 40 to 330 keV/u. Summary of these data can be found in figure 5.7. Missing capture cross section for C^{5+} where derived with Knudsen *et al.* [Knudsen et al., 1981] and Schlachter *et al.* [Schlachter et al., 1983] scaling laws. Knudsen scaling law is widely used and has been found to be in very good agreement with experimental points for C^{3+} ions [Santos et al., 2010], and oxygen ions [Boman et al., 1989] in the energy range of our experiment. In this model, capture probability scales with $q^{1.8}$ in the range 10 keV/u to 3 MeV/u (where q is the ion charge). Integrating these carbon cross sections into the set of equations 5.2 leads to carbon population ratios shown Fig. 5.6. We used as initial conditions population ratios derived from Fig. 5.4.

Finally, in the energy range of the neutral signal (30 to 200 keV/u), capture and loss processes for either species are of the same order of magnitude, leading to significant albeit not total neutralization of the ion beam.

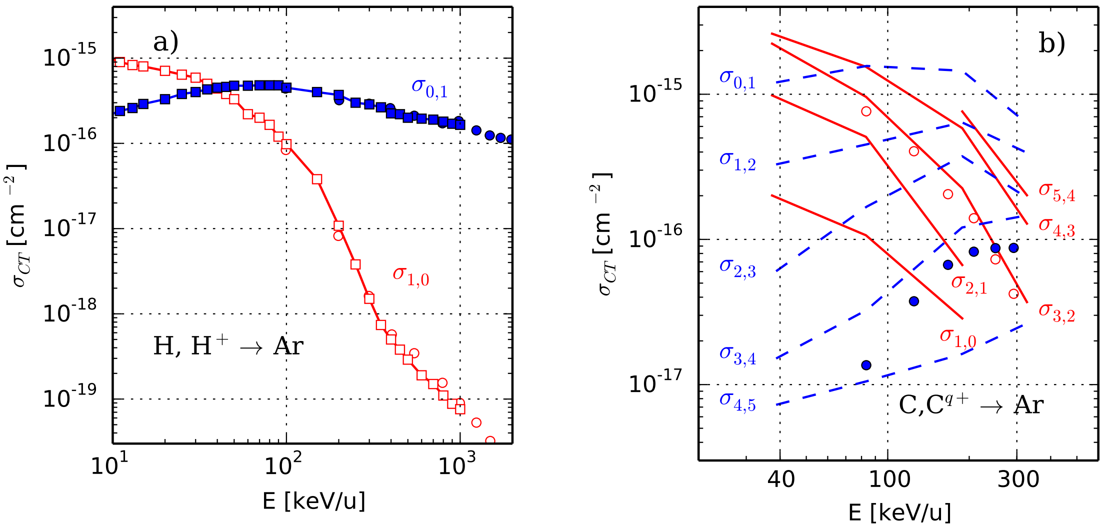

Figure 5.7 – (a) Single-electron capture (red, open symbols) and loss (blue, full symbols) cross sections for protons and atomic hydrogen on argon, as function of energy. Experimental data from Toburen *et al.* (open circle: capture, full circle: loss ; [Toburen et al., 1968]) and Allison *et al.* (open square: capture, full square: loss ; [Allison, 1958]). (b) Single electron capture (solid line) and loss (dashed) cross sections of carbon ions in argon derived from Dmitriev's experimental data [Dmitriev et al., 2008]. Experimental data of Melo *et al.* [Melo et al., 1999] on C^{3+} (open circle: capture, full circle: loss).

5.3.2 Neutralization discussions

Figure 5.8 shows the neutral fraction: Experimental data (circle) represents neutral over ion signal ratio on the ToF MCP, integrated from 60 to 100 keV/u. ToF Ion signals above 100 keV/u is saturated, which restrains the analysis below this value. The dashed line is the neutral fraction for hydrogen from resolution of the set of equation 5.1 in the hydrogen case. Derivation of equation 5.1 shows that hydrogen and neutral carbon, in the range 60-100 keV/u, reach at most respectively 25 % of hydrogen species and 3.5 % of all carbon species. The expected neutral beam contains then only ≈ 1 % of carbon ions, the rest being hydrogen. Experimental ratio of final neutral count over initial ion count of all particles of energy 60 to 100 keV/u, is so expected to be 25 %. As shown in figure 5.8, this ratio is coherent with observed ratio at high density, but doesn't explain the maximum efficiency at $3.8 \times 10^{16}\,\mathrm{cm}^{-2}$. A similar carbon neutralization experiment through gas medium by Schnuerer *et al.* [Schnürer et al., 2013] noticed also unexpected electron capture. Recent work [Rajeev et al., 2013] outlines the role of target excitation: excited argon clusters would loose electrons with higher probabilities and may explain the improved neutralization efficiency. Excitation would come from electrons or X-rays concurrent with the ion emission [Mora, 2003; Popescu et al., 2005], however, Schnuerer *et al.* tried to increase the distance between the source and the neutralizer, thus decreasing an hypothetical excitation by a factor 300, but they couldn't confirm any dependency with this parameter.

TNSA model [Mora, 2003, 2005; Macchi et al., 2013] predicts than the TNSA beam (excluding the front shock) is globally neutral. Assuming an equal number of electrons

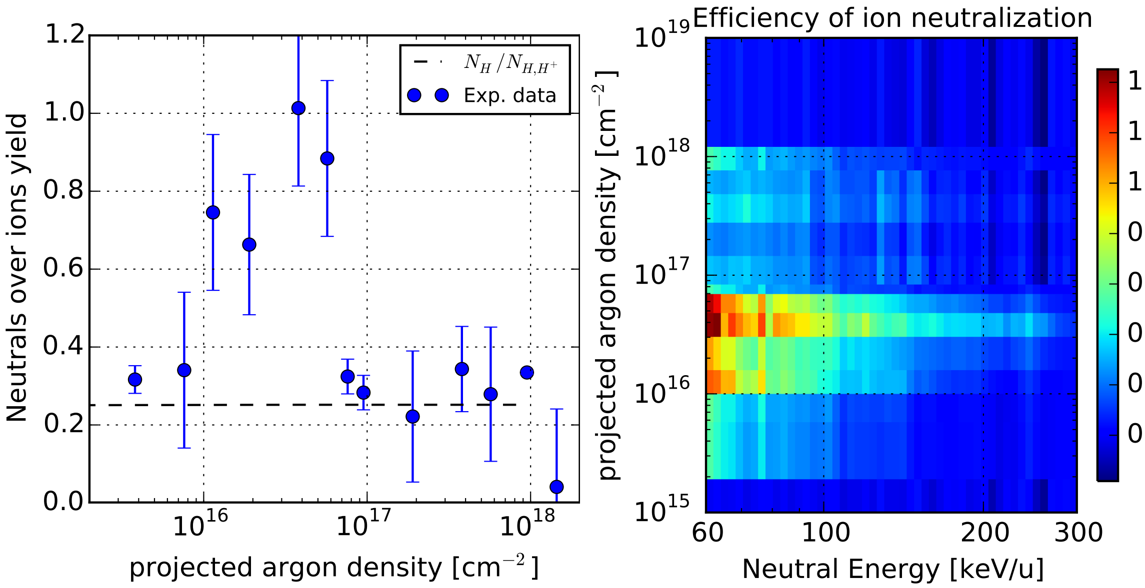

Figure 5.8 – (a) Experimental and computed neutralization efficiency of ions in the range 60-100 keV/u crossing an argon jet, for different argon surfacic density. Experimental data show the ratio of integrated signal on the ToF MCP between the case with magnet and gas over the case without magnet and gas, both in the same energy range. Computed neutralization efficiency (dotted: hydrogen) derived from equations 5.1. (b) Neutralisation efficiency dependency with the surfacic argon density and the projectile energy. Value greater than one are the effect of low statistics.

and ions at same velocity, we derived a maximum of $\approx 10^{12}$ electrons in the range 50-150 eV (neglecting electron recirculating through the target). At the gas jet plane, it leads to $\approx 10^{15}$ electrons per cm^2, so argon atoms outnumber electrons by several orders of magnitude. Furthemore electron impact ionization of argon [McCallion et al., 1992] is maximum for electrons at 100 eV. Cross sections reach 2.5×10^{-16} cm^2 for single ionization and 2×10^{-17} cm^2 for double ionization. Total cross section for electron impact excitation for the 16 most likely excitation levels or argon [Chutjian and Cartwright, 1981] is below 2×10^{-17} cm^2 for electron in the range 30 to 100 eV. In conclusion, majority of 100 eV electrons are colliding and ionizing argon, but only a fraction of argon atoms is ionized, and an even smaller fraction is in metastable excited states.

A review of X-rays production by intense laser-solid interaction is beyond the scope of this work. Nevertheless, argon absorption [Chantler, 1995] of black-body radiation of the target (10-100 eV photons) is non-negligible and ranges from $\approx 5\,\%$ to $99\,\%$ for argon surfacic density between 10^{16} cm^{-2} and 10^{18} cm^{-2}. Absorption at this energy results in ionization [Marr and West, 1976] of outer shells of argon, but no conclusion can be drawn without absolute X-ray spectrum.

Ionizing argon doesn't favor charge capture by protons: Bohrs's scaling laws show that the capture cross section scales with the inverse of the orbital velocity of the to-be-captured target electron (Eq 4.3 in [Betz, 1972]. To the best of our knowledge, no experimental data is available for Ar$^+$. In the case of H$^+$ impacting Li or Li$^+$, reduced capture cross-section induced by target ionization is observed [Varghese et al., 1984; Sinha et al., 1982].

5.4 Conclusions

In conclusion, we demonstrated the possibility of creating a neutral hydrogen beam by collisional recombination of TNSA accelerated protons. The beam presents a broad spectrum, inherited from the ion spectrum, with atomic kinetic energy up to 200 keV/u. The neutral conversion efficiency can reach ≈100 % for incident protons at 80 keV through an areal density of $3.8 \times 10^{16}\,\mathrm{cm}^{-2}$, a value far above prediction from single charge transfer models, but in qualitative agreement with observations from Schnuerer *et al.* [Schnürer et al., 2013]. For neutralizer density higher than $10^{17}\,\mathrm{cm}^{-2}$, the neutralization ratio is coherent with single charge transfer models. Soft X-rays and co-propagating electrons (both in the 10-100 eV range) could ionize a fraction of argon targets, but this mechanism doesn't favor electron capture. Further experiments are needed to investigate the possible influence of pre-excitation and cluster formation on the charge exchange process, and to explain the observed behavior at low density. Exploration of these mechanisms can open paths toward a better comprehension of the neutralization of ion beams during their propagations.

Conclusion and Perspectives

The development of multi-Petawatt laser facilities across the world accelerates the need to bring laser-driven ion acceleration closer to its applications. While promising new mechanisms on ultra-thin solid targets deliver new laser-driven ion energy records, the development on regenerative targets is the best path to achieve high repetition rate laser-based ion acceleration. In near-critical or critical targets, several promising regimes have been described, such as Collisionless Shock Acceleration or Magnetic Vortex Acceleration. Few experimental demonstrations of these mechanisms has yet been achieved. Low repetition rate CO_2 laser experiments used the long laser wavelength to relax constraints on gas density and gradients, and managed to launch CSA. We emphasize the importance of the plasma tailoring in these experiments, mandatory to launch CSA. On the other hand, experiments claiming to indirectly observe MVA did not provide direct, in situ, measure of the vortex magnetic field. Yet forward acceleration of ions with a femtosecond laser in gas jet is still to be achieved.

We saw that requirements on plasma density of these regimes are at the edge of what is possible for high-pressure state-of the art gas jet. But gradients are the most critical: in PIC simulations, both MVA and CSA require gradients of only few wavelengths, while CSA has been demonstrated in pre-tailored targets achieving comparable gradient values. In the continuity of numerous targets innovations, we demonstrated the possibility to tailor the density profile of a supersonic gas jet by superposition of shock waves, using a compact nozzle design. Our nozzle achieved an atomic density of helium of $3.5 \times 10^{20}\,\mathrm{cm}^{-3}$ ($n_e = 0.4n_c$) with a peaked density profile of FWHM 120 µm at safe distance from the nozzle (600 µm). These gradients are still not steep enough to drive MVA or CSA, but this new nozzle presents an integrated solution that uses the inherent steep profile of supersonic shocks. Success on laser-driven acceleration in gas can only come with a strict control of the target and its gradients, and this nozzle type open new possibilities in this domain, more robust and reproducible than blade apparatus.

In the smooth gradient of an helium sonic target at $0.1n_c$, we were able to propagate the laser to the target rear side. With shock targets at the same density, the laser could not cross the gas, and collapsed at the density peak position. The self-similar expansion of the plasma channel was observed at sub-nanosecond timescale, and it shows evidence of a strong radiative shock in argon, while fast canal expansion in helium may be explained by the heating of the surrounding medium, radiating energy into the transverse shock wave. Forward electrons acceleration up to (100 ± 25) MeV is observed, with a rising charge for higher plasma density, up to $0.3n_c$. We observed also the modulation of the electron beam in the transverse direction. These properties suggest a different acceleration regime than the bubble regime, and are potential evidences of Direct Laser

Acceleration. Collimated, unstable electron beams could be seen at lower density, in accordance with PIC simulations, where acceleration in the cavity could occur at early stage of the propagation. We observed forward accelerated protons above 1 MeV with the sonic jet, but we couldn't identify the correct conditions to reproduce this result. Finally we studied the neutralization of a laser-driven ion beam by neutral argon. In accordance with other publications, we found an excess of neutralisation in the range 50 to 150 keV, and negligible neutralization above 1 MeV, where the neutralization rate is well described by single electron charge transfer cross sections. Further experiments are needed to isolate the mechanisms improving the neutralization.

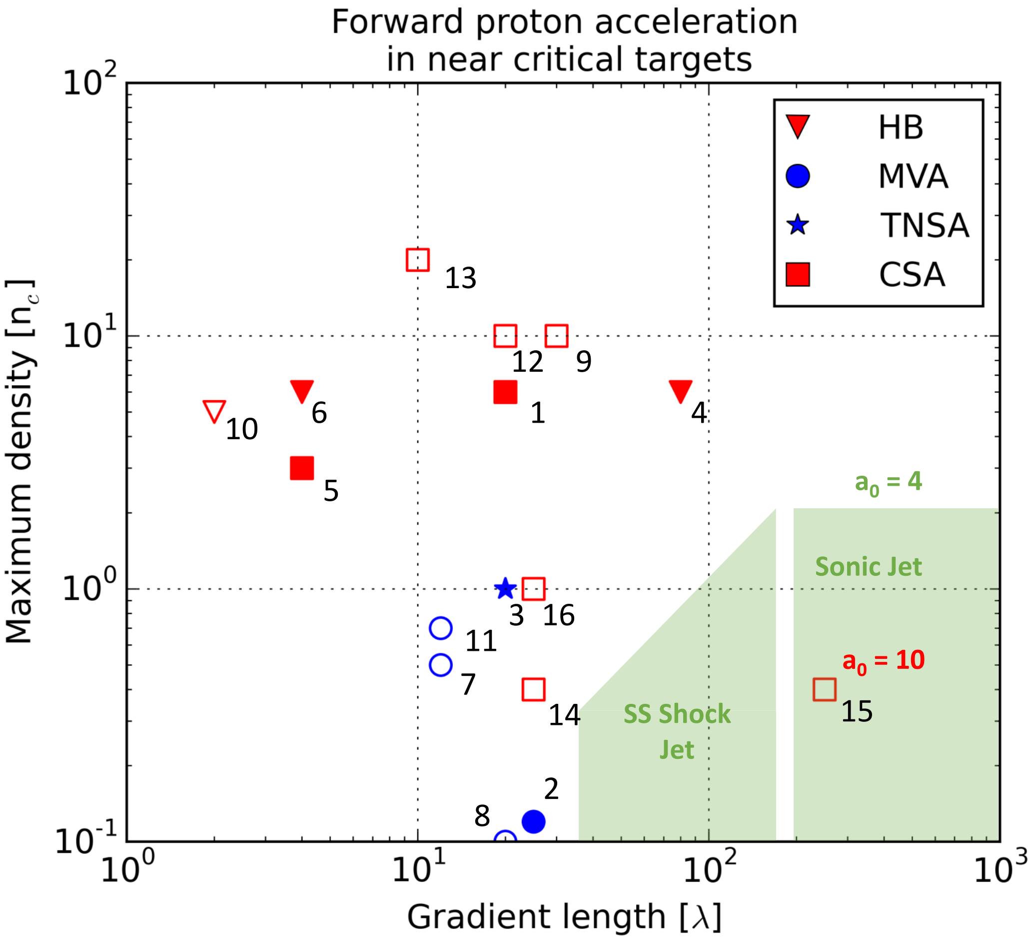

Figure 5.9 – Parametric space of target explored for ion acceleration in near-critical density target. The green area is the parametric space explore in this thesis at $a_0 = 4$. Experimental work are shown with solid markers, simulation in hollow ones. These works feature MVA (○), Hole boring (HB ▽), TNSA (⋆) and CSA mechanisms (□). Subscript number denotes the reference : 1: [Haberberger et al., 2012];2: [Willingale et al., 2006];3: [Antici et al., 2009];4: [Palmer et al., 2011];5: [Zhang et al., 2015];6: [Tresca et al., 2015];7-8: [Matsukado et al., 2003];9: [Silva et al., 2004];10: [Macchi et al., 2005];11: [Nakamura et al., 2010];12: [Fiuza et al., 2012];13: [Macchi et al., 2012];14-15-15: [d'Humières et al., 2013b]

Perspectives

This work is a first step towards ion acceleration by laser from self-replenishing targets. These targets open the way for high repetition rates, and bring closer laser-driven ion acceleration to medical applications and protontherapy, where control of the ion sources is critical. This work opened as well ion acceleration physics to new fields of plasma physics, like two streams mixing, Weibel instability in vortex, plasma solitons. We set a limit for the range of interaction parameters suitable for laser driven ion acceleration and defined the relevancy of specific diagnostics. It enables us to derive several assumptions on the future research paths for laser-driven ions in gas. As we have seen, this goal cannot be achieved without perfect control of the target gradients and profiles, and a perfect monitoring of the interaction. First I will describe the path towards future target innovations, second I will present the diagnostic improvements necessary to monitor the interaction. Third I suggest a realistic roadmap toward laser-driven ion acceleration in gas jets.

Target Innovation

The high-pressure electrovalve works perfectly above 400 bar, but reached its operation limits because of the small nozzle aperture preventing the proper closing of the valve. This issue could be solved by the development of an exhaust aperture. By ensuring a free gas flow after the laser-plasma interaction, the sealing ball would come back properly in position. With such development, density up to $2n_c$ could be reached in helium, bringing closer the MVA and CSA models described in PIC simulations. Without a full characterization of its clusterization, argon gas must be avoided. Exact plasma density cannot be known, and is likely to be very inhomogeneous at early time. Scattering on clusters debris could be an explanation for the argon plasma opacity against the probe beam, even at underdense densities. Supersonic shock nozzle could be improved by investigating the effect of turbulence and temperature, with the objectives to decrease the hydrodynamic shock width. CFD software has shown accurate prediction, but cannot be substituted to characterization on a test stand. Few machining providers of micrometric nozzle meet the quality standards needed for a correct flow tailoring. Nozzles must be designed in close collaboration with providers, to ensure the compatibility with their machining processes. It should trigger a questioning on innovative ways of machining. For instance in a near future, additive machining would give access to new shapes and designs. It would relieve machining constraints on asymmetric shock nozzles for instance, reproducing the effect of a blade in a supersonic shock. Smooth front-gradients are better for the laser injection in the plasma, while steep rear-gradient are adapted to ion acceleration. Experimental results with CO_2 shows the importance of plasma tailoring by laser. Part of the main laser beam, or an additional laser beam, could be used to pre-heat the plasma picoseconds before the main pulse. Such heating would start plasma expansion, decreasing its density, while leaving other part of the gas untouched. Relevancy of the resulting density gradient for laser ion acceleration should be evaluated before further developments.

Diagnostics

Ion detection and plasma density alone do not give sufficient physical information about the interaction. In absence of ion signal and quantitative data, interaction parameters cannot be adjusted towards ion acceleration regimes, and development of quantitative diagnostics is mandatory. First, plasma density in the near-critical, relativistic regime is fairly perturbed. Thus special care must be taken in the density probing design. High optics numerical aperture > 0.2 should limit effects of the probe scattering. Probe phase reconstruction is very sensible to intensity homogeneities as well. Density diagnostics may be blinded by intense non-linear Thomson scattering, to solve this, a filter in the imagery Fourier plane would limit imagery collection from the interaction itself and ensure collection of the probe light only. Higher magnification than those presented into this work would provide meaningful data on the channel formation at early time, on plasma shocks or magnetic vortex. Electron spectrum yields valuable information on the laser propagation regime. Therefore a dedicated, shielded and calibrated electron spectrometer should be designed for further studies. Both high energy (>10 MeV) and low energy part (<10 MeV) of the spectrum must be measured, as they result from different mechanisms. An electron spectrometer could be as well installed backward to measure the electronic return current, as a first step toward demonstration of two-stream phase mixing heating. Electron temperature could also be derived from the Thomson scattering of the laser. Plasma channel expansion may give an estimate of the ion temperature, a critical parameter for plasma shock generation, and otherwise difficult to measure. Before this PhD, a SPL team performed magnetic field measurement of the propagation of a femtosecond intense laser into a plasma [Flacco et al., 2015]. Similar efforts should now be applied to magnetic field measurement in near-critical targets. Poloidal magnetic field data would be a direct evidence of MVA, and would complete the interaction picture. Such diagnostic relies on the Faraday rotation of the probe beam when it crosses a magnetized plasma. The result is the convolution of the poloidal B-Field with the local density. In order to deconvolve the measure and to reconstruct the magnetic vortex, both density and poloidal B-field should be acquired simultaneously on the same imaging line.

Finally, ion detection is also a challenge, due to its unknown directivity, charge, and divergence. Thomson Parabola and Time of Flight, despite spectrum acquisition, have only limited aperture, and off-axis ions may be missed, especially if alignment between the laser axis and the diagnostics is off. Scintillators and CR39s are difficult to interpret because of the various effects that may cause "false positive", like electrons, or X-rays. A new ion detector name RadEye has recently been commercialized. It features $\sim 40\,\mu\mathrm{m}^2$ "pixel" for a total surface of several cm^2. Its response is linear with respect to ion fluence in a fluence range compatible with laser-driven ion beam. This new diagnostic could be an in-line alternative to scintillators, and is more sensible than a B-404 plastic scintillator, and less fragile than MCPs.

Experimental Roadmap

As a first step, diagnostics must be developed and tested with a controlled target, and an axi-symmetric plasma. For instance a 400 µm diameter supersonic helium jet, whose density is gradually increased from $0.01 n_c$, where small laser filamentation is expected, to $\sim 0.3n_c$, when the laser is expected to totally deplete in the plasma. Plasma density must be imaged with magnification resolving the plasma channel width ($\sim 10\,\mu$m) with high numerical aperture. Both transverse expansion and spectrum of the electron beam should be measured with respect to target density and laser energy, bringing clear confirmation or infirmation of Direct Laser Acceleration. Channel expansion speed at picosecond time scale coupled with direct laser transmission measurement, and calibrated electron charge measures would provide a picture of the laser depletion and the energy transferred to ions. No technological obstacles are present for these first steps, as density and electron diagnostics are already developed. The second and more challenging step is the development of the poloidal magnetic field diagnostics, still with a controlled, supersonic helium target. Success lies in the probe beam and polarizer quality, and in the quality of the density reconstruction. Analysis software and experimental methods have already been developed by Flacco et al. at LOA, limiting incertitudes relative to this diagnostics. In parallel, development of exhaust safety valve on high pressure electrovalve would enable the valve to close properly. Safer operating conditions and neutral densities above n_c with nozzle diameters below $400\,\mu$m would become possible. It would reduce the size of the low density tail surrounding the peak gas density, improving laser propagation toward the target rear side. Simulation effort should explore smoother throat designs limiting turbulences, thus steepening the gas gradients. The last step would be to applied the previous diagnostics to supersonic shock targets, with hydrogen gas, or a mixtureof helium/hydrogen. Proton detection diagnostics should not limit the operation of the other diagnostics, as the main objective is to give a complete picture of the plasma density, ion temperature, accelerated electrons, laser absorption and magnetic vortex. Even without detection of laser driven protons, such roadmap would provide an exciting insight picture of interaction of an ultra-intense, ultra-short laser in a near-critical plasma. Demonstration of magnetic vortex in such experiments would be the world first. Based on the first explorations of this thesis work, we set a limit for the range of interaction parameters suitable for laser driven ion acceleration and we evaluated diagnostics requirements in this novel interaction regime. I hope that it will open the path for further and fascinating developments in this fields.

Appendix A

Annexes

A.1 Modified Hartmann wavefront sensor

A.1.1 Motivation

First wavefront sensor is attributed to Hartmann in 1900. Hartmann made use of a mask of regularly spaced square holes. Placing this mask near the imaging plane of a telescope, holes break the incoming light into an array of light beams, resulting on distincts star images in the image plane. Lateral displacement of each image regarding to the hole position is proportional with the wavefront tilt and with the distance between mask and image plane. It is therefore possible to link these tilt samples to a phase map of the incoming light, and to decompose it on a relevant aberration base, like Zernike polynomials. Increasing the distance between mask and image plane leads to better resolution, in the limit imposed by diffraction. Hartmann Masks (HM) have numerous advantages : it possible to retrieve both intensity and wavefront, and in the limit allowed for ray-tracing, it is an achromatic technique. One the downside, transmission is poor, and it fosters innovative variations, like the Shack-Hartmann lens array. In this variation proposed in the 60's [Shack and Platt, 1971], the mask is replaced by a lens array. Then, the resolution and image plane are imposed by lenses size and focal length. Transmission is enhanced but lenses introduce some achromaticity. Shack-Hartmann wavefront sensor are widely used in adaptive optic system, in astronomy or eye surgery.

A.1.2 Hartmann Mask

In order to increase resolution and minimize blurring effects due to diffraction, an alternative Hartmann mask, with achromatic design, has been proposed by Primot et al. [Primot and Guérineau, 2000]. This Modified Hartmann Mask (MHM) enables compact, achromatic QWLSI. MHM has been implemented by *Phasics S.A.* in France, and we used their system (SID4-HR) including high-resolution camera, MHM, and analysis software, in order to retrieve probe beam phase fronts. We will analyze in the following section properties of the MHM.

At close distance from the mask, ray tracing approximation is no longer valid, and interference figure is the intensity of the sum of all orders of diffraction. Let's consider first a classic Hartmann mask, simplified in 1-D as shown Fig. A.1a), with square holes

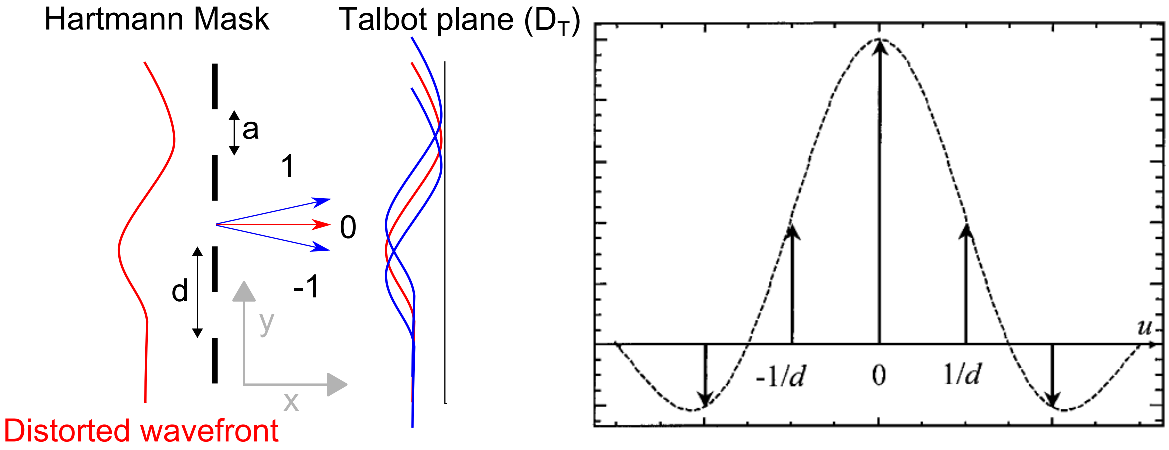

Figure A.1 – Left :Schematic representation of a 1-D Hartmann mask. The HM, made from regularly spaced square holes of pitch d and size a, act as a grating, first orders of diffraction are represented with their directions. Right : (from [Primot and Guérineau, 2000]) Relative intensity of first diffraction orders, with $u = k_y/2\pi$ in x-axis. Orders of diffraction are distant by $1/d$ in u coordinate, and modulated by $\sin(\pi ua)/\pi ua$

of size $a = 66\,\mu\text{m}$ and pitch $d = 100\,\mu\text{m}$. Transmission function of the mask is then :

$$t(y) = [\Pi_a * \text{III}_d](y) \tag{A.1}$$

Where Π_a denotes the gate function of width a, III_d the Dirac comb function of period d and $'*'$ stand for the convolution operation.

Let's consider an impinging wave on the grating with a scalar field:

$$E(x = 0, y) = E_0 e^{i2\pi g(y)/\lambda} \tag{A.2}$$

The interference pattern will have the best contrast in a plane called *Talbot plane* [Primot and Guérineau, 2000]. As contrast is critical for phase reconstruction, CCD chip is placed at Talbot distance D_T behind the HM. For the MHM, compacity can be improved and the CCD plane can be put at $D_T/6$. The Talbot plane is defined as the plane where orders of diffraction from a grating interfere in such way that they reconstruct the initial transmission function : all orders of diffraction have relative $0[2\pi]$ phase shift. Despite being called some time *self-imaging*, this effect must be interpreted as an interference and not as an image, as no correlation exists between a given hole and any specific intensity features. This effect occurs at distance $D_T = 2d^2/\lambda$ [Kim et al., 2012]. For the a grating of period/pitch $d = 100\,\mu\text{m}$ it gives $D_T = 40\,\text{mm}$ at $\lambda = 500\,\text{nm}$. Despite Fraunhofer approximation requiring $D >> 2a^2/\lambda = 13\,\text{mm}$, it still give meaningful results close to the experiment (see Primot et al. [Primot and Guérineau, 2000]). On a plane at distance D, Fraunhofer equation gives :

$$E(x = D, y) = \frac{e^{ikD}}{i\lambda D} e^{iky^2/2D} \mathbf{TF}\left(tE\right)\left(y/\lambda D\right) \tag{A.3}$$

Where $\mathbf{TF}(f)(k) = \int f(y) e^{-2i\pi ky} dy$ is the unitary Fourier Transform of f and t the transmission function.

$$\begin{aligned} E(D,y) &= \frac{e^{ikD}}{i\lambda D} e^{iky^2/2D} \left[\mathbf{TF}(t) * \mathbf{TF}(E)\right](y/\lambda D) && \text{(A.4)} \\ &= \frac{e^{ikD}}{i\lambda D} e^{iky^2/2D} (a/d) \left[\mathbf{sinc_{a\pi}}\text{Ш}_{\mathbf{1/d}} * \mathbf{TF}(E)\right](y/\lambda D) && \text{(A.5)} \\ &= E_0(D) e^{i\Psi(y,D)} \left[\mathbf{sinc_{a\pi}}\text{Ш}_{\mathbf{1/d}} * \mathbf{TF}(E)\right](y/\lambda D) && \text{(A.6)} \end{aligned}$$

As a and d are roughly equal, the cardinal sinus decreases quickly for $u > 1/d$ (Fig A.1), and then the transmission fourier transform $\mathbf{sinc_{a\pi}}\text{Ш}_{\mathbf{1/d}}$ is restricted to the sum of the first orders of diffraction : -1,0,1.

$$\begin{aligned} E(D,y) &= E_0(D) e^{i\Psi(y,D)} \left[\left(C_0\delta(0) + C_1\delta_{1/d} + C_{-1}\delta_{-1/d}\right) * \mathbf{TF}(E)\right](y/\lambda D) && \text{(A.7)} \\ &= E_0(D) e^{i\Psi(y,D)} \sum_{p=-1}^{1} C_p \mathbf{TF}(E)(y/\lambda D - p/d) && \text{(A.8)} \end{aligned}$$

Intensity can be write :

$$\begin{aligned} I(y,z) = M_0 + M_1 \cos\left[\frac{2\pi}{d}\left(y - z\frac{dg}{dy}\right)\right] && \text{(A.9)} \\ + M_2 \cos\left[\frac{4\pi}{d}\left(y - z\frac{dg}{dy}\right)\right] && \text{(A.10)} \end{aligned}$$

where :

$$\begin{aligned} M_0 &= C_0^2 + 2C_1^2 && \text{(A.11)} \\ M_1 &= 4C_0C_1\cos(\pi\lambda/d^2) && \text{(A.12)} \\ M_2 &= 2C_1^2 && \text{(A.13)} \end{aligned}$$

As shown in Eq. A.10, the derivative of the unknown function g is encoded into the frequency modulation of the intensity. In the expression of M_2, one can recognize the Talbot distance D_T. This term degrades the contrast in practical application. It should be noted that M_2 is also dependant of λ: in polychromatic illumination, the intensities for each wavelengths add up incoherently and the contrast decreases as the bandwith get broader. Those two effects limit the use of the Hartmann Mask. The addition of a phase chessboard of π on the grating enables to overcome these limitations.

A.1.3 Modified Hartmann Mask

The phase chessboard as a pitch twice the pitch of the grating, and its phase shift is π over the visible and NIR light spectrum. Keeping the same notations as previously, the transmission of the MHM is :

$$t(y) = \Pi_a(y) * \left[\text{Ш}_d(y)\exp(i\pi y/d)\right] \quad \text{(A.14)}$$

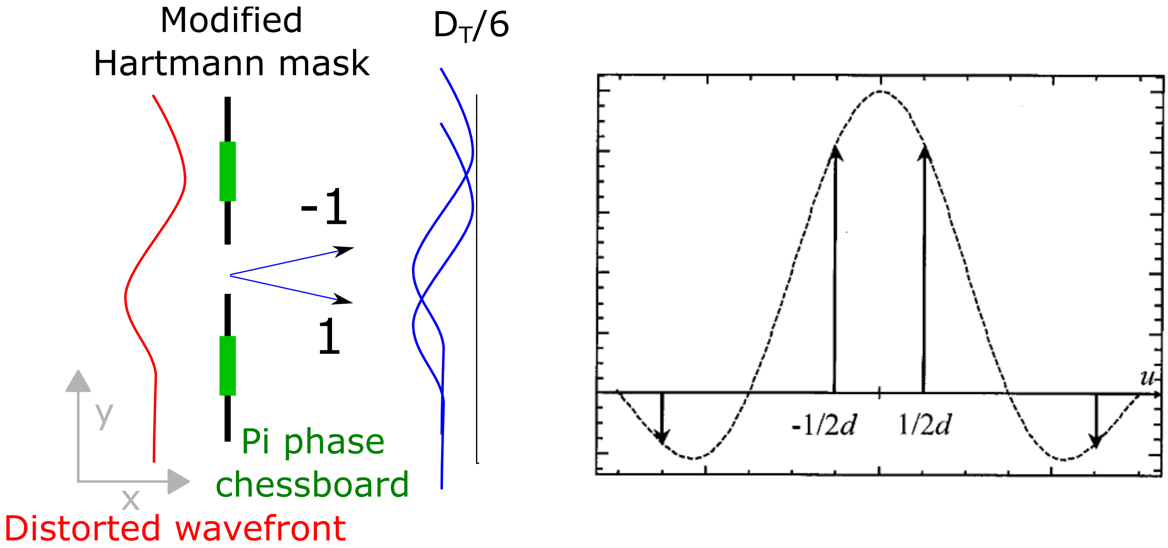

Figure A.2 – Left :Schematic representation of a 1-D Modified Hartmann mask. In addition of the Hartmann Mask of pitch d and size a, a phase chessboard of pitch $2d$ add a phase π on half the holes. As results, it shifts first orders of diffraction, and only two symmetric modes remain. With a correct a/d ratio (2/3) it is possible to coincide second orders of diffraction with the zeros of the cardinal sinus. Right : (from [Primot and Guérineau, 2000]) Relative intensity of first diffraction orders, with $u = k_y/2\pi$ in x-axis. Orders of diffraction are distant by $1/d$ in u coordinate, and modulated by $\sin(\pi ua)/\pi ua$

where the exponential function models the alternating phase $(0, \pi)$. The amplitude of diffracted orders are :

$$\mathbf{TF}(k_y) = \mathbf{sinc_{a\pi}}\left[\text{Ш}_{\mathbf{1/d}}(k_y) * \delta(k_y - 1/2d)\right] \tag{A.15}$$

where δ is the Dirac function. The phase chessboard shift the order of diffraction by an angle $\lambda/2d$. The two preponderent order are now symmetric relatively to the z-axis, and their interference is invarient by propagation. It gives :

$$I(y, z) = 2C_{1/2}^2\left\{1 + \cos\left[\frac{2\pi}{d}\left(y - z\frac{dg}{dy}\right)\right]\right\} \tag{A.16}$$

As the contrast is invariant with illumination wavelength, the MHM allows to analyse interferogram made with polychromatic illumination (within the limitation of the π phase chessboard, which may be not exactly flat on the whole visible spectrum). In our case, it is well-suited for illumination with broadband femtosecond laser.

Finally, derivative of the phase $\nabla \cdot \mathbf{g}$ acts as a frequency modulation of a sinusoidal function. With proper demodulation algorithm, it is possible to retrieve the phase gradient of the incoming wave. By applying a low-pass filter, one can also retrieve the intensity map, which is a considerable advantage over other wave-front sensor techniques like Normasky/DIC. Getting the two maps (phase and intensity) from a single interferogram has a price, which is a loss in resolution. Demodulation algorithm extracts a quarter (in both dimension) of the spectrum. If the interferogram had a dimension of $N_x \times N_y$ pixels, then the phase map is made of $N_x/4 \times N_y/4$ pixels, same for the intensity map, as the low-pass filter must cancel the carrier frequency, equal to roughly 4 pixels.

A.2 Numerical implementation of Abel inversion

A.2.1 axis-symmetric medium

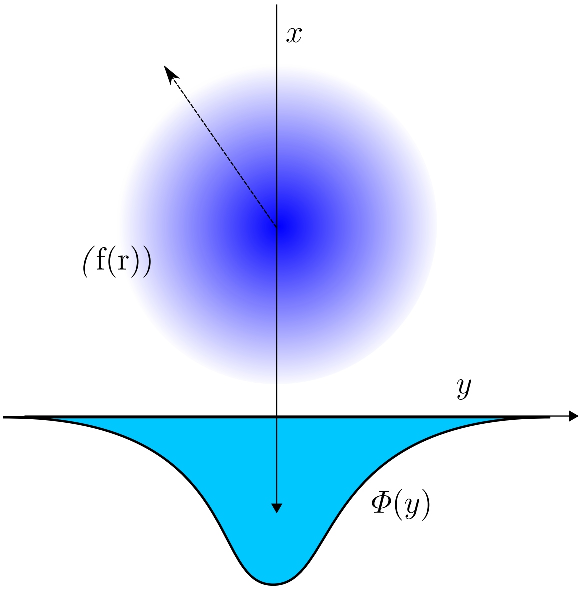

Figure A.3 – axis-symmetric medium with density $f(r)$ probed along the x-axis. $\Phi(y)$ is the phase measured by the sensor i.e. the integrated optical path along the x-axis. The figure is invariant by translation along the z-axis (toward the reader)

Let's assume the probe beam propagates straight through the medium, without change of direction. The phase map is proportional to the projection of the refractive index η along the illumination axis. To reconstruct the full 3-D density map, projection along a single axis is not enough. For asymmetric object, it may be necessary to measure the projection along multiple directions and to reconstruct by tomography the density map. But in our case, objects of interest (plasma channel or atomic neutral flow) are essentially axis-symmetric, meaning that a single projection contains already all the relevant information. How does the phase of the probe relates to the refractive index η ? Let's consider again the problem in 1-D (Fig. A.3), with y the axis of the wavefront sensor, and $\Phi(y)$ the phase measured by the sensor. It comes:

$$\Phi(y) = \frac{2\pi}{\lambda}\int_{-\infty}^{\infty}\eta(r,z)dx = \Phi_0 + \frac{2\pi}{\lambda}\int_{-\infty}^{\infty}(\eta(r,z)-1)dx \tag{A.17}$$

Assuming axis-symmetry, it is now possible to derive $\eta(r,z)-1$ from $\Phi(y)$ by Abel Inversion. Finally, density $n(r,z)$ is related to $\eta(r,z)$ by dispersion relations, different in atomic neutral gas or in plasma.

Case 1: Atomic neutral gas

Lorentz-Lorentz formula express relationship, between the gas refractive index η, the polarizabiliy α, and the particule density n.

$$\frac{\eta^2 - 1}{\eta^2 + 2} = \frac{4\pi}{3} n\alpha = A\frac{n}{N_A} \tag{A.18}$$

Where A is the molar refractive index ($A_{\text{argon}} = 4.2\,\text{cm}^3/\text{mol}$, $A_{\text{helium}} = 0.519\,\text{cm}^3/\text{mol}$), N_A the Avogadro constant. In the gas of interest for our experiments (argon, helium, hydrogen) the refractive index is close to 1 ($\eta_{\text{argon}} - 1 \approx 10^{-4}$)) then :$\eta + 1 \approx 2$ and $\eta^2 + 2 \approx 3$. It yields :

$$n = (\eta^2 - 1)\frac{N_A}{3A} \tag{A.19}$$

Molar refractive index is weakly dependent of the illumination wavelength ($A_{\text{helium}}[\text{cm}^3/\text{mol}] = 0.5172 + 1197/\lambda^2[\text{nm}]$), therefore, white light illumination is relevant for neutral gas density characterization.

Case 2: Plasma

Dispersion relation in a plasma follow the well-known equations:

$$\eta = \sqrt{1 - \frac{n_e}{n_c}} \tag{A.20}$$

where n_e is the plasma electronic density,and $n_c = \omega_0 \epsilon_0 m_e/e^2$ the critical density.(ω_0 probe pulsation, ϵ_0 vacuum permittivity , m_e the electron mass). It yields $n_c[\text{cm}^{-3}] = 1.1 \times 10^{21}/\lambda^2[\text{µm}]$ and then:

$$n_e[\text{cm}^{-3}] = (1 - \eta^2)\frac{1.1 \times 10^{21}}{\lambda^2[\text{µm}]} \tag{A.21}$$

A.2.2 Abel inversion

In Fall 2016 I got the opportunity to implement a density module in the sofware of *Phasics S.A.* company. I implemented in C++ the previous equations, and the Abel inversion. The objective was to be able to perform *in-line* density measure from the wavefront directly inside the SID4 software. Hence, computation efficiency was important in the choice of Abel implementation, and this section explains our choice. Let's express the Abel inversion :

Considering f axis-symmetric from $\mathbf{R}^2$ to $\mathbf{R}$ with finite support, its Abel transform along x F is written :

$$F(y) = \int_{-\infty}^{\infty} f\left(\sqrt{x^2 + y^2}\right)\, dx \tag{A.22}$$

and the inverse Abel Transform of F is

$$f(r) = \mathfrak{A}^{-1}[F](r) = -\frac{1}{\pi}\int_r^{\infty} \frac{dF}{dy}\frac{dy}{\sqrt{y^2 - r^2}} \tag{A.23}$$

The integrand is not defined in r, but a quick analysis (assuming for simplicity dF/dy is C^{∞}) shows that this integral is well-defined: First, if $r \neq 0$ then $dF/dy\, 1/\sqrt{y^2 - r^2} = \mathcal{O}((y-r)^{-1/2})$ integrable over $]r, \infty]$. Finally in $r = 0$, $dF/dy = 0$, because F is symmetric. Then the development $dF/dy(y) = y dF^2/dy^2(y) + \mathcal{O}(y^2)$ leads to $\frac{dF}{dy}\frac{1}{\sqrt{y^2}} = \mathcal{O}(1)$

In our data f is discretized over sensor pixel of position $r_i = i\Delta r$ with $r_{max} = r_N$:

$$f(r_i) = -\frac{1}{\pi}\int_{r_i}^{r_{N-1}} \frac{dF}{dy}\frac{dy}{\sqrt{y^2 - r_i^2}} \tag{A.24}$$

In 1992 Dasch [Dasch, 1992] shown that all numerical Abel inversions could be written as a linear operation :

$$f(r_i) = \frac{1}{\delta r}\sum_{j=0}^{\infty} \mathbf{D}_{ij} F(r_j) \tag{A.25}$$

The deconvolution operator $\mathbf{D}$ is independent of δr. It needs to be calculated once only. This formalism enables to compare most of numerical Abel inversion technics. As explained in [Dasch, 1992], $\mathbf{D}$ acts as a differential operator, localized around r_i, meaning that $\mathbf{D}$ is mostly diagonal. As $\mathbf{D}$ is independent of δr, sampling size of F is not critical, even worst: if oversampling leads to variation of F comparable to the noise, deconvolution becomes highly inaccurate. Various methods derive A.25 from A.24, leading to different $\mathbf{D}_{ij}$, and different accuracy in the reconstruction. These results are presented Fig. A.4 extract from Kolhe. Relative error and noise propagation are best with the so-called *two-point formula* described thereafter. This method has been implemented in the SID4 sofware module.

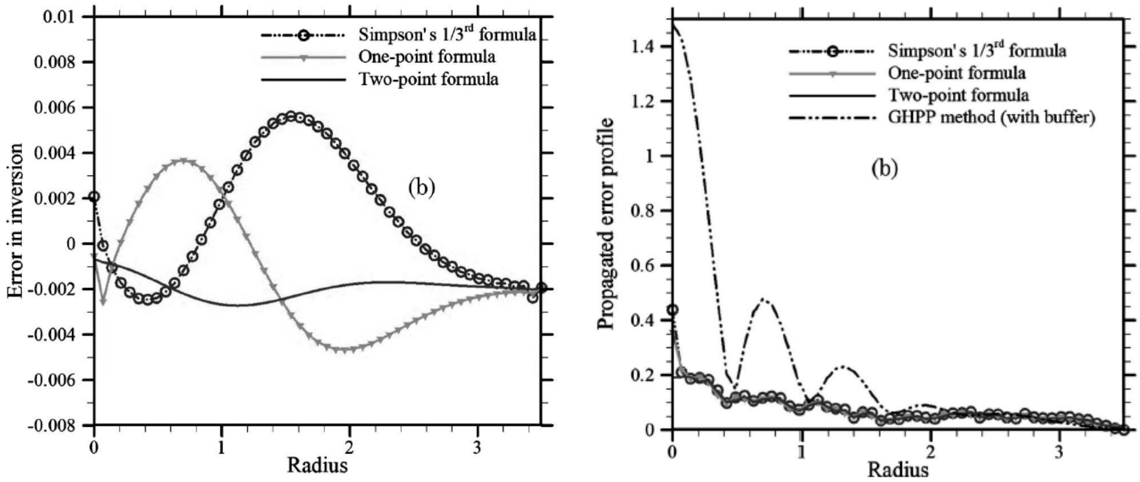

Figure A.4 – From [Kolhe and Agrawal, 2009] Left : Error in the reconstruction of a gaussian profile by Abel inversion, using various set of deconvolution operator. Right : Abel reconstruction of a white random noise in the interval $[0, 1]$ for various deconvolution operator.

Let's write $\frac{dF}{dy}$ as dF and $dF_i = \frac{dF}{dy}(r_i = i\Delta_r)$. It should be noted that dF_0 is on the inversion axis. To solve the integral of Eq. A.24 dF is approximated by a straight line on each segment $[r_i, r_{i+1}]$. Meaning that for all $j \leq N-1$ and $y \leq \Delta_r$:

$$dF(r_j + y) = dF_j + y\frac{dF_{j+1} - dF_j}{\Delta_r} \tag{A.26}$$

Then :

$$f(r_i) = -\frac{1}{\pi}\sum_{j=0}^{N-2}\int_{r_j}^{r_{j+1}} [dF_j + (y - r_j)\frac{dF_{j+1} - dF_j}{\Delta_r}]\,\frac{dy}{\sqrt{y^2 - r_i^2}} \tag{A.27}$$

By change of variable $t = (y - r_j)/\delta r$:

$$f_i = -\frac{1}{\pi}\sum_{j=0}^{N-2}\int_0^1 [dF_j + t(dF_{j+1} - dF_j)]\,\frac{dt}{\sqrt{(j+t)^2 - i^2}} \tag{A.28}$$

Where integrals $\int_0^1((j+t)^2 - i^2)^{-1/2}\,dt$ et $\int_0^1 t((j+t)^2 - i^2)^{-1/2}\,dt$ are function of i and j, and are well defined for $j > i$ and $j = i \neq 0$. They are named respectively $B_{i,j}$ et $A_{i,j} - jB_{i,j}$. Decomposition of the sum yields to [Dasch, 1992; Kolhe and Agrawal, 2009]:

$$f_{i-1} = \sum_{j=1}^{N} dF_{j-1}D_{i,j} \tag{A.29}$$

$$D_{ij} = \begin{cases} 0 & \text{if } j = i = 1 \text{ or } j < i \\ \frac{1}{\pi}(A_{i,j} - jB_{i,j}) & \text{if } \ j = i \,\text{and}\, i \neq 1 \\ \frac{1}{\pi}(A_{i,j} - jB_{i,j} - 1) & \text{if } j > i \,\text{and}\, j = 2 \\ \frac{1}{\pi}(A_{i,j} - A_{i,j-1} - jB_{i,j} + (j-2)B_{i,j-1}) & \text{if}\, j > i \,\text{and}\, j \neq 2 \end{cases} \tag{A.30}$$

This Two-Point formula algorithm was characterized by inversion of a gaussian profile, where analytic solution can be derived. Error between reconstructed and analytic profiles was at maximum 0.005%.

Inversion axis

A typical issue is the determination of the inversion axis in actual data, asymmetric data. Plasma density especially are only roughly axisymmetric. How to understand Abel inversion in this situation ? Performing Abel inversion correspond to the assumption that the medium profile has the same characteristic length in every direction transverse to an axis. A common method is to extract the symmetric part of the phase Φ around an inversion point x_0 ($\Phi_{sym} = (\Phi(x_0 + x) + \Phi(x_0 - x))/2$) , choosing x_0 such as $\int(\Phi(x_0 + x) + \Phi(x_0 - x))^2 dx$ is minimized. Then two solutions may be chosen : 1) Perform Abel inversion on Φ_{sym} 2) Perform Abel inversion separately on each side of the inversion line.

Method 1 gives accurate and continuous profile on the axis, but becomes highly wrong far from the axis, especially if the asymmetry is strong.

Method 2 has the advantages to avoid data loss in the "mean" operation, keeping each half of reconstructed density independent from the phase of the other half, which is actually more physically correct. Nonetheless, for non-symmetric data, this method will lead to irrelevant discontinuities in the density profile. Those discontinuities occur on the inversion axis. As the density far from the axis is weakly dependent of the axis position, we chose to find the axis by iteration, keeping the one assuring best continuity.

Density values are more correct far from the axis, giving us information on the wing of the gas profile in the mm range, at density down to 1 % of the pic density. These data fit ANSYS fluent simulation, and are critical for proper PIC simulation of the early laser/gas-ramp interaction. Best-continuity method give also a smooth profile *along* the inversion axis, which is critical for plasma diagnostic, as this axis is the laser path.

Fig. A.5 give abel reconstruction of a slightly asymmetric density slice given by equation :

$$n(x,y) = \begin{cases} \exp(-r^2/2) & \text{if } x > 0 \\ (A+Bx)\exp(-((x-x_0)^2+y^2)/2) & \text{if } \ x <= 0 \\ A = \exp(x_0^2/2) & \\ B = -x_0\exp(x_0^2/2) & \end{cases} \tag{A.31}$$

A and B chosen for continuity of both n and $\partial n/\partial x, y$. Inversion accuracy is very profile-dependent in this case, but exemple Fig. A.5 gives general insight: asymmetry leads to huge discontinuity near the axis when abel inversion is processed for each half independently. Inversion point chosen at maximum of Φ or at symmetry lead to maximum discrepancy up to 40 %. That's why we prefered the choice of an inversion point optimizing continuity on the axis (red curve Fig A.5: with maximum discrepancy of 18 %) we avoid large inversion error, while the mean discrepancy is always near 12 %.

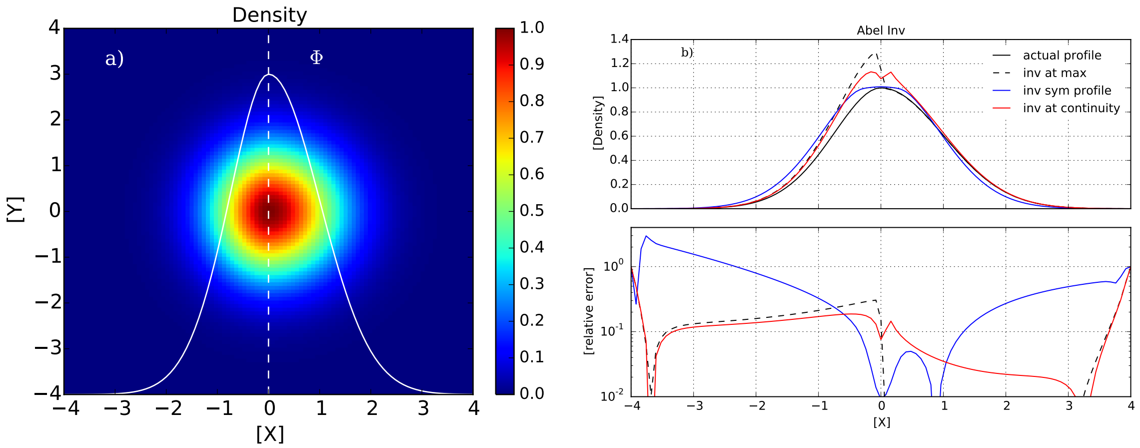

Figure A.5 – a) : Asymmetric density slice used in test of Abel inversion. Arbitrary units for distance and density. Density on the positive X side has rotational symmetry in $(X, Y) = (0, 0)$ while the negative side is adjust for continuity and continuity of the derivative. White curve Φ denotes the integrated density along the y-axis. b) Abel inversion of the projection Φ for various inversion points i) max of Φ (dashed line) ii) inversion of symmetrized profile (blue line) iii) best continuity between both half-profile (red line). Initial density in plain line. Inversion point at $X = 0$ give exact reconstruction for $X > 0$ (dashed line), as density is really axis-symmetric for this half. c) give relative error versus axes distance for all method. While very accurate near the inversion axis, symmetrization method (blue line) becomes irrelevant far from the axis.

From numeric inversion to density

Let's express the refractive index η with Abel inversion : Eq. A.17 states $\Phi_{[\mathrm{rad}]} = \frac{2\pi}{\lambda}\int_{-\infty}^{\infty}(\eta(r,z)-1)dx$ as measured by the Phasics.

$$(\eta(r)-1)\frac{2\pi}{\lambda} = \mathfrak{A}^{-1}(\Phi_{[\mathrm{rad}]}) = \frac{1}{\varDelta_r}\mathfrak{A}^{-1}_{\mathrm{num}}(\Phi_{[\mathrm{rad}]}) \tag{A.32}$$

Division by $\varDelta_r$ is needed because the numeric Abel inversion is compute dimensionless ($d\Phi_i = (\Phi_{i+1} - \Phi_{i-1})/2)$. Then for neutral gas:

$$n = \frac{2N_A}{6\pi A}\frac{\lambda}{\varDelta_r}\mathfrak{A}^{-1}_{\mathrm{num}}(\Phi_{[\mathrm{rad}]}) \tag{A.33}$$

and for plasma :

$$\eta = 1 + \frac{\lambda}{2\pi\varDelta_r}\mathfrak{A}^{-1}_{\mathrm{num}}(\Phi_{[\mathrm{rad}]}) \tag{A.34}$$

$$n = \left(1-\eta^2\right)\frac{n_c}{\lambda^2} \tag{A.35}$$

It should be noted that density is linear with Abel inversion of the phase only for neutral gas, not plasma.

Acknowledgments

I like to acknowledge first the members of the jury for their careful reading and their suggestions, giving this work the opportunity to meet the best, I hope, quality standards of scientific publications. I would like to thanks warmly Victor Malka, my PhD director and team leader at LOA, and Alessandro Flacco, my co-director. Victor offered me the precious opportunity to tackle a challenging subject under optimal conditions. He was always extremely available for guidance and directions, and in the same time, giving freedom, confidence, and the necessary resources to meet our goals. Without Alessandro, I would have never seen a single photon. His staunch dedication to the SAPHIR platform, his experimental skills, were critical in our projects. In the same time he gave me gradually the tools and its confidence to design and operate fully the experimental area, and I couldn't thank him enough for his patient teaching. My warm acknowledgements are going as well to François Sylla, who led the first research in LOA over ion acceleration in near-critical targets. He was definitely a mentor. He offered me numerous opportunities with SourceLAB : I had a counsel mission with Phasics SA over a diagnostic development, and we developed together the next generation of gas targets. Finally, I couldn't have achieved any plasma simulation in parallel of my experimental work without the key support of Agustin Lifschitz, our lead theorician. His teaching, his broad physics knowledge and his availability were invaluable.

This thesis was also the opportunity to develop rich collaborations. During all these years, we were in close contacts with Laurent Gremillet and Arnaud Debayle from CEA-DAM. We worked on electron heating mechanisms and laser propagation in our experimental conditions. I was welcomed in MBI in Berlin by Matthias Schnuerer during the LaserLab experimental campaign on neutral emissions. I was invited twice in South Korea to work in GIST by Pr. Chang Hee Nam and Pr. Hyung Taek Kim on their experimental campaigns. The welcoming from our hosts and from the whole korean team was incredible. Finally, for the last experimental and numerical efforts, I collaborated with Yang Wan. Yang was a visiting PhD from Tsinghua University in Beijing, his help and his talent were critical. I would like to thank deeply all these collaborators for the scientific and life experiences they made possible. They contributions, along with all the support from my colleagues at LOA, have made the journey of this thesis truly fulfilling.

Bibliography

F. Abicht, R. Prasad, M. Borghesi, G. Priebe, J. Braenzel, A. Andreev, P. V. Nickles, M. Schnuerer, S. Jequier, G. Revet, V. Tikhonchuk, and S. Ter-Avetisyan. Energetic beams of negative and neutral hydrogen from intense laser plasma interaction. *Applied Physics Letters*, 103(25):253501, 2013. doi: http://dx.doi.org/10.1063/1.4850456. URL `http://scitation.aip.org/content/aip/journal/apl/103/25/10.1063/1.4850456`. 145

Samuel K. Allison. Experimental results on charge-changing collisions of hydrogen and helium atoms and ions at kinetic energies above 0.2 kev. *Rev. Mod. Phys.*, 30:1137–1168, Oct 1958. doi: 10.1103/RevModPhys.30.1137. URL `http://link.aps.org/doi/10.1103/RevModPhys.30.1137`. 151, 152

M.V. Ammosov, N.B. Delone, and V.P. Krainov. Tunnel ionization of complex atoms and of atomic ions in an alternating electromagnetic field. *JETP*, 64(6):1191, 1986. URL `http://www.jetp.ac.ru/cgi-bin/dn/e_064_06_1191.pdf`. 27

D.A. Anderson, J.C. Tannehill, and R.H. Pletcher. *Computational fluid mechanics and heat transfer*. Hemisphere Publishing,New York, NY, 2001. 74

J.D. Anderson. *Fundamentals of Aerodynamics*. McGraw-Hill,New York, NY, 2001. ISBN 0072373350. URL `http://ocw.mit.edu/courses/aeronautics-and-astronautics/16-01-unified-engineering-i-ii-iii-iv-fall-2005-spring-2006/fluid-mechanics/`. 82

P Antici, J Fuchs, E d'Humières, J Robiche, E Brambrink, S Atzeni, A Schiavi, Y Sentoku, P Audebert, and H Pépin. Laser acceleration of high-energy protons in variable density plasmas. *New Journal of Physics*, 11(2):023038, 2009. URL `http://stacks.iop.org/1367-2630/11/i=2/a=023038`. 8, 10, 59, 156

G. Beaudoin, A. Champagne, H. Jeremie, and L. Lessard. The detection of electrons in the 10 mev range by plastic scintillators. *Nuclear Instruments and Methods in Physics Research Section A: Accelerators, Spectrometers, Detectors and Associated Equipment*, 249(2):379 – 385, 1986. ISSN 0168-9002. doi: http://dx.doi.org/10.1016/0168-9002(86)90691-1. URL `http://www.sciencedirect.com/science/article/pii/0168900286906911`. 111

F.D. Becchetti, C.E. Thorn, and M.J. Levine. Response of plastic scintillator detectors to heavy ions, z $<$ 35, e $<$ 170 mev. *Nuclear Instruments and Methods*, 138(1):93 – 104, 1976. ISSN 0029-554X. doi: http://dx.doi.org/10.1016/

0029-554X(76)90154-3. URL `http://www.sciencedirect.com/science/article/pii/0029554X76901543`. 110, 111

M. Belli, R. Cherubini, G. Galeazzi, S. Mazzucato, G. Moschini, O. Sapora, G. Simone, and M.A. Tabocchini. Proton irradiation facility for radiobiological studies at a 7 mv van de graaff accelerator. *Nuclear Instruments and Methods in Physics Research Section A: Accelerators, Spectrometers, Detectors and Associated Equipment*, 256(3):576 – 580, 1987. ISSN 0168-9002. doi: http://dx.doi.org/10.1016/0168-9002(87)90304-4. URL `http://www.sciencedirect.com/science/article/pii/0168900287903044`. 107

M.J. Berger, J.S. Coursey, M.A. Zucker, and J. Chang. Estar, pstar, and astar: Computer programs for calculating stopping-power and range tables for electrons, protons, and helium ions (version 1.2.3). *NIST*, 2005. URL `http://physics.nist.gov/Star20160726`. 121

H. Betz. Charge states and charge-changing cross sections of fast heavy ions penetrating through gaseous and solid media. *Rev. Mod. Phys.*, 44:465–539, Jul 1972. doi: 10.1103/RevModPhys.44.465. URL `http://link.aps.org/doi/10.1103/RevModPhys.44.465`. 150, 153

N. Bohr and J. Lindhard. Electron capture and loss by heavy ions penetrating through matter. *Dan. Mat. Fys. Medd.*, 28, 1954. 150

S. A. Boman, E. M. Bernstein, and J. A. Tanis. Single-electron capture and loss cross sections versus target Z for 1 mev/u oxygen ions incident on gases. *Phys. Rev. A*, 39:4423–4427, May 1989. doi: 10.1103/PhysRevA.39.4423. URL `http://link.aps.org/doi/10.1103/PhysRevA.39.4423`. 151

Pierre Bon, Guillaume Maucort, Benoit Wattellier, and Serge Monneret. Quadriwave lateral shearing interferometry for quantitative phase microscopy of living cells. *Opt. Express*, 17(15):13080–13094, Jul 2009. doi: 10.1364/OE.17.013080. URL `http://www.opticsexpress.org/abstract.cfm?URI=oe-17-15-13080`. 64

Valeria Casanova Borca, Massimo Pasquino, Giuliana Russo, Pierangelo Grosso, Domenico Cante, Piera Sciacero, Giuseppe Girelli, Maria Rosa La Porta, and Santi Tofani. Dosimetric characterization and use of gafchromic ebt3 film for imrt dose verification. *Journal of Applied Clinical Medical Physics*, 14(2), 2013. ISSN 15269914. URL `http://www.jacmp.org/index.php/jacmp/article/view/4111`. 107

M. Borghesi, D. H. Campbell, A. Schiavi, M. G. Haines, O. Willi, A. J. MacKinnon, P. Patel, L. A. Gizzi, M. Galimberti, R. J. Clarke, F. Pegoraro, H. Ruhl, and S. Bulanov. Electric field detection in laser-plasma interaction experiments via the proton imaging technique. *Physics of Plasmas*, 9(5):2214–2220, 2002. doi: http://dx.doi.org/10.1063/1.1459457. URL `http://scitation.aip.org/content/aip/journal/pop/9/5/10.1063/1.1459457`. 4

S. Buffechoux, J. Psikal, M. Nakatsutsumi, L. Romagnani, A. Andreev, K. Zeil, M. Amin, P. Antici, T. Burris-Mog, A. Compant-La-Fontaine, E. d'Humières,

S. Fourmaux, S. Gaillard, F. Gobet, F. Hannachi, S. Kraft, A. Mancic, C. Plaisir, G. Sarri, M. Tarisien, T. Toncian, U. Schramm, M. Tampo, P. Audebert, O. Willi, T. E. Cowan, H. Pépin, V. Tikhonchuk, M. Borghesi, and J. Fuchs. Hot electrons transverse refluxing in ultraintense laser-solid interactions. *Phys. Rev. Lett.*, 105: 015005, Jul 2010. doi: 10.1103/PhysRevLett.105.015005. URL `http://link.aps.org/doi/10.1103/PhysRevLett.105.015005`. 59

S. V. Bulanov and T. Zh. Esirkepov. Comment on "collimated multi-mev ion beams from high-intensity laser interactions with underdense plasma". *Phys. Rev. Lett.*, 98: 049503, Jan 2007. doi: 10.1103/PhysRevLett.98.049503. URL `http://link.aps.org/doi/10.1103/PhysRevLett.98.049503`. 9, 27, 34

S. V. Bulanov, I. N. Inovenkov, V. I. Kirsanov, N. M. Naumova, and A. S. Sakharov. Nonlinear depletion of ultrashort and relativistically strong laser pulses in an underdense plasma. *Physics of Fluids B*, 4(7):1935–1942, 1992. doi: http://dx.doi.org/10.1063/1.860046. URL `http://scitation.aip.org/content/aip/journal/pofb/4/7/10.1063/1.860046`. 54

S. V. Bulanov, F. Pegoraro, A. M. Pukhov, and A. S. Sakharov. Transverse-wake wave breaking. *Phys. Rev. Lett.*, 78:4205–4208, Jun 1997. doi: 10.1103/PhysRevLett.78.4205. URL `http://link.aps.org/doi/10.1103/PhysRevLett.78.4205`. 45

Stepan S. Bulanov, Valery Yu. Bychenkov, Vladimir Chvykov, Galina Kalinchenko, Dale William Litzenberg, Takeshi Matsuoka, Alexander G. R. Thomas, Louise Willingale, Victor Yanovsky, Karl Krushelnick, and Anatoly Maksimchuk. Generation of gev protons from 1 pw laser interaction with near critical density targets. *Physics of Plasmas*, 17(4):043105, 2010. doi: http://dx.doi.org/10.1063/1.3372840. URL `http://scitation.aip.org/content/aip/journal/pop/17/4/10.1063/1.3372840`. 9, 25

S.V Bulanov, T.Zh Esirkepov, V.S Khoroshkov, A.V Kuznetsov, and F Pegoraro. Oncological hadrontherapy with laser ion accelerators. *Physics Letters A*, 299(2–3):240 – 247, 2002. ISSN 0375-9601. doi: http://dx.doi.org/10.1016/S0375-9601(02)00521-2. URL `http://www.sciencedirect.com/science/article/pii/S0375960102005212`. 4

T. Ceccotti, A. Lévy, H. Popescu, F. Réau, P. D'Oliveira, P. Monot, J. P. Geindre, E. Lefebvre, and Ph. Martin. Proton acceleration with high-intensity ultrahigh-contrast laser pulses. *Phys. Rev. Lett.*, 99:185002, Oct 2007. doi: 10.1103/PhysRevLett.99.185002. URL `http://link.aps.org/doi/10.1103/PhysRevLett.99.185002`. 4

T. Ceccotti, V. Floquet, A. Sgattoni, A. Bigongiari, O. Klimo, M. Raynaud, C. Riconda, A. Heron, F. Baffigi, L. Labate, L. A. Gizzi, L. Vassura, J. Fuchs, M. Passoni, M. Květon, F. Novotny, M. Possolt, J. Prokůpek, J. Proška, J. Pšikal, L. Štolcová, A. Velyhan, M. Bougeard, P. D'Oliveira, O. Tcherbakoff, F. Réau, P. Martin, and A. Macchi. Evidence of resonant surface-wave excitation in the relativistic regime through measurements of proton acceleration from grating targets. *Phys.*

Rev. Lett., 111:185001, Oct 2013. doi: 10.1103/PhysRevLett.111.185001. URL `http://link.aps.org/doi/10.1103/PhysRevLett.111.185001`. 6, 59

C. T. Chantler. Theoretical form factor, attenuation, and scattering tabulation for z=1–92 from e=1–10 ev to e=0.4–1.0 mev. *Journal of Physical and Chemical Reference Data*, 24(1):71–643, 1995. doi: http://dx.doi.org/10.1063/1.555974. URL `http://physics.nist.gov/PhysRefData/FFast/html/form.html`. 153

Jiři Charvát and František Spurný. Etching characteristics of cellulose nitrate and cr-39 after high dose electron irradiation. *International Journal of Radiation Applications and Instrumentation. Part D. Nuclear Tracks and Radiation Measurements*, 14(4):451 – 455, 1988. ISSN 1359-0189. doi: http://dx.doi.org/10.1016/1359-0189(88)90004-0. URL `http://www.sciencedirect.com/science/article/pii/1359018988900040`. 108

A. Chutjian and D. C. Cartwright. Electron-impact excitation of electronic states in argon at incident energies between 16 and 100 ev. *Phys. Rev. A*, 23:2178–2193, May 1981. doi: 10.1103/PhysRevA.23.2178. URL `http://link.aps.org/doi/10.1103/PhysRevA.23.2178`. 153

E. L. Clark, K. Krushelnick, J. R. Davies, M. Zepf, M. Tatarakis, F. N. Beg, A. Machacek, P. A. Norreys, M. I. K. Santala, I. Watts, and A. E. Dangor. Measurements of energetic proton transport through magnetized plasma from intense laser interactions with solids. *Phys. Rev. Lett.*, 84:670–673, Jan 2000. doi: 10.1103/PhysRevLett.84.670. URL `http://link.aps.org/doi/10.1103/PhysRevLett.84.670`. 3

Hiroyuki Daido, Mamiko Nishiuchi, and Alexander S Pirozhkov. Review of laser-driven ion sources and their applications. *Reports on Progress in Physics*, 75(5):056401, 2012. URL `http://stacks.iop.org/0034-4885/75/i=5/a=056401`. 6, 7

Colin Danson, David Hillier, Nicholas Hopps, and David Neely. Petawatt class lasers worldwide. *High Power Laser Science and Engineering*, 3, 001 2015. doi: 10.1017/hpl.2014.52. URL `https://www.cambridge.org/core/article/petawatt-class-lasers-worldwide/77B55882D24E72D26E233B691A8376D2`. 2, 145

C. J. Dasch. One-dimensional tomography: a comparison of abel, onion-peeling, and filtered backprojection methods. *Appl. Opt.*, 31(8):1146–1152, Mar 1992. doi: 10.1364/AO.31.001146. URL `http://ao.osa.org/abstract.cfm?URI=ao-31-8-1146`. 166, 167

B.J. Delarue and S.B. Pope. Application of pdf methods to compressible turbulent flows. *Phys. Fluids*, 9(9):2704, 1997. doi: http://dx.doi.org/10.1063/1.869382. 93

Emmanuel d'Humieres, Erik Lefebvre, Laurent Gremillet, and Victor Malka. Proton acceleration mechanisms in high-intensity laser interaction with thin foils. *Physics of Plasmas*, 12(6):062704, 2005. doi: http://dx.doi.org/10.1063/1.1927097. URL `http://scitation.aip.org/content/aip/journal/pop/12/6/10.1063/1.1927097`. 6

E d'Humières, P Antici, M Glesser, J Boeker, F Cardelli, S Chen, J L Feugeas, F Filippi, M Gauthier, A Levy, P Nicolaï, H Pépin, L Romagnani, M Scisciò, V T Tikhonchuk, O Willi, J C Kieffer, and J Fuchs. Investigation of laser ion acceleration in low-density targets using exploded foils. *Plasma Physics and Controlled Fusion*, 55(12): 124025, 2013a. URL `http://stacks.iop.org/0741-3335/55/i=12/a=124025`. 8, 11, 145

E. d'Humières, A. Brantov, V. Yu. Bychenkov, and V. T. Tikhonchuk. Optimization of laser-target interaction for proton acceleration. *Physics of Plasmas*, 20(2):023103, 2013b. doi: http://dx.doi.org/10.1063/1.4791655. URL `http://scitation.aip.org/content/aip/journal/pop/20/2/10.1063/1.4791655`. 8, 11, 59, 156

T. Ditmire, J. W. G. Tisch, E. Springate, M. B. Mason, N. Hay, R. A. Smith, J. Marangos, and M. H. R. Hutchinson. High-energy ions produced in explosions of superheated atomic clusters. *Nature*, 386(6620):54–56, Mar 1997. doi: 10.1038/386054a0. URL `http://dx.doi.org/10.1038/386054a0`. 3

I.S. Dmitriev, Ya.A. Teplova, Yu.A. Belkova, and N.V. Novikov. Charge exchange cross sections of carbon ions. *Journal of Surface Investigation. X-ray, Synchrotron and Neutron Techniques*, 2(2):270–273, 2008. ISSN 1027-4510. doi: 10.1134/S1027451008020195. URL `http://dx.doi.org/10.1134/S1027451008020195`. 151, 152

F. Dollar, C. Zulick, A. G. R. Thomas, V. Chvykov, J. Davis, G. Kalinchenko, T. Matsuoka, C. McGuffey, G. M. Petrov, L. Willingale, V. Yanovsky, A. Maksimchuk, and K. Krushelnick. Finite spot effects on radiation pressure acceleration from intense high-contrast laser interactions with thin targets. *Phys. Rev. Lett.*, 108:175005, Apr 2012. doi: 10.1103/PhysRevLett.108.175005. URL `http://link.aps.org/doi/10.1103/PhysRevLett.108.175005`. 6

G. Doumy, F. Quéré, O. Gobert, M. Perdrix, Ph. Martin, P. Audebert, J. C. Gauthier, J.-P. Geindre, and T. Wittmann. Complete characterization of a plasma mirror for the production of high-contrast ultraintense laser pulses. *Phys. Rev. E*, 69:026402, Feb 2004. doi: 10.1103/PhysRevE.69.026402. URL `http://link.aps.org/doi/10.1103/PhysRevE.69.026402`. 6

M. J. Edwards, A. J. MacKinnon, J. Zweiback, K. Shigemori, D. Ryutov, A. M. Rubenchik, K. A. Keilty, E. Liang, B. A. Remington, and T. Ditmire. Investigation of ultrafast laser-driven radiative blast waves. *Phys. Rev. Lett.*, 87:085004, Aug 2001. doi: 10.1103/PhysRevLett.87.085004. URL `http://link.aps.org/doi/10.1103/PhysRevLett.87.085004`. 134, 135

E. Esarey, P. Sprangle, M. Pilloff, and J. Krall. Theory and group velocity of ultrashort, tightly focused laser pulses. *J. Opt. Soc. Am. B*, 12(9):1695–1703, Sep 1995. doi: 10.1364/JOSAB.12.001695. URL `http://josab.osa.org/abstract.cfm?URI=josab-12-9-1695`. 119

E. Esarey, P. Sprangle, J. Krall, and A. Ting. Overview of plasma-based accelerator concepts. *IEEE Transactions on Plasma Science*, 24(2):252–288, Apr 1996. ISSN 0093-3813. doi: 10.1109/27.509991. 116

T. Esirkepov, M. Borghesi, S. V. Bulanov, G. Mourou, and T. Tajima. Highly efficient relativistic-ion generation in the laser-piston regime. *Phys. Rev. Lett.*, 92:175003, Apr 2004. doi: 10.1103/PhysRevLett.92.175003. URL `http://link.aps.org/doi/10.1103/PhysRevLett.92.175003`. 6, 33, 145

J. Faure, Y. Glinec, J. J. Santos, F. Ewald, J.-P. Rousseau, S. Kiselev, A. Pukhov, T. Hosokai, and V. Malka. Observation of laser-pulse shortening in nonlinear plasma waves. *Phys. Rev. Lett.*, 95:205003, Nov 2005. doi: 10.1103/PhysRevLett.95.205003. URL `http://link.aps.org/doi/10.1103/PhysRevLett.95.205003`. 25, 136

A. P. Fews, P. A. Norreys, F. N. Beg, A. R. Bell, A. E. Dangor, C. N. Danson, P. Lee, and S. J. Rose. Plasma ion emission from high intensity picosecond laser pulse interactions with solid targets. *Phys. Rev. Lett.*, 73:1801–1804, Sep 1994. doi: 10.1103/PhysRevLett.73.1801. URL `http://link.aps.org/doi/10.1103/PhysRevLett.73.1801`. 3

F. Fiuza, A. Stockem, E. Boella, R. A. Fonseca, L. O. Silva, D. Haberberger, S. Tochitsky, C. Gong, W. B. Mori, and C. Joshi. Laser-driven shock acceleration of monoenergetic ion beams. *Phys. Rev. Lett.*, 109:215001, Nov 2012. doi: 10.1103/PhysRevLett.109.215001. URL `http://link.aps.org/doi/10.1103/PhysRevLett.109.215001`. 11, 53, 54, 156

A. Flacco, J. Vieira, A. Lifschitz, F. Sylla, S. Kahaly, M. Veltcheva, L. O. Silva, and V. Malka. Persistence of magnetic field driven by relativistic electrons in a plasma. *Nat Phys*, 11, May 2015. 7, 9, 158

V. Floquet, O. Klimo, J. Psikal, A. Velyhan, J. Limpouch, J. Proska, F. Novotny, L. Stolcova, A. Macchi, A. Sgattoni, L. Vassura, L. Labate, F. Baffigi, L. A. Gizzi, Ph. Martin, and T. Ceccotti. Micro-sphere layered targets efficiency in laser driven proton acceleration. *Journal of Applied Physics*, 114(8):083305, 2013. doi: http://dx.doi.org/10.1063/1.4819239. URL `http://scitation.aip.org/content/aip/journal/jap/114/8/10.1063/1.4819239`. 6

R. A. Fonseca, L. O. Silva, F. S. Tsung, V. K. Decyk, W. Lu, C. Ren, W. B. Mori, S. Deng, S. Lee, T. Katsouleas, and J. C. Adam. *OSIRIS: A Three-Dimensional, Fully Relativistic Particle in Cell Code for Modeling Plasma Based Accelerators*, pages 342–351. Springer Berlin Heidelberg, Berlin, Heidelberg, 2002. ISBN 978-3-540-47789-1. doi: 10.1007/3-540-47789-6_36. URL `http://dx.doi.org/10.1007/3-540-47789-6_36`. 36

P. Franzen, H. Falter, B. Heinemann, Ch. Martens, U. Fantz, M. Berger, S. Christ-Koch, M. Fröschle, D. Holtum, W. Kraus, S. Leyer, P. McNeely, R. Riedl, R. Suess, S. Obermayer, E. Speth, and D. Wuenderlich. Radi—a {RF} source size-scaling experiment towards the {ITER} neutral beam negative ion source. *Fusion Engineering and Design*, 82(4):407 – 423, 2007. ISSN 0920-3796. doi: http://dx.doi.org/10.1016/j.fusengdes.2007.03.041. URL `http://www.sciencedirect.com/science/article/pii/S0920379607001275`. 145

S. Fritzler, V. Malka, G. Grillon, J. P. Rousseau, F. Burgy, E. Lefebvre, E. d'Humières, P. McKenna, and K. W. D. Ledingham. Proton beams generated with high-intensity lasers: Applications to medical isotope production. *Applied Physics Letters*, 83(15):3039–3041, 2003. doi: http://dx.doi.org/10.1063/1.1616661. URL `http://scitation.aip.org/content/aip/journal/apl/83/15/10.1063/1.1616661`. 4

M. Fromm, F. Membrey, A. El Rahamany, and A. Chambaudet. Principle of light ions micromapping and dosimetry using a cr-39 polymeric detector: Modelized and experimental uncertainties. *Nuclear Tracks and Radiation Measurements*, 21(3):357 – 365, 1993. ISSN 0969-8078. doi: http://dx.doi.org/10.1016/0969-8078(93)90230-2. URL `http://www.sciencedirect.com/science/article/pii/0969807893902302`. 107

J. Fuchs, P. Antici, E. d/'Humieres, E. Lefebvre, M. Borghesi, E. Brambrink, C. A. Cecchetti, M. Kaluza, V. Malka, M. Manclossi, S. Meyroneinc, P. Mora, J. Schreiber, T. Toncian, H. Pepin, and P. Audebert. Laser-driven proton scaling laws and new paths towards energy increase. *Nat Phys*, 2(1):48–54, Jan 2006. ISSN 1745-2473. doi: 10.1038/nphys199. URL `http://dx.doi.org/10.1038/nphys199`. 4

Y. Fukuda, A. Ya. Faenov, M. Tampo, T. A. Pikuz, T. Nakamura, M. Kando, Y. Hayashi, A. Yogo, H. Sakaki, T. Kameshima, A. S. Pirozhkov, K. Ogura, M. Mori, T. Zh. Esirkepov, J. Koga, A. S. Boldarev, V. A. Gasilov, A. I. Magunov, T. Yamauchi, R. Kodama, P. R. Bolton, Y. Kato, T. Tajima, H. Daido, and S. V. Bulanov. Energy increase in multi-mev ion acceleration in the interaction of a short pulse laser with a cluster-gas target. *Phys. Rev. Lett.*, 103:165002, Oct 2009. doi: 10.1103/PhysRevLett.103.165002. URL `http://link.aps.org/doi/10.1103/PhysRevLett.103.165002`. 9, 27, 34

C. Gahn, G. D. Tsakiris, A. Pukhov, J. Meyer-ter Vehn, G. Pretzler, P. Thirolf, D. Habs, and K. J. Witte. Multi-mev electron beam generation by direct laser acceleration in high-density plasma channels. *Phys. Rev. Lett.*, 83:4772–4775, Dec 1999. doi: 10.1103/PhysRevLett.83.4772. URL `http://link.aps.org/doi/10.1103/PhysRevLett.83.4772`. 139, 140

S A Gaillard, K A Flippo, M E Lowenstern, J E Mucino, J M Rassuchine, D C Gautier, J Workman, and T E Cowan. Proton acceleration from ultrahigh-intensity short-pulse laser-matter interactions with cu micro-cone targets at an intrinsic 10-8 contrast. *Journal of Physics: Conference Series*, 244(2):022034, 2010. URL `http://stacks.iop.org/1742-6596/244/i=2/a=022034`. 59

P. Gibbon. *Short Pulse Laser Interactions with Matter*, chapter 9. Imperial College Press, 2005. ISBN 978-1-86094-135-1. 20, 26

L. M. Gorbunov, P. Mora, and A. A. Solodov. Plasma ions dynamics in the wake of a short laser pulse. *Phys. Rev. Lett.*, 86:3332–3335, Apr 2001. doi: 10.1103/PhysRevLett.86.3332. URL `http://link.aps.org/doi/10.1103/PhysRevLett.86.3332`. 28, 34, 49, 52

W. G. Graham, K. H. Berkner, R. V. Pyle, A. S. Schlachter, J. W. Stearns, and J. A. Tanis. Charge-transfer cross sections for multiply charged ions colliding with gaseous targets at energies from 310 kev/amu to 8.5 mev/amu. *Phys. Rev. A*, 30:722–728, Aug 1984. doi: 10.1103/PhysRevA.30.722. URL http://link.aps.org/doi/10.1103/PhysRevA.30.722. 150

E. F. Greene, G. R. Cowan, and D. F. Hornig. The thickness of shock fronts in argon and nitrogen and rotational heat capacity lags. *The Journal of Chemical Physics*, 19(4):427–434, 1951. doi: http://dx.doi.org/10.1063/1.1748241. URL http://scitation.aip.org/content/aip/journal/jcp/19/4/10.1063/1.1748241. 60

D. Haberberger, S. Tochitsky, F. Fiuza, C. Gong, R. A. Fonseca, L. O. Silva, W. B. Mori, and C. Joshi. Collisionless shocks in laser-produced plasma generate monoenergetic high-energy proton beams. *Nature Phys.*, 8:95–99, 2012. doi: 10.1038/nphys2130. URL http://dx.doi.org/10.1038/nphys2130. 7, 8, 9, 10, 11, 27, 33, 34, 53, 59, 107, 145, 156

Otto F. Hagena. Nucleation and growth of clusters in expanding nozzle flows. *Surface Science*, 106(1–3):101 – 116, 1981. ISSN 0039-6028. doi: http://dx.doi.org/10.1016/0039-6028(81)90187-4. URL http://www.sciencedirect.com/science/article/pii/0039602881901874. 118, 125

M. Hegelich, S. Karsch, G. Pretzler, D. Habs, K. Witte, W. Guenther, M. Allen, A. Blazevic, J. Fuchs, J. C. Gauthier, M. Geissel, P. Audebert, T. Cowan, and M. Roth. Mev ion jets from short-pulse-laser interaction with thin foils. *Phys. Rev. Lett.*, 89:085002, Aug 2002. doi: 10.1103/PhysRevLett.89.085002. URL http://link.aps.org/doi/10.1103/PhysRevLett.89.085002. 3

A. Henig, D. Kiefer, K. Markey, D. C. Gautier, K. A. Flippo, S. Letzring, R. P. Johnson, T. Shimada, L. Yin, B. J. Albright, K. J. Bowers, J. C. Fernández, S. G. Rykovanov, H.-C. Wu, M. Zepf, D. Jung, V. Kh. Liechtenstein, J. Schreiber, D. Habs, and B. M. Hegelich. Enhanced laser-driven ion acceleration in the relativistic transparency regime. *Phys. Rev. Lett.*, 103:045002, Jul 2009. doi: 10.1103/PhysRevLett.103.045002. URL http://link.aps.org/doi/10.1103/PhysRevLett.103.045002. 6

Miguel Arevallilo Herráez, David R. Burton, Michael J. Lalor, and Munther A. Gdeisat. Fast two-dimensional phase-unwrapping algorithm based on sorting by reliability following a noncontinuous path. *Appl. Opt.*, 41(35):7437–7444, Dec 2002. doi: 10.1364/AO.41.007437. URL http://ao.osa.org/abstract.cfm?URI=ao-41-35-7437. 64

Ansys Inc. Ansys fluent theory guide, 2013. 85

J.E. Jensen, W.A. Tuttle, R.B Stewart, H. Brechna, and A.G Prodell. *Selected Cryogenic Data Notebook*. Brookhaven National Laboratory, 1980. URL https://www.bnl.gov/magnets/staff/gupta/cryogenic-data-handbook/Section2.pdf. 68

Aurelie Jullien, Olivier Albert, Frédéric Burgy, Guy Hamoniaux, Jean-Philippe Rousseau, Jean-Paul Chambaret, Frédérika Augé-Rochereau, Gilles Chériaux, Jean Etchepare, Nikolay Minkovski, and Solomon M. Saltiel. 10?10 temporal contrast for femtosecond ultraintense lasers by cross-polarized wave generation. *Opt. Lett.*, 30(8):920–922, Apr 2005. doi: 10.1364/OL.30.000920. URL http://ol.osa.org/abstract.cfm?URI=ol-30-8-920. 6, 104

S. Kahaly, F. Sylla, A. Lifschitz, A. Flacco, M. Veltcheva, and V. Malka. Detailed experimental study of ion acceleration by interaction of an ultra-short intense laser with an underdense plasma. *Scientific Reports*, 6:31647, Aug 2016. URL `http://dx.doi.org/10.1038/srep31647`. 8, 10, 27, 36, 101

S. Kalmykov, S. A. Yi, V. Khudik, and G. Shvets. Electron self-injection and trapping into an evolving plasma bubble. *Phys. Rev. Lett.*, 103:135004, Sep 2009. doi: 10.1103/PhysRevLett.103.135004. URL `http://link.aps.org/doi/10.1103/PhysRevLett.103.135004`. 45

M. Kaluza, J. Schreiber, M. I. K. Santala, G. D. Tsakiris, K. Eidmann, J. Meyer-ter Vehn, and K. J. Witte. Influence of the laser prepulse on proton acceleration in thin-foil experiments. *Phys. Rev. Lett.*, 93:045003, Jul 2004. doi: 10.1103/PhysRevLett.93.045003. URL `http://link.aps.org/doi/10.1103/PhysRevLett.93.045003`. 6

Masato Kanasaki, Atsuto Hattori, Hironao Sakaki, Yuji Fukuda, Akifumi Yogo, Satoshi Jinno, Mamiko Nishiuchi, Koichi Ogura, Kiminori Kondo, Keiji Oda, and Tomoya Yamauchi. A high energy component of the intense laser-accelerated proton beams detected by stacked cr-39. *Radiation Measurements*, 50:46 – 49, 2013. ISSN 1350-4487. doi: http://dx.doi.org/10.1016/j.radmeas.2012.10.009. URL `http://www.sciencedirect.com/science/article/pii/S1350448712003046`. 25th {ICNTS}. 107

L. V. Keldysh. Ionization in the field of a strong electromagnetic wave. *JETP*, 20(5): 1307, 1965. URL `http://www.jetp.ac.ru/cgi-bin/dn/e_020_05_1307.pdf`. 26

I Jong Kim, Ki Hong Pae, Chul Min Kim, Hyung Taek Kim, Jae Hee Sung, Seong Ku Lee, Tae Jun Yu, Il Woo Choi, Chang-Lyoul Lee, Kee Hwan Nam, Peter V. Nickles, Tae Moon Jeong, and Jongmin Lee. Transition of proton energy scaling using an ultrathin target irradiated by linearly polarized femtosecond laser pulses. *Phys. Rev. Lett.*, 111:165003, Oct 2013. doi: 10.1103/PhysRevLett.111.165003. URL `http://link.aps.org/doi/10.1103/PhysRevLett.111.165003`. 6, 7, 145

I. Jong Kim, Ki Hong Pae, Il Woo Choi, Chang-Lyoul Lee, Hyung Taek Kim, Himanshu Singhal, Jae Hee Sung, Seong Ku Lee, Hwang Woon Lee, Peter V. Nickles, Tae Moon Jeong, Chul Min Kim, and Chang Hee Nam. Radiation pressure acceleration of protons to 93 mev with circularly polarized petawatt laser pulses. *Physics of Plasmas*, 23(7):070701, 2016. doi: http://dx.doi.org/10.1063/1.4958654. URL `http://scitation.aip.org/content/aip/journal/pop/23/7/10.1063/1.4958654`. 6, 7, 59

Myun-Sik Kim, Toralf Scharf, Christoph Menzel, Carsten Rockstuhl, and Hans Peter Herzig. Talbot images of wavelength-scale amplitude gratings. *Opt. Express*, 20(5):4903–4920, Feb 2012. doi: 10.1364/OE.20.004903. URL `http://www.opticsexpress.org/abstract.cfm?URI=oe-20-5-4903`. 161

G. F. Knoll. *Radiation Detection and Measurement*. Wiley, New York, 2010. ISBN 978-0-470-13148-0. 4

H. Knudsen, H. K. Haugen, and P. Hvelplund. Single-electron-capture cross section for medium- and high-velocity, highly charged ions colliding with atoms. *Phys. Rev. A*, 23:597–610, Feb 1981. doi: 10.1103/PhysRevA.23.597. URL `http://link.aps.org/doi/10.1103/PhysRevA.23.597`. 151

M Koenig, A Benuzzi-Mounaix, A Ravasio, T Vinci, N Ozaki, S Lepape, D Batani, G Huser, T Hall, D Hicks, A MacKinnon, P Patel, H S Park, T Boehly, M Borghesi, S Kar, and L Romagnani. Progress in the study of warm dense matter. *Plasma Physics and Controlled Fusion*, 47(12B):B441, 2005. URL `http://stacks.iop.org/0741-3335/47/i=12B/a=S31`. 4

Pankaj S. Kolhe and Ajay K. Agrawal. Abel inversion of deflectometric data: comparison of accuracy and noise propagation of existing techniques. *Appl. Opt.*, 48 (20):3894–3902, Jul 2009. doi: 10.1364/AO.48.003894. URL `http://ao.osa.org/abstract.cfm?URI=ao-48-20-3894`. 166, 167

I Kostyukov, E Nerush, A Pukhov, and V Seredov. A multidimensional theory for electron trapping by a plasma wake generated in the bubble regime. *New Journal of Physics*, 12(4):045009, 2010. URL `http://stacks.iop.org/1367-2630/12/i=4/a=045009`. 45

K. Krushelnick, E. L. Clark, Z. Najmudin, M. Salvati, M. I. K. Santala, M. Tatarakis, A. E. Dangor, V. Malka, D. Neely, R. Allott, and C. Danson. Multi-mev ion production from high-intensity laser interactions with underdense plasmas. *Phys. Rev. Lett.*, 83:737–740, Jul 1999. doi: 10.1103/PhysRevLett.83.737. URL `http://link.aps.org/doi/10.1103/PhysRevLett.83.737`. 3, 7, 10, 27, 28, 36

A. V. Kuznetsov, T. Zh. Esirkepov, F. F. Kamenets, and S. V. Bulanov. Efficiency of ion acceleration by a relativistically strong laser pulse in an underdense plasma. *Plasma Physics Reports*, 27(3):211–220, 2001. ISSN 1562-6938. doi: 10.1134/1.1354219. URL `http://dx.doi.org/10.1134/1.1354219`. 34

B.E. Launder and B.I. Sharma. Application of the energy-dissipation model of turbulence to the calculation of flow near a spinning disc. *Letters in Heat and Mass Transfer*, 1(2):131 – 137, 1974. ISSN 0094-4548. doi: http://dx.doi.org/10.1016/0094-4548(74)90150-7. URL `http://www.sciencedirect.com/science/article/pii/0094454874901507`. 91

Brian Edward Launder. Second-moment closure and its use in modelling turbulent industrial flows. *International Journal for Numerical Methods in Fluids*, 9(8):963–985, 1989. 91

K. W. D. Ledingham, P. McKenna, and R. P. Singhal. Applications for nuclear phenomena generated by ultra-intense lasers. *Science*, 300(5622):1107–1111, 2003. ISSN 0036-8075. doi: 10.1126/science.1080552. URL `http://science.sciencemag.org/content/300/5622/1107`. 4

W. P. Leemans, P. Catravas, E. Esarey, C. G. R. Geddes, C. Toth, R. Trines, C. B. Schroeder, B. A. Shadwick, J. van Tilborg, and J. Faure. Electron-yield enhancement in a laser-wakefield accelerator driven by asymmetric laser pulses. *Phys. Rev. Lett.*, 89:174802, Oct 2002. doi: 10.1103/PhysRevLett.89.174802. URL http://link.aps.org/doi/10.1103/PhysRevLett.89.174802. 136

A Lifschitz, F Sylla, S Kahaly, A Flacco, M Veltcheva, G Sanchez-Arriaga, E Lefebvre, and V Malka. Ion acceleration in underdense plasmas by ultra-short laser pulses. *New Journal of Physics*, 16(3):033031, 2014. URL http://stacks.iop.org/1367-2630/16/i=3/a=033031. 8, 27, 29, 34, 36, 51, 114

A. F. Lifschitz, X. Davoine, E. Lefebvre, J. Faure, C. Rechatin, and V. Malka. Particle-in-cell modelling of laser-plasma interaction using fourier decomposition. *J. Comput. Phys.*, 228(5):1803–1814, March 2009. ISSN 0021-9991. doi: 10.1016/j.jcp.2008.11.017. URL http://dx.doi.org/10.1016/j.jcp.2008.11.017. 36, 37

F. Lindau, O. Lundh, A. Persson, P. McKenna, K. Osvay, D. Batani, and C.-G. Wahlström. Laser-accelerated protons with energy-dependent beam direction. *Phys. Rev. Lett.*, 95:175002, Oct 2005. doi: 10.1103/PhysRevLett.95.175002. URL http://link.aps.org/doi/10.1103/PhysRevLett.95.175002. 3, 145

Hang Liu, Jianguan Yao, and Ashok Puri. Second and third harmonic generation in bbo by femtosecond ti: sapphire laser pulses. *Optics Communications*, 109(1):139 – 144, 1994. ISSN 0030-4018. doi: http://dx.doi.org/10.1016/0030-4018(94)90751-X. URL http://www.sciencedirect.com/science/article/pii/003040189490751X. 112

W. Lu, C. Huang, M. Zhou, W. B. Mori, and T. Katsouleas. Nonlinear theory for relativistic plasma wakefields in the blowout regime. *Phys. Rev. Lett.*, 96:165002, Apr 2006. doi: 10.1103/PhysRevLett.96.165002. URL http://link.aps.org/doi/10.1103/PhysRevLett.96.165002. 38

W. Lu, M. Tzoufras, C. Joshi, F. S. Tsung, W. B. Mori, J. Vieira, R. A. Fonseca, and L. O. Silva. Generating multi-gev electron bunches using single stage laser wakefield acceleration in a 3d nonlinear regime. *Phys. Rev. ST Accel. Beams*, 10:061301, Jun 2007. doi: 10.1103/PhysRevSTAB.10.061301. URL http://link.aps.org/doi/10.1103/PhysRevSTAB.10.061301. 25, 38, 44

A. Macchi. *A superintense Laser-plasma Interaction Theory Primer*. Springer Briefs in Physics, New-York, 2013. ISBN 978-94-007-6124-7. 29

Andrea Macchi, Federica Cattani, Tatiana V. Liseykina, and Fulvio Cornolti. Laser acceleration of ion bunches at the front surface of overdense plasmas. *Phys. Rev. Lett.*, 94:165003, Apr 2005. doi: 10.1103/PhysRevLett.94.165003. URL http://link.aps.org/doi/10.1103/PhysRevLett.94.165003. 10, 11, 156

Andrea Macchi, Silvia Veghini, Tatyana V Liseykina, and Francesco Pegoraro. Radiation pressure acceleration of ultrathin foils. *New Journal of Physics*, 12(4):045013, 2010. URL http://stacks.iop.org/1367-2630/12/i=4/a=045013. 6

Andrea Macchi, Amritpal Singh Nindrayog, and Francesco Pegoraro. Solitary versus shock wave acceleration in laser-plasma interactions. *Phys. Rev. E*, 85:046402, Apr 2012. doi: 10.1103/PhysRevE.85.046402. URL http://link.aps.org/doi/10.1103/PhysRevE.85.046402. 11, 27, 32, 33, 59, 156

Andrea Macchi, Marco Borghesi, and Matteo Passoni. Ion acceleration by superintense laser-plasma interaction. *Rev. Mod. Phys.*, 85:751–793, May 2013. doi: 10.1103/RevModPhys.85.751. URL http://link.aps.org/doi/10.1103/RevModPhys.85.751. 6, 152

A. J. Mackinnon, P. K. Patel, R. P. Town, M. J. Edwards, T. Phillips, S. C. Lerner, D. W. Price, D. Hicks, M. H. Key, S. Hatchett, S. C. Wilks, M. Borghesi, L. Romagnani, S. Kar, T. Toncian, G. Pretzler, O. Willi, M. Koenig, E. Martinolli, S. Lepape, A. Benuzzi-Mounaix, P. Audebert, J. C. Gauthier, J. King, R. Snavely, R. R. Freeman, and T. Boehlly. Proton radiography as an electromagnetic field and density perturbation diagnostic (invited). *Review of Scientific Instruments*, 75(10):3531–3536, 2004. doi: http://dx.doi.org/10.1063/1.1788893. URL http://scitation.aip.org/content/aip/journal/rsi/75/10/10.1063/1.1788893. 4

T. H. Maiman. Stimulated optical radiation in ruby. *Nature*, 187(4736):493–494, Aug 1960. doi: 10.1038/187493a0. URL http://dx.doi.org/10.1038/187493a0. 2

G. Mainfray and G. Manus. Multiphoton ionization of atoms. *Reports on Progress in Physics*, 54(10):1333, 1991. URL http://stacks.iop.org/0034-4885/54/i=10/a=002. 26

A. Maksimchuk, S. Gu, K. Flippo, D. Umstadter, and V. Yu. Bychenkov. Forward ion acceleration in thin films driven by a high-intensity laser. *Phys. Rev. Lett.*, 84:4108–4111, May 2000. doi: 10.1103/PhysRevLett.84.4108. URL http://link.aps.org/doi/10.1103/PhysRevLett.84.4108. 3

V. Malk. On the use of gas jet targets for laser plasma interaction physics with nanosecond laser pulses. *J. Phys. IV France*, 133:289–294, 2006. doi: 10.1051/jp4:2006133057. URL http://dx.doi.org/10.1051/jp4:2006133057. 59

V. Malka, J. Faure, J. R. Marques, F. Amiranoff, J. P. Rousseau, S. Ranc, J. P. Chambaret, Z. Najmudin, B. Walton, P. Mora, and A. Solodov. Characterization of electron beams produced by ultrashort (30 fs) laser pulses. *Physics of Plasmas*, 8(6):2605–2608, 2001. doi: http://dx.doi.org/10.1063/1.1374584. URL http://scitation.aip.org/content/aip/journal/pop/8/6/10.1063/1.1374584. 140

V. Malka, S. Fritzler, E. Lefebvre, M.-M. Aleonard, F. Burgy, J.-P. Chambaret, J.-F. Chemin, K. Krushelnick, G. Malka, S. P. D. Mangles, Z. Najmudin, M. Pittman, J.-P. Rousseau, J.-N. Scheurer, B. Walton, and A. E. Dangor. Electron acceleration by a wake field forced by an intense ultrashort laser pulse. *Science*, 298(5598):1596–1600, 2002. ISSN 0036-8075. doi: 10.1126/science.1076782. URL http://science.sciencemag.org/content/298/5598/1596. 2

Victor Malka, Sven Fritzler, Erik Lefebvre, Emmanuel d'Humières, Régis Ferrand, Georges Grillon, Claude Albaret, Samuel Meyroneinc, Jean-Paul Chambaret, Andre Antonetti, and Danièle Hulin. Practicability of protontherapy using compact laser systems. *Medical Physics*, 31(6):1587–1592, 2004. doi: http://dx.doi.org/10.1118/1.1747751. URL http://scitation.aip.org/content/aapm/journal/medphys/31/6/10.1118/1.1747751. 4

G.V. Marr and J.B. West. Absolute photoionization cross-section tables for helium, neon, argon, and krypton in the vuv spectral regions. *Atomic Data and Nuclear Data Tables*, 18(5):497 – 508, 1976. ISSN 0092-640X. doi: http://dx.doi.org/10.1016/0092-640X(76)90015-2. URL http://www.sciencedirect.com/science/article/pii/0092640X76900152. 153

K. Matsukado, T. Esirkepov, K. Kinoshita, H. Daido, T. Utsumi, Z. Li, A. Fukumi, Y. Hayashi, S. Orimo, M. Nishiuchi, S. V. Bulanov, T. Tajima, A. Noda, Y. Iwashita, T. Shirai, T. Takeuchi, S. Nakamura, A. Yamazaki, M. Ikegami, T. Mihara, A. Morita, M. Uesaka, K. Yoshii, T. Watanabe, T. Hosokai, A. Zhidkov, A. Ogata, Y. Wada, and T. Kubota. Energetic protons from a few-micron metallic foil evaporated by an intense laser pulse. *Phys. Rev. Lett.*, 91:215001, Nov 2003. doi: 10.1103/PhysRevLett.91.215001. URL http://link.aps.org/doi/10.1103/PhysRevLett.91.215001. 9, 10, 11, 34, 59, 156

P McCallion, M B Shah, and H B Gilbody. A crossed beam study of the multiple ionization of argon by electron impact. *Journal of Physics B: Atomic, Molecular and Optical Physics*, 25(5):1061, 1992. URL http://stacks.iop.org/0953-4075/25/i=5/a=017. 153

P. McKenna, K. W. D. Ledingham, J. M. Yang, L. Robson, T. McCanny, S. Shimizu, R. J. Clarke, D. Neely, K. Spohr, R. Chapman, R. P. Singhal, K. Krushelnick, M. S. Wei, and P. A. Norreys. Characterization of proton and heavier ion acceleration in ultrahigh-intensity laser interactions with heated target foils. *Phys. Rev. E*, 70:036405, Sep 2004. doi: 10.1103/PhysRevE.70.036405. URL http://link.aps.org/doi/10.1103/PhysRevE.70.036405. 4

P. McKenna, K. W. D. Ledingham, S. Shimizu, J. M. Yang, L. Robson, T. McCanny, J. Galy, J. Magill, R. J. Clarke, D. Neely, P. A. Norreys, R. P. Singhal, K. Krushelnick, and M. S. Wei. Broad energy spectrum of laser-accelerated protons for spallation-related physics. *Phys. Rev. Lett.*, 94:084801, Mar 2005. doi: 10.1103/PhysRevLett.94.084801. URL http://link.aps.org/doi/10.1103/PhysRevLett.94.084801. 4

W. S. Melo, M. M. Sant'Anna, A. C. F. Santos, G. M. Sigaud, and E. C. Montenegro. Electron loss and single and double capture of c^{3+} and o^{5+} ions in collisions with noble gases. *Phys. Rev. A*, 60:1124–1134, Aug 1999. doi: 10.1103/PhysRevA.60.1124. URL http://link.aps.org/doi/10.1103/PhysRevA.60.1124. 151, 152

C. Michaut, C. Stehlé, S. Leygnac, T. Lanz, and L. Boireau. Jump conditions in hypersonic shocks. *The European Physical Journal D - Atomic, Molecular, Optical and Plasma Physics*, 28(3):381–392, 2004. ISSN 1434-6079. doi: 10.1140/epjd/e2003-00322-3. URL http://dx.doi.org/10.1140/epjd/e2003-00322-3. 135

F Mollica, L Antonelli, A Flacco, J Braenzel, B Vauzour, G Folpini, G Birindelli, M Schnuerer, D Batani, and V Malka. Efficient laser production of energetic neutral beams. *Plasma Physics and Controlled Fusion*, 58(3):034016, 2016. URL `http://stacks.iop.org/0741-3335/58/i=3/a=034016`. 144

P. Mora. Plasma expansion into a vacuum. *Phys. Rev. Lett.*, 90:185002, May 2003. doi: 10.1103/PhysRevLett.90.185002. URL `http://link.aps.org/doi/10.1103/PhysRevLett.90.185002`. 3, 54, 152

P. Mora. Thin-foil expansion into a vacuum. *Phys. Rev. E*, 72:056401, Nov 2005. doi: 10.1103/PhysRevE.72.056401. URL `http://link.aps.org/doi/10.1103/PhysRevE.72.056401`. 145, 152

W. B. Mori. The physics of the nonlinear optics of plasmas at relativistic intensities for short-pulse lasers. *IEEE Journal of Quantum Electronics*, 33(11):1942–1953, Nov 1997. ISSN 0018-9197. doi: 10.1109/3.641309. 23, 25

H. M. Mott-Smith. The solution of the boltzmann equation for a shock wave. *Phys. Rev.*, 82:885–892, Jun 1951. doi: 10.1103/PhysRev.82.885. URL `http://link.aps.org/doi/10.1103/PhysRev.82.885`. 60, 126

T. Nakamura, Y. Fukuda, A. Yogo, M. Tampo, M. Kando, Y. Hayashi, T. Kameshima, A.S. Pirozhkov, T.Zh. Esirkepov, T.A. Pikuz, A.Ya. Faenov, H. Daido, and S.V. Bulanov. Coulomb implosion mechanism of negative ion acceleration in laser plasmas. *Physics Letters A*, 373(30):2584 – 2587, 2009. ISSN 0375-9601. doi: http://dx.doi.org/10.1016/j.physleta.2009.05.043. URL `http://www.sciencedirect.com/science/article/pii/S0375960109006306`. 145

Tatsufumi Nakamura, Sergei V. Bulanov, Timur Zh. Esirkepov, and Masaki Kando. High-energy ions from near-critical density plasmas via magnetic vortex acceleration. *Phys. Rev. Lett.*, 105:135002, Sep 2010. doi: 10.1103/PhysRevLett.105.135002. URL `http://link.aps.org/doi/10.1103/PhysRevLett.105.135002`. 9, 10, 11, 27, 34, 60, 156

D. Neely, P. Foster, A. Robinson, F. Lindau, O. Lundh, A. Persson, C.-G. Wahlström, and P. McKenna. Enhanced proton beams from ultrathin targets driven by high contrast laser pulses. *Applied Physics Letters*, 89(2):021502, 2006. doi: http://dx.doi.org/10.1063/1.2220011. URL `http://scitation.aip.org/content/aip/journal/apl/89/2/10.1063/1.2220011`. 4

I. Nezu and W.Rodi. Open-channel flow measurements with a laser doppler anemometer. *Journal of Hydraulic Engineering*, 112(5):335–355, 1986. doi: http://dx.doi.org/10.1061/(ASCE)0733-9429(1986)112:5(335). 87

Steven A Orszag, Victor Yakhot, William S Flannery, Ferit Boysan, Dipankar Choudhury, Joseph Maruzewski, and Bart Patel. Renormalization group modeling and turbulence simulations. *Near-wall turbulent flows*, pages 1031–1046, 1993. 91

J Osterhoff, D R Symes, A D Edens, A S Moore, E Hellewell, and T Ditmire. Radiative shell thinning in intense laser-driven blast waves. *New Journal of Physics*, 11(2): 023022, 2009. URL `http://stacks.iop.org/1367-2630/11/i=2/a=023022`. 120, 121, 134

Sasi Palaniyappan, B. Manuel Hegelich, Hui-Chun Wu, Daniel Jung, Donald C. Gautier, Lin Yin, Brian J. Albright, Randall P. Johnson, Tsutomu Shimada, Samuel Letzring, Dustin T. Offermann, Jun Ren, Chengkun Huang, Rainer Horlein, Brendan Dromey, Juan C. Fernandez, and Rahul C. Shah. Dynamics of relativistic transparency and optical shuttering in expanding overdense plasmas. *Nat Phys*, 8(10):763–769, Oct 2012. ISSN 1745-2473. doi: 10.1038/nphys2390. URL `http://dx.doi.org/10.1038/nphys2390`. 6

Sasi Palaniyappan, Chengkun Huang, Donald C. Gautier, Christopher E. Hamilton, Miguel A. Santiago, Christian Kreuzer, Adam B. Sefkow, Rahul C. Shah, and Juan C. Fernandez. Efficient quasi-monoenergetic ion beams from laser-driven relativistic plasmas. *Nat Commun*, 6, Dec 2015. URL `http://dx.doi.org/10.1038/ncomms10170`. Supplementary information available for this article at http://www.nature.com/ncomms/2015/151211/ncomms10170/suppinfo/ncomms10170_S1.html. 6

Charlotte A. J. Palmer, N. P. Dover, I. Pogorelsky, M. Babzien, G. I. Dudnikova, M. Ispiriyan, M. N. Polyanskiy, J. Schreiber, P. Shkolnikov, V. Yakimenko, and Z. Najmudin. Monoenergetic proton beams accelerated by a radiation pressure driven shock. *Phys. Rev. Lett.*, 106:014801, Jan 2011. doi: 10.1103/PhysRevLett.106.014801. URL `http://link.aps.org/doi/10.1103/PhysRevLett.106.014801`. 6, 8, 9, 10, 11, 27, 124, 156

M Passoni, A Zani, A Sgattoni, D Dellasega, A Macchi, I Prencipe, V Floquet, P Martin, T V Liseykina, and T Ceccotti. Energetic ions at moderate laser intensities using foam-based multi-layered targets. *Plasma Physics and Controlled Fusion*, 56 (4):045001, 2014. URL `http://stacks.iop.org/0741-3335/56/i=4/a=045001`. 6, 59

P. K. Patel, A. J. Mackinnon, M. H. Key, T. E. Cowan, M. E. Foord, M. Allen, D. F. Price, H. Ruhl, P. T. Springer, and R. Stephens. Isochoric heating of solid-density matter with an ultrafast proton beam. *Phys. Rev. Lett.*, 91:125004, Sep 2003. doi: 10.1103/PhysRevLett.91.125004. URL `http://link.aps.org/doi/10.1103/PhysRevLett.91.125004`. 4

V B Pathak, J Vieira, R A Fonseca, and L O Silva. Effect of the frequency chirp on laser wakefield acceleration. *New Journal of Physics*, 14(2):023057, 2012. URL `http://stacks.iop.org/1367-2630/14/i=2/a=023057`. 136

F. Pegoraro and S. V. Bulanov. Photon bubbles and ion acceleration in a plasma dominated by the radiation pressure of an electromagnetic pulse. *Phys. Rev. Lett.*, 99:065002, Aug 2007. doi: 10.1103/PhysRevLett.99.065002. URL `http://link.aps.org/doi/10.1103/PhysRevLett.99.065002`. 6

R. A. Phaneuf, F. W. Meyer, and R. H. McKnight. Single-electron capture by multiply charged ions of carbon, nitrogen, and oxygen in atomic and molecular hydrogen. *Phys. Rev. A*, 17:534–545, Feb 1978. doi: 10.1103/PhysRevA.17.534. URL `http://link.aps.org/doi/10.1103/PhysRevA.17.534`. 150

G. R. Plateau, N. H. Matlis, C. G. R. Geddes, A. J. Gonsalves, S. Shiraishi, C. Lin, R. A. van Mourik, and W. P. Leemans. Wavefront-sensor-based electron density measurements for laser-plasma accelerators. *Review of Scientific Instruments*, 81(3): 033108, 2010. doi: http://dx.doi.org/10.1063/1.3360889. URL `http://scitation.aip.org/content/aip/journal/rsi/81/3/10.1063/1.3360889`. 64, 146

H. Popescu, S. D. Baton, F. Amiranoff, C. Rousseaux, M. Rabec Le Gloahec, J. J. Santos, L. Gremillet, M. Koenig, E. Martinolli, T. Hall, J. C. Adam, A. Heron, and D. Batani. Subfemtosecond, coherent, relativistic, and ballistic electron bunches generated at omega0 and 2omega0 in high intensity laser-matter interaction. *Physics of Plasmas*, 12(6):063106, 2005. doi: http://dx.doi.org/10.1063/1.1927328. URL `http://scitation.aip.org/content/aip/journal/pop/12/6/10.1063/1.1927328`. 152

R. Prasad, D. Doria, S. Ter-Avetisyan, P.S. Foster, K.E. Quinn, L. Romagnani, C.M. Brenner, J.S. Green, P. Gallegos, M.J.V. Streeter, D.C. Carroll, O. Tresca, N. Dover, C.A.J. Palmer, J. Schreiber, D. Neely, Z. Najmudin, P. McKenna, M. Zepf, and M. Borghesi. Calibration of thomson parabola—mcp assembly for multi-mev ion spectroscopy. *Nuclear Instruments and Methods in Physics Research Section A: Accelerators, Spectrometers, Detectors and Associated Equipment*, 623(2):712 – 715, 2010. ISSN 0168-9002. doi: http://dx.doi.org/10.1016/j.nima.2010.02.078. URL `http://www.sciencedirect.com/science/article/pii/S0168900210002767`. 109, 147

R. Prasad, F. Abicht, M. Borghesi, J. Braenzel, P. V. Nickles, G. Priebe, M. Schnuerer, and S. Ter-Avetisyan. Thomson spectrometer–microchannel plate assembly calibration for mev-range positive and negative ions, and neutral atoms. *Review of Scientific Instruments*, 84(5):053302, 2013. doi: http://dx.doi.org/10.1063/1.4803670. URL `http://scitation.aip.org/content/aip/journal/rsi/84/5/10.1063/1.4803670`. 147

Jérôme Primot and Nicolas Guérineau. Extended hartmann test based on the pseudoguiding property of a hartmann mask completed by a phase chessboard. *Appl. Opt.*, 39(31):5715–5720, Nov 2000. doi: 10.1364/AO.39.005715. URL `http://ao.osa.org/abstract.cfm?URI=ao-39-31-5715`. 160, 161, 163

A. Pukhov and J. Meyer-ter Vehn. Laser wake field acceleration: the highly non-linear broken-wave regime. *Applied Physics B*, 74(4):355–361, 2002. ISSN 1432-0649. doi: 10.1007/s003400200795. URL `http://dx.doi.org/10.1007/s003400200795`. 38

R. Rajeev, K. P. M. Madhu Trivikram, T. Rishad, V. Narayanan, E. Krishnakumar, and M. Krishnamurthy. A compact laser-driven plasma accelerator for megaelectronvolt-energy neutral atoms. *Nature Physics*, 9:185–190, 2013. doi: http://dx.doi.org/

10.1038/nphys2526. URL http://www.nature.com/nphys/journal/v9/n3/full/nphys2526.html#supplementary-information. 145, 146, 152

A P L Robinson, P Gibbon, S M Pfotenhauer, O Jäckel, and J Polz. Scaling of the proton density reduction scheme for the laser acceleration of proton beams with a narrow energy spread. *Plasma Physics and Controlled Fusion*, 51(2):024001, 2009. URL http://stacks.iop.org/0741-3335/51/i=2/a=024001. 6

L. Robson, P. T. Simpson, R. J. Clarke, K. W. D. Ledingham, F. Lindau, O. Lundh, T. McCanny, P. Mora, D. Neely, C.-G. Wahlstrom, M. Zepf, and P. McKenna. Scaling of proton acceleration driven by petawatt-laser-plasma interactions. *Nat Phys*, 3(1):58–62, Jan 2007. ISSN 1745-2473. doi: 10.1038/nphys476. URL http://dx.doi.org/10.1038/nphys476. 4

J. Rojas-Herrera, H. G. Rinderknecht, A. B. Zylstra, M. Gatu Johnson, D. Orozco, M. J. Rosenberg, H. Sio, F. H. Seguin, J. A. Frenje, C. K. Li, and R. D. Petrasso. Impact of x-ray dose on the response of cr-39 to 1–5.5 mev alphas. *Review of Scientific Instruments*, 86(3):033501, 2015. doi: http://dx.doi.org/10.1063/1.4913906. URL http://scitation.aip.org/content/aip/journal/rsi/86/3/10.1063/1.4913906. 108

L. Romagnani, J. Fuchs, M. Borghesi, P. Antici, P. Audebert, F. Ceccherini, T. Cowan, T. Grismayer, S. Kar, A. Macchi, P. Mora, G. Pretzler, A. Schiavi, T. Toncian, and O. Willi. Dynamics of electric fields driving the laser acceleration of multi-mev protons. *Phys. Rev. Lett.*, 95:195001, Oct 2005. doi: 10.1103/PhysRevLett.95.195001. URL http://link.aps.org/doi/10.1103/PhysRevLett.95.195001. 4, 5

M. Roth, T. E. Cowan, M. H. Key, S. P. Hatchett, C. Brown, W. Fountain, J. Johnson, D. M. Pennington, R. A. Snavely, S. C. Wilks, K. Yasuike, H. Ruhl, F. Pegoraro, S. V. Bulanov, E. M. Campbell, M. D. Perry, and H. Powell. Fast ignition by intense laser-accelerated proton beams. *Phys. Rev. Lett.*, 86:436–439, Jan 2001. doi: 10.1103/PhysRevLett.86.436. URL http://link.aps.org/doi/10.1103/PhysRevLett.86.436. 4

Antoine Rousse, Kim Ta Phuoc, Rahul Shah, Alexander Pukhov, Eric Lefebvre, Victor Malka, Sergey Kiselev, Frederic Burgy, Jean-Philippe Rousseau, Donald Umstadter, and Daniele Hulin. Production of a kev x-ray beam from synchrotron radiation in relativistic laser-plasma interaction. *Phys. Rev. Lett.*, 93:135005, Sep 2004. doi: 10.1103/PhysRevLett.93.135005. URL http://link.aps.org/doi/10.1103/PhysRevLett.93.135005. 108

G. Saffarini, Nidal Dwaikat, Mousa El-Hasan, Fuminobu Sato, Yushi Kato, and Toshiyuki Iida. The effect of infrared laser on the activation energy of cr-39 polymeric detector. *Nuclear Instruments and Methods in Physics Research Section A: Accelerators, Spectrometers, Detectors and Associated Equipment*, 680:82 – 85, 2012. ISSN 0168-9002. doi: http://dx.doi.org/10.1016/j.nima.2012.04.003. URL http://www.sciencedirect.com/science/article/pii/S0168900212003555. 108

Aakash A. Sahai, Frank S. Tsung, Adam R. Tableman, Warren B. Mori, and Thomas C. Katsouleas. Relativistically induced transparency acceleration of light ions by an ultrashort laser pulse interacting with a heavy-ion-plasma density gradient. *Phys. Rev. E*, 88:043105, Oct 2013. doi: 10.1103/PhysRevE.88.043105. URL `http://link.aps.org/doi/10.1103/PhysRevE.88.043105`. 117

A. C. F. Santos, G. M. Sigaud, W. S. Melo, M. M. Sant'Anna, and E. C. Montenegro. Absolute cross sections for electron loss, electron capture, and multiple ionization in collisions of c^{3+} with noble gases. *Phys. Rev. A*, 82:012704, Jul 2010. doi: 10.1103/PhysRevA.82.012704. URL `http://link.aps.org/doi/10.1103/PhysRevA.82.012704`. 151

S.K. Saraf, N. Al-Niemi, C.E. Brient, S.M. Grimes, and R.S. Pedroni. Determination of the light response of bc-404 plastic scintillator for 3he and 4he with energies between 3 and 13 mev. *Nuclear Instruments and Methods in Physics Research Section A: Accelerators, Spectrometers, Detectors and Associated Equipment*, 288(2):451 – 454, 1990. ISSN 0168-9002. doi: http://dx.doi.org/10.1016/0168-9002(90)90136-T. URL `http://www.sciencedirect.com/science/article/pii/016890029090136T`. 110

A. S. Schlachter, J. W. Stearns, W. G. Graham, K. H. Berkner, R. V. Pyle, and J. A. Tanis. Electron capture for fast highly charged ions in gas targets: An empirical scaling rule. *Phys. Rev. A*, 27:3372–3374, Jun 1983. doi: 10.1103/PhysRevA.27.3372. URL `http://link.aps.org/doi/10.1103/PhysRevA.27.3372`. 151

T. Schlegel, N. Naumova, V. T. Tikhonchuk, C. Labaune, I. V. Sokolov, and G. Mourou. Relativistic laser piston model: Ponderomotive ion acceleration in dense plasmas using ultraintense laser pulses. *Physics of Plasmas*, 16(8):083103, 2009. doi: 10.1063/1.3196845. URL `http://dx.doi.org/10.1063/1.319684`. 6

K. Schmid, A. Buck, C. M. S. Sears, J. M. Mikhailova, R. Tautz, D. Herrmann, M. Geissler, F. Krausz, and L. Veisz. Density-transition based electron injector for laser driven wakefield accelerators. *Phys. Rev. ST Accel. Beams*, 13:091301, Sep 2010. doi: 10.1103/PhysRevSTAB.13.091301. URL `http://link.aps.org/doi/10.1103/PhysRevSTAB.13.091301`. 59, 125, 126

M. Schnürer, F. Abicht, R. Prasad, M. Borghesi, G. Priebe, J. Braenzel, A. Andreev, P. V. Nickles, S. Jequier, V. Tikhonchuk, and S. Ter-Avetisyan. Charge steering of laser plasma accelerated fast ions in a liquid spray — creation of mev negative ion and neutral atom beams. *Physics of Plasmas (1994-present)*, 20(11):113105, 2013. doi: http://dx.doi.org/10.1063/1.4829005. URL `http://scitation.aip.org/content/aip/journal/pop/20/11/10.1063/1.4829005`. 145, 152, 154

J. Schreiber, C. Bellei, S. P. D. Mangles, C. Kamperidis, S. Kneip, S. R. Nagel, C. A. J. Palmer, P. P. Rajeev, M. J. V. Streeter, and Z. Najmudin. Complete temporal characterization of asymmetric pulse compression in a laser wakefield. *Phys. Rev. Lett.*, 105:235003, Dec 2010. doi: 10.1103/PhysRevLett.105.235003. URL `http://link.aps.org/doi/10.1103/PhysRevLett.105.235003`. 25, 136

C. B. Schroeder, E. Esarey, B. A. Shadwick, and W. P. Leemans. Trapping, dark current, and wave breaking in nonlinear plasma waves. *Physics of Plasmas*, 13(3): 033103, 2006. doi: http://dx.doi.org/10.1063/1.2173960. URL `http://scitation.aip.org/content/aip/journal/pop/13/3/10.1063/1.2173960`. 45

H. Schwoerer, S. Pfotenhauer, O. Jackel, K.-U. Amthor, B. Liesfeld, W. Ziegler, R. Sauerbrey, K. W. D. Ledingham, and T. Esirkepov. Laser-plasma acceleration of quasi-monoenergetic protons from microstructured targets. *Nature*, 439 (7075):445–448, Jan 2006. ISSN 0028-0836. doi: 10.1038/nature04492. URL `http://dx.doi.org/10.1038/nature04492`. 6, 59

R.V. Shack and B.C. Platt. Production and use of a lenticular hartmann screen. *J. Opt. Soc. Am.*, 61(5):656, 1971. doi: 10.1364/JOSA.61.000648. 160

L. O. Silva, Michael Marti, Jonathan R. Davies, Ricardo A. Fonseca, Chuang Ren, Frank S. Tsung, and Warren B. Mori. Proton shock acceleration in laser-plasma interactions. *Phys. Rev. Lett.*, 92:015002, Jan 2004. doi: 10.1103/PhysRevLett.92.015002. URL `http://link.aps.org/doi/10.1103/PhysRevLett.92.015002`. 6, 10, 11, 27, 29, 33, 59, 145, 156

C. Sinha, S. Guha, P. K. Roy, and N. C. Sil. Electron capture by protons passing through heliumlike ions. *Phys. Rev. A*, 26:2586–2591, Nov 1982. doi: 10.1103/PhysRevA.26.2586. URL `http://link.aps.org/doi/10.1103/PhysRevA.26.2586`. 153

R. A. Snavely, M. H. Key, S. P. Hatchett, T. E. Cowan, M. Roth, T. W. Phillips, M. A. Stoyer, E. A. Henry, T. C. Sangster, M. S. Singh, S. C. Wilks, A. MacKinnon, A. Offenberger, D. M. Pennington, K. Yasuike, A. B. Langdon, B. F. Lasinski, J. Johnson, M. D. Perry, and E. M. Campbell. Intense high-energy proton beams from petawatt-laser irradiation of solids. *Phys. Rev. Lett.*, 85:2945–2948, Oct 2000. doi: 10.1103/PhysRevLett.85.2945. URL `http://link.aps.org/doi/10.1103/PhysRevLett.85.2945`. 3, 4

G. Sorasio, M. Marti, R. Fonseca, and L. O. Silva. Very high mach-number electrostatic shocks in collisionless plasmas. *Phys. Rev. Lett.*, 96:045005, Feb 2006. doi: 10.1103/PhysRevLett.96.045005. URL `http://link.aps.org/doi/10.1103/PhysRevLett.96.045005`. 7, 53

P. Sprangle, C. M. Tang, and E. Esarey. Relativistic self-focusing of short-pulse radiation beams in plasmas. *IEEE Transactions on Plasma Science*, 15(2):145–153, April 1987. ISSN 0093-3813. doi: 10.1109/TPS.1987.4316677. 23, 24, 25, 36, 41, 56, 116, 117

D. Strickland and G. Mourou. Compression of amplified chirped optical pulses. *Optics Communications*, 55(6):447 – 449, 1985. ISSN 0030-4018. doi: http://dx.doi.org/10.1016/0030-4018(85)90151-8. URL `http://www.sciencedirect.com/science/article/pii/0030401885901518`. 2

F. Sylla, A. Flacco, S. Kahaly, M. Veltcheva, A. Lifschitz, G. Sanchez-Arriaga, E. Lefebvre, and V. Malka. Anticorrelation between ion acceleration and nonlinear coherent structures from laser-underdense plasma interaction. *Phys. Rev. Lett.*, 108:115003, Mar 2012a. doi: 10.1103/PhysRevLett.108.115003. URL `http://link.aps.org/doi/10.1103/PhysRevLett.108.115003`. 101, 114, 145

F. Sylla, M. Veltcheva, S. Kahaly, A. Flacco, and V. Malka. Development and characterization of very dense submillimetric gas jets for laser-plasma interaction. *Review of Scientific Instruments*, 83(3):033507, 2012b. doi: http://dx.doi.org/10.1063/1.3697859. URL `http://scitation.aip.org/content/aip/journal/rsi/83/3/10.1063/1.3697859`. 61

S.F. Sylla, V.A. Malka, A.F. Flacco, M.I. Veltcheva, and S. Kahaly. Method and arrangement for generating a jet of fluid, method and system for transforming the jet into a plasma, and uses of said system, September 11 2014. URL `https://www.google.com/patents/US20140254766`. US Patent App. 14/123,791. 60, 61

D.R. Symes, M. Hohenberger, J. Lazarus, J. Osterhoff, A.S. Moore, R.R. Fäustlin, A.D. Edens, H.W. Doyle, R.E. Carley, A. Marocchino, J.P. Chittenden, A.C. Bernstein, E.T. Gumbrell, Mike Dunne, R.A. Smith, and T. Ditmire. Investigations of laser-driven radiative blast waves in clustered gases. *High Energy Density Physics*, 6(2):274 – 279, 2010. ISSN 1574-1818. doi: http://dx.doi.org/10.1016/j.hedp.2009.11.006. URL `http://www.sciencedirect.com/science/article/pii/S157418180900127X`. {ICHED} 2009 - 2nd International Conference on High Energy Density Physics. 134, 135

T. Tajima and J. M. Dawson. Laser electron accelerator. *Phys. Rev. Lett.*, 43:267–270, Jul 1979. doi: 10.1103/PhysRevLett.43.267. URL `http://link.aps.org/doi/10.1103/PhysRevLett.43.267`. 2

S. Ter-Avetisyan, B. Ramakrishna, M. Borghesi, D. Doria, M. Zepf, G. Sarri, L. Ehrentraut, A. Andreev, P. V. Nickles, S. Steinke, W. Sandner, M. Schnürer, and V. Tikhonchuk. Mev negative ion generation from ultra-intense laser interaction with a water spray. *Applied Physics Letters*, 99(5):051501, 2011. doi: http://dx.doi.org/10.1063/1.3622664. URL `http://scitation.aip.org/content/aip/journal/apl/99/5/10.1063/1.3622664`. 59, 145, 146

S. Ter-Avetisyan, B. Ramakrishna, R. Prasad, M. Borghesi, P. V. Nickles, S. Steinke, M. Schnürer, K. I. Popov, L. Ramunno, N. V. Zmitrenko, and V. Yu. Bychenkov. Generation of a quasi-monoergetic proton beam from laser-irradiated sub-micron droplets. *Physics of Plasmas*, 19(7):073112, 2012. doi: http://dx.doi.org/10.1063/1.4731712. URL `http://scitation.aip.org/content/aip/journal/pop/19/7/10.1063/1.4731712`. 59

Denis Teychenne, Guy Bonnaud, and Jean Louis Bobin. Electrostatic and kinetic energies in the wake wave of a short laser pulse. *Physics of Plasmas*, 1(6):1771–1773, 1994. doi: http://dx.doi.org/10.1063/1.870682. URL `http://scitation.aip.org/content/aip/journal/pop/1/6/10.1063/1.870682`. 54

K.M. Thabayneh and M.Y. Shoeib. Studying some properties of cr-39 detector under the effect of different gamma doses. *Journal of the Association of Arab Universities for Basic and Applied Sciences*, 20:55 – 60, 2016. ISSN 1815-3852. doi: http://dx.doi.org/10.1016/j.jaubas.2014.11.003. URL `http://www.sciencedirect.com/science/article/pii/S1815385214000601`. 108

C. Thaury, E. Guillaume, A. Dopp, R. Lehe, A. Lifschitz, K. Ta Phuoc, J. Gautier, J.-P. Goddet, A. Tafzi, A. Flacco, F. Tissandier, S. Sebban, A. Rousse, and V. Malka. Demonstration of relativistic electron beam focusing by a laser-plasma lens. *Nat Commun*, 6, Apr 2015a. URL `http://dx.doi.org/10.1038/ncomms7860`. Supplementary information available for this article at http://www.nature.com/ncomms/2015/150416/ncomms7860/suppinfo/ncomms7860_S1.html. 59

C. Thaury, E. Guillaume, A. Lifschitz, K. Ta Phuoc, M. Hansson, G. Grittani, J. Gautier, J-P. Goddet, A. Tafzi, O. Lundh, and V. Malka. Shock assisted ionization injection in laser-plasma accelerators. *Scientific Reports*, 5:054802, 2015b. doi: 10.1038/srep16310. URL `http://www.ncbi.nlm.nih.gov/pmc/articles/PMC4637871/`. 125

M. Thevenet, A. Leblanc, S. Kahaly, H Vincenti, A. Vernier, F. Quere, and J. Faure. Vacuum laser acceleration of relativistic electrons using plasma mirror injectors. *Nat. Phys.*, 12(4):355–360, 2016. ISSN 1745-2473. doi: 10.1038/nphys3597. URL `http://dx.doi.org/10.1038/nphys3597`. 138, 139

A. G. R. Thomas, S. P. D. Mangles, Z. Najmudin, M. C. Kaluza, C. D. Murphy, and K. Krushelnick. Measurements of wave-breaking radiation from a laser-wakefield accelerator. *Phys. Rev. Lett.*, 98:054802, Feb 2007a. doi: 10.1103/PhysRevLett.98.054802. URL `http://link.aps.org/doi/10.1103/PhysRevLett.98.054802`. 113, 118

A. G. R. Thomas, Z. Najmudin, S. P. D. Mangles, C. D. Murphy, A. E. Dangor, C. Kamperidis, K. L. Lancaster, W. B. Mori, P. A. Norreys, W. Rozmus, and K. Krushelnick. Effect of laser-focusing conditions on propagation and monoenergetic electron production in laser-wakefield accelerators. *Phys. Rev. Lett.*, 98:095004, Mar 2007b. doi: 10.1103/PhysRevLett.98.095004. URL `http://link.aps.org/doi/10.1103/PhysRevLett.98.095004`. 25

D.A. Tidman and N.A. Krall. *Shock Waves in Collisionless Plasmas*. Wiley-Interscience, New-York, 1971. ISBN 9780471867852. 6, 18, 29, 31

L. H. Toburen, M. Y. Nakai, and R. A. Langley. Measurement of high-energy charge-transfer cross sections for incident protons and atomic hydrogen in various gases. *Phys. Rev.*, 171:114–122, Jul 1968. doi: 10.1103/PhysRev.171.114. URL `http://link.aps.org/doi/10.1103/PhysRev.171.114`. 151, 152

O. Tresca, N. P. Dover, N. Cook, C. Maharjan, M. N. Polyanskiy, Z. Najmudin, P. Shkolnikov, and I. Pogorelsky. Spectral modification of shock accelerated ions using a hydrodynamically shaped gas target. *Phys. Rev. Lett.*, 115:094802, Aug 2015. doi: 10.1103/PhysRevLett.115.094802. URL `http://link.aps.org/doi/10.1103/PhysRevLett.115.094802`. 7, 8, 9, 10, 11, 27, 34, 53, 156

S. L. Varghese, W. Waggoner, and C. L. Cocke. Electron capture from lithium by protons and helium ions. *Phys. Rev. A*, 29:2453–2456, May 1984. doi: 10.1103/PhysRevA.29.2453. URL `http://link.aps.org/doi/10.1103/PhysRevA.29.2453`. 153

V. I. Veksler. The principle of coherent acceleration of charged particles. *The Soviet Journal of Atomic Energy*, 2(5):525–528, 1957. ISSN 1573-8205. doi: 10.1007/BF01491001. URL `http://dx.doi.org/10.1007/BF01491001`. 2

J.R. Viegas and C.C. Horstman. Comparison of multiequation turbulence models for several shock boundary-layer interaction flows. *AIAA Journal*, 17(8):811–820, 1979. doi: doi:10.2514/3.61232. URL `http://dx.doi.org/10.2514/3.61232`. 91

J Vieira, F Fiúza, L O Silva, M Tzoufras, and W B Mori. Onset of self-steepening of intense laser pulses in plasmas. *New Journal of Physics*, 12(4):045025, 2010. URL `http://stacks.iop.org/1367-2630/12/i=4/a=045025`. 25, 36, 38, 40, 44, 56, 116, 117, 136

R.V. Volkov, V.M. Gordienko, I.M. Lachko, P.M. Mikheev, B.V. Mar'in, A.B. Savel'ev, and O.V. Chutko. Generation of high-energy negative hydrogen ions upon the interaction of superintense femtosecond laser radiation with a solid target. *Journal of Experimental and Theoretical Physics Letters*, 76(3):139–142, 2002. ISSN 0021-3640. doi: 10.1134/1.1514755. URL `http://dx.doi.org/10.1134/1.1514755`. 145

T. von Karman. Turbulence and skin friction. *J. of the Aeronautical Sciences*, 1(1): 1–20, 1934. URL `http://arc.aiaa.org/doi/abs/10.2514/8.5`. 86

Christopher G. Wahl and James G. McLean. Response of cr-39 to medium energy electron irradiation. *Radiation Measurements*, 40(1):43 – 49, 2005. ISSN 1350-4487. doi: http://dx.doi.org/10.1016/j.radmeas.2004.12.003. URL `http://www.sciencedirect.com/science/article/pii/S1350448704002598`. 108

B. Wattellier, J. Fuchs, J. P. Zou, K. Abdeli, C. Haefner, and H. Pépin. High-power short-pulse laser repetition rate improvement by adaptive wave front correction. *Review of Scientific Instruments*, 75(12):5186–5192, 2004. doi: http://dx.doi.org/10.1063/1.1819379. URL `http://scitation.aip.org/content/aip/journal/rsi/75/12/10.1063/1.1819379`. 64

M. S. Wei, S. P. D. Mangles, Z. Najmudin, B. Walton, A. Gopal, M. Tatarakis, A. E. Dangor, E. L. Clark, R. G. Evans, S. Fritzler, R. J. Clarke, C. Hernandez-Gomez, D. Neely, W. Mori, M. Tzoufras, and K. Krushelnick. Ion acceleration by collisionless shocks in high-intensity-laser–underdense-plasma interaction. *Phys. Rev. Lett.*, 93: 155003, Oct 2004. doi: 10.1103/PhysRevLett.93.155003. URL `http://link.aps.org/doi/10.1103/PhysRevLett.93.155003`. 6, 7, 10

Nikita Wells. Production of neutral beams from negative ion beam systems in the ussr. Technical Report R-2909/1-ARPA, RAND, Defense Advanced Research Projects Agency, 1982. 145

S. C. Wilks, A. B. Langdon, T. E. Cowan, M. Roth, M. Singh, S. Hatchett, M. H. Key, D. Pennington, A. MacKinnon, and R. A. Snavely. Energetic proton generation in ultra-intense laser–solid interactions. *Physics of Plasmas*, 8(2):542–549, 2001. doi: http://dx.doi.org/10.1063/1.1333697. URL `http://scitation.aip.org/content/aip/journal/pop/8/2/10.1063/1.1333697`. 3

L. Willingale, S. P. D. Mangles, P. M. Nilson, R. J. Clarke, A. E. Dangor, M. C. Kaluza, S. Karsch, K. L. Lancaster, W. B. Mori, Z. Najmudin, J. Schreiber, A. G. R. Thomas, M. S. Wei, and K. Krushelnick. Collimated multi-mev ion beams from high-intensity laser interactions with underdense plasma. *Phys. Rev. Lett.*, 96:245002, Jun 2006. doi: 10.1103/PhysRevLett.96.245002. URL `http://link.aps.org/doi/10.1103/PhysRevLett.96.245002`. 8, 9, 10, 27, 34, 59, 98, 107, 124, 126, 156

L. Willingale, S. P. D. Mangles, P. M. Nilson, R. J. Clarke, A. E. Dangor, M. C. Kaluza, S. Karsch, K. L. Lancaster, W. B. Mori, Z. Najmudin, J. Schreiber, A. G. R. Thomas, M. S. Wei, and K. Krushelnick. Willingale *et al.* reply:. *Phys. Rev. Lett.*, 98:049504, Jan 2007. doi: 10.1103/PhysRevLett.98.049504. URL `http://link.aps.org/doi/10.1103/PhysRevLett.98.049504`. 9, 34

L. Willingale, S. R. Nagel, A. G. R. Thomas, C. Bellei, R. J. Clarke, A. E. Dangor, R. Heathcote, M. C. Kaluza, C. Kamperidis, S. Kneip, K. Krushelnick, N. Lopes, S. P. D. Mangles, W. Nazarov, P. M. Nilson, and Z. Najmudin. Characterization of high-intensity laser propagation in the relativistic transparent regime through measurements of energetic proton beams. *Phys. Rev. Lett.*, 102:125002, Mar 2009. doi: 10.1103/PhysRevLett.102.125002. URL `http://link.aps.org/doi/10.1103/PhysRevLett.102.125002`. 11, 43, 59

J C Wolfe and B P Craver. Neutral particle lithography: a simple solution to charge-related artefacts in ion beam proximity printing. *Journal of Physics D: Applied Physics*, 41(2):024007, 2008. URL `http://stacks.iop.org/0022-3727/41/i=2/a=024007`. 145

M. Wolfshtein. The velocity and temperature distribution in one-dimensional flow with turbulence augmentation and pressure gradient. *International Journal of Heat and Mass Transfer*, 12(3):301 – 318, 1969. ISSN 0017-9310. doi: http://dx.doi.org/10.1016/0017-9310(69)90012-X. URL `http://www.sciencedirect.com/science/article/pii/001793106990012X`. 93

L. Yin, B. J. Albright, B. M. Hegelich, K. J. Bowers, K. A. Flippo, T. J. T. Kwan, and J. C. Fernández. Monoenergetic and gev ion acceleration from the laser breakout afterburner using ultrathin targetsa). *Physics of Plasmas*, 14(5):056706, 2007. doi: http://dx.doi.org/10.1063/1.2436857. URL `http://scitation.aip.org/content/aip/journal/pop/14/5/10.1063/1.2436857`. 6

L. Yin, B. J. Albright, D. Jung, K. J. Bowers, R. C. Shah, S. Palaniyappan, J. C. Fernández, and B. M. Hegelich. Mono-energetic ion beam acceleration in solitary waves during relativistic transparency using high-contrast circularly polarized short-pulse laser and nanoscale targets. *Physics of Plasmas*, 18(5):053103, 2011. doi:

http://dx.doi.org/10.1063/1.3587110. URL `http://scitation.aip.org/content/aip/journal/pop/18/5/10.1063/1.3587110`. 6

A. Yogo, H. Daido, S. V. Bulanov, K. Nemoto, Y. Oishi, T. Nayuki, T. Fujii, K. Ogura, S. Orimo, A. Sagisaka, J.-L. Ma, T. Zh. Esirkepov, M. Mori, M. Nishiuchi, A. S. Pirozhkov, S. Nakamura, A. Noda, H. Nagatomo, T. Kimura, and T. Tajima. Laser ion acceleration via control of the near-critical density target. *Phys. Rev. E*, 77: 016401, Jan 2008. doi: 10.1103/PhysRevE.77.016401. URL `http://link.aps.org/doi/10.1103/PhysRevE.77.016401`. 9, 34

A. Yogo, K. Sato, M. Nishikino, M. Mori, T. Teshima, H. Numasaki, M. Murakami, Y. Demizu, S. Akagi, S. Nagayama, K. Ogura, A. Sagisaka, S. Orimo, M. Nishiuchi, A. S. Pirozhkov, M. Ikegami, M. Tampo, H. Sakaki, M. Suzuki, I. Daito, Y. Oishi, H. Sugiyama, H. Kiriyama, H. Okada, S. Kanazawa, S. Kondo, T. Shimomura, Y. Nakai, M. Tanoue, H. Sasao, D. Wakai, P. R. Bolton, and H. Daido. Application of laser-accelerated protons to the demonstration of dna double-strand breaks in human cancer cells. *Applied Physics Letters*, 94(18):181502, 2009. doi: http://dx.doi.org/10.1063/1.3126452. URL `http://scitation.aip.org/content/aip/journal/apl/94/18/10.1063/1.3126452`. 4

B. A. Younglove and H. J. M. Hanley. The viscosity and thermal conductivity coefficients of gaseous and liquid argon. *Journal of Physical and Chemical Reference Data*, 15(4):1323–1337, 1986. doi: http://dx.doi.org/10.1063/1.555765. URL `http://scitation.aip.org/content/aip/journal/jpcrd/15/4/10.1063/1.555765`. 68

K Zeil, S D Kraft, S Bock, M Bussmann, T E Cowan, T Kluge, J Metzkes, T Richter, R Sauerbrey, and U Schramm. The scaling of proton energies in ultrashort pulse laser plasma acceleration. *New Journal of Physics*, 12(4):045015, 2010. URL `http://stacks.iop.org/1367-2630/12/i=4/a=045015`. 5

K Zeil, J Metzkes, T Kluge, M Bussmann, T E Cowan, S D Kraft, R Sauerbrey, B Schmidt, M Zier, and U Schramm. Robust energy enhancement of ultrashort pulse laser accelerated protons from reduced mass targets. *Plasma Physics and Controlled Fusion*, 56(8):084004, 2014. URL `http://stacks.iop.org/0741-3335/56/i=8/a=084004`. 4, 59

H. Zhang, B. F. Shen, W. P. Wang, Y. Xu, Y. Q. Liu, X. Y. Liang, Y. X. Leng, R. X. Li, X. Q. Yan, J. E. Chen, and Z. Z. Xu. Collisionless shocks driven by 800nm laser pulses generate high-energy carbon ions. *Physics of Plasmas*, 22(1):013113, 2015. doi: http://dx.doi.org/10.1063/1.4907194. URL `http://scitation.aip.org/content/aip/journal/pop/22/1/10.1063/1.4907194`. 7, 10, 156

A. Zigler, T. Palchan, N. Bruner, E. Schleifer, S. Eisenmann, M. Botton, Z. Henis, S. A. Pikuz, A. Y. Faenov, D. Gordon, and P. Sprangle. 5.5–7.5 mev proton generation by a moderate-intensity ultrashort-pulse laser interaction with h_2O nanowire targets. *Phys. Rev. Lett.*, 106:134801, Mar 2011. doi: 10.1103/PhysRevLett.106.134801. URL `http://link.aps.org/doi/10.1103/PhysRevLett.106.134801`. 6, 59

université PARIS-SACLAY
ÉCOLE DOCTORALE
Ondes et Matière
(EDOM)

Titre : Interaction laser-plasma ultra-intense à la densité proche-critique pour l'accélération d'ions

Mots-clés : laser femtosecond, plasma, cible gazeuses, interaction laser-plasma relativiste, accélération d'ions.

Résumé : L'interaction d'un laser ultra-intense et ultra-court avec la matière donne naissance à des phénomènes plasmas collectifs capables de soutenir des champs intenses pouvant dépasser le $\mathrm{TV} \cdot \mathrm{m}^{-1}$. Ces champs ouvrent la possibilité de réaliser des accélérateurs de particules compacts, aussi bien d'électrons que d'ions. Des sources laser-plasma d'ions de plusieurs dizaines de MeV ont été démontré au début des années 2000, et depuis, de nombreuses applications ont été proposées : création d'isotope d'intérêt médicaux, réaction de spallation, étude de la matière dense, chauffage de combustible de fusion nucléaire, radiobiologie à haut débit de dose. L'innovation sur les cibles a été un moteur majeur de l'amélioration de ces sources. Dans la continuité de cette dynamique, l'utilisation de cibles gazeuses dîtes sous-denses ou proche critiques, a été proposé afin d'alléger les contraintes expérimentales. Les travaux présentés dans cette thèse constituent une exploration expérimentale des paramètres plasmas nécessaires à l'accélération d'ion dans des cibles de jet de gaz de densité proche-critique. Pour la première fois ces régimes sont explorés avec un laser ultra-intense femtoseconde de 150 TW. Une partie des travaux est consacrée à la réalisation d'une cible innovante, adaptée à ces nouveaux régimes d'accélération. Ensuite les travaux expérimentaux décrivent la propagation du laser et l'accélération d'électrons dans des cibles proche-critiques. Enfin une dernière partie décrit la production d'un faisceau d'atome issue d'une source d'ion laser.

Title : Ultra-intense laser-plasma interaction at near-critical density for ion acceleration

Keywords : femtosecond laser, plasma, gas target, laser-plasma relativistic interaction, ion acceleration

Abstract :

Interaction of ultra-intense, ultra-short laser with matter gives rise to collective plasma processes able to sustain intense electric fields, up to $1\,\mathrm{TV} \cdot \mathrm{m}^{-1}$. This property spurred early interest in laser accelerator as compact, next-generation source of accelerated electrons and ions. Laser-driven ion source of several MeV had been demonstrated in early 2000. In the wake of this result, numerous applications had been proposed: isotope production of medical interest, spallation reaction, isochoric heating for Warm-Dense-Matter or nuclear fusion, radiobiology at high dose rate, protontherapy. New gaseous targets, called under-dense or near-critical, had been proposed in order to relax experimental constraints. The work presented in this thesis is an experimental exploration of the plasma conditions required to drive ion acceleration in gaseous near-critical target. For the first time, these regimes are explored with an ultra-intense, femtosecond laser of 150 TW. A part of this work has been dedicated to the design of an innovative gas target relevant to these new acceleration regimes. Then the experimental works describe laser propagation and electron acceleration in near-critical targets. Finally the last part reports the efficient production of an atomic beam neutralized from a laser-driven ion source.